International Journal of Interactive Multimedia and Artificial Intelligence

September 2022, Vol. VII, Number 5
ISSN: 1989-1660

unir LA UNIVERSIDAD EN INTERNET

"And just like any company that blissfully ignored the Internet at the turn of the century, the ones that dismiss the Internet of Things risk getting left behind."
Jared Newman

Special Issue on Multimedia Streaming and Processing in Internet of Things with Edge Intelligence

INTERNATIONAL JOURNAL OF INTERACTIVE MULTIMEDIA AND ARTIFICIAL INTELLIGENCE

ISSN: 1989-1660 –VOL. 7, NUMBER 5

Editor's Note

As the Internet of Things (IoT) further develops and expands to the Internet of Everything (IoE), high-speed multimedia streaming data processing, analysis, and shorter response times are increasingly becoming the demands of today. Driven by the Internet of Things (IoT), a new computing paradigm, Edge computing, is currently developing rapidly. Compared with traditional centralized general-purpose computing, Edge computing is a distributed architecture. The operations of applications, data and services are moved from the central node of the network to the edge nodes on the network logic for processing. Under this structure, the analysis of data and the generation of knowledge are closer to the source of the data, so it is more suitable for processing. However, with the rapid development of 5G, IoT and other services and scenarios, there are more and more intelligent terminal devices. Multimedia streaming processing in IoT becomes a very prominent problem. To overcome this problem, the adoption of intelligent Edge or Artificial Intelligence (AI) powered Edge computing (Edge-AI) can achieve the goals of lower cost, higher security, lower latency, and ease of management.

Recently, many network modeling methods, computing algorithms, and signal processing technologies have been successfully developed and applied to multimedia streaming processing in IoT with Edge Intelligence. A total of 13 papers are presented in this special issue for the purpose of collecting the latest developments and results on this research topic. We divide them into three categories: production and life applications, security, and text and image processing.

In the first set, Shi et al., in medical signal processing, constructed a framework for Electroencephalogram (EEG) signal recognition of epileptic seizures based on cloud-edge computing. Through local signal acquisition, edge signal processing and cloud signal recognition, the diagnosis of epilepsy is realized, which provides new ideas for real-time diagnosis and feedback of EEG during epileptic seizures. In addition to this, there is another paper in Electromyography (EMG) signal processing in which Proaño et al. proposed an adaptive filtering system based on embedded processing, which is an excellent alternative to sensor-computer-actuator systems and classical digital signal processors (DSP) devices. Romany et al., in intelligent surveillance, developed an integrated artificial intelligence technology for video surveillance in IoT-enabled wireless multimedia sensor networks (WMSN). The innovation of this study focuses on the object detection design of compression and clustering technologies for WMSN. In the Internet of Things for agriculture, aiming at the Unmanned Aerial Vehicle (UAV) path planning problem involved in monitoring technology in agricultural information monitoring, Qun et al. proposed an Improved Grey Wolf Optimization (IGWO) algorithm, which realizes the flight path planning of UAV in crop pest monitoring. Finally, in urban planning, Wen et al. proposed an integrated model of street tree detection and extraction from remote sensing images based on YOLOv4 and Unet network, which realizes the automation of street tree contour extraction and more accurate estimation of street tree coverage ratio.

Security has always been an important topic in the computer field. This special issue features three related studies, one focusing on doppelganger attacks on connected networks, one focusing on IoT software chain security situational awareness and the last focusing on information security in agricultural IoT.

The former is authored by Deepak et al., who developed a new technology called Steering Convention for Vitality Effective Systems (SC-VFS) to detect doppelganger attacks in IoT-based intelligent health applications. The main advantage of this study is that it improves vitality proficiency, a key constraint in the WSN framework. The second, by Xu et al., proposed an IoT software chain security situational awareness framework, which mainly includes two processes: IoT security situation classification based on support vector machines and security situation awareness based on Markov game model. It shows great potential in IoT system protection. Finally, Guo et al. proposed a general IoT blockchain terminal system architecture that integrates cryptography, blockchain and Interplanetary File System (IPFS) technologies, which strongly supports the integration of IoT and blockchain technologies.

The third set of articles focuses on the processing of text and images. For example, in text processing, Yong et al., with the help of the recently proposed Extended Variational Inference (EVI) framework, proposed a new function to replace the original variational object function to avoid the intractable moment computation, which can be used in an efficient way to derive analytically tractable solutions to invert Beta-Liouville mixture model (IBLMM). Chao et al., found that the interactive causality of the correlation between labels was often ignored, and proposed an Interactive Causal Correlation Space Reshape Multi-Label Classification (CCSRMC) algorithm, which reduces redundant information in the model and improves the performance of multi-label classifiers to a certain extent. In image processing, Shao et al. improved the representation power of importance maps using a Squeeze-and-Excitation (SE) block, and proposed a multi-depth structure to reconstruct non-important channel information at low bit rate. Dynamic Receptive Field Convolution (DRFc) is introduced to improve the ability of ordinary convolution to extract edge information, thereby increasing the weight of edge content in the importance map and improving the reconstruction quality of edge regions. Hong et al. proposed a novel end-to-end dehazing method, using the Encoder-Decoder structure to extract the texture and semantic features of hazy images, and obtained very good dehazing performance. Finally, Rabia et al., proposed a Diverse Domain Generative Adversarial Network (DD-GAN) for style transfer on real-time photographs, which realizes fast diverse domain style transfer on human face images with higher efficiency.

Finally, we would like to thank both the authors and reviewers who contributed to the special issue. Thank you so much for your hard work and support throughout the process.

Lei Shu[1]
Joel J. P. C. Rodrigues[2]
Anthony G Cohn[3]
Qirong Mao[4]
Maozhen Li[5]

[1] Nanjing Agricultural University, China / University of Lincoln, UK
[2] Federal University of Piauí, Brazil
[3] University of Leeds, UK
[4] Jiangsu University, China
[5] Brunel University, UK

DOI: 10.9781/ijimai.2022.08.010

TABLE OF CONTENTS

OPEN ACCESS JOURNAL

ISSN: 1989-1660

The International Journal of Interactive Multimedia and Artificial Intelligence is covered in Clarivate Analytics services and products. Specifically, this publication is indexed and abstracted in: *Science Citation Index Expanded, Journal Citation Reports/ Science Edition, Current Contents®/Engineering Computing and Technology.*

An EEG Signal Recognition Algorithm During Epileptic Seizure Based on Distributed Edge Computing

Shi Qiu[1], Keyang Cheng[2]*, Tao Zhou[3], Rabia Tahir[2], Liang Ting[4]*

[1] Key Laboratory of Spectral Imaging Technology CAS, Xi'an Institute of Optics and Precision Mechanics, Chinese Academy of Sciences, Xi'an, 710119 (P. R. China)
[2] School of Computer Science and Communication Engineering, Jiangsu University, Zhenjiang, 212000 (P. R. China)
[3] School of Computer Science and Engineering, North minzu University, Yinchuan, 750021 (P. R. China)
[4] Department of Radiology, the First Affiliated Hospital of Xi'an Jiaotong University, Xi'an, 71006 (P. R. China)

Received 2 July 2021 | Accepted 20 April 2022 | Published 12 July 2022

Abstract

Epilepsy is one kind of brain diseases, and its sudden unpredictability is the main cause of disability and even death. Thus, it is of great significance to identify electroencephalogram (EEG) during the seizure quickly and accurately. With the rise of cloud computing and edge computing, the interface between local detection and cloud recognition is established, which promotes the development of portable EEG detection and diagnosis. Thus, we construct a framework for identifying EEG signals in epileptic seizure based on cloud-edge computing. The EEG signals are obtained in real time locally, and the horizontal viewable model is established at the edge to enhance the internal correlation of the signals. The Takagi-Sugeno-Kang (TSK) fuzzy system is established to analyze the epileptic signals. In the cloud, the fusion of clinical features and signal features is established to establish a deep learning framework. Through local signal acquisition, edge signal processing and cloud signal recognition, the diagnosis of epilepsy is realized, which can provide a new idea for the real-time diagnosis and feedback of EEG during epileptic seizure.

Keywords

Clinical Feature, Cloud Computing, Deep Learning, Edge Computing, EEG Signal, Epilepsy, Seizure, Takagi-Sugeno-Kang (TSK).

DOI: 10.9781/ijimai.2022.07.001

I. Introduction

The epilepsy is a brain disease. Although most people with epilepsy are the same as normal people during the period of non-seizure, the unpredictability of epileptic sudden occurrence is the main cause of disability and even death of epileptic patients. The uncertainty of seizure seriously affects the life of patients [1]. Epilepsy is a chronic brain disease with recurrent seizures. Epilepsy is mainly caused by excessive discharge of brain neurons. It has the characteristics of paroxysmal, transient, repetitive and stereotyped. It can be manifested in sensory, motor, consciousness, spirit, behavior and autonomic nerve dysfunction. Human epilepsy has two characteristics: epileptiform discharges on electroencephalogram (EEG) and clinical seizures. The medical history is the main basis for the diagnosis of epilepsy. Doctors need to know through medical history: the characteristics of generalized tonic clonic seizures are loss of consciousness and generalized convulsions. If there is only general convulsion without sudden loss of consciousness, this does not support the diagnosis of epilepsy. Absence of consciousness, pseudoseizures or hypocalcemic convulsions should occur to tumble down. If the loss of consciousness is accompanied by a fall, the possibility of syncope is greater than that of absence attack. Automatism is characterized by abnormal behavior with disturbance of consciousness, seemingly purposeful but actually aimless. If the details of the seizure can be repeated after the seizure, it does not support the diagnosis of epilepsy. Epileptiform discharge on EEG is an important diagnostic evidence of epilepsy. It uses electrophysiological indexes to record the changes of electrical waves in the cerebral cortex when the brain is active. It is the overall reflection of the activity of neurons in the cerebral cortex [2]. In the field of electrical signal research in biomedical research, the EEG intelligence has been promoted, and a series of achievements have shown that signal in abnormal state is different from that in normal state due to the abnormal discharge of brain neurons during epileptic seizure. Therefore, recognizing the EEG signal is an effective epileptic detection method [3].

* Corresponding author.

E-mail addresses: kycheng@ujs.edu.cn (Keyang Cheng), liangting31500@126.com (Ting Liang).

In recent years, with the development of artificial intelligence, edge computing and cloud computing, the development of the medical field been promoted [4]. Gu et al. [5] construct a fog computing framework to manage medical big data. Abirami et al [6] compare the brain tumor data collected locally with the cloud to realize the focus detection. Shi et al. [7] analyze the opportunities and challenges of edge computing, and they indicate that edge computing is the development trend of smart medicine. Aggarwal et al. [8] establish a model from data security to realize data protection. Hosseini et al. [9] construct an edge computing framework to model multimodal data to detect epilepsy. Singh et al. [10] use edge computing to describe medical semantics. Li et al. [11] implement heart rate detection in the cloud. Oueida et al.

[12] implement medical data management based on edge computing. Abdellatif et al. [13] analyze the problems and challenges of edge computing in the medical field. Lin et al. [14] applie edge calculations to data allocation. Pustokhina et al. [15] move a deep learning network to an edge computing framework. Dou et al. [16] analyze short-time signals based on cloud computing. Rahman et al. [17] establish an edge computing framework to track the disease through the analysis of network data. Although cloud computing and edge computing have made a lot of achievements in medical treatment, there are few researches on epilepsy recognition, which are mostly based on clinical data analysis stage. A lot of researches have been carried out in epilepsy recognition: Xu et al. [18] analyze the methods of epilepsy treatment. Jefferys et al. [19] analyze the mechanism of epilepsy. Berg et al. [20] study the epilepsy characterization from clinical perspective. Koçer et al. [21] use the convolutional neural network to classify epilepsy. Pack et al. [22] analyze the cause of epilepsy from the perspective of Neurology. Margrove et al. [23] specify treatment plans based on different types of epilepsy. Rafiuddin et al. [24] establish the wavelet transform mechanism to analyze epilepsy. Pediaditis et al. [25] review the history of epilepsy. Musselman et al. [26] extract the epilepsy information from EEG signals. Chang et al. [27] use the machine learning to construct epileptic signal selection mechanism. Rosas et al. [28] analyze epileptic signals from the perspective of energy. Hosseini et al. [29] construct the quantitative and qualitative evaluation mechanism of EEG signals. Kiranyaz et al. [30] fuse time-domain and frequency-domain information to realize epileptic signal recognition. Gomez et al. [31] identify seizures by facial and eye movements. Villar et al. [32] use the signal acceleration to analyze EEG. Tao et al. [33] establish the Adaboost to realize EEG signal classification. Samiee et al. [34] use texture features to classify EEG. Yan et al. [35] establish the maximum entropy to measure epileptic patients. Qazi et al. [36] use the artificial intelligence technology to realize epileptic signal recognition. Li et al. [37] use a DWT algorithm to analyze EEG signals. Sepeta et al. [38] analyze the local EEG signal of epilepsy. Falco et al. [39] propose a new definition and classification of epilepsy. Qiu et al. [40] use the deep learning framework to detect signals. Jiang et al. [41] integrate the prior information to recognize epileptic signals. Parthiban et al. [42] establish a hybrid dragonfly optimization-based artificial neural network to realize epilepsy recognition. Si et al. [1] review the development of artificial intelligence in EEG signal detection. Thanaraj et al. [43] establish a convolutional neural network based on the entropy to detect epileptic signals.

The main problems of epilepsy recognition by EEG signals are as follows: 1) EEG signal processing has a large amount of computation and high local computational complexity. 2) It is difficult to distinguish between healthy period and epilepsy seizure. 3) It is limited to build the model only from the signal point of view.

To deal with these problems, our contributions are as follows: 1) We build a cloud-edge computing framework, manage data hierarchically, build a horizontal viewable model at the edge end and fully mining the signal correlation. 2) From the perspective of the fuzzy set, The Takagi-Sugeno-Kang (TSK) fuzzy system is established to analyze epileptic signals. 3) In the cloud, the deep learning framework is established by combining clinical features and signal features.

II. Algorithm

The signal is relatively stable during health and fluctuates greatly during seizures, as shown in . The algorithm pipeline is designed to build edge and cloud processing modules, as shown in Fig. 2. In order to enhance the difference between healthy signals and epileptic seizure, the EEG signals are sampled at the edge, the horizontal viewable algorithm is established, the strong correlation of the signals is established, and the weighted TSK fuzzy system is established. The EEG signal is predicted by an SVM classifier and the direct feedback display terminal with high prediction accuracy probability. For uncertain prediction, the advantages of cloud processor computing power are brought into full play to transmit data to the cloud in real time. Through the establishment of clinical big data, feature extraction and training model are built to achieve epileptic seizure recognition, and the database is updated by asynchronous transmission.

A. The Algorithm Based on Horizontal Viewable Image

The epileptic EEG signal belongs to time series. Each sampling point of time series is regarded as a viewable node, and the adjacent edges between nodes are regarded as viewable edges. The connectivity between different nodes depends on local convex constraints. When the connection between the sampling values at two times is not cut off by the sampling points at any other time within the interval there is an edge connection between two points; on the contrary, there is no edge connection, Fig. 3 shows the flow chart.

Based on the above analysis, we propose a horizontal viewable algorithm, which is defined as:

$$a_{ij} = \begin{cases} 1 & (n_k \le min(n_i, n_j)) \\ 0 & others \end{cases} \tag{1}$$

where n_i and n_j are nodes and a_{ij} are connected boundary values. When the value of any sampling time n_k between two nodes is less than the minimum value of the two nodes, there is an edge connection between two nodes, and a_{ij}=1, otherwise, there is no connection a_{ij}=0.

Each node in a complex network represents a point in the time series. When the values of other points between two points in the time series are less than these two points, the two points have edge connection.

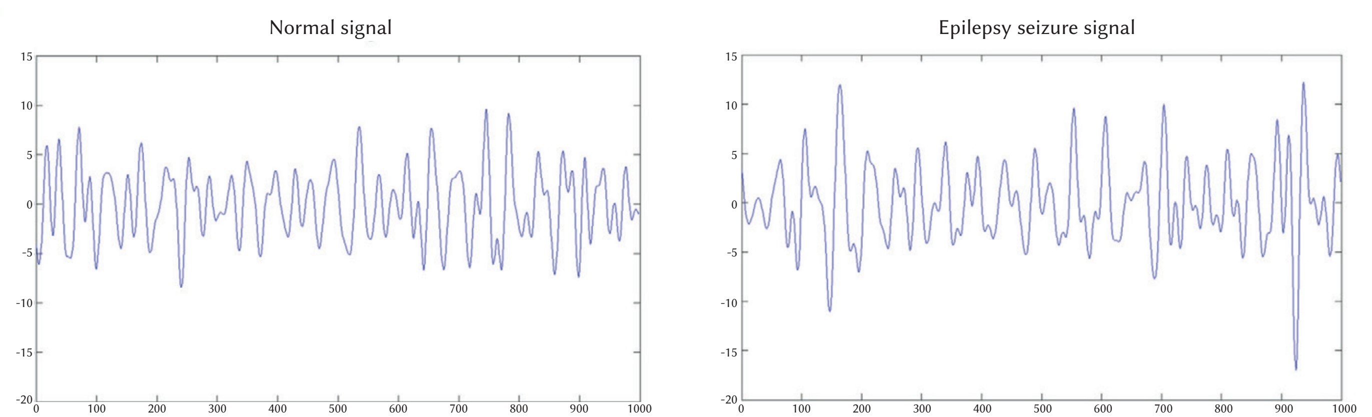

Fig. 1. EEG signal.

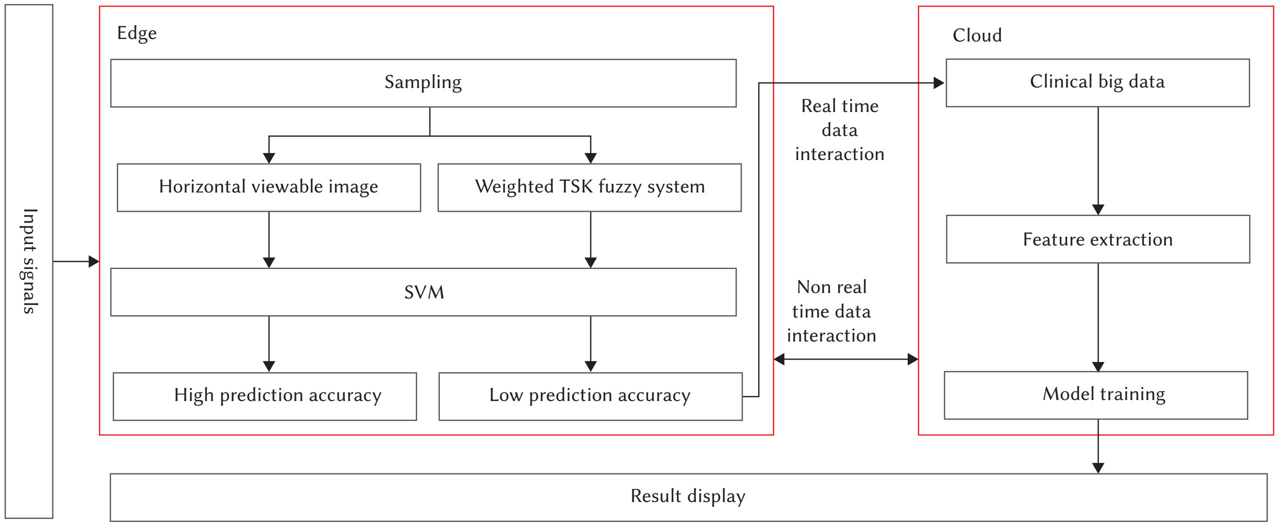

Fig. 2. Algorithm pipeline.

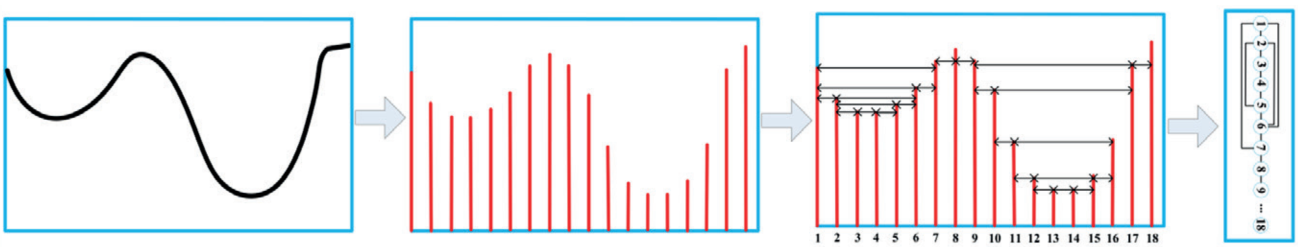

Fig. 3. Flow chart.

An important feature of complex network is the degree of complex network. Degree is defined as the number of adjacent edges of a node in the network, that is, several edges of the node are connected with other nodes. Suppose there are N nodes in the network, the expression of degree k_i of node i is:

$$k_i = \sum_{j=1}^{N} a_{ij} \tag{2}$$

Degree reflects the basic topological characteristics of complex networks, and describes the dynamic characteristics of the original time series. The average of different EEG signals is very different. In order to make the difference of degree more obvious, the power of degree is calculated as a new feature. The square of degree is extracted as the topological statistical feature from horizontal viewable image. The expression of the mean square is:

$$K_{DD} = \frac{1}{N}\sum_{j=1}^{N} k_i^2 \tag{3}$$

The complex network constructed by horizontal viewable image is a kind of binary complex network, with only 1 and 0 connected edges. On this basis, considering that there are different weights in the real complex network, this study improves the weighted level viewable algorithm. Under the criterion of horizontally viewable image, w_{ij} of edge connected a_{ij} is:

$$w_{ij} = \begin{cases} \left|\arctan\left(\dfrac{n_j - n_i}{j - i}\right)\right| & i < j, a_{ij} = 1 \\ 0 & others \end{cases} \tag{4}$$

where w_{ij} is the weight, which is expressed by the angle between two connected nodes, arctan is an arctangent transformation, and |.| is the absolute value. It is found that there are obvious differences between the angles of different complex network nodes, which reflect the fluctuation of the original time series. For time series with different dynamic structures, the complex network structures are different. Considering the concept of information entropy, this study proposes a new measurement feature for complex network structure, i.e., weight heavy distribution entropy, which reflects the topological structure information and connection complexity of complex networks. The entropy of complex networks with different features is very different. For the weighted level visualization graph, the entropy $E(i)$ of weight distribution of node n_i is:

$$E(i) = -\sum_{j=1}^{m} p_{ij}\log(p_{ij}) \tag{5}$$

$$p_{ij} = \frac{w_{ij}}{\sum_{k=1}^{m} w_{ik}} \tag{6}$$

where m is the number of nodes connected to n_i. The entropy of the average weight distribution of the weighted complex network is:

$$\bar{E} = \frac{1}{N}\sum_{i=1}^{N} E(i) \tag{7}$$

B. Weighted TSK Fuzzy System

The multi perspective features constructed from shallow and deep features have good expression ability and less information loss, but how to effectively use these features for epilepsy detection is very important. But at present, most of the researches lack the interpretability, which is very important in the practical application such as disease diagnosis. Therefore, in the development of the epileptic EEG detection technology based on multi perspective learning, a higher interpretable model is needed.

A TSK fuzzy system is an excellent model based on a rule system, which has better interpretability. Based on a TSK fuzzy system, we build an interpretable multi-view classifier for EEG detection. The TSK fuzzy system's output $f(x)$ is defined as:

$$f(x) = \sum_{k=1}^{K} \tilde{u}^k(x) f^k(x) \quad (8)$$

$$\begin{cases} \tilde{u}^k(x) = \frac{u^k(x)}{\sum_{k=1}^{K} u^k(x)} \\ f^k(x) = \sum_{i=1}^{d} p_i^k x_i \end{cases} \quad (9)$$

where p_i^k is the coefficient of x_i on the k-th rule of a linear function. $\mu^k(x)$ is the fuzzy membership degree of the k-th rule, $\tilde{u}^k(x)$ is the normalization of $\mu^k(x)$. The objective function of TSK fuzzy system is defined as:

$$\min_{\mathbf{P}_g} J(\mathbf{P}_{g,j}) = \frac{1}{2}\sum_{j=1}^{C}\sum_{i=1}^{N} \left\| (\mathbf{P}_{g,j})^T \mathbf{x}_{gi} - y_{ij} \right\|^2 + \frac{\lambda}{2}\sum_{j=1}^{C} (\mathbf{P}_{g,j})^T \mathbf{P}_{g,j} \quad (10)$$

where $\mathbf{P}_g$ is the parameter of the TSK fuzzy system. The first item expects to learn the best $\mathbf{P}_{g,j}$ to classify the training samples; The second term is the regularization penalty term, which improves the generalization ability of the TSK fuzzy system.

The calculation formula of $\mathbf{P}_g$ optimal value is:

$$\mathbf{P}_{g,j} = \left(\lambda_1 \mathbf{I}_{d\times d} + \sum_{i=1}^{N} \mathbf{x}_{gi} (\mathbf{x}_{gi})^T\right)^{-1} \left(\sum_{i=1}^{N} \mathbf{x}_{gi} y_{i,j}\right) \quad (11)$$

Given a multi-view epilepsy data set, the weighting mechanism of multi-view TSK fuzzy system is as follows:

$$Y = \frac{\lambda}{2}\sum_{k=1}^{K}\sum_{j=1}^{C}\sum_{i=1}^{N} \left\| (\mathbf{p}_{g,j}^k)\mathbf{x}_{gi}^k - \frac{1}{k-1}\sum_{l=1,l\neq k}^{K} (\tilde{\mathbf{p}}_{g,j}^k)^T \mathbf{x}_{gi}^k \right\|^2 \quad (12)$$

where $\mathbf{x}_{gi}^k$ is the k-th perspective of the i-th sample; $\mathbf{p}_{g,j}^k$ is a posteriori parameter of the k-th view of the multi-view TSK fuzzy system; $\tilde{\mathbf{p}}_{g,j}^k$ is the prior information, C is the total number of categories, K is the total number of perspectives, N is the number of samples in the data set, and λ is the regularization parameter.

It can realize multi-view cooperative learning mechanism, which ensures that all perspectives reach the same decision. λ controls the consistency between different views. If λ is too large, the prediction value of the k-th view will be too close to the prior decision value of all other views. The value of λ can be determined by the cross validation.

Based on the weighting mechanism and cooperative learning mechanism of multi-view fuzzy system, the objective function of multi-view TSK fuzzy system is constructed as follows:

$$\begin{aligned} &\min_{\mathbf{p}_g^k, w} J(\mathbf{P}_g^k, \mathbf{w}) = Q(\mathbf{P}_g^k, \mathbf{w}) + V(\mathbf{P}_g^k) + B(\mathbf{P}_g^k) \\ &V(\mathbf{P}_g^k) = \lambda_1 \sum_{k=1}^{K}\sum_{j=1}^{C} (\mathbf{P}_{g,j}^k)^T \mathbf{P}_{g,j}^k \\ &B(\mathbf{P}_g^k) = \frac{\lambda_2}{2}\sum_{k=1}^{K}\sum_{j=1}^{C}\sum_{i=1}^{N} \left\| (\mathbf{P}_{g,j}^k)^T \mathbf{x}_{gi}^k - \frac{1}{k-1}\sum_{l=1,l\neq k}^{K} (\tilde{\mathbf{P}}_{g,j}^l)^T \mathbf{x}_{gi}^l \right\|^2 \end{aligned} \quad (13)$$

where $Q(\mathbf{P}_g^k, \mathbf{w})$ is the improved multi-view weighting mechanism, w_k is the weight of the k-th view, m is the fuzzy index of w_k. By introducing the perspective weight index, we can study the updating rules of the weight in the optimal multi perspective model. $V(\mathbf{P}_g^k)$ is the regularization term, which can prevent the over-fitting phenomenon of the multi-view model. λ_1 is the coefficient of the regularization term, which is used to change the penalty of the regularization term. $B(\mathbf{P}_g^k)$ is a multi-perspective collaborative learning item, which expects each perspective to acquire the same decision value.

When updating $\mathbf{P}_g^k$, w_k is treated as a constant. Calculate $\mathbf{P}_g^k$ to acquire the gradient solution:

$$\begin{aligned} &\mathbf{P}_g^k = \mathbf{D}^{-1}\mathbf{H} \\ &\mathbf{D} = (w_k)^m \sum_{i=1}^{N} (\mathbf{x}_{gi}^k)^T \mathbf{x}_{gi}^k + \lambda_1 \mathbf{I} + \lambda_2 \sum_{i=1}^{N} (\mathbf{x}_{gi}^k)^T \mathbf{x}_{gi}^k \\ &\mathbf{H} = (w_k)^m \sum_{i=1}^{N} \mathbf{x}_{gi}^k y_{ij} + \frac{\lambda_2}{K-1}\sum_{l=1,l\neq k}^{K}\sum_{i=1}^{N} (\mathbf{x}_{gi}^l)^T \mathbf{x}_{gi}^l \tilde{\mathbf{p}}_{g,j}^l \end{aligned} \quad (14)$$

when updating w_k, $\mathbf{P}_g^k$ is treated as a constant. Calculate w_k to acquire the gradient solution:

$$w_k = \frac{\left(\sum_{j=1}^{C}\sum_{i=1}^{N} \left\| (\mathbf{p}_{g,j}^k)^T \mathbf{x}_{gi}^k - y_{i,j} \right\|^2\right)^{\frac{1}{1-m}}}{\left(\sum_{h=1}^{K}\sum_{j=1}^{C}\sum_{i=1}^{N} \left\| (\mathbf{p}_{g,j}^k)^T \mathbf{x}_{gi}^h - y_{i,j} \right\|^2\right)^{\frac{1}{1-m}}} \quad (15)$$

After multiple iterations, the optimal parameters $\mathbf{P}_g^k$ and w_k of the model are obtained. The final decision value of the model can be obtained by linear combination of decision values from different perspectives:

$$f(\mathbf{x}_{gi}^k) = sign\left(\sum_{i=1}^{N} w_k (\mathbf{p}_{g,j}^k)^T \mathbf{x}_{gi}^k\right) \quad (16)$$

C. Deep Learning Framework of Clinical and Signal Features

Epilepsy disease can be analyzed from the images and clinical information, so we fuse clinical information and signal information and propose an algorithm. Diagnosis can generally be made according to the medical history, clinical manifestations, such as recurrent muscle twitch, disturbance of consciousness and the results of relevant auxiliary examinations, such as EEG, positron tomography, etc. In the process of diagnosis, doctors need to exclude pseudoepileptic seizures, convulsive syncope, hypertensive encephalopathy, febrile convulsion and other diseases. The specific clinical features mainly include: age, gender, blood pressure, weight, disease, etc.

Due to the certain difference between healthy EEG signals and epileptic EEG signals, not all SVM classifiers can achieve good results, and there is also a correlation between the parameter setting of SVM and the quality of data. Therefore, we abandon the SVM classifiers with low accuracy, but these classifiers should also contain some information. In the future, we will carry out further research based on this.

The convolution neural network is used to automatically extract the viewable information and fuzzy information of the EEG signal, and obtain the corresponding deep features. The CNN network uses the back propagation mechanism in training. Since the eigenvector calculated by the penultimate layer only passes through one full connection layer to the output layer, it can be considered that the expression of the output eigenvector of the penultimate layer is optimized while the network structure is optimized according to the output layer training. Its network structure as shown in Fig. 4. Two types of structures are adopted. Class A and B structures that we design are mainly based on the following three reasons: 1) Class A structure learns bottom layer information. 2) Class B structure learns top layer information. 3) Class A and B structures can be effectively connected. Through the expansion of data set, the stability of a deep learning network is improved.

III. Experiment and Result Analysis

A. Experiment Data

We used Linux operating system and wrote programs with Python software. In this paper, the CHB_MIT dataset [44] is used for experimental studies. The data set collected EEG signals from 23 patients at Boston Children's hospital. These records from 23 patients were divided into 24 groups (Group 21 is the data of the first patient after resampling a few years later). Each group contains the EEG signals of one patient for more than ten consecutive hours. These consecutive signals are sampled at 256Hz, which means that there are 256 sampling points for one second signal. Each patient's EEG signal is collected from 18 points to form a single channel data set, and the subsequent processing becomes multi-channel data of 23 channels. Because the data is highly unbalanced, that is, the ratio of epileptic samples to non-epileptic samples is 1:100, if all the data are used directly, the effect of the proposed algorithm will face serious

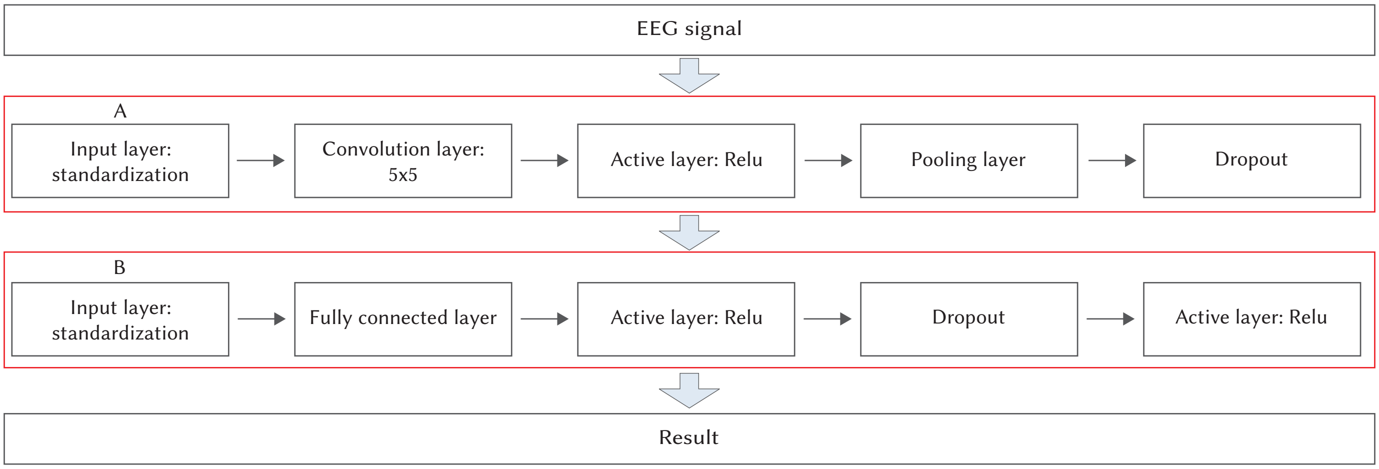

Fig. 4. The network structure.

over-fitting problem. In order to solve this problem, we discard some EEG signal data of non-epileptic, and apply over sampling technology to EEG signal data of epilepsy. A sliding window is used to divide the continuous EEG signal into several signal segments with a length of one second. The EEG signal of epilepsy is oversampled by allowing the overlap between the two windows.

B. Algorithm Performance

We verify the performance of the algorithm from the iterative curve of the algorithm, the target recognition curve with different signal-to-noise ratios, and the processing time of the algorithm.

Fig. 5 is the iteration curve of the algorithm. It can be seen that the algorithm shows an upward trend before the number of iterations reaches 50, reaches the maximum when the number of iterations is 53, and then shows a downward trend, so we will conduct research under the condition of 53 iterations.

Fig. 6 shows the detection performance of the algorithm under different signal-to-noise ratio conditions. It can be seen that as the signal-to-noise ratio increases, the effect is on the rise. In the case of a low signal-to-noise ratio, if it is less than -8DB, it still has a better recognition effect. This is because the horizontally visible image algorithm proposed in this article comprehensively considers the surrounding information and has strong noise suppression ability.

Table I shows the Time consumption. Because the transmission process is related to bandwidth, we do not count the transmission time. Normal signal is better than paroxysmal signal, and normal signal can be distinguished by primary operation. The signal processed at the edge is lower than that in the cloud. It is because the algorithm of edge processing is relatively simple, and complex signals need to be transmitted to the cloud for further processing. However, cloud is a deep learning algorithm composed of clinical big data, which is time-consuming. From the stability analysis, the variance of normal signal is better than that of paroxysmal signal because the normal signal has strong regularity. To sum up, the processing time of the algorithm can be controlled within 4s.

TABLE I. Computing Time

	Edge		Cloud	
	Normal	Seizure	Normal	Seizure
Mean	0.41 s	0.68 s	1.50 s	2.31 s
Variance	0.06 s	0.09 s	0.07 s	0.12 s
Maximum	0.72 s	0.95 s	2.10 s	2.68 s
Minimum	0.34 s	0.51 s	1.23 s	2.01 s

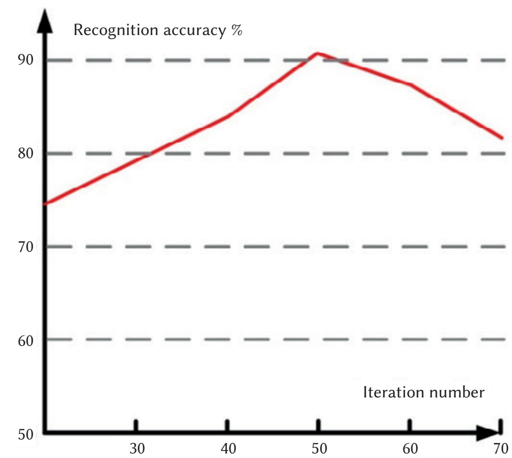

Fig. 5. The iteration curve of the proposed algorithm.

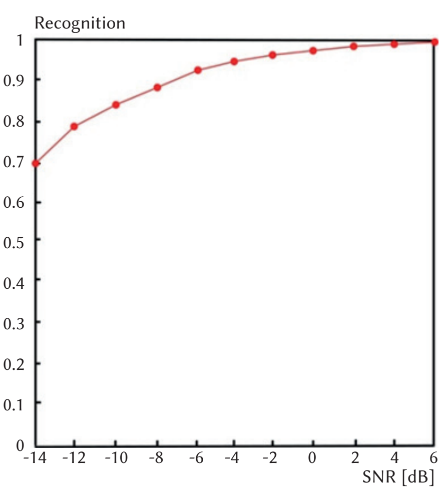

Fig. 6. Detection performance of the algorithm under different SNR.

C. Feature Extraction

To verify the detection performance of different algorithms, we introduce Sensitivity, Specificity and Accuracy as evaluation metrics.

$$Sensitivity = \frac{TP}{TP+FN} \tag{17}$$

$$Specificity = \frac{TN}{TN+FP} \tag{18}$$

$$Accuracy = \frac{TP+TN}{TP+FP+TN+FN} \quad (19)$$

where *TP* is the number of correctly predicted epileptic fragments, *FN* is the number of epileptic fragments that are predicted as non-epileptic fragments, *FP* is the number of non-epileptic fragments that are predicted as epilepsy, *TN* is the number of non-epileptic fragments that are predicted as non-epileptic fragments.

Accuracy represents the proportion of the correct classification of the classifier, and the higher the ratio represents, the better the classification performance of the classifier; Sensitivity represents the proportion of the correct classification of all epileptic fragments, and the higher the ratio represents, the higher the prediction accuracy of the classifier for epileptic fragments; Specificity indicates the proportion of all non-epileptic fragments correctly classified, and the higher the ratio, the higher the prediction accuracy of non-epileptic fragments.

Kiranyaz et al. [30] do not use cross validation to fuse time-domain and frequency-domain information, which could not effectively prove the performance of epilepsy detection. Tao et al. [35] use the AdaBoost multi-scale decomposition for signals in order to avoid too few epileptic samples in the verification set. Only 25% samples were used for training. Samiee et al. [34] use the amplitude features of the EEG signal to recognize epileptic signals. Jiang et al. [41] integrated prior information into the model to recognize epileptic signals. Parthiban et al. [42] analyze epileptic signals from the perspective of energy entropy. Different oversampling methods are used to increase the number of epileptic samples. Due to the data imbalance, the accuracy and sensitivity of most algorithms are relatively low, but the proposed algorithm in this paper shows better accuracy and sensitivity under the condition of maintaining the same specificity, as shown in Table II.

D. Comparison of Classification Algorithms

We constructed time-domain similarity data set and frequency-domain similarity data set, to analyze the classification of EEG signals. ROC curves can show the performance of different algorithms. Musselman et al. [26] establish time domain model to realize EEG signal. Rafiuddin et al. [24] establish energy domain model to classify EEG signal. Kiranyaz et al. [30] establish time-energy model to realize EEG signal.

As shown in Fig. 7-a, the time domain model cannot effectively distinguish the time-domain similarity data. The energy domain model transforms time domain signals into frequency domains for research. Based on the difference of frequency domains, it can achieve better data classification. As shown in Fig. 7-b, the energy domain model cannot effectively distinguish the frequency-domain similarity data. The time domain model realizes signal classification based on the significant difference of Time domain. The time-energy model comprehensively considers the difference between time domain and frequency domain, so they have a good effect in the face of similar classification effects in Time domain or frequency domain. The proposed algorithm establishes the Horizontal Viewable model from the time domain, enhances the anti-noise ability of the algorithm, establishes the TSK model from the frequency domain to realize the energy, and achieves accurate classification based on clinical diagnosis and clinical representation data.

IV. Conclusion

Epilepsy is acute, which is of great significance for its early recognition. Through the study of EEG signals, aiming at the problem of difficult recognition of epileptic signals, an epileptic brain signal

TABLE II. Detection Effect

	Fusion [30]	AdaBoost [35]	Texture [34]	Prior [41]	Entropy [42]	Ours
Specificity	0.802	0.814	0.812	0.841	0.865	**0.915**
Sensitivity	0.821	0.836	0.835	0.865	0.879	**0.925**
Accuracy	0.814	0.845	0.812	0.865	0.912	**0.934**

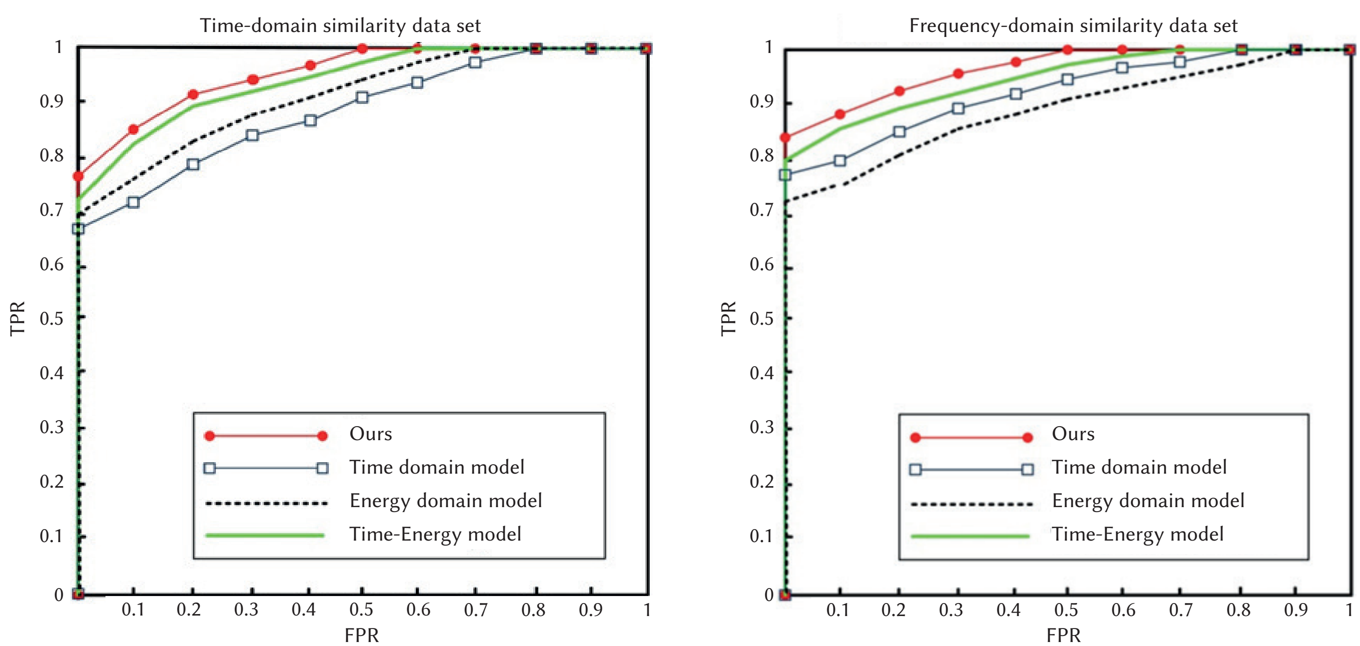

(a) The model ROC curve of time-domain similarity data

(b) The model ROC curve of frequency-domain similarity data

Fig. 7. ROC curve.

recognition algorithm based on cloud edge computing is proposed. A horizontal visualization model is constructed at the edge to enhance the internal correlation of signals, and a TSK fuzzy analysis system of epileptic signals is established. For more complex data, the deep learning network of clinical representation is constructed through cloud to identify the EEG signals during seizures, which provides the accuracy of epilepsy diagnosis. Our research can be extended to other intelligent medical fields.

Acknowledgment

This work is supported by Science and Technology Rising Star of Shaanxi Youth (2021KJXX-61), The Shanxi National Science Foundation (2020JQ-518), Natural Science Foundation of China (62062003), North Minzu University Research Project of Talent Introduction (2020KYQD08), Key Research and Development Project of Ningxia (2020BEB04022), The Open Project Program of the State Key Lab of CAD&CG (A2206).

Conflicts of Interest

The authors declare no conflict of interest.

References

[1] Y. Si, "Machine learning applications for electroencephalograph signals in epilepsy: a quick review," *Acta Epileptologica*, vol. 2, pp. 1-7, 2020.

[2] A. Sharmila, and P. Geethanjali, "DWT Based Time Domain Features on Detection of Epilepsy Seizures from EEG Signal," *In Biomedical Signal Processing. Springer, Singapore*. pp. 181-200, 2020.

[3] C. R. Coughlin, "Pyridoxine-dependent epilepsy is more than just epilepsy," *Developmental Medicine & Child Neurology*, vol. 62, no. 3, pp. 268-268, 2020.

[4] T. Zhou, H. Lu, Z. Yang, S. Qiu, B. Huo and Y. Dong, "The ensemble deep learning model for novel COVID-19 on CT images," *Applied Soft Computing*, vol. 98, p. 106885, 2021.

[5] L. Gu, D. Zeng, S. Guo, A. Barnawi and Y. Xiang, "Cost efficient resource management in fog computing supported medical cyber-physical system," *IEEE Transactions on Emerging Topics in Computing*, vol. 5, no. 1, pp. 108-119, 2015.

[6] N. Abirami, S. Karthik and M. Kanimozhi, "Automated brain tumor detection and identification using medical imaging," *International Journal of Research in Computer Applications and Robotics*, vol. 3, no. 9, pp. 85-91, 2015.

[7] W. Shi, J. Cao, Q. Zhang, Y. Li and L. Xu, "Edge computing: Vision and challenges," *IEEE internet of things journal*, vol. 3, no. 5, pp. 637-646, 2016.

[8] C. Aggarwal and K. Srivastava, "Securing IoT devices using SDN and edge computing," *In 2016 2nd International Conference on Next Generation Computing Technologies (NGCT) IEEE*, pp. 877-882, 2016.

[9] M. P. Hosseini, T. X. Tran, D. Pompili, K. Elisevich and H. Soltanian-Zadeh, "Deep learning with edge computing for localization of epileptogenicity using multimodal rs-fMRI and EEG big data," *In 2017 IEEE international conference on autonomic computing (ICAC) IEEE*, pp. 83-92,2017.

[10] D. Singh, G. Tripathi, A. M. Alberti and A. Jara, "Semantic edge computing and IoT architecture for military health services in battlefield," *In 2017 14th IEEE Annual Consumer Communications & Networking Conference (CCNC) IEEE*, pp. 185-190, 2017.

[11] X. Li, R. Ding, X. Liu, W. Yan, J. Xu, H. Gao and X. Zheng, "Comec: Computation offloading for video-based heart rate detection app in mobile edge computing," *In 2018 IEEE Intl Conf on Parallel & Distributed Processing with Applications, Ubiquitous Computing & Communications, Big Data & Cloud Computing, Social Computing & Networking, Sustainable Computing & Communications ,IEEE, pp.* 1038-1039, 2018.

[12] S. Oueida, Y. Kotb, M. Aloqaily, Y. Jararweh, T. Baker, "An edge computing based smart healthcare framework for resource management," *Sensors*, vol. 18, no. 12, pp. 4307, 2018.

[13] A. A. Abdellatif, A. Mohamed, C. F. Chiasserini, M. Tlili and A. Erbad, "Edge computing for smart health: Context-aware approaches, opportunities, and challenges," *IEEE Network*, vol. 33, no. 3, pp. 196-203, 2019.

[14] D. Lin and Y. Tang, "Edge computing-based mobile health system: network architecture and resource allocation," *IEEE Systems Journal*, vol. 14, no. 2, pp. 1716-1727, 2019.

[15] I. V. Pustokhina, D. A. Pustokhin, D. Gupta, A. Khanna, K. Shankar and G. N. Nguyen, "An effective training scheme for deep neural network in edge computing enabled Internet of medical things (IoMT) systems," *IEEE Access*, vol. 8, pp. 107112-107123, 2020.

[16] C. Dou, S. Zhang, H. Wang, L. Sun, Y. Huang and W. Yue, "Adhd fmri short-time analysis method for edge computing based on multi-instance learning," *Journal of Systems Architecture*, vol. 111, pp. 101834, 2020.

[17] M. A. Rahman and M. S. Hossain, "An internet of medical things-enabled edge computing framework for tackling COVID-19," *IEEE Internet of Things Journal.* vol. 8, no. 21, pp. 15847-15854, 2021.

[18] L. Xu and M. Xu, "Epilepsy surgery in China: past, present, and future," *European journal of neurology*, vol. 17,no. 2, pp. 189-193, 2010.

[19] J. G. Jefferys, "Advances in understanding basic mechanisms of epilepsy and seizures," *Seizure*, vol. 19, no. 10, pp. 638-646, 2010.

[20] A. T. Berg, "Epilepsy, cognition, and behavior: the clinical picture," *Epilepsia*, vol. 52, no.7-12, 2011.

[21] S. Koçer and M. R. Canal, "Classifying epilepsy diseases using artificial neural networks and genetic algorithm," *Journal of medical systems*, vol. 35, no. 4, pp. 489-498, 2011.

[22] A. M. Pack, D. S. Reddy, S. Duncan and A. Herzog, "Neuroendocrinological aspects of epilepsy: important issues and trends in future research," *Epilepsy & Behavior*, vol.22, no. 1, pp. 94-102, 2011.

[23] K. L. Margrove, A. K. Thapar, S. A. Mensah and Kerr, M. P. "Help-seeking and treatment preferences for depression in epilepsy," *Epilepsy & Behavior*, vol. 22, no. 4, pp. 740-744, 2011.

[24] N. Rafiuddin, Y. U. Khan and O. Farooq, "Feature extraction and classification of EEG for automatic seizure detection," *In 2011 International Conference on Multimedia, Signal Processing and Communication Technologies*, pp.184-187, 2011.

[25] M. Pediaditis, M. Tsiknakis and N. Leitgeb, "Vision-based motion detection, analysis and recognition of epileptic seizures-a systematic review," *Computer methods and programs in biomedicine*, vol. 108, no, 3, pp. 1133-1148, 2012.

[26] M. Musselman and D. Djurdjanovic, "Time-frequency distributions in the classification of epilepsy from EEG signals," *Expert systems with applications*, vol. 39, no. 13, pp. 11413-11422, 2012.

[27] N. F. Chang, T. C. Chen, C. Y. Chiang and L. G. Chen, "Channel selection for epilepsy seizure prediction method based on machine learning," *In 2012 Annual International Conference of the IEEE Engineering in Medicine and Biology Society*, pp.5162-5165, 2012.

[28] K. Rosas, I. Parrón, P. Serrano and J. M. Cimadevilla, "Spatial recognition memory in a virtual reality task is altered in refractory temporal lobe epilepsy," *Epilepsy & Behavior*, vol. 28, no. 2, pp.227-2312013.

[29] S. A. Hosseini, M. R. Akbarzadeh-T and M. B. Naghibi-Sistani, "Qualitative and quantitative evaluation of EEG signals in epileptic seizure recognition," *International Journal of Intelligent Systems and Applications*, vol. 5, no. 6, p. 41,2013.

[30] S. Kiranyaz, T. Ince, M. Zabihi and D. Ince, "Automated patient-specific classification of long-term electroencephalography," *Journal of biomedical informatics*, vol. 49, pp.16-31, 2014.

[31] A. Gomez-Ibañez, E. Urrestarazu and C. Viteri, "Recognition of facial emotions and identity in patients with mesial temporal lobe and idiopathic generalized epilepsy: an eye-tracking study," *Seizure*, vol. 23, no. 10, pp. 892-898, 2014.

[32] J. R. Villar, M. Menéndez, J. Sedano, E. de la Cal and V. M. González, "Analyzing accelerometer data for epilepsy episode recognition." *In 10th International Conference on Soft Computing Models in Industrial and Environmental Applications*, pp.39-48, 2015.

[33] Z. Tao, C. Wan-Zhong and L. Ming-Yang, "Recognition of epilepsy electroencephalography based on Ada Boost algorithm," *Acta Physica Sinica*, vol. 64, no. 12, pp. 128701, 2015.

[34] K. Samiee, S. Kiranyaz, M. Gabbouj, T. Saramäki, "Long-term epileptic EEG classification via 2D mapping and textural features," *Expert Systems with Applications*, vol.42, no. 20, pp. 7175-7185, 2015.

[35] J. Yan, Y. Wang, G. Ouyang, T. Yu and X. Li, "Using max entropy ratio of recurrence plot to measure electrocorticogram changes in epilepsy patients," *Physica A: Statistical Mechanics and its Applications*, vol. 443, pp. 109-116, 2016.

[36] K. I. Qazi, H. K. Lam, B. Xiao, G. Ouyang and X. Yin, "Classification of epilepsy using computational intelligence techniques," *CAAI Transactions on Intelligence Technology*, vol. 1, no. 2, pp. 137-149, 2016.

[37] M. Li, W. Chen and T. Zhang, "Classification of epilepsy EEG signals using DWT-based envelope analysis and neural network ensemble," *Biomedical Signal Processing and Control*, vol. 31, pp. 357-365, 2017.

[38] L. N. Sepeta, K. B. Casaletto, V. Terwilliger , J. Facella-Ervolini, M. Sady, J. Mayo, M. M. Berl, "The role of executive functioning in memory performance in pediatric focal epilepsy," *Epilepsia*, vol. 58, no. 2, pp. 300-310, 2017.

[39] S. Qiu, J. Li, M. Cong, C. Wu, Y. Qin and T. Liang, "Detection of solitary pulmonary nodules based on brain-computer interface," *Computational and Mathematical Methods in Medicine*, pp. 1-10, 2020.

[40] I. Ullah, M. Hussain and H. Aboalsamh, "An automated system for epilepsy detection using EEG brain signals based on deep learning approach," *Expert Systems with Applications*, vol. 107, pp. 61-71, 2018.

[41] Z. Jiang, F. L. Chung and S. Wang, "Recognition of multiclass epileptic EEG signals based on knowledge and label space inductive transfer," *IEEE Transactions on Neural Systems and Rehabilitation Engineering*, vol. 27, no.4, pp. 630-642, 2019.

[42] K. G. Parthiban, S. Vijayachitra and R. Dhanapal, "Hybrid dragonfly optimization-based artificial neural network for the recognition of epilepsy," *International Journal of Computational Intelligence Systems*, vol. 12, no. 2, pp.1261-1269, 2019.

[43] K. P. Thanaraj, B. Parvathavarthini, U. J. Tanik, V. Rajinikanth, S. Kadry and K. Kamalanand, "Implementation of deep neural networks to classify EEG signals using gramian angular summation field for epilepsy diagnosis," *Computer Vision and Pattern Recognition*, 2020.

[44] J. Prasanna, M. S. P. Subathra, M. A. Mohammed, R. Damaševičius, N. J. Sairamya and S. T. George, "Automated epileptic seizure detection in pediatric subjects of CHB-MIT EEG database-a survey," *Journal of Personalized Medicine*, vol. 11, no. 10, p. 1028, 2021.

Shi Qiu

Shi Qiu received the M.S. degree at Xidian University, Xi'an, P. R. China, in 2012, the Ph.D. degree at University of Chinese Academy of Sciences, Xi'an, P. R. China, in 2016. He is associate research fellow with Xi'an Institute of Optics and Precision Mechanics, Chinese Academy of Sciences, Xi'an, P. R. China. He has coauthored more than 60 journal and conference papers. His research interests include image restoration, sparse representation, and object detection. He is Young Scholars in Western China and Youth Rising Star in Science and Technology of Shaanxi province.

KeYang Cheng

KeYang Cheng is a Professor in the Department of Computer Science and Telecommunications Engineering of the Jiangsu University. He got Ph.D. degree from the School of Computer Science and Engineering, Nanjing University of Aeronautics and Astronau-tics, in 2015. He was a Postdoctoral Researcher with the University of Warwick, U.K., in 2016. Besides, he has coauthored more than 50 journal and conference papers. His current research interests include in the areas of pattern recognition, computational intelligence, and computer vision. He is a member of CCF.

Tao Zhou

Tao Zhou received Ph.D. degrees in computer science and technology from the Northwest Polytechnic University in 2010. Now, He is a Professor and director of the Chinese society of image graphics, Chinese society of stereology. His current research interests are in the areas of medical image processing, pattern recognition, big data analysis.

Rabia Tahir

Rabia Tahir is an PhD student in the Department of Computer Science and Telecommunications Engineering of the Jiangsu University. She is a M.Sc in computer science graduated from School of Comsats University Islamabad in 2017. She is currently pursuing the Ph.D degree in computer science with Jiangsu University, Zhenjiang. Besides, her research interests include computer vision, image processing, deep learning, and person re-identification.

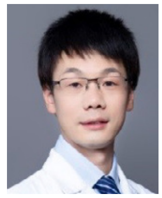

Ting Liang

Ting Liang is an attending doctor in the department of imaging of the First Affiliated Hospital of Xi'an Jiaotong University, he received the M.S. degree at Tongji University, Shanghai, P. R. China, in 2013. He specializes in CT-guided puncture biopsies, and has coauthored more than 20 journal and conference papers. His research interests include lung and EEG signal processing.

Design of Integrated Artificial Intelligence Techniques for Video Surveillance on IoT Enabled Wireless Multimedia Sensor Networks

Romany F. Mansour[1]*, Carlos Soto[2], Roosvel Soto-Díaz[3], José Escorcia Gutierrez[4,5], Deepak Gupta[6], Ashish Khanna[6]

[1] Department of Mathematics, Faculty of Science, New Valley University, El-Kharga, (Egypt)
[2] Mechanical Engineering Program, Universidad Autónoma del Caribe, 08001 Barranquilla (Colombia)
[3] Mechatronic Engineering Program, Universidad Simón Bolívar, 08001 Barranquilla (Colombia)
[4] Electronics and Telecommunications Engineering Program, Universidad Autónoma del Caribe, 08001 Barranquilla (Colombia)
[5] Biomedical Engineering Program, Corporación Universitaria Reformada, 08001 Barranquilla (Colombia)
[6] Department of Computer Science & Engineering, Maharaja Agrasen Institute of Technology, Delhi (India)

Received 1 August 2021 | Accepted 20 June 2022 | Published 8 August 2022

unir
LA UNIVERSIDAD EN INTERNET

Abstract

The recent advancements in the Internet of Things (IoT) and Wireless Multimedia Sensor Networks (WMSN) made high-speed multimedia streaming, data processing, and essential analytics processes with minimal delay. Multimedia sensors used in WMSN-based surveillance applications are beneficial helpful in attaining accurate and elaborate details. However, it has become essential to design an effective and lightweight solution for data traffic management in WMSN owing to the massive quantities of data, generated by multimedia sensors. The development of Artificial Intelligence (AI) and Machine Learning (ML) techniques can be leveraged to investigate, collect, store, and process multimedia streaming data for decision-making in real-time scenarios. In this aspect, the current study develops an Integrated AI technique for Video Surveillance in IoT-enabled WMSN, called IAIVS-WMSN. The proposed IAIVS-WMSN technique aims to design a practical scheme for object detection and data transmission in WMSN. The proposed IAIVS-WMSN approach encompasses three stages: object detection, image compression, and clustering. The Mask Regional Convolutional Neural Network (Mask RCNN) technique is primarily utilized for object detection in the target region. Besides, Neighbourhood Correlation Sequence-based Image Compression (NCSIC) technique is applied to reduce data transmission. Finally, Artificial Flora Algorithm (AFA)-based clustering technique is designed for the election of Cluster Heads (CHs) and construction clusters. The design of object detection with compression and clustering techniques for WMSN shows the novelty of the work. These three processes' designs enable one to accomplish effective data transmission in IoT-enabled WMSN. The researchers conducted multiple simulations to highlight the supreme performance of the IAIVS-WMSN approach. The simulation outcomes inferred the enhanced performance of the IAIVS-WMSN algorithm to the existing approaches.

Keywords

Artificial Intelligence, Intelligent Surveillance, Internet Of Things, Object Detection, WMSN.

DOI: 10.9781/ijimai.2022.08.005

I. Introduction

The advancements made in miniaturization technology allow the incorporation of heterogeneous sensing devices on single sensing platforms. A single prolific advantage of the miniaturization process is the accessibility of a Complementary Metal Oxide Semiconductor (CMOS) camera. When the latter is incorporated into conventional Wireless Sensor Networks (WSN), it transforms the WSN into Wireless Multimedia Sensor Networks (WMSN). This network evolution allow the execution of multi-dimension signal processing methods on sensing platforms [1]. Further, it also provides advanced services compared to conventional WSN. WMSN includes various relay nodes and camera motes while the latter needs to be placed in the target region to monitor the existence of intruders and transfer the data to the monitoring location. Currently, WMSN is utilized in several surveillance applications such as monitoring elders, identifying anomalies in secure regions, traffic monitoring, among others. In the event of a surveillance application, the camera mote captures the video and transfers it to the monitoring place through relay nodes [2]. If no change is observed in the scene, it is not necessary to transfer the whole video in a resource-limited environment such as WMSN. Fig. 1 shows the common framework of cluster-based WMSN.

* Corresponding author.

E-mail address: romanyf@sci.nvu.edu.eg

WMSN enables both individuals and organizations to stream video/audio data and still transmit the images together with scalar sensor data. Therefore, it has become possible to transmit the group of data from distinct modalities under a complex environment which was not the case in WMSN in previous years [3]. The significant differences between WMSN and conventional WSNs are the size and nature of the data collected, processed, and transmitted in the former [4]. In general, scalar data is the major kind of data in WSN that can be transmitted and processed in a simple manner. Nevertheless, multimedia data like audio, video and image have a complex structure that makes data processing, a highly complex task. Further, multimedia data is also prominent in size, which incurs high wireless transmission costs and is decided based on network bandwidth and consumed energy [5].

Furthermore, they can be utilized in resource-constrained, challenging, and unattended regions. However, some specific constraints in terms of data processing must be overcome when developing novel methods in WMSN. These constraints include limited processing, limited memory, limited battery power, and narrow bandwidth [6]. Hence, the cognition of amendment in conventional multi-dimension signal processing is an early-stage development prior to real-world execution in WMSN. In order to achieve this coherency, the current study emphasizes adjusting the conventional data processing model from WMSN. Mainly, the aim is to extend the lifespan of nodes by mitigating costs incurred upon in-node processing. As a result, tracking processes and visual object identification are performed at the sink node, where the realization of object geometry allows the remote node to decide the additional operation in its sensing region.

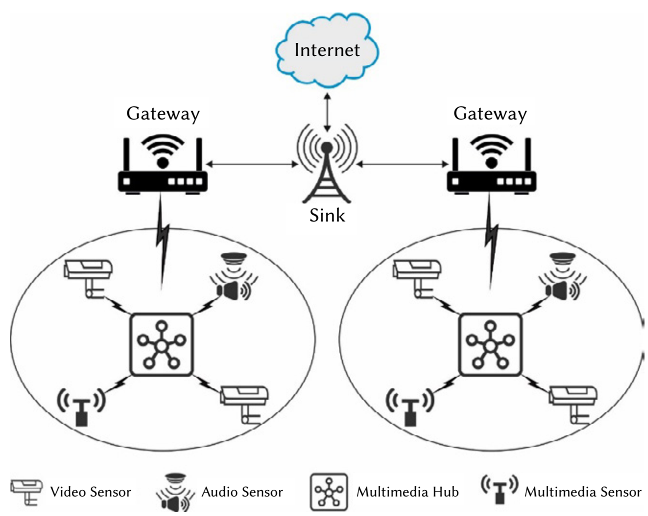

Fig. 1. The general structure of cluster-based WMSN.

In other words, each kind of WSN node has constrained resources like battery power, CPU, RAM, secondary storage, and communication bandwidth. Such limitation paves the way for developing practical algorithms and techniques to be incorporated into WMSN. To minimize the data size of the transferred multimedia, various researchers have proposed image compression algorithms or modified the previous algorithms for WMSN [7]. Most of the studies were aimed at reducing the quantity of data to be transferred, when utilizing energy-effective and simple image compression algorithms. The results show that the objective could be obtained to a specific level by compression algorithms [8]. However, it is still impossible to claim that resource limitation problems can be overcome in WMSN. Other solutions were also presented to solve the aforementioned problems based on extraction and detection of the objects present in the image [9]. This method aims to process multimedia data and extract more useful data, i.e., small informative data than massive raw multimedia data, at the node level. Since the data that needs to be transferred is smaller in size, there is a parallel reduction observed in energy consumption for data transmission. Finally, processing effort at the sensors level might get altered based on various aspects.

To the best of the researcher's knowledge, no works conducted earlier have integrated all three major processes of WSN such as object detection, compression, and clustering. The current study develops an Integrated AI technique for Video Surveillance in IoT-enabled WMSN, called IAIVS-WMSN. The proposed IAIVS-WMSN approach contains three significant processes: object detection, image compression, and clustering. A Mask Regional Convolutional Neural Network (Mask RCNN) technique is utilized for object detection in target region. Moreover, the Neighborhood Correlation Sequence-based Image Compression (NCSIC) technique is applied to minimize the quantity of data transmission. At last, the Artificial Flora Algorithm (AFA)-based clustering technique is used in Cluster Heads (CHs) and constructing clusters. A comprehensive experimental analysis was executed to showcase the superiority of the proposed IAIVS-WMSN algorithm.

II. Related Works

In Rehman et al. [10], new object detection and image transmission method were presented for WMSN. An image segment is broadcasted instead of whole images. In this sense, minimal image content transmission and in-node energy conservation to the sink node are assured. The efficiency of the presented system was determined based on the reconstructed image and in-node energy consumption level. In Guo [11], an effective compressive sensing method-based customized memory gradient pursuit approach using earlier terminations in WSN was proposed. This method was able to strike compelling tradeoffs amongst energy dissipation for wireless communication, specific kinds of minimum storage, and bandwidth. Later, the presented method adapted an unscented particle filter to predict the target position.

Koyuncu et al. [12] explored the effect of combining audio-visual multimedia and scalar data gathered by sensors from WMSN in order to achieve energy-effective and precise object classification and detection. To perform this method, the researchers presented a wireless multimedia sensor with video and audio processing and capturing capabilities along with ordinary or traditional scalar sensor nodes. Multimedia sensor nodes are maintained in sleep mode to save energy until they get activated by the scalar sensor nodes which are active all the time. Sukumaran et al. [13] constructed a CS-BS architecture using a new threshold approach for anomaly detection through less measurement in a protected indoor environment. In CS-BS architecture, CS is implemented on variance frame i.e., sparse, which reduces the usage of bandwidth, energy, and memory. In this architecture, a foreground thresholding is presented based on a measurement matrix to extract the motion objects from a scene.

Wang et al. [14] proposed EDACR for WMSN by taking limitations of energy consumption and QoS into account. In this study, the researchers primarily designed an RL-based method to ensure energy-balanced routing and QoS based on the knowledge of reliability and delay. The experimental results infer a decline in energy consumption while in parallel, QoS is guaranteed in terms of conventional and distributed adoptive cooperative protocols. Akter et al. [15] introduced a comprehensive tracking and localization method in WSN. Considering the limitations of static cluster, an energy-effective incremental clustering approach was proposed in this study, after which the Gaussian adoptive resonance concept was presented at the border area. The presented work was permitted to learn, create, update and retain the clusters gradually through online learning to adopt continuous motion patterns. At last, the trilateration method was employed for the accurate location of a dynamic object through a sensor network.

Shao [16] proposed a dynamic clustering target tracking method for moving trends. In this method, a dynamic cluster is formed in networks whereas the CH dynamically schedules the nodes to track the target collaboratively. The tracking approach primarily consists of two phases. In the first phase, the CH establishes a 'noighbor node set' within its transmission range, and the noighbor node is selected in the 'noighbor node set' based on the distances between the node and the targets to create an 'intracluster member set' to perform on the target. In Sathyaprakash and Prakasam [17], an RBMLCA approach was presented using a randomized method. It involves optimising QoS parameters, cluster head formation, and clustering of nodes. The adapted clustering method helped in data transmission on multimedia sensor networks, whereas the RBMLCA method yielded an optimal quality of evolutional parameters.

Heng et al. [18] proposed a holistic WMSN framework for image transmission that performs well on different images. This method was proposed based on standard deviation and leveraging its saliency features. Then, FLS was utilized to determine the suitable features while the samplings were assigned, and all the respective blocks were resized with CS. The integrated FLS & BCS approaches were executed by SPL recreation to determine the convergence speed. Alqaralleh et al. [19] presented a novel Reliable MultiObject Tracking Model with DL and Energy-Effective WMSN. At first, the FL method was applied to determine the CHs and achieve energy efficacy. Then, a new tracking approach RNN-T was proposed using RNN with tumbling effects. The presented RNN-T model was implemented in all the sensors and CH executed the tracking approach to track all the animals. Lastly, the tracking outcomes were transferred to cloud server for research purposes.

III. The Proposed Model

The proposed IAIVS-WMSN approach comprises three stages Mask RCNN-based object detection, AFA-based clustering, and NCSIC-based image compression. In the first stage, the objects in the target regions are detected with the help of the Mask RCNN technique. Next, the AFA technique is implemented to determine the CHs and optimally construct the images. Furthermore, the NCSIC technique is applied to compress the images at CMs and CHs prior to data transmission to the BS. A detailed discussion of these processes is offered in the upcoming subsections.

A. System Model

This section deals with the network's topology that is utilized to transmit the image. The analysis of in-network energy utilization inspires it during image frame broadcasting. In image broadcasting, the energy utilization occurs continuously on the superior side like in-node processing. Then, the vital goal of presenting the topology has to define the entire energy utilization when broadcasting the group of image frames. Assume that energy utilization occurs arbitrarily in the WMSN node. All the WMSN nodes are equipped with the restricted resource. Consequently, there is no channel impairment in the network. For a reliable transmission of the image within networks and to avoid collision, due to simultaneous broadcast of image data by more than two nodes, all the WMSN nodes are separated into two classes such as Cluster head (CH) and Monitoring Node (MN). The network topology is demonstrated in Fig. 2.

B. Design of Object Detection Technique

In this primary step, the Mask-RCNN technique is applied to detect the presence of objects in the target region. In general, Mask-RCNN is theoretically a flexible and simple architecture, for

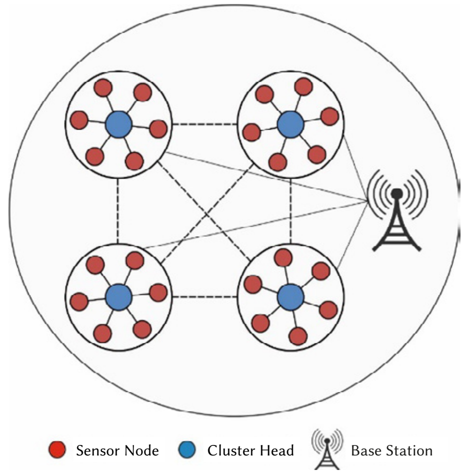

Fig. 2. Network Model.

instance, segmentation, object recognition, and detection. It can effectively identify the objects in an image, when producing a high-quality segmentation mask during all instances. The FPN for object identification, the primary block framework of Mask-RCNN, is accountable for removing the features. The RPN and Mask RCNN share full image convolution features with the detection network. Thus, it allows near cost-free region suggestions. Afterward, fast RCNN is prolonged to make Mask RCNN by including a branch for prediction of object mask like the present branch for bound box detection. RPN is utilized for masking the RCNN before 'elective searching' so that the RPN can share the convolution feature of the whole map with the detection network. It can predict the object score as well as boundary position at all the locations while it is also an FCN.

Fast RCNN exploits RPN as a regional generation network to generate the candidate region. FPS depends on the Fast RCNN approach as much as five times while its MAP, verified on VOC 2012, improved by 70.4%. Further, to enhance the detection accuracy of the target, Mask RCNN exploits a bilinear interpolation approach in which ROI align is used rather than ROI pool, based on Fast RCNN [20]. ROI align approach is utilized to determine the precise values of the input features, according to bilinear interpolations at four regular sampled places from every ROI bin and the result is aggregated. This technique enhances the precision of Mask RCNN to 10%. In order to ensure Mask RCNN executes the mask function and attains highly accurate instance segmentation in pixel-to-pixel alignment, the mask branch is included in RCNN. Mask RCNN has the ability to execute three processes such as target detection, segmentation, and recognition. Its detection speed can still attain 5 FPS. The diagram of Mask RCNN is displayed in Fig. 3.

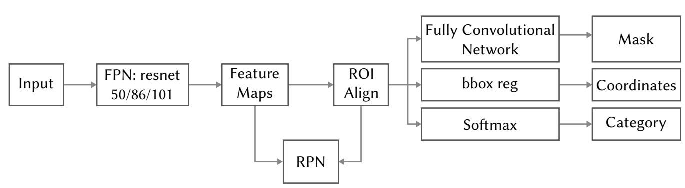

Fig. 3. Structure of Mask RCNN.

Next, the candidate regions are integrated with the feature map so that the scheme can attain the target's classification, detection, and mask. Depending on Mask RCNN, a technique named SF-FPN was proposed earlier to improve the speed and detection accuracy using Resnet86. This work enhanced RPN parameter settings, dataset, and FPN structure. The enhanced technique, projected in this work, cloud perform segmentation, recognition, and detection of the targets simultaneously.

C. Design of Clustering Technique

AFA is designed based on the migration and reproduction of the flora. The procedure of identifying an optimum survival place for flora to flourish, is employed to define an optimum solution for the problem. Offspring Plant (OSP), Original Plant (OP), Propagation Distance (PD), and plant location are four essential components of MOAF. Spreading, selection, and evolution behavior are three major behavioral forms. Primarily, this process arbitrarily makes the OP. Later, it spreads seeds to the position within an arbitrary spreading scope. The spreading scope is determined using PD. Then, the fitness of a seed in a specific location is evaluated based on the objective function whereas 'fitness' denotes the quality of the solution. Eventually, roulette is employed to decide the survival seeds. These survival seeds develop a novel OP. The iterations are repeated till the termination condition is arrived at. This process includes external documents to save the optimal solution.

In this study, each decision variable of the test function contains an upper limit $\vec{X}^{max} = [X_1^{\max}, X_2^{\max}, \ldots, X_D^{\max}]^T$ and a lower limit $\vec{X}^{min} = [X^{\min}, X^{\min}, \ldots, X_D^{\min}]^T$. Primarily, this process makes N OP to be dependent upon the decision variable's upper and lower limits, arbitrarily. It uses i row and j column matrix P_{ij} to represent the location of OP, in which i = 1, 2, ..., D indicates the dimension and j = 1, 2, ..., N signifies the amount of OP [21]: The population is give in (1):

$$P_{ij} = rand(0,1) \cdot (X_i^{\max} - X_i^{min}) + X_i^{min} \tag{1}$$

Whereas $rand(0,1)$ refers to uniform distribution amount in the range of 0 and1.

OP spreads their offspring within a specific scope using radius i.e., PD while novel PD stimulates the PD of the grandparent and parent plants as given in (2).

$$d_j = d_{lj} \cdot rand(0,1) \cdot c_1 + d_{2j} \cdot rand(0,1) \cdot c_2 \tag{2}$$

Here, c_1 & c_2 denote the learning coefficients, d_{lj} and d_{2j} represent the PD of parent and grandparent plants correspondingly, and rand (0, 1) stands for uniform distribution amount in the range of 0 and1. Parent PD becomes the novel grandparent PD, as provided in (3).

$$d'_{1j} = d_{2j} \tag{3}$$

The regular AF optimization approach uses the standard deviation between the locations of OP and OSP as novel parent PD, as defined in (4).

$$d'_{2j} = \sqrt{\sum_{i=1}^{N} (P_{ij} - P'_{ij})^2 / N} \tag{4}$$

To maintain the data of optimal solution arrived at till now, MOAF optimized approach uses the plant in an external document. Equation (5) shows the novel parent PD, i.e. the difference between the location of the plant in external document P^*_{id} and OSP P'_{id}:

$$d'_{2j} = P^*_{ij} - P'_{ij} \tag{5}$$

The spreading behavior creates the OSP based on OP position and novel PD as given in (6).

$$P'_{i,j\cdot b} = G_{i,j\cdot b} + P_{i,j} \tag{6}$$

Here, b = 1, 2, ..., B, B refers to the number of OSP where the OP could transmit, $P'_{i,j\cdot b}$ represents the position of OSP, $P_{i,j}$ represents the location of OP and $G_{i,j\cdot b}$ denotes the arbitrary amount utilizing Gaussian distribution with mean 0 and variance j. A novel OP is generated based on Eq. (2), when there are no OSP endures.

In the standard AF approach, the survival likelihood is defined based on the survival of OSP. The survival likelihood is calculated through (7):

$$p = \left| \sqrt{F(P'_{i,j\cdot b})/F_{max}} \right| \cdot Q_x^{(j\cdot b-1)}. \tag{7}$$

Here, Q_X denotes the electing likelihood range between 0 and1. $F_{\max}$ indicates the fitness of OSP using maximum fitness. $F(P'_{i,j\cdot b})$ represents the fitness of the $(j \cdot b)th$ solution. The computation equation of fitness is the function of the main problem. In the MOAF approach, Pareto dominance relationships are employed. The survival likelihood is given in (8).

$$p = 0.9 \cdot \frac{domi(j \cdot b)}{B} + 0.1 \tag{8}$$

Here, domi $(j \cdot b)$signifies the number of solutions dominated using the solution, $(j \cdot b)$. B indicates the number of OSP that OP can transmit. The objective function allows the effectual election of CHs, including energy, distance, delay, link lifetime, inter-cluster and intra-cluster distances as shown in (9).

$$F = \omega_1 \times E + \omega_2 \times (1 - D) + \omega_3 \times (1 - \partial^{inter}) + \omega_4 \times \partial^{\text{intra}} + \omega_5 \times (1 - d) + \omega_6 \times L \tag{9}$$

where ω_1, ω_2, ω_3, ω_4, ω_5, and ω_6 denote the weights. The energy of the nodes is denoted as E, D denotes the delay in transmission, ∂^{inter} represents the intercluster distance, ∂^{intra} specifies the intracluster distance, d indicates the distance between two nodes, and l corresponds to link time.

D. Design of Image Compression Technique

The presented technique is a reliable image compression method mainly established to save energy-constrained sensor nodes in WMSN. It functions on two levels: bit decrease utilizing the NCSIC technique and encoding by LZMA. NCSIC technique creates the optimum codeword to all the individual pixel values based on the 'bit traversal method utilizing 0's and 1's' [22]. With the help of 0's based and 1's based traversal, the NCSIC technique creates two codewords for all individual pixel values. The codeword with minimal bits is elected as the optimum codeword. Assuming that G is an input image with pixel $\phi_{m,n}$ and is demonstrated as a 2D array as provided in (10).

$$G = \begin{bmatrix} \phi_{0,0} & \phi_{0,1} & \cdots & \phi_{0,n-1} \\ \phi_{1,0} & \phi_{1,1} & \cdots & \phi_{1,n-1} \\ \vdots & \vdots & \ddots & \vdots \\ \phi_{m-1,0} & \phi_{m-1,1} & \cdots & \phi_{m-1,n-1} \end{bmatrix} \tag{10}$$

Here, m and n refer to the height and width of the input image, G. A value of m × n = N gives the full resolution of the image G, and $\phi_{m,n}$ implies the place of pixels in the m^{th} row and n^{th} column of grayscale image, G. The entire count of bits required to store the optimum codeword Opt_{size} of the input image is estimated in (11).

$$\mathrm{Opt_{size}} = \sum_{i=1}^{N} \mathrm{NCSIC_{opt}(i)} + \text{control bits} \tag{11}$$

Here, NCSIC_{opt} denotes the number of current bits in codewords. Further, the NCSIC technique requires eight control bits for an optimum amount of bits in the compressed data. Especially, the quantuty of bits required on average to store a separate pixel in an image is defined in (12).

$$\mathrm{NCSIC_{ch\_av}} = \frac{\mathrm{Opt_{size}}}{\mathrm{N}}, \quad 0 \leq \mathrm{NCSIC_{ch\_av}} \leq 5 \tag{12}$$

As the RGB values of grayscale images are established to be similar, it is sufficient to encode some RGB values to all the pixels of the individual. Therefore, in principle, the NCSIC technique needs less than 0 bits and a maximum of five bits for representing some possible pixel values. In order to further improve the compression model, an optimum codeword is encoded by LZMA, and the compressed file is created.

Primarily, the NCSIC technique reads the pixel value from the original image and converts the pixel values to an equivalent binary method. If the initial bit is 0, 0's based-traversal occurs and saves the control bit like 00 or 01. After determining the value of 0's, the equivalent places (p) are saved as the portion of optimum codeword ($00 - p_1$). These processes continue still each 0's in the order are recognized and the places are upgraded ($00 - p_1, p_2, \ldots$) respectively. However, 1's-based traversal appears to occur in 1's, while 0's based traversal looks towards the incidence of 0's in binary form. To all the pixel values, two codewords are created based on 0's and 1's based traversals. Next, the codeword with fewer bits is elected as a better codeword. Then, LZMA is implemented to encode an optimum codeword created by the NCSIC technique. The presented technique follows a symmetrical manner in which the compression and decompression are inverse functions of one another.

IV. Performance Validation

The current section provides the performance analysis results of the proposed technique under different aspects. The proposed model was simulated using the MATLAB tool. The results were inspected in three distinct ways. At first, the object detection performance of the Mask RCNN model was determined by identifying two objects namely 'Human' and 'Vehicle'. Table 1 shows the object detection outcomes of the Mask-RCNN approach and other existing techniques.

Fig. 4 depicts the object detection outcomes accomplished by Mask.

RCNN technique and other existing approaches on the applied object, 'Human'. The figure depicts that the Support Vector Machine with Speeded Up Robust Feature (SVM-SURF) method attained poor object detection outcomes with a $prec_n$ of 49%, $reca_l$ of 46%, and an $F_{measure}$ of 47%. Likewise, the k-nearest neighbors (k-NN) technique gained a slightly increased performance with a $prec_n$ of 51%, $reca_l$ of 35%, and an $F_{measure}$ of 42%. In the meantime, the Support Vector Machine with Structural Features (SVM-SF) technique achieved a moderate outcome with a $prec_n$ of 55%, $reca_l$ of 32%, and a $F_{measure}$ of 40%. Along with that, k-NN+SVM and SVM-SF+SVM-SURF techniques demonstrated near-optimal outcomes. However, the Mask RCNN approach reached the maximum object detection performance with a high $prec_n$ of 61%, $reca_l$ of 65%, and an $F_{measure}$ of 64%.

Fig. 5 showcases the object detection results achieved by the Mask RCNN approach and other techniques on the applied object, 'Vehicle'. The figure shows that the k-NN+SVM algorithm attained the least object detection result with a $prec_n$ of 84%, $reca_l$ of 96%, and a $F_{measure}$ of 90%. Likewise, the k-NN technique reached somewhat improved performance with a $prec_n$ of 85%, $reca_l$ of 95%, and an $F_{measure}$ of 90%.

Meanwhile, SVM-SF and SVM-SF+SVM-SURF methods produced moderate and similar outcomes with a $prec_n$ of 86%, $reca_l$ of 93%, and an $F_{measure}$ of 89%. In addition, the SVM-SURF technique portrayed near-optimal outcomes with a precision of 87%, $reca_l$ of 68%, and a $F_{measure}$ of 76%. Finally, the Mask RCNN approach achieved the highest object detection performance with its $prec_n$ value of 89%, $reca_l$ value of 98%, and $F_{measure}$ value of 94%.

Next, the image compression performance of the NCSIC technique was examined in terms of Compression Ratio (CR), Compression Factor (CF), and Space Saving (SS), and the results are shown in Table II. The results portray that the NBWT system reached a minor compression outcome with CR, CF, and SS values such as 0.2598, 3.8494, and 74.022% respectively. Also, the LZMA technique attained a somewhat increased compression performance with CR, CF, and SS values such as 0.2469, 4.0502, and 75.310%, respectively. Moreover, the JPEG technique produced a moderately closer compression outcome with CR, CF, and SS values such as 0.2332, 4.2877, and 76.677% respectively. However, the NCSIS technique resulted in an effective outcome with a CR of 0.2159, CF of 4.6308, and an SS of 78.406%.

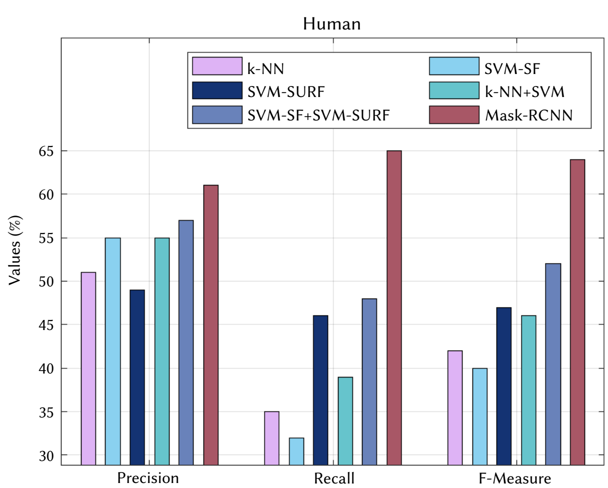

Fig. 4. Object Detection Analysis Results of Mask RCNN model on Human.

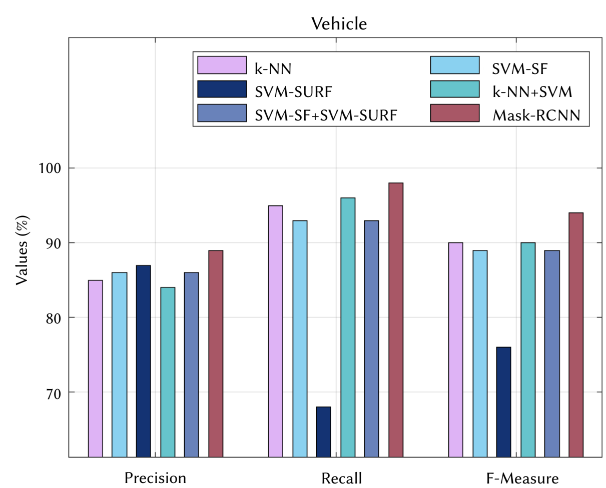

Fig. 5. Object detection analysis Results of Mask RCNN model on Vehicle.

TABLE I. Results of the Analysis of Existing Techniques and the Proposed Mask-RCNN Method Under Distinct. Measures

Models	Human			Vehicle		
	Precision	Recall	F-Measure	Precision	Recall	F-Measure
k-NN	51.00	35.00	42.00	85.00	95.00	90.00
SVM-SF	55.00	32.00	40.00	86.00	93.00	89.00
SVM-SURF	49.00	46.00	47.00	87.00	68.00	76.00
k-NN+SVM	55.00	39.00	46.00	84.00	96.00	90.00
SVM-SF+SVM-SURF	57.00	48.00	52.00	86.00	93.00	89.00
Mask-RCNN	61.00	65.00	64.00	89.00	98.00	94.00

TABLE II. Analysis Results of the Proposed and Existing Methods Under Different Measures

Methods	CR	CF	Space Savings (%)
NCSIC	0.2159	4.6308	78.406
JPEG	0.2332	4.2877	76.677
LZMA	0.2469	4.0502	75.310
BWT	0.2598	3.8494	74.022

Afterward, the performance analysis of the proposed IAIVS-WMSN approach was conducted conserning to First Node Die (FND), Half Node Dies (HND), and the Total Remaining Energy (TRE) and the results are shown in Table III and Fig. 6. The outcomes show that Clamped Homogenous Electric Field (CHEF) method obtained the least compression outcome with FND, HND, and TRE values such as 10, 139, and 160J, respectively.

TABLE III. Analysis Results of the Proposed IAIVS-WMSN Method and Existing Methods Under Distinct Measures

Methods	FND (# of rounds)	HND (# of rounds)	TRE (J)
CHEF	10	139	160
EEUC	12	151	220
MOFCA-Original	16	155	233
MOFCA-Optimized	16	167	243
TTDFP	18	179	259
IAIVS-WMSN	25	184	278

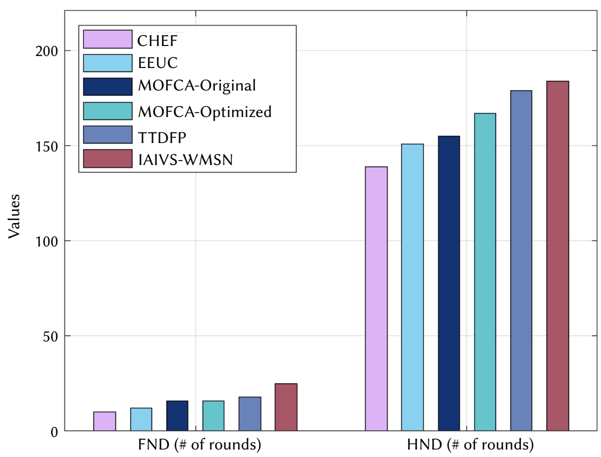

Fig. 6. Results of the Analysis of IAIVS-WMSN Model under Distinct Measures.

Simultaneously, Energy Efficient Unequal Clustering (EEUC) approach gained somewhat improved compression performance results with FND, HND, and TRE values such as 12, 151, and 220J respectively. The Multiobjective Fuzzy Clustering Algorithm (MOFCA)-an original technique demonstrated even more enhanced results with FND, HND, and TRE values such as 16, 155, and 223J respectively. Besides, the MOFCA-Optimized method reached somewhat higher performance with FND, HND, and TRE values such as 16, 167, and 243J correspondingly. JPEG algorithm produced a moderately closer compression result with FND, HND, and TRE values such as 18, 179, and 259J correspondingly. Eventually, the IAIVS-WMSN methodology produced effectual outcomes with an FND of 25, HND of 184, and a TRE of 278J.

Table IV shows the comparative analysis results achieved by the IAIVS-WMSN model and other existing techniques in terms of Packet Delivery Ratio (PDR), End to End Delay (ETED), and throughput. Fig. 7 shows the PDR analysis results of the IAIVS-WMSN algorithm under several nodes. The figure implies that the proposed IAIVS-WMSN system showcased better outcomes with a maximum PDR over other algorithms. For sample, with 100 nodes, the IAIVS-WMSN system reached an enhanced PDR of 91%, whereas TTDFP, MOFCA-opt., MOFCA-Org., EEUC, and CHEF offered fewer PDR values such as 90%, 90%, 90%, 90%, and 89% respectively. In the meantime, with 300 nodes, the proposed IAIVS-WMSN manner gained a superior PDR of 92%, whereas TTDFP, MOFCA-opt., MOFCA-Org., EEUC, and CHEF obtained the least PDR values such as 90%, 89%, 89%, 88%, and 86% correspondingly. Eventually, with 500 nodes, the proposed IAIVS-WMSN algorithm achieved the highest PDR of 90%, whereas TTDFP, MOFCA-opt., MOFCA-Org., EEUC, and CHEF accomplished the least PDR values such as 89%, 88%, 87%, 86%, and 84% correspondingly.

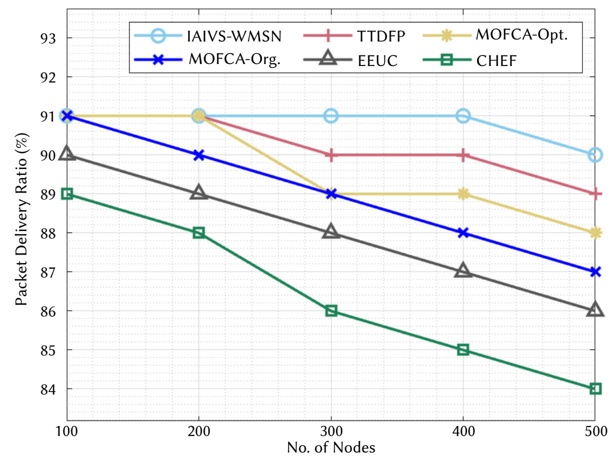

Fig. 7. PDR Analysis Results of IAIVS-WMSN Model and other Existing Techniques.

Fig. 8 shows the ETED analysis results of the proposed IAIVS-WMSN technique under several counts of nodes. The figure portrays that the proposed IAIVS-WMSN technique provided an effective outcome with the least ETED over other systems. For a sample, with 100 nodes, the IAIVS-WMSN algorithm achieved a minimum ETED of 3.70s, whereas TTDFP, MOFCA-opt., MOFCA-Org., EEUC, and CHEF achieved the maximum ETED values such as 3.80s, 3.85s, 3.90s, 4.50s, and 5.80s respectively. Moreover, with 300 nodes, the IAIVS-WMSN method demanded a minimal ETED of 4.60s, whereas TTDFP, MOFCA-opt., MOFCA-Org., EEUC, and CHEF demanded high ETED values such as 5.00s, 5.30s, 6.50s, 7.80s, and 8.10s respectively. Furthermore, with 500 nodes, the proposed IAIVS-WMSN approach demanded the least ETED of 6.80s, whereas TTDFP, MOFCA-opt., MOFCA-Org., EEUC, and CHEF required high ETED values such as 7.50s, 7.70s, 7.90s, 10.60s, and 11.00s correspondingly.

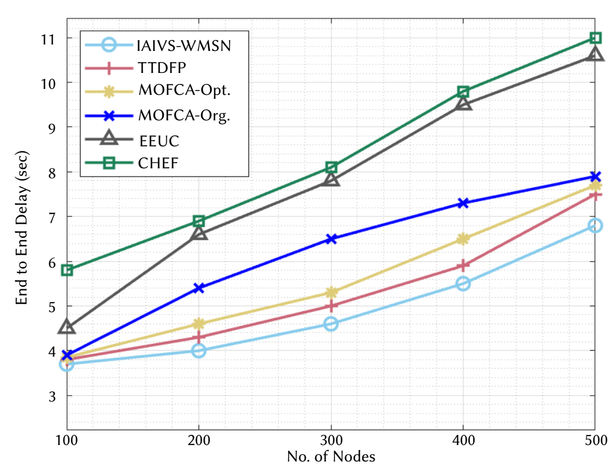

Fig. 8. ETED Analysis Results of IAIVS-WMSN Model and other Existing Techniques.

TABLE IV. Analysis Results of the Proposed and Existing Methods Under Different Measures

No. of Nodes	Packet Delivery Ratio (%)					
	IAIVS-WMSN	TTDFP	MOFCA-opt.	MOFCA-Org.	EEUC	CHEF
100	91.00	90.00	90.00	90.00	90.00	89.00
200	92.00	91.00	91.00	90.00	89.00	88.00
300	92.00	90.00	89.00	89.00	88.00	86.00
400	93.00	90.00	89.00	88.00	87.00	85.00
500	90.00	89.00	88.00	87.00	86.00	84.00
No. of Nodes	End to End Delay (sec)					
	IAIVS-WMSN	TTDFP	MOFCA-opt.	MOFCA-Org.	EEUC	CHEF
100	3.70	3.80	3.85	3.90	4.50	5.80
200	4.00	4.30	4.60	5.40	6.60	6.90
300	4.60	5.00	5.30	6.50	7.80	8.10
400	5.50	5.90	6.50	7.30	9.50	9.80
500	6.80	7.50	7.70	7.90	10.60	11.00
No. of Nodes	Throughput (Mbps)					
	IAIVS-WMSN	TTDFP	MOFCA-opt.	MOFCA-Org.	EEUC	CHEF
100	94.00	93.00	92.00	91.00	87.00	76.00
200	91.00	87.00	81.00	78.00	74.00	65.00
300	85.00	80.00	72.00	68.00	65.00	56.00
400	77.00	72.00	66.00	61.00	54.00	49.00
500	74.00	68.00	61.00	57.00	49.00	42.00

Fig. 9 shows the throughput analysis results achieved by the IAIVS-WMSN approach and other techniques under various node counts. The figure reveals that the proposed IAIVS-WMSN technique outperformed all other techniques with optimum results and maximal throughput. For a sample, with 100 nodes, the IAIVS-WMSN algorithm gained a superior throughput of 94Mbps, whereas TTDFP, MOFCA-opt., MOFCA-Org., EEUC, and CHEF achieved the least throughput values such as 93Mbps, 92Mbps, 91Mbps, 87Mbps, and 76Mbps correspondingly. Besides, with 300 nodes, the proposed IAIVS-WMSN system gained an improved throughput of 85Mbps, whereas TTDFP, MOFCA-opt., MOFCA-Org., EEUC, and CHEF achieved the least throughput values such as 80Mbps, 72Mbps, 68Mbps, 65Mbps, and 56Mbps correspondingly. Finally, with 500 nodes, the proposed IAIVS-WMSN technique achieved the maximum throughput of 74Mbps, whereas TTDFP, MOFCA-opt., MOFCA-Org., EEUC, and CHEF attained the least throughput values such as 68Mbps, 61Mbps, 57Mbps, 49Mbps, and 42Mbps correspondingly. From the results mentioned above and the discussion, it is clear that the proposed IAIVS-WMSN algorithm is an excellent tool for effective communication in WMSN.

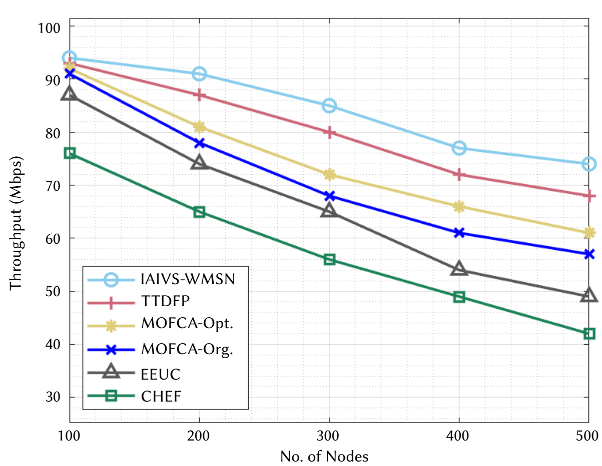

Fig. 9. Throughput Analysis results of IAIVS-WMSN Model and other Existing Techniques.

V. Conclusion

In this study, a novel IAIVS-WMSN algorithm has been designed and developed to accomplish effectual data transmission in WMSN. The presented IAIVS-WMSN system comprises three stages: Mask RCNN-based object detection, NCSIC-based image compression, and the AFA-based clustering. In addition, AFA system derived a Fitness Function containing various input parameters for effective selection of CHs and proper construction of clusters in WMSN. A comprehensive experimental analysis was conducted to validate the superiority of the proposed the IAIVS-WMSN technique. The simulation outcomes confirmed the enhanced performance of IAIVS-WMSN approach to the existing algorithms. In future, effective background subtraction and multipath route planning techniques can be designed to improve network efficiency.

References

[1] I. F. Akyildiz, T. Melodia, and K. R. Chowdhury, "A survey on wireless multimedia sensor networks," Computer networks, vol. 51, no. 4, pp. 921–960, 2007.

[2] W. Fang, D. H. Wang, and Y. Wang, "Energy-efficient distributed target tracking in wireless video sensor networks," International Journal of Wireless Information Networks, pp. 1– 11, 2015.

[3] M. Koyuncu, A. Yazici, M. Civelek, A. Cosar and M. Sert, "Visual and auditory data fusion for energy-efficient and improved object recognition in wireless multimedia sensor networks," IEEE Sensors Journal, 19(5), pp.1839-1849, 2018.

[4] H. ZainEldin, M. A. Elhosseini and H. A. Ali, "Image compression algorithms in wireless multimedia sensor networks: A survey," Ain Shams Engineering Journal, vol. 6, pp. 481–490, 2015.

[5] Q. Lu, W. Luo, J. Wanga and B. Chen, "Low-complexity and energy efficient image compression scheme for wireless sensor networks," Computer Networks, vol. 52, pp. 2594–2603, 2008.

[6] Donoho DL. Compressed sensing. IEEE Trans Inform Theory2006;52:1289–306.

[7] T. Sheltami, M. Musaddiq and E. Shakshuki, "Data compression techniques in Wireless Sensor Networks," Future Generation Computer Systems, vol. 64, pp. 151-162, 2016.

[8] D. M. Pham and S. M. Aziz, "Object extraction scheme and protocol for energy efficient image communication over wireless sensor networks,"

Computer Networks, vol. 57, pp. 2949–2960, 2013.

[9] M. Civelek and A. Yazici, "Automated moving object classification in wireless multimedia sensor networks," IEEE Sensors Journal, vol. 17, pp. 1116-1131, 2017.

[10] Y.A.U. Rehman, M. Tariq and T. Sato, "A novel energy efficient object detection and image transmission approach for wireless multimedia sensor networks," IEEE Sensors Journal, 16(15), pp.5942-5949, 2016.

[11] Q. Guo, "Enhanced compressed sensing for visual target tracking in wireless visual sensor networks," Journal of Electronic Imaging, 26(6), p.063028.

[12] M. Koyuncu, A. Yazici, M. Civelek, A. Cosar and M. Sert, "Visual and auditory data fusion for energy-efficient and improved object recognition in wireless multimedia sensor networks," IEEE Sensors Journal, 19(5), pp.1839-1849, 2018.

[13] A.N. Sukumaran, R. Sankararajan, and M. Swaminathan, "Compressed sensing based foreground detection vector for object detection in wireless visual sensor networks," AEU-International Journal of Electronics and Communications, 72, pp.216-224, 2017.

[14] D. Wang, J. Liu, D. Yao and I.E.E.E. Member, "An energy-efficient distributed adaptive cooperative routing based on reinforcement learning in wireless multimedia sensor networks," Computer Networks, 178, p.107313.

[15] M. Akter, M.O. Rahman, M.N. Islam, M.M. Hassan, A. Alsanad, and A.K. Sangaiah, "Energy-efficient tracking and localization of objects in wireless sensor networks," IEEE Access, 6, pp.17165-17177.

[16] Y. Shao, "Wireless multimedia sensor network video object detection method using dynamic clustering algorithm," Multimedia Tools and Applications, 79(23), pp.16927-16940.

[17] P. Sathyaprakash, and P. Prakasam, "Boltzmann randomized clustering algorithm for providing quality of evolution in wireless multimedia sensor networks," Wireless Personal Communications, 112(4), pp.2335-2349.

[18] S.Heng, Aimtongkham, P., Vo, V.N., Nguyen, T.G. and So-In, C., 2020. Fuzzy Adaptive-Sampling Block Compressed Sensing for Wireless Multimedia Sensor Networks. Sensors, 20(21), p.6217.

[19] B. A. Y. Alqaralleh, S. N. Mohanty, D. Gupta, A. Khanna, K. Shankar and T. Vaiyapuri, "Reliable Multi-Object Tracking Model Using Deep Learning and Energy Efficient Wireless Multimedia Sensor Networks," in IEEE Access, vol. 8, pp. 213426-213436, 2020, doi: 10.1109/ACCESS.2020.3039695.

[20] C. Xu, G. Wang, S. Yan, J. Yu, B. Zhang, S. Dai, Y. Li and L. Xu, "Fast Vehicle and Pedestrian Detection Using Improved Mask R-CNN," Mathematical Problems in Engineering, 2020.

[21] X. Wu, H. Shao, S. Wang and W. Wang, "A Multi-objective Artificial Flora Optimization Algorithm," In International Conference on Simulation Tools and Techniques (pp. 267-277). Springer, Cham.

[22] J. Uthayakumar, M. Elhoseny and K. Shankar, "Highly reliable and low-complexity image compression scheme using neighborhood correlation sequence algorithm in WSN," IEEE Transactions on Reliability, 69(4), pp.1398-1423, Dec. 2020.

Romany Fouad Mansour

Romany Fouad Mansour received a Ph.D. degree from the University of Assiut in 2009, He is currently working as an Associate Professor at Department of Mathematics, Faculty of science, New Valley University, Egypt. His research interests include Artificial Intelligence, Computer Vision, Computer Networks, Soft computing, Image Processing and Bioinformatics.

Carlos Soto

Carlos Soto received a B.S. degree in Mechanical Engineering from the Universidad del Norte (Colombia) in 2005. He was holder an Erasmus Mundus Scholarship in a Master of Advanced Materials Science and Engineering in 2007, by Universidad Politécnica de Cataluña (Spain) and Luleå Technology University (Sweden). Currently, he is a full-time professor in the Engineering Faculty of Universidad Autónoma del Caribe since 2016.

Roosvel Soto-Díaz

Roosvel Soto-Díaz received the B.S. and M.Sc. degrees in Materials Engineering and Mechanical Engineering from Universidad Autónoma del Caribe, respectively, in 2016 and 2018. He obtained meritorious and scientific distinction from his undergraduate and master's degree work. At present, he is a professor at the Universidad Simón Bolívar since 2021.

José Escorcia-Gutierrez

José Escorcia-Gutierrez received a Ph.D. degree in Computer Engineering and Mathematics of Security from the Universitat Rovira i Virgili in 2021 (Spain). In 2009 and 2011, he received the B.S. and M.Sc. degrees in Electronic Engineering from the Universidad del Norte (Colombia). His research interests include image processing, pattern recognition, computer vision, machine learning, and medical image analysis. Currently, He is a full-time professor in the Electronics and Telecommunication Engineering program of the Universidad Autónoma del Caribe, and he works under contract at the Corporación Universitaria Reformada.

Deepak Gupta

Dr. Deepak Gupta received a B.Tech. degree in 2006 from the Guru Gobind Singh Indraprastha University, Delhi, India. He received M.E. degree in 2010 from Delhi Technological University, India and Ph. D. degree in 2017 from Dr. APJ Abdul Kalam Technical University (AKTU), Lucknow, India. He has completed his Post-Doc from National Institute of Telecommunications (Inatel), Brazil in 2018. He has co-authored more than 145 journal articles including 109 SCI papers and 45 conference articles. He has authored/edited 53 books, published by IEEE-Wiley, Elsevier, Springer, Wiley, CRC Press, DeGruyter and Katsons. He has filled four Indian patents. He is convener of ICICC, ICDAM & DoSCI Springer conferences series. Currently he is Associate Editor of Expert Systems (Wiley), and Intelligent Decision Technologies (IOS Press). He is the recipient of 2021 IEEE System Council Best Paper Award. He has been featured in the list of top 2% scientist/researcher database in the world [Table-S7-singleyr-2019]. He is also working towards promoting Startups and also serving as a Startup Consultant. He is also a series editor of "Elsevier Biomedical Engineering" at Academic Press, Elsevier, "Intelligent Biomedical Data Analysis" at De Gruyter, Germany, "Explainable AI (XAI) for Engineering Applications" at CRC Press. He is appointed as Consulting Editor at Elsevier.

Ashish Khanna

Dr. Ashish Khanna [IEEE Member'2019, Senor Member'2020] has expertise in Teaching, Entrepreneurship, and Research & Development with specialization in Computer Science Engineering Subjects. He received his Ph.D. degree from National Institute of Technology, Kurukshetra in March 2017. He has completed his M. Tech. in 2009 and B. Tech. from GGSIPU, Delhi in 2004. He also has completed his Post Doc from INATEL, Brazil and Universiity of Valladolid, Spain. He has around 170 accepted and published research papers and book chapters in reputed SCI, Scopus journals, conferences and reputed book series including 90 papers accepted and published in SCI indexed Journals. He also has 8 published Patents and design patents to his credit. Additionally, He has co-authored, edited and editing around 45 books. He has also served as a keynote speaker, resource person and given several invited. He was resource person speaker and delivered a lecture at the online ATAL program at JNU in 2020. He has worked as Guest Editor in several reputed SCI and SCOPUS journals. He is also serving as Series Editor in publishing houses like De Gruyter (Germany) of "Intelligent Biomedical Data Analysis" series, Elsevier of "Intelligent Biomedical Data Analysis" and CRC Press of "Intelligent Techniques in Distributed Systems: Principles and Applications". He is also acting as a consulting editor for Elsevier. His research interest includes, Distributed Systems and its variants (MANET, FANET, VANET, IoT), Machine learning. He is the recipient of 2021 IEEE System Council Best Paper Award. He is serving as convener in some springer international conferences series like ICICC, ICCCN, ICDAM, and DoSCI. He is senior IEEE member

(SMIEEE) and ACM member too. He has played key role in promoting and initiating several startups and is also a startup consultant. He has also played the key role in the establishment of Bhavya Books (A Delhi Based Publishing House) and also promoted Smart India Hackathon at MAIT. He is key member and originator of Universal Inovator an International Research Lab. He initiated the first ever of its kind event in India "WHERE STARTUP MEETS INVESTOR" in collaboration with Universal Inovator and SIIF SSCBS, DU under the banner of ICICC-2020 international conference. First time a Research based conference was conducted along with a Startup funding event. He also played the key role in the India's first conference on Patents (ICIIP-2021) in association with UI and IGDTUW Delhi.

A Method of the Coverage Ratio of Street Trees Based on Deep Learning

Wen Han, Lei Cao, Sheng Xu*

Nanjing Forestry University, Nanjing (China)

Received 15 November 2021 | Accepted 3 June 2022 | Published 25 July 2022

Abstract

The street trees coverage ratio provides reliable data support for urban ecological environment assessment, which plays an important part in the ecological environment index calculation. Aiming at the statistical estimation of urban street trees coverage ratio, an integrated model based on YOLOv4 and Unet network for detecting and extracting street trees from remote sensing images is proposed, and obtain the estimated street trees coverage ratio in images accurately. The experiments are carried out under self-made dataset, and the results show that the accuracy of street trees detection is 94.91%, and the street trees coverage ratio is 16.30% and 13.81% in the two experimental urban scenes. The MIoU of contour extraction is 98.25%, and the estimated coverage accuracy is improved by 6.89% and 5.79%, respectively. The result indicates that the proposed model achieves the automation of contour extraction of street trees and more accurate estimation of street trees coverage ratio.

Keywords

Ecological Environment Index, Object Detection, Remote Sensing Image, Street Trees Coverage Ratio, Unet, YOLOv4.

DOI: 10.9781/ijimai.2022.07.003

I. Introduction

The coverage ratio of street trees is an important indicator affecting the urban ecological environment index [1], which can provide reliable data support for urban ecological environment assessment. With the development of deep learning [2], the method of estimating the coverage ratio of street trees in remote sensing images based on deep learning can reduce manual intervention, improve the efficiency of measurement and provide more accurate data information to relevant administrative departments.

In terms of image processing [3], the convolutional neural network [4] (CNN) is widely used. Among the field of image processing methods, CNN is the most outstanding model in deep learning. It is a special multi-layer perceptron designed to detect two-dimensional images. The essence of the convolutional kernel is a feature extractor. CNN has the structural characteristics of local perception region, weight sharing and pooling. Local perception region and weight sharing significantly reduce the number of parameters of CNN and improve the network performance. The spatial subsampling enables CNN to have a certain scaling and translation invariance and has a stronger generalization ability. CNN incorporates feature extraction into model learning, organically combines feature learning with classification learning, and realizes image interpretation more effectively.

Today, there are few studies on the estimation of street trees coverage ratio in remote sensing images based on deep learning in the domestic and overseas. However, there are still some scholars at home and abroad who have studied the street greening ratio based on different streetscape data platforms. For example, Long Ying [5] has studied street greening in 245 major cities in China based on Tencent Streetscape Platform; Li Xiaojiang et al [6]. modified the green landscape index by combining it with Google Streets View, and achieved the automatic measurement of urban street green ratio; Seiferling et al. [7] quantified street trees in New York and Boston based on Google Street View images. Yan Li et al. [8] proposed a vegetation extraction method based on attention model in remote sensing image, under different environmental topographic and climatic conditions, vegetation differentiation and symbiosis with other land features can separate a single vegetation. Although the above researches reflect the coverage ratio of street trees to a certain extent, the street scenery taken from different angles will have geometric deformation, and the observation information of images is limited and hard to be used for accurate measurement and calculation. However, observation information of remote sensing images is more macroscopic and accurate, and we can get more detailed messages from the given images, so, it is beneficial for us to use remote sensing images to study street trees coverage ratio. There are also many challenges, such as shading between trees, insufficient lighting, and weather and seasonal factors that cause errors in estimates of street trees coverage ratio.

Contributions of our work are as follows:(1) YOLOv4 [9] is used to detect the street trees in remote sensing images, and the coverage ratio of the street trees is estimated through the coordinate information of the bounding box; (2) an integrated model of remote sensing images object detection and contour extraction is proposed, which is an end-to-end process [10]. While calculating the street trees coverage ratio through this model, the problems arising in estimation based on object detection model and instance segmentation can be effectively solved, and the estimated value is closer to the real value.

The structure of this document is as follows: section II gives introduction about related algorithms to this work, section III provides experimental preparation, including dataset, hardware environment and evaluation index, section IV presents the experiment results, gives full discussion about the varieties of cases what occur in the

* Corresponding author.

E-mail address: xusheng@njfu.edu.cn

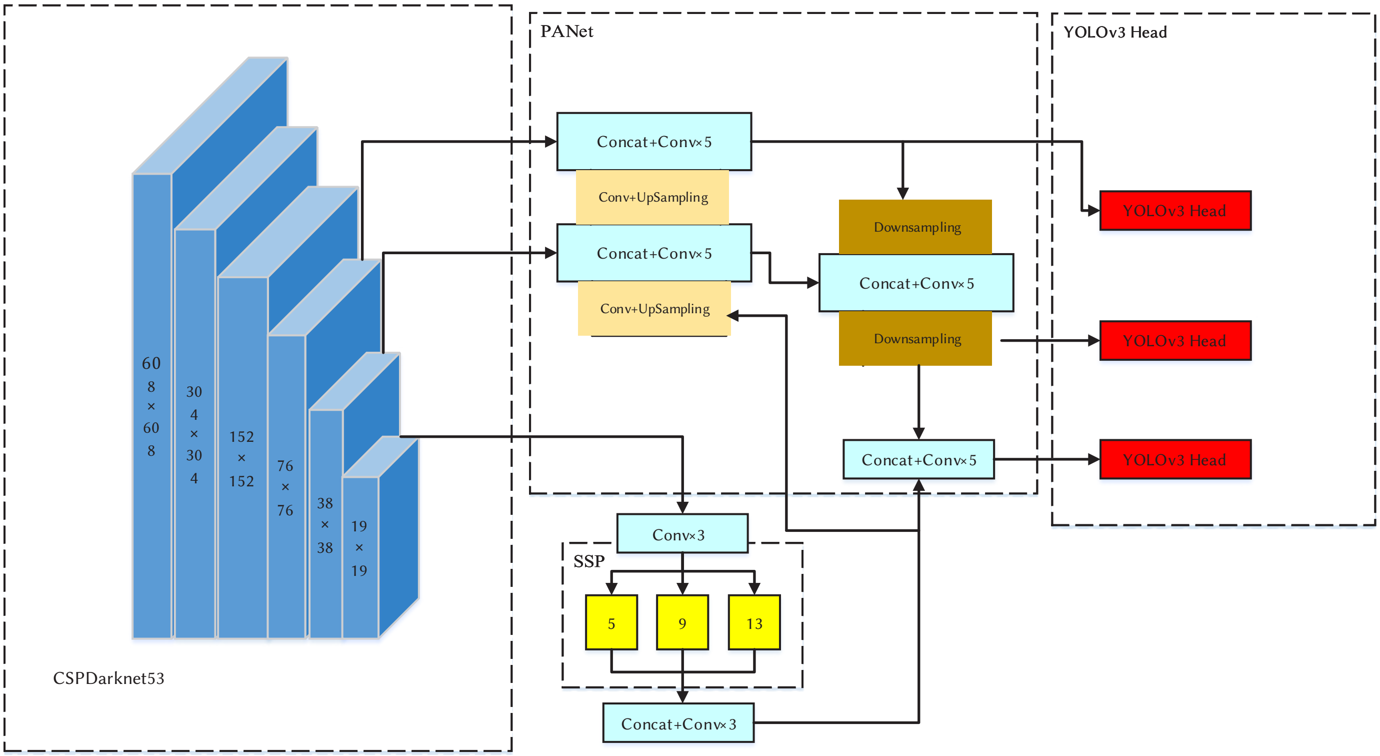

Fig. 1. The network structure of YOLOv4.

experiment, and carry out a comparative experiment among some mainstream algorithms to prove the superiority of the proposed algorithm, Section V makes a summary of the work and puts forward the vision of future work.

II. Related Algorithms

A. The Structure of YOLOv4

Object detection is an important application of artificial intelligence, which is to identify the object in the image and mark the position of the object. Here we used YOLOv4 to detect the street trees in the remote sensing images.

By introducing Mosaic and GA [11] to select the optimal hyper-parameters, YOLOv4 improves the existing methods to a lower training threshold, which can achieve better results under the limited GPU resources. The network structure of YOLOv4 is shown in Fig.1 below. CSPDarknet53 is the backbone, SPP [12] (Spatial Pyramid Pooling) is the additional module of neck, PANet [13] (Path Aggregation Network) is the feature fusion module of neck, and YOLOv3-head [14] is the head. CSPDarknet53 added CSPNet (Cross Stage Partial Network) to each large residual block of Darknet53 and integrated it into the feature map through gradient changes. The feature map was divided into two parts, one of which was convolutional operation. The other part is combined with the last convolution. PANet makes full use of feature Aggregation. The fusion method is changed from addition to multiplication, which makes object detection capability more accurate. In order to get the extraction of the contour of the street trees, we introduce Unet [15] to achieve this goal.

B. Unet Network Model

Image segmentation algorithms based on deep learning mainly have two core frameworks: one is image feature extraction based on CNN, and the other is the upsampling/deconvolution segmentation framework based on global neural network, such as FCN [16] (Fully Convolutional Networks). The former cannot be accurately segmented because the category probability of each pixel cannot be identified by the full connection layer. The latter changes the full connection layer of the former to the convolution layer, and introduces the upsampling before multiple pooling operations, which solves the problem of accurate segmentation, but the effect of edge extraction is not good enough.

Unet draws on the characteristics of FCN. The network structure consists of two symmetric parts: contracting path and expanding path. Contracting paths adopt 3×3 convolution and pooled down-sampling, which can obtain shallow features and deep features, then capture the relationship among pixels. The 3×3 convolution and upsampling are used in expansion paths. While upsampling, the deep features and shallow features are combined in a cascading way to obtain the accurate position of the image to be segmented. The network structure of Unet is shown in Fig.2 below.

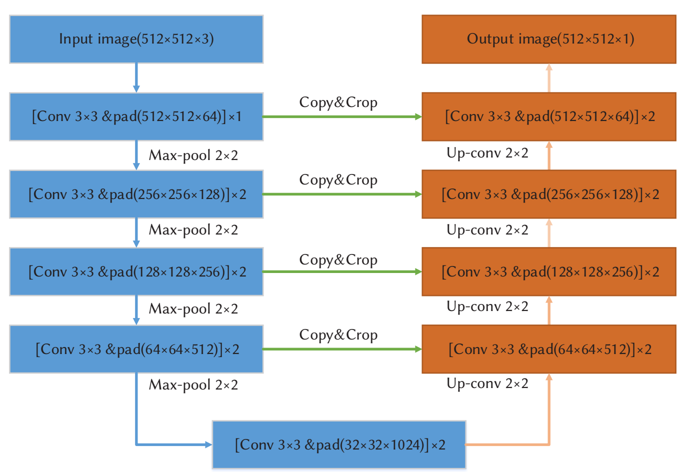

Fig. 2. The network structure of Unet.

C. Integration of Object Detection and Contour Extraction From Images

Based on deep learning, an integrated process of object detection and contour extraction in remote sensing image is proposed. This is an end-to-end process. Firstly, according to the detection results of YOLOv4, the coordinate information and bounding box are acquired, and the segmentation image of the corresponding region is obtained by Unet. Finally, the obtained segmentation image of the corresponding region is fused with the corresponding region of the object detection to get the final result of object detection and contour extraction. As is shown in Fig.3.

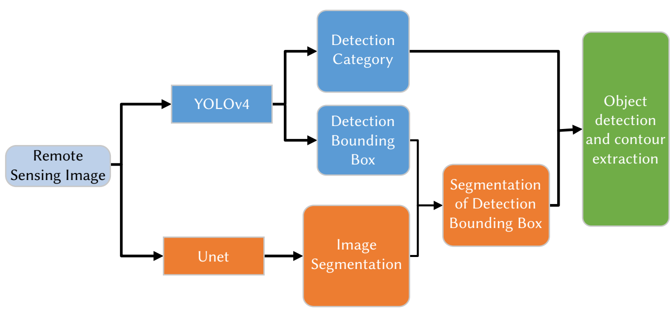

Fig. 3. Integrated flow chart of object detection and contour extraction.

III. Experiment Preparation

A. Dataset and Hardware Environment

The data used in this study are high-resolution remote sensing images, and the data are provided by Jiangsu Bureau of Surveying and Mapping with a resolution of 0.3 meter.

Due to the large size of remote sensing images, it needs to be cut and segmented, and we selecte abundant images of different urban scenes as samples for training and testing. Finally, 58,640 images containing street trees are collected, and 45,000 of them are used as the training data set, 5,000 images are used as the valid test and the remaining 8,640 images are used as the test set. Meanwhile, the data set contain the street trees information of different varieties of trees and growth environments, which effectively improves the robustness of the model. During the period of data annotation, there would be only tree class labeled.

This experiment is conducted on windows10 operating system; memory size is 32G; GPU: NVIDIA GeForce 3070; the learning frameworks are tensorflow-gpu 1.13.1, keras 2.1.5, cuda10.0 and cudnn 7.4.1.5.

B. Evaluation Index

When evaluating the detection effect of the model, Precision, Recall and F1 of the model usually appear as vital indicators. The calculation Equations are Equation (1)- (3). Precision is based on the predicted results, showing the proportion of the number of correct samples in the total number of samples; Recall is the proportion of positive cases that can be correctly predicted.

$$Precision = \frac{TP}{TP+FP} \quad (1)$$

$$Recall = \frac{TP}{TP+FN} \quad (2)$$

$$F1 = \frac{2\times Precision\times Recall}{Precision+Recall} \quad (3)$$

TP stands for the number that was a street tree and correctly detected; FP stands for the number that is not a street tree, but is wrongly identified as a street tree; FN stands for the number which the street tree is not identified or wrongly identified. In the evaluation, the higher Precision and Recall, the closer the better detection effect would be. However, there is a contradictory relationship between the two, the most common way is by calculating F1 score.

Mean Intersection Over Union (MIoU): A standard measure for semantic segmentation. It calculates the parallel and cross-ratio of two sets. In semantic segmentation, these two sets are ground truth and predicted segmentation respectively. The calculation is in Equation (4).

$$MIoU = \frac{1}{k+1}\sum_{i=0}^{k}\frac{TP}{TP+FP+FN} \quad (4)$$

Average precision (AP) is also a popular metric in measuring the accuracy of semantic segmentation like FCN, Unet, etc. AP computes the average Precision for Recall over 0 to 1. Mathematically, AP is defined in (5), where p stands for Precision and r stands for Recall.

$$AP = \int_0^1 p(r)dr \quad (5)$$

IV. Experiment and Discussion

A. Street Trees Detection and Contour Extraction

After the dataset trained by YOLOv4 network, 8,640 images in the test set are tested, with a total of 13,040 street trees.TP value is 11918, FP value is 639, FN value is 483. According to Eq. (1)-(3), the Precision, Recall and F1 score of the experiment can be calculated as 94.91%, 96.11% and 95.51%, respectively, showing that this model is strong. Here, Precision and Recall are consistent with the calculation methods of YOLOv4 evaluation indexes. We only labeled a tree class, so mAP is equal to AP and the MIoU is the same as IoU, and calculated by Unet is 98.25%, and AP is 99.29%.

Part of the detection results by YOLOv4 network and the segmentation effect of Unet network are shown in Fig.4. It is obvious that there exist omissions in the object detection task of street trees and the street trees can be basically segmented after semantic segmentation algorithm.

B. Integration of Street Trees Detection and Contour Extraction in Remote Sensing Images

The integrated processing model of street trees detection and contour extraction in remote sensing images is composed of two sub-models. The specific process is as follows: (1) the street trees are detected in remote sensing images through YOLOv4, and the coordinate information of the bounding box and confidence coefficient are obtained;(2) the images are sent to the Unet to classify the street trees pixel by pixel;(3) the detected result based on the YOLOv4 is fused with the corresponding region on the segmentation result to obtain the effect of street trees detection and contour extraction. The processing flow and effect is shown in Fig.5.

C. Estimation of Street Trees Coverage Ratio in Urban Scenes

Two different road scenarios were selected from the test set for discussion, including different varieties of trees and light environments. The test results are shown in Fig.6: straight road scene detection results; Fig.7: small roadside parking lot detection results, the left side of each image shows the result based on YOLOV4; and the right side shows the result of the proposed method.

The Equation (6) is to calculate the coverage ratio of street trees [17], where the coverage ratio of street trees is denoted as P, the total area of the vertical projection of street trees is denoted as S, and the total area of urban land is denoted as St. In the process of street trees detection, the information of the detection bounding box can be output together with the detection confidence coefficient. Here, S is acquired

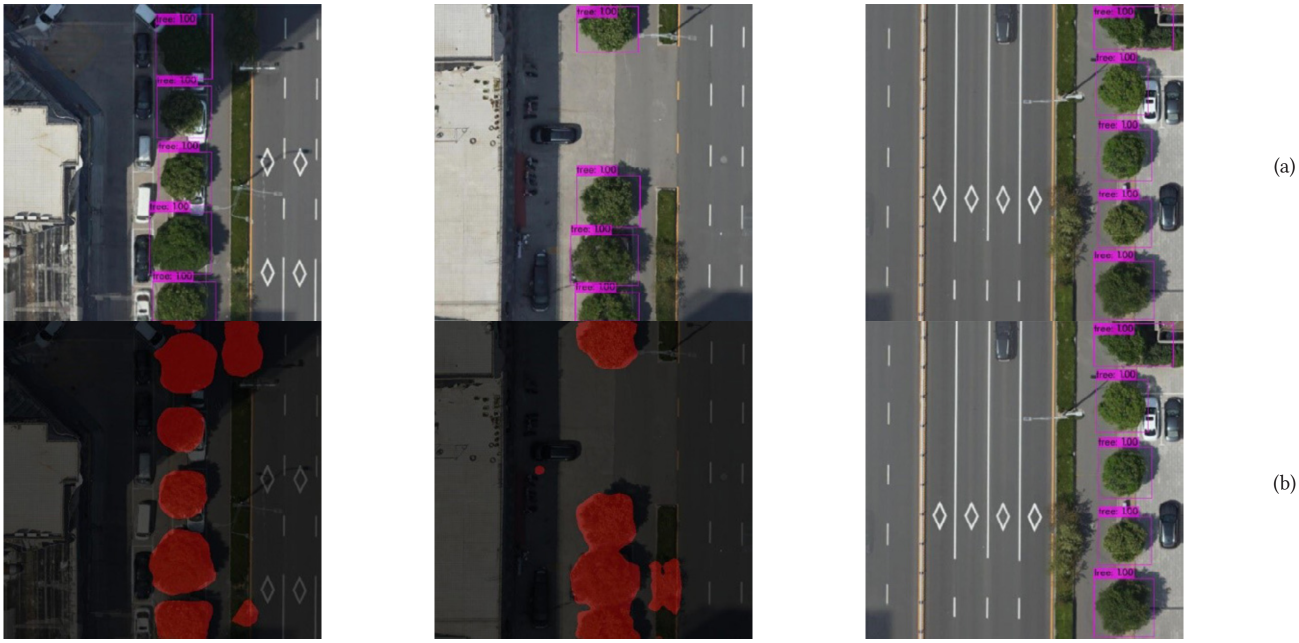

Fig. 4. (a) Results of street trees detection based on YOLOv4; (b) Results of street trees segmentation based on Unet.

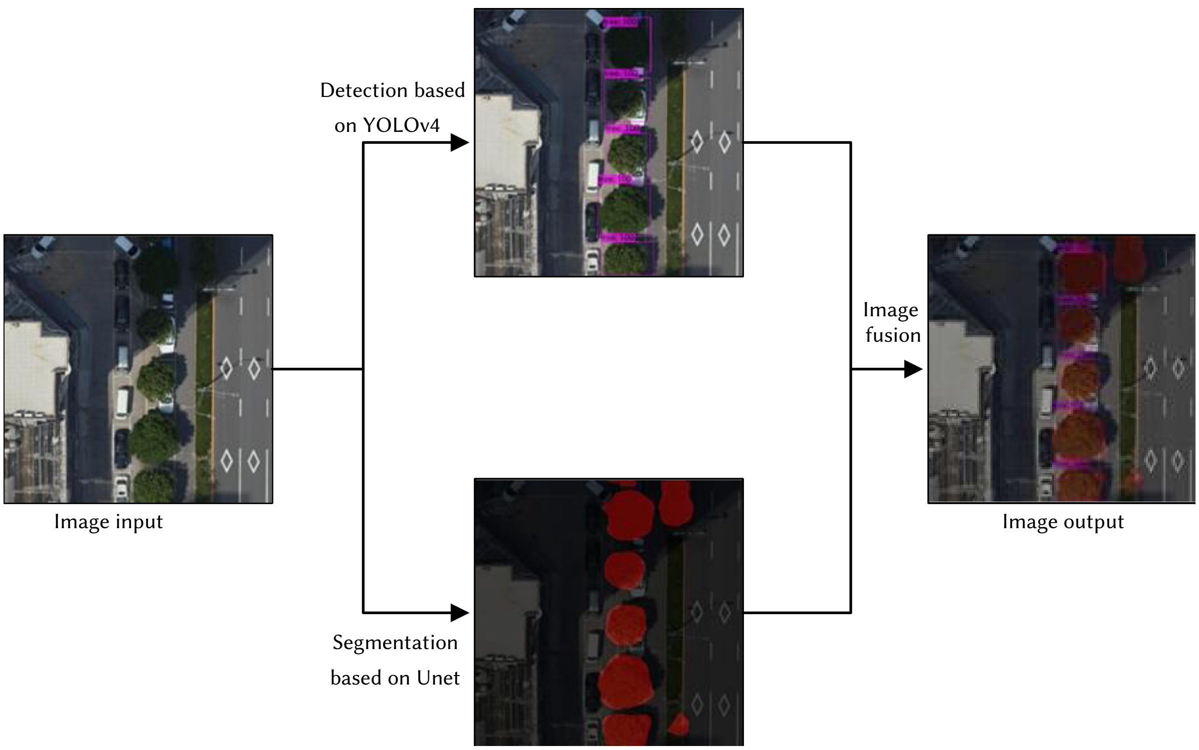

Fig. 5. Schematic diagram of integrated processing of street trees detection and contour extraction.

by the product of the obtained height and length. When the contour of the street trees is extracted, the size and area of the obtained contour pixel are calculated as the desired S, and St is the actual area of the detected remote sensing image.

$$P = \frac{S}{St} \tag{6}$$

Through Equation (6), we can get the street trees coverage ratio of these two scenes, we named the straight road scene and small roadside parking lot scene as S1 and S2 respectively. S1 and S2 based on YOLOv4 are 13.81% and 16.3% respectively, S1 and S2 based on the integrated processing model are 8.08% and 9.47% respectively. It is easy to see that the estimated value of urban street trees coverage ratio obtained by the proposed algorithm is close to the actual value.

D. Discussion

As can be seen from the above, object detection of street trees through YOLOv4 is in good condition, but there exist some cases that may lead to exceptional detection: when the illumination is uneven, it cannot be detected; when the street trees grow densely, the complete information of trees cannot be well detected; meanwhile, when the shape and outline of street trees have a visual difference, it will lead to omitting trees to be detected. However, the integrated method of street trees detection and contour extraction in remote sensing images can

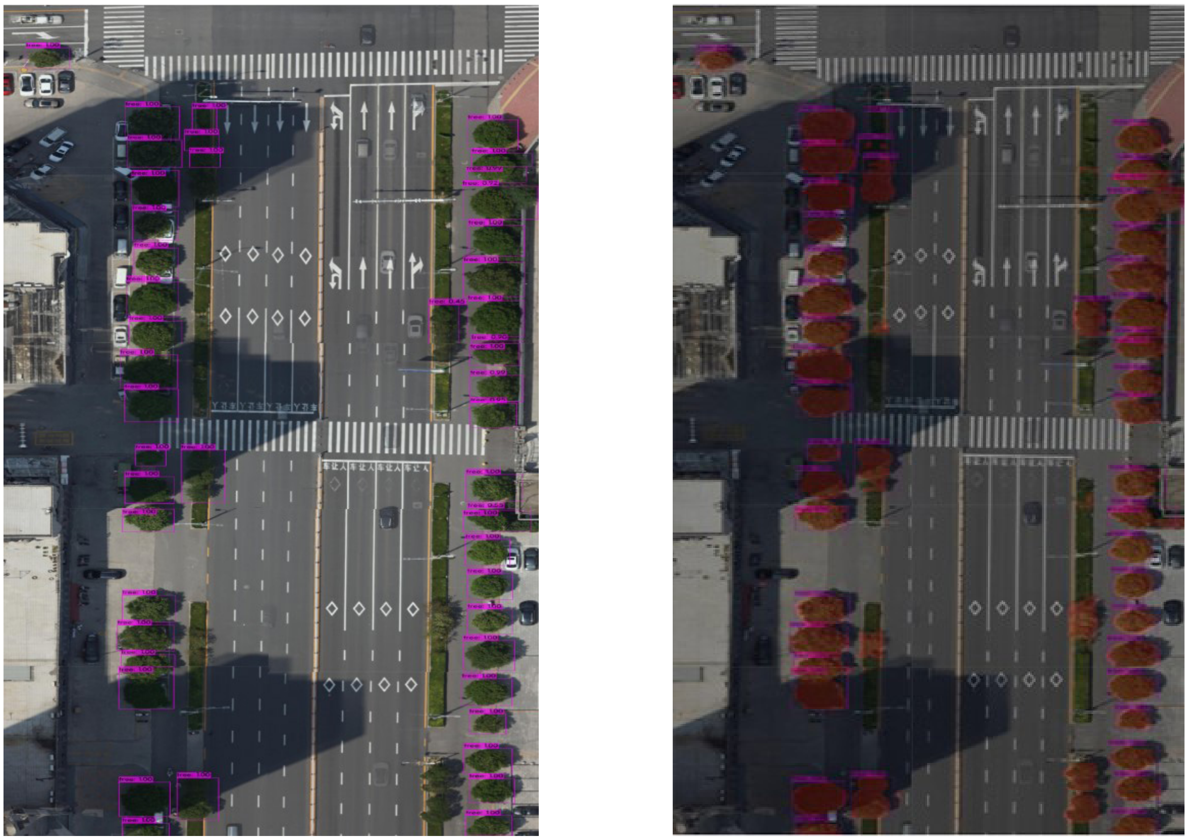

Fig. 6. Detection results of straight road scene.

Fig. 7. Scene detection results of small roadside parking lot.

solve these problems. For comparison, we used the Mask RCNN [18] to train the same data set. The following are the comparative results of each network model on the street trees, as is shown in Fig. 8.

As can be seen from Fig.8(a), street trees or part of street trees that are not detected in the YOLOv4 are marked with a red oval shape, including the following situations: street trees that cannot be detected in areas with weak illumination; where the street trees grow densely, the complete trees cannot be detected; meanwhile, when the shape and outline of the street tree have no obvious visual characteristics, there will be the situation of missing detection. All of the above will cause errors in coverage ratio calculation. As can be seen from Fig.8 (b), the green oval is used to mark the improvement and existing problems by the Mask RCNN. Undoubtedly, part of the above problems can be solved, there still exist some issues to settle. The street trees will be detected where the illumination is insufficient and there is also a partial missing of street trees in pixel detection. When this method was used for the identification and coverage ratio estimation of street trees, many issues will occur. For example, in the figure on the far left, there is a condition of repeated detection, so the coverage ratio of street trees will be bigger than the real value. In the other two images, the same problem appeares in the detection results of the YOLOv4, that is, in the detection process, there will be missed detection of street trees, the detection information of street trees is incomplete, and when the shape and outline of street trees has no obvious visual characteristics, there will lead to miss detection of street trees. The above cases will cause errors in the estimation of the street trees coverage ratio. As can be seen in Fig.8 (c), these problems can be totally solved through the integrated processing of detection and contour extraction model of the street trees. The yellow oval is used to mark the improvement and optimization of the information of the street trees can be obtained

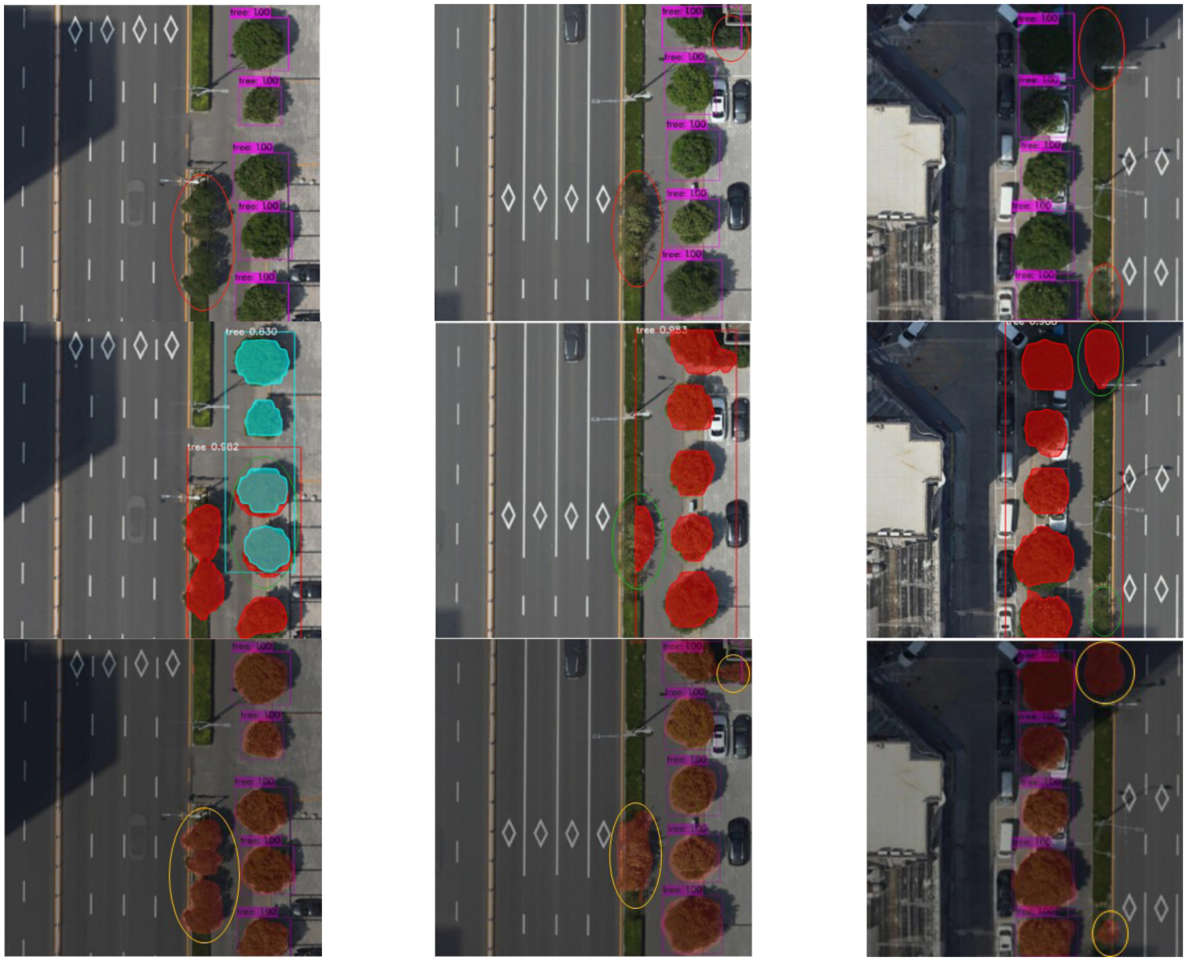

(a)

(b)

(c)

Fig. 8. (a) Results of Street tree detection based on YOLOv4;(b) Results of Street tree detection based on Mask RCNN;(c) The integrated detection results of street tree detection and contour extraction

through the proposed method. When calculating the covered area of the street trees, it was closer to the real value, which can improve the estimation accuracy of the covered area of the street trees in local scenes. In this case, the coverage ratio of the street trees obtained is closer to the real coverage ratio of the street trees themselves, so that the estimated coverage ratio of the street trees in local city scenes is closer to the real value.

E. Comparative Experiments With Other Mainstream Algorithms

The configuration information of the training platform remains unchanged. YOLOv3, YOLOv4, Mask RCNN and the proposed model were used for training and testing on the same data set. Comparison of mAP of different models is shown in Table I.

In the process of object detection, the mAP of the proposed model is superior to other mentioned models, indicating that the prediction accuracy of the proposed model is greatly improved compared with the method in the Table I.

TABLE I. Comparison of Model Performance

Detection model	mAP(%)
YOLOv3	81.72
YOLOv4	89.21
Mask RCNN	88.86
Proposed	99.29

F. Experiments Under VHR-10 Dataset

In order to verify the robustness of the proposed model, we also trained and tested the VHR-10 [19] [20] [21] dataset in different models. Table II listed the AP of five categories for the four methods (YOLOv3, YOLOv4, Mask RCNN, Proposed). We can find that AP values of these categories were significantly improved by detection of the proposed method, and the model was robust.

TABLE II. AP (%) of 5 Categories Targets of VHR-10 Dataset

Category	method			
	YOLOv3	YOLOv4	Mask RCNN	Proposed
Airplane	90.89	90.86	89.56	97.48
Baseball diamond	96.59	97.20	96.72	98.86
Tennis court	90.23	90.35	90.00	92.31
Ground track field	99.40	99.38	99.35	99.72
Bridge	86.78	87.32	87.35	88.85

V. Conclusion

In this study, we used the object detection method based on the YOLOv4 to carry out object detection on street trees and obtain the bounding box information and confidence coefficient at the same time, and calculated the coverage ratio of the street trees in urban scenes. Due to the non-tree-side part in bounding box or undetected trees, this method exits some errors. In order to solve these problems, we put forward the integration of remote sensing image object detection and contour extraction of street trees along the model to improve the accuracy of the coverage ratio.

The proposed model has the following three advantages when used to calculate the coverage ratio of street trees. Firstly, since there was only one tree class, a great loss value can be obtained by only iterating about 100 times when training under Unet network. Meanwhile, MIoU and AP are 98.25% and 99.29% respectively, compared with the mentioned models, the result is better. Then, b because there is no limit to the image size of the network, you can input any size images. Finally, through the proposed method, we can solve the problems occurring in street trees detection based on YOLOv4 and Mask RCNN, such as there exist the non-tree-side part in the bounding box and undetected trees while detecting, we can further obtain all information of street trees, and calculate the coverage ratio which is much closer to the real coverage ratio of trees.

Acknowledgment

This work was supported in part by the National Natural Science Foundation of China (Grant No. 62102184), in part by the Natural Science Foundation of Jiangsu Province (Grant No. BK20200784), in part by the Natural Science Foundation of the Higher Education Institutions of Jiangsu Province (Grant No. 19KJB520010), in part by China Postdoctoral Science Foundation (Grant No. 2019M661852) and in party by the National Key Research and Development Program of China (2019YFD1100404).

References

[1] B.T. Wang, W.J. Wang, S.H. Cui, Y.Z. Pan, and J.H. Zhang, "Research on the methods of urban ecological environmental quality assessment," in Acta Ecologica Sinica, vol. 29, no. 3, pp. 1068-1073,2009.

[2] Y. LeCun, Y. Bengio, and G. Hinton, "Deep learning," in NATURE, vol. 521, no. 7553, pp. 436-444, 2015.

[3] J. Kuruvilla, D. Sukumaran, A. Sankar, and S.P. Joy, "A Review on Image Processing and Image Segmentation," in International Conference on Data Mining and Advanced Computing, Kadayiruppu, INDIA, 2016, pp. 198-203.

[4] A. Krizhevsky, I. Sutskever, and G.E. Hinton, "ImageNet Classification with Deep Convolutional Neural Networks," in COMMUNICATIONS OF THE ACM, vol. 60, no. 6, pp. 84-90, 2017.

[5] Y. Long, "New ideas for urban research and planning under the new data environment of street urbanism," Time Architecture, vol. 02, pp. 128-132, 2016.

[6] X. Li, C. Zhang, W. Li., "Assessing street-level urban greenery using Google Street View and a modified green view index," in Urban Forestry & Urban Greening, vol. 14, no. 3, pp. 675-685,2015.

[7] I. Seiferling, N. Naik, C. Ratti, 2 "Green Streets-Quantifying and mapping urban trees with street-level imagery and computer vision," in Landscape and Urban Planning, vol. 165, pp. 93-101, 2017.

[8] L. Yan, Q. Xu, Y. Liu, "Vegetation extraction from remote Sensing Images based on attention network," in Surveying and mapping geographic information, vol. 46, no. S1, pp. 44-48, 2021.

[9] A. Bochkovskiy, C.Y. Wang, H.Y.M. Liao, "Yolov4: Optimal speed and accuracy of object detection,"2020. Accessed: Apr. 23, 2020. [Online]. Available: https://arxiv.org/abs/2004.10934, doi: arXiv:2004.10934.

[10] N. Abbas, F.Q. Yu, "A Comprehensive Analysis of the End-to-End Delay for Wireless Multimedia Sensor Networks" in Journal of Electrical Engineering & Technology, vol. 13, no. 6, pp. 2456-2467,2018.

[11] P.F. Guo, X.Z. Wang, Y.S. Han, "The Enhanced Genetic Algorithms for the Optimization Design," in 2010 3RD International Conference on Biomedical Engineering and Informatics, pp. 2990-2994, 2010.

[12] K. He, X. Zhang, S. Ren, "Spatial Pyramid Pooling in Deep Convolutional Networks for Visual Recognition," in IEEE Transactions on Pattern Analysis and Machine Intelligence, vol. 37, no. 9, pp. 1904-1916, 2015.

[13] S. Liu, L. Qi, H.F. Qin, J.P. Shi, J.Y. Jia, "Path Aggregation Network for Instance Segmentation," in 2018 IEEE/CVF Conference on Computer Vision and Pattern Recognition, pp. 8759-8768,2018.

[14] J. Redmon, A. Farhadi, "Yolov3: An incremental improvement," 2018. Accessed: Apr. 8, 2018. [Online]. Available: https://arxiv.org/abs/1804.02767, doi: arXiv:1804.02767.

[15] O. Ronneberger, P. Fischer, T. Brox, "U-net: Convolutional networks for biomedical image segmentation," in International Conference on Medical image computing and computer-assisted intervention. Springer, Cham, pp. 234-241, 2015.

[16] J. Long, E. Shelhamer, T. Darrell, "Fully Convolutional Networks for Semantic Segmentation," in 2015 IEEE Conference on Computer Vision and Pattern Recognition, pp. 3431-3440, 2015.

[17] L.W. Yang, Z.X. Zeng, and C.J. Zhao, " Study on Statistical Technique of Urban Roadway Tree Greening Coverage," in Chinese Landscape Architecture, vol. 04, pp. 38-39, 1996.

[18] K. He, G. Gkioxari, P. Dollar, and R. Girshick, "Mask R-CNN," in IEEE Transactions on Pattern Analysis and Machine Intelligence, vol. 42, no. 2, pp. 386–397,2018.

[19] G. Cheng, J.W. Han, "A survey on object detection in optical remote sensing images," Journal of Photogrammetry and Remote Sensing, vol. 117, pp. 11-28, 2016.

[20] G. Cheng, P. Zhou and J. Han, "Learning Rotation-Invariant Convolutional Neural Networks for Object Detection in VHR Optical Remote Sensing Images," in IEEE Transactions on Geoscience and Remote Sensing, vol. 54, no. 12, pp. 7405-7415, 2016.

[21] Cheng G, Han J, Zhou P, "Multi-class geospatial object detection and geographic image classification based on collection of part detectors" in ISPRS Journal of Photogrammetry and Remote Sensing, vol. 98, pp. 119-132,2014.

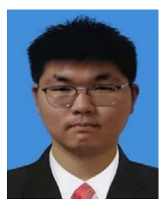

Wen Han

Wen Han received his B.S. degree in software engineering in 2018 from Yangtze University, Jing Zhou, China. Now, he is studying for the master degree at the College of Information Technology in Nanjing Forestry University. His research interests include computer vision and deep learning. He has published several papers and patents in domestic and international journals. He has two years of experience working in a fortune 500 company and is currently an intern in a research institute.

Lei Cao

Lei Cao received his bachelor degree in Communication Engineering in 2021 from Information College Huaibei Normal University, China. Now, He is studying for his master degree at the College of Information Science and Technology from Nanjing Forestry University. His research interests include Computer Vision and Image Processing.

Sheng Xu

Sheng Xu received his Ph.D degree from the University of Calgary in 2018, He joined the College of Information Science and Technology at Nanjing Forestry University. At present, he has published more than 40 papers on international and domestic journal conferences. In recent five years, he has published more than 10 SCI papers on IEEE Trans. TPAMI, IEEE Trans. TIST, IEEE Trans. His research interests include Three-dimensional spatial information processing, point cloud data analysis and computer vision.

Improved GWO Algorithm for UAV Path Planning on Crop Pest Monitoring

Qun Ding[1], Xiaolong Xu[2]*

[1] Jiangsu Key Laboratory of Big Data Security and Intelligent Processing, Nanjing University of Posts and Telecommunications, Nanjing (China)
[2] School of Computer Science, Nanjing University of Posts and Telecommunications, Nanjing (China)

Received 1 December 2021 | Accepted 3 June 2022 | Published 12 July 2022

Abstract

Agricultural information monitoring is the monitoring of the agricultural production process, and its task is to monitor the growth process of major crops systematically. When assessing the pest situation of crops in this process, the traditional satellite monitoring method has the defects of poor real-time and high operating cost, whereas the pest monitoring through Unmanned Aerial Vehicles (UAVs) effectively solves the above problems, so this method is widely used. An important key issue involved in monitoring technology is path planning. In this paper, we proposed an Improved Grey Wolf Optimization algorithm, IGWO, to realize the flight path planning of UAV in crop pest monitoring. A map environment model is simulated, and information traversal is performed, then the search of feasible paths for UAV flight is carried out by the Grey Wolf Optimization algorithm (GWO). However, the algorithm search process has the defect of falling into local optimum which leading to path planning failure. To avoid such a situation, we introduced the probabilistic leap mechanism of the Simulated Annealing algorithm (SA). Besides, the convergence factor is modified with an exponential decay mode for improving the convergence rate of the algorithm. Compared with the GWO algorithm, IGWO has the 8.3%, 16.7%, 28.6% and 39.6% lower total cost of path distance on map models with precision of 15, 20, 25 and 30 respectively, and also has better path planning results in contrast to other swarm intelligence algorithms.

Keywords

Grey Wolf Optimization Algorithm, Path Planning, Pest Monitoring, Simulated Annealing Algorithm, Unmanned Aerial Vehicle.

DOI: 10.9781/ijimai.2022.07.002

I. Introduction

As an aerial vehicle with an independent power system, UAVs (Unmanned Aerial Vehicles) are capable of carrying out various monitoring and exclusion tasks in different environments with a variety of mission equipment. Unmanned Aerial Vehicle, is also called drone, affected by the service demand and business model of various modern industries, has become one of the most promising and fastest-growing industries after decades of development. UAV is more and more relevant to daily life. At present, the main application fields and directions of UAV are agriculture and animal husbandry, electric power, forest fire prevention, military, border defense and so on. As the technology advances rapidly, such as UAV express service and UAV security inspection, these applications are gradually becoming practical as well. In addition, the rise of UAV performance, a more environmentally friendly and free performance form, has replaced the traditional fireworks performance. The market potential of UAV is being tapped. With the miniaturization of UAV's technical characteristics, the battery that UAV could carry is always limited, so the path planning of UAV during flight is a key problem. in modern agriculture, whose application is rapidly expanding for crop drug spraying, pest monitoring, etc. When conducting crop pest monitoring, UAVs patrol over farmland and monitor by using the crop analysis equipment carried. Limited by the shortage of UAVs in terms of endurance and load capacity, UAVs are often required for path planning when assessing the growth status of crops. Previous research has provided a series of traditional path planning algorithms such as the A star algorithm [1] based on direct search for solving shortest paths in static nets, artificial potential field method [2] who simulates the feedback control mechanism of gravitational potential field action, or the Voronoi diagram method [3], visibility-based diagram method [4] and rapid search random tree method (RRT) [5] and so on, which have rapidly advanced the technical development of UAV path planning. However, the traditional planning methods have some unsolvable drawbacks, slow convergence speed and inability to handle high-dimensional space, greatly limiting the path planning of UAVs in complex environments. In contrast, swarm intelligence methods can find global optimal solutions with better convergence in a more complex objective space, so the research of swarm intelligence algorithms is in rapid development. Misra [6] and others used Genetic Algorithm and Particle Swarm Optimization algorithm to find the best path with highly dynamic nature and compared the state space generated between cost functions; Santiago [7] and others used Genetic Algorithm for collision-free navigation in node-connected networks. Since 2014, related scholars proposed the Grey Wolf Optimization algorithm by simulating the hierarchy and hunting pattern of the grey wolf population [8], the algorithm has been applied to a wide range of fields and has been studied and improved by many scholars. Ghorpade

* Corresponding author.

E-mail address: xuxl@njupt.edu.cn

et al. [9] designed a multi-objective grey wolf optimization constraint considering the objective function as a topological constraint of distance and geometry, Ge et al. [10] introduced the algorithmic mechanism of Fruit Fly local optimization to regulate the generation of optimal paths. Guo et al. [11] added an individual learning strategy to the standard Grey Wolf Optimization algorithm to balance the exploration and development capabilities of the algorithm. Gu et al. [12] used a trivial nonlinear change function to converge the objective search of the Grey Wolf Optimization algorithm. While another swarm intelligence algorithm achieves the optimal solution search by simulating the principle of solid cooling, i.e., the Simulated Annealing algorithm [13]. Li et al. [14] evaluated the flight control of UAVs over a large range based on Simulated Annealing algorithm, and Hassan et al. [15] collected and analyzed the sensor information of multiple UAVs in the environment by Simulated Annealing algorithm.

It is easy to fall into local optimum when there are many feasible solutions in the solution space by general iterative methods facing with planning scenes, while the Genetic Algorithm seeks the optimal solution by imitating the selection and genetic mechanism in nature, which effectively avoids this problem. However, it takes more time for Genetic Algorithm to get a more accurate solution depending on parameters such as crossover rate and mutation rate, which will greatly increase the risk that may be caused by feedback delay in the flight of UAV. The Simulated Annealing algorithm is optimized by simulating the molecular movement when the solid is cooled down, which has strong global searching ability. This method has similar shortcomings to Genetic Algorithm, the searching ability affected by the cooling rate of temperature will take a long time to find a better solution to the problem. Considering the Grey Wolf Optimization algorithm, the strict strategy of obeying the group rank makes its convergence performance better, but getting a better solution quickly will also increase the risk of the algorithm falling into local optimum.

In view of the above research, in order to balance the global search ability and convergence speed, avoid the algorithm falling into local optimum prematurely, which will lead to the failure of path planning and affect the flight stability of UAV, and at the same time plan a better flight route. In this paper, an Improved Grey Wolf Optimization algorithm (IGWO) is proposed to solve this problem. At the same time, the slow convergence speed in the later period of the algorithm itself is adjusted by increasing the convergence coefficient.

The main contributions of this work are as follows:

(1) In this paper, the path planning problem of UAVs in a multi-obstacle environment is abstracted into a multi-constrained objective planning problem in the context of crop pest monitoring and solved by the Grey Wolf Optimization algorithm.

(2) An improved Grey Wolf Optimization algorithm is proposed to with the Simulate Annealing algorithm which has the sudden leap probabilistically to ensure that the UAV can find the optimal path to a predetermined location.

(3) The effectiveness of the improved algorithm is demonstrated by comparing the Grey Wolf Optimization algorithm, the Simulated Annealing algorithm and the Genetic Algorithm through the designed experiments.

The structure of this paper is as follows: Section II of this paper makes theoretical analysis, establishes the environment model and transforms the UAV path planning problem into a constrained optimization problem, then the next part of this section explores the mechanism of the GWO algorithm and the IGWO algorithm. Section III analyzes the feasibility of its improvement; Section IV gives the relevant results and comparisons of simulation experiments, and concludes in Section V.

II. Methods

A. Preliminaries

For the problem of UAV path planning on crop pest monitoring proposed in this paper, first of all, it is necessary to analyze the problem and establish a model. This problem is essentially a planning constraint problem, which constrains the flight path of UAV to conform to a certain flight trajectory. Therefore, it is necessary to model the flight map of UAV. Secondly, the planning problem is transformed into an optimization problem. In a certain space range, the best flight path of UAV can be found by some methods, which is described by mathematical language, that is, finding a set of optimal solutions in a certain solution space, attaching a certain amount of constraints at the same time.

After the completion of modeling, effective methods and ideas can solve the above problems excellently. In the existing methods, there are some shortcomings, such as the low search rate of GA algorithm and SA algorithm, the problem that the GWO algorithm is easy to fall into local optimum. Therefore, a method to balance search results and search rate is worthy of being proposed. Considering the efficient structure of GWO algorithm and the easy scalability of SA algorithm, it is possible to introduce the structure of SA algorithm into GWO algorithm mechanism. Based on the complex algorithm structure and excellent global searching ability of GA algorithm. Therefore, in the subsequent experiments, it is compared with the original GWO algorithm and SA algorithm as the proposed algorithm for reference analysis.

B. Path Planning Strategies

1. Environment Modeling

The UAV in the crop monitoring [16] not only follows a certain route to cover the target point, but also need to avoid trees, buildings and other obstacles, usually in the flight process, the UAV will have an over-the-horizon area, so the use of relay equipment on the signal tower to establish a communication link for data communication to solve the signal attenuation and interference problems arising from the excessive distance and obstacle blockage, the UAV containing the task crop pest monitoring is shown in Fig. 1. When the UAV is close to the ground vehicle-mounted terminal, the UAV establishes a communication link directly with the terminal; when the flight range is expanded and the distance becomes long, the signal relay is relayed through the relay equipment on the signal tower to establish a communication link.

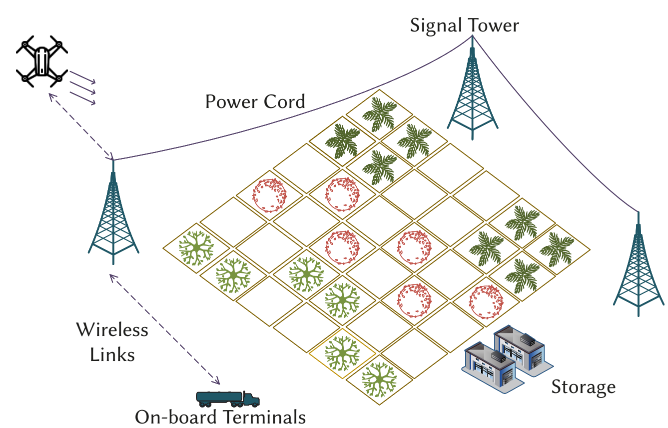

Fig. 1. Crop pest monitoring by UAV in farmland.

In the monitoring process, the UAV flight path is planned, and the first work to be completed before the UAV path planning is the modeling of the environment. In the path planning problem, avoiding obstacles is the benchmark element for the optimized path [17]. In practice, buildings, trees and various facilities in the environment can be considered as obstacle factors on the way of the UAV. In this study, the UAV inspection environment area is defined by the raster method [18], specifying the starting and ending points and quantifying the real obstacles to reduce errors, as shown in Fig. 2. Assuming that the UAV is a particle in the established map environment, the path planning algorithm is used to calculate the best path from the starting point to the end point while avoiding all obstacles.

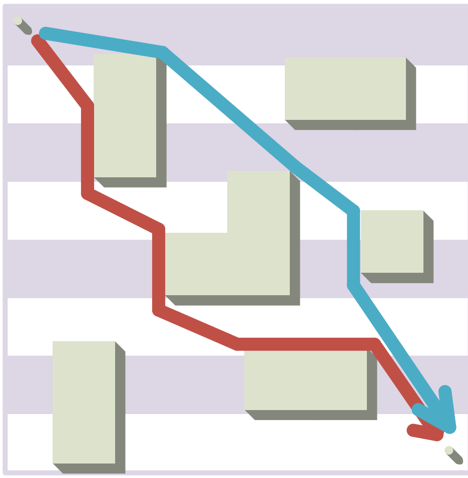

Fig. 2. Rasterized monitoring map by UAV.

The coordinates of the starting point and the end point of the UAV flight are defined as (x_l,y_l) and (x_r, y_c). The r values of (x_1, x_2, x_3, ..., x_r) in the x-axis range correspond to the c values of (y_1, y_2, y_3, ..., y_c) in the y-axis range to form r*c path points. Define the raster map precision as G. Equation in (1) and Equation in (2) define the mapping relationship between each raster coordinate (x_n, y_n) and raster number N in the map(*INT* is defined as rounding operation).

$$x_n = \left(N\% \frac{x_r}{G}\right) * G \tag{1}$$

$$y_n = INT\left(N/\frac{x_r}{G}\right) * G + \frac{G}{2} \tag{2}$$

Based on this definition, each path point Ln = (x_n, y_n) in the UAV travel path forms a set of sequences S=(L_1, L_2, L_3, ..., L_r) as a set of feasible solutions for the UAV path, where each path point can reach the next path point along 8 directions, as shown in Fig. 3. By connecting these path points on each set of sequence, a path line can be formed, and the UAV path planning problem is transformed into an optimization problem of obtaining the optimal coordinate sequence.

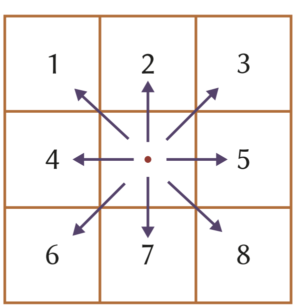

Fig. 3. Flight directions of UAV.

When raster modeling the map, the accuracy of the raster has a critical impact on the path planning. The higher the accuracy, the smaller the raster granularity, the larger the resolution of the environment, and the more information storage, the slower the algorithm decision. When the UAV enters the map environment, the map information is unknown, the UAV traverses the environment, detects the obstacle location, and finds the corresponding grid according to the obstacle location seeking address, and modifies the grid value. The no-obstacle raster value is 1, and the obstacle raster is assigned a value of 0.

2. Problem Formulation

The path planning problem by the UAV for crop monitoring in agricultural fields is described in this paper as a constrained optimization problem [19] with the shortest flight distance from the starting point of travel to the end point, and Equation in (3) defines the general constrained optimization problem form.

$$\begin{cases} \min\limits_{x\in X} f(x) \\ \quad s.t. \\ g_i(x) \le 0 \\ h_j(x) = 0 \\ i,j = 1,2,3,\ldots \end{cases} \tag{3}$$

where $f(x)$ is the objective function, which represents the shortest distance of the UAV flight path in the constraint problem; X is the objective function feasible domain, which is the coordinate limit of the path point located in the map during the UAV flight; g_i and h_i are the equation constraint and inequality constraint in the constraint optimization in the UAV path planning problem, it is desirable to limit the flight distance and obstacle avoidance of the UAV through the constraint, which can shorten the UAV flight time as well as ensure the safety of the device.

In the planning problem, the path length of the UAV flight is a critical factor in the overall planning objective. So Equation in (4) defines the objective function that is the UAV flight path length function as follows.

$$f(x) = \sum_1^{r} \sqrt{(x_{k+1} - x_k)^2 + (y_{k+1} - y_k)^2} \tag{4}$$

The constraints that can be placed on the UAV flight during path planning are: the total direction of travel of the UAV is the end direction, which limits the fold back path points; another constraint is the collision avoidance constraint, where the flight path does not pass within or on the boundary of the defined obstacle. Equation in (5) defines the collision avoidance constraint. The distance between the UAV's position for each travel and the previous position to avoid the obstacle, ζ is defined as the safe range of the obstacle.

$$\frac{y_{ii}-y_i}{x_{ii}-x_i} * x_k + \zeta - y_k \neq 0 \tag{5}$$

C. Algorithmic Mechanism

1. Grey Wolf Optimization Algorithm

The Grey Wolf Optimization algorithm proposed by Mirjalili et al. in 2014 is a newer swarm intelligence optimization algorithm [20], inspired by the hunting behavior of grey wolf packs. In the algorithm, the wolves set up a hierarchy of ranks, as shown in Fig. 4, and the first four of the ranks are defined as α wolves, β wolves, γ wolves, and ω wolves. The head wolf, i.e. rank of wolf α, is at the highest position and makes the decision of the whole pack intelligence optimization, and wolf β is responsible for assisting with the hierarchical differentiation. When there is a vacancy of α in the wolf pack, wolf β becomes wolf α, and each rank behind rises one level at a time. GWO achieves the purpose of optimization by simulating the predatory behavior of the grey wolf pack based on the mechanism of wolf pack collaboration. The GWO algorithm is characterized by simple structure, few parameters to be adjusted and easy implementation, in which there exists a convergence factor that can be adjusted adaptively and an information feedback mechanism that can achieve a balance between local search for excellence and global search, so it has good performance in terms of solution accuracy and convergence speed for the problem.

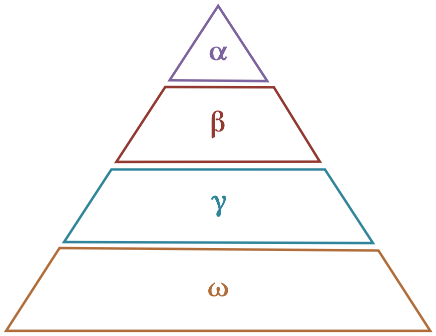

Fig. 4. Hierarchy of the grey wolf.

When path planning is carried out through the Grey Wolf Optimization algorithm, the hierarchical system is strictly implemented, and the low-level wolves are close to the high-level wolves, while the "prey" is captured by the distance, that is, the algorithm searches for the global optimal solution: it will select and determine the wolf α, β and γ with the highest rank according to the distance from the prey (global optimal solution). Under the leadership of the top three, the whole wolf pack will identify and surround the prey, and constantly update the level of the wolf pack. After determining the prey, the hunting of the wolf pack will be finished, and the algorithm will get the optimal feasible solution of the plan. Each individual grey wolf has its own location in the solution space, i.e., corresponding to the path feasible solution, and the optimal feasible solution of the whole optimization is the location of wolves α, and in turn wolves β and wolves γ are considered to be the second and third optimal solutions of the optimization algorithm. The number of path points in the path line of the location map environment is regarded as the sub-element of each feasible solution, i.e., the solution space dimension.

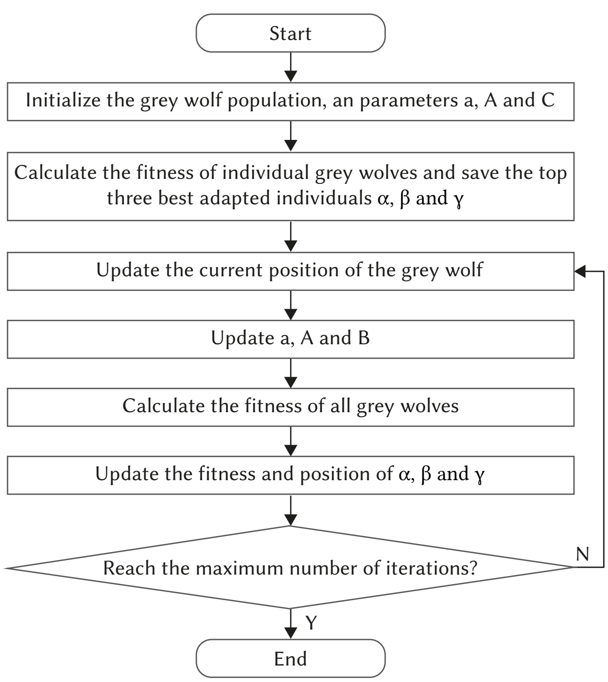

Fig. 5. Flow chart of the GWO algorithm.

The flow of Grey Wolf Optimization algorithm is shown in Fig. 5. In the whole iterative process of the algorithm, the Grey Wolf Optimization algorithm has the following defects: the wolf α searched by the algorithm as the current optimal solution of the algorithm may not be the global optimal point, and in the continuous iteration, the wolf ω gradually approaches the α, β and γ wolves, resulting in the whole optimal search falling into the local optimal; in the algorithm mechanism, the wolves mainly judge the distance to the top three wolves of the rank based on the distance to the search mechanism of judging the solution by distance causes the convergence rate of the algorithm to become slower in the later period. Based on this consideration, the second subsection of this chapter explores how to overcome the shortcomings of the Grey Wolf Optimization algorithm itself and the analysis of its rationality.

2. Improved Grey Wolf Optimization Algorithm

From the perspective of simulating wolf hunting behavior, the core behavior of the whole Grey Wolf Optimization algorithm is hunting, and Equation in (6) defines the hunting behavior as follows. D indicates the distance between the individual and the prey, and the current grey wolf moves toward the target, and the grey wolf position is updated as shown in Fig. 6. Besides, Equation in (7) defines the coordinates of wolves. t is the number of iterations of the algorithm, and there are two random vectors C and A defined in this equation for the update of the grey wolf position and the convergence of the algorithm when iterating as a whole (a is the improved convergence factor, r_1 and r_2 vectors modulo random numbers between 0 and 1).

$$D = |C * X_p(t) - X(t)| \\ C = 2 * r_1 \tag{6}$$

$$X(t+1) = X_p(t) - A * D \\ A = 2a * r_2 - a \\ a = 2(1 - \frac{t^2}{T^2}) \tag{7}$$

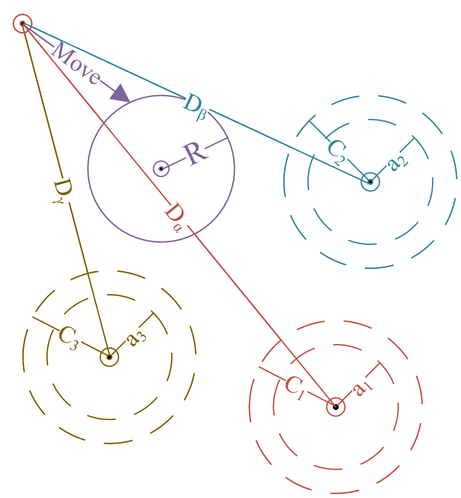

Fig. 6. Update schematic of the location for grey wolf.

Equation in (8) defines the distance at which each grey wolf performs hunting. D_α, D_β, and D_γ denote the distances between wolves α, β, γ and other individual grey wolves respectively; X_α, X_β, and X_γ denote the current positions of wolves α, β, and γ; X is the current position of the grey wolf, while C_1, C_2, and C_3 in Equation are random vectors.

$$\begin{cases} D_\alpha = |C_1 * X_\alpha - X| \\ D_\beta = |C_2 * X_\beta - X| \\ D_\gamma = |C_3 * X_\gamma - X| \end{cases} \tag{8}$$

During the hunting process, grey wolves are able to identify the location of prey and surround them. When the grey wolf identifies the location of the prey, β, γ, led by α, guides the wolf pack to surround the prey. In the decision space of the optimization problem, the best solution (the location of the prey) is not known. Therefore, in order to simulate the hunting behavior of grey wolves, define α, β, γ to know more about the potential location of the prey. α, β, γ wolves that is, who saved the three optimal solutions obtained under the current and use the location of these three to judge the location of the prey, while forcing other grey wolf individuals including ω to update their location based on the location of the optimal grey wolf individuals to gradually approach the prey, and Equation in (9) defines the location updating.

$$\begin{cases} X_1 = X_\alpha - A_1 * D_\alpha \\ X_2 = X_\beta - A_2 * D_\beta \\ X_3 = X_\gamma - A_3 * D_\gamma \\ X(t+1) = \frac{X_1+X_2+X_3}{3} \end{cases} \quad (9)$$

When the grey wolf algorithm is caught in a local optimum in the search process and cannot jump out by its own search mechanism, this paper introduces the probabilistic sudden leap mechanism of the Simulated Annealing algorithm to overcome this defect. The earliest idea of the Simulated Annealing algorithm is a heuristic algorithm proposed by N. Metropolis in 1953 based on the annealing process in thermodynamic systems. The Simulated Annealing algorithm starts from some higher initial temperature, and the continuous decrease of the temperature parameter, combined with a certain probability of sudden leap in the whole solution space to randomly find the global optimal solution of the objective function, so it can be able to probabilistically jump out when the feasible solution of the algorithm falls into the local optimum, and the probability of getting the optimal solution will be greatly increased and eventually converge to the global optimum because of the introduction of more random factors. This is done by performing a small perturbation on the current optimal solution to generate a new solution, judging whether this new solution meets the output conditions according to the Metropolis criterion, and continuously iterating until the maximum number of iterations is reached.

Since the unique new solution acceptance criterion of Simulated Annealing algorithm allows convergence to avoid falling into local extremes, it makes up for the deficiency of the Grey Wolf Optimization algorithm that tends to fall into local optima, making the introduction of this mechanism desirably.

The workflow of the Improved GWO algorithm is as follows.

- Step 1: Define obstacles, starting point, and end point according to the environment model.
- Step 2: Initialize the values of relevant parameters of the Grey Wolf Optimization algorithm as well as the Simulated Annealing algorithm, such as population size, maximum number of iterations, initial temperature, etc.
- Step 3: Obtain the location of wolf α according to the convergence process of the Grey Wolf Optimization algorithm, i.e., the path feasible solution, record and output to the mechanism of the Simulated Annealing algorithm, consider the solution as the current optimal solution and carry out the Simulated Annealing convergence process.
- Step 4: Reach the maximum convergence number to output the final path optimal solution.

The overall workflow of the algorithm is shown in Fig. 7.

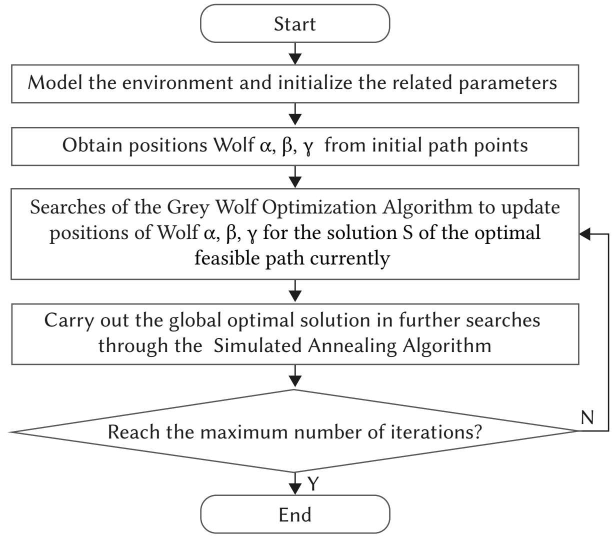

Fig. 7. Flow chart of the Improved GWO algorithm.

After considering the problem of how to adjust to achieve the optimal solution for the path points and to speed up the convergence, it is also necessary to add obstacle avoidance constraints to the designed combinatorial algorithm, which constrains so that all path points so that the overall path does not pass through obstacle regions on the linkage. Therefore, the path planning problem of UAV is considered as a constrained optimization problem with the main objective function of optimizing so that the overall path sum is minimized and the constraint condition of avoiding all obstacle regions. The overall search steps of the designed algorithm are as follows in Table I.

TABLE I. The Improved GWO Algorithm

Algorithm: Improved GWO Algorithm Input: *pop*, *Max_iteration*, *n*, *lb*, *ub*, *T* Output: $X = \{X(1), X(2), X(3), ..., X(n)\}$, $Y = \{Y(1), Y(2), Y(3), ..., Y(n)\}$

$pos_{\alpha,\beta,\gamma} \leftarrow zeros_{1,n}$;
$val_{\alpha,\beta,\gamma} \leftarrow inf$;
$X(1) \leftarrow 1$;
$Y(1) \leftarrow val$;
While 1 < Max_iteration **do**
  for $j = lb; j \leq ub$ **do**
    compute $val_{\alpha,\beta,\gamma}(j, n)$ $(n \in (lb, ub))$;
    $Y(j) \leftarrow Min(val_{\alpha,\beta,\gamma}(j, n))$;
    While $0 < T$ **do**
      compute $Y_t + 1(j)(j, t)$;
      $a \leftarrow 2(1 - t^2/T^2)$;
      $\Delta y \leftarrow Y_{t+1} - Y_t$;
      if $Y_{t+1} \leq Y_t$ **then**
        replace $Y_t(j)$ with Y_{t+1};
      else
        if *exp*(-Δy/T ≤ *random* [0,1]) **then**
          $T = 0.99 * T$;
      t++;
  for $i = lb; i \leq ub$ **do**
    for $k = 1; k \leq n$ **do**
      compute $pos_{\alpha,\beta,\gamma}(i, k)$;
      $r_{1,2,3,4,5,6} \leftarrow random[0,1]$;
      compute $X_{1,2,3}(pos_{\alpha,\beta,\gamma}, a, r_m, X(i)) m \in (1,6)$;
      $X(i) \leftarrow (X_1 + X_2 + X_3))/3$;
Return *X*,*Y*

III. Feasibility Analysis For Improvement

On account of the simple structure and easy implementation of the population intelligence optimization algorithm, it has been applied to solve various complex optimization planning problems. With the continuous development of heuristic search, the Grey Wolf Optimization algorithm has been widely used in various scheduling problems and path planning because of its high performance in problem solving optimization since its introduction.

Theoretically, in the UAV path planning problem, because the algorithm imitates the strict social hierarchy of grey wolves, it can follow the three best positioned wolves like a wolf pack hunting, and can search the best UAV path point quickly and accurately, and in the parameter selection by a linear decreasing convergence factor and two random weight parameters make the algorithm in local optimization and The algorithm maintains a good balance between local optimization and global optimization. However, in terms of the limitations of the algorithm, if the individual wolf with the highest rank is selected as the local optimum instead of the global optimum, the strict wolf-closing hierarchy will make the algorithm fall into a local optimum that cannot be jumped out, and the search mechanism of the algorithm by virtue of the distance between the wolf and the target will lead to the slow convergence of the grey wolf algorithm at the later period. Thus, there is some space for improvement in the optimization problem of UAV path planning.

Considering the deficiency of slow convergence rate in the late period of the algorithm search, the convergence factor parameter in the Grey Wolf Optimization algorithm is adjusted. The convergence mode of the factor is changed from linear decreasing to exponential decreasing. For another difficulty, the algorithm could fall into local optimum when iteratively searching the solution space of the path points. This paper designs a method to introduce the mechanism of Simulated Annealing algorithm into the Grey Wolf Optimization algorithm. The property of probabilistic leap out of the local optimum of Simulated Annealing algorithm is utilized to improve the performance of Grey Wolf Optimization algorithm search with a view to achieving a better optimization search effect.

IV. Experimental Results and Discussion

A. Performance Indicators

In this paper, we focus on the path planning of crop pest monitoring by UAV in a farmland environment, which is a constrained combinatorial optimization problem, so the performance index is compared with the optimal path length L_{total} that is successfully completed by the algorithm under different precision simulation environments. The total path length is an important indicator to reflect the best result of the proposed algorithm in the current precision of the map environment. As Equation in (10) is shown below.

$$L_{total} = \sum_{i=1}^{r} L_i \tag{10}$$

From the perspective of the constrained optimization problem, the problem exists multiple feasible paths under the premise of avoiding collision obstacles, so the search for the optimal path becomes necessary for path planning, while setting the obstacle collision index, as Equation in (11) is shown below. The experimental phase of this paper is designed to compare the search results with some other heuristic algorithms, according to the established indicators used to judge the superiority of the algorithm to meet the shortest path and has avoided all obstacles on the path, and made a comparison of the final experimental results.

$$\frac{y_{ii}-y_i}{x_{ii}-x_i} * x_k + \zeta - y_k \neq 0 \tag{11}$$

After controlling the UAV to complete the overall crop pest monitoring target in farmland, the shorter the flight path, the less the battery usage and the lower the energy consumption, which also reduces the flight cost, while the realization of obstacle avoidance indicators greatly reduces the risk during the flight of the UAV.

The simulated experimental test environment is simulated on raster map models with precision of 15, 20, 25 and 30, and the path search planning of IGWO, GWO, SA and GA algorithms are performed to analyze the reliability of the designed algorithms by comparing the relevant indexes. First, the basic Grey Wolf Optimization algorithm, Simulated Annealing algorithm, and Genetic algorithm will be used to perform path search optimization after traversing each map to obtain the total path length index and collision obstacle situation, and then the Improved Grey Wolf Optimization algorithm will be used to conduct the experiments, and the relevant index data will also be recorded.

B. Experimental Analysis

The simulation experiments were conducted on a 3.8 GHz, 32 GB RAM computer with Matlab 2020a. A path planning of the GWO algorithm was firstly conducted on a simple map model when experimenting with the idea of the designed algorithm, and the GWO algorithm spent a total distance of 24 for the target path after planning the UAV flight path successfully, and then an improved GWO algorithm experiment was implemented, of which the results are shown in Fig. 8, and the total distance at this moment was reduced to 20 whose result was slightly improved. Meanwhile, the convergence rate which is shown in Fig. 9 is accelerated after the algorithm's improvement.

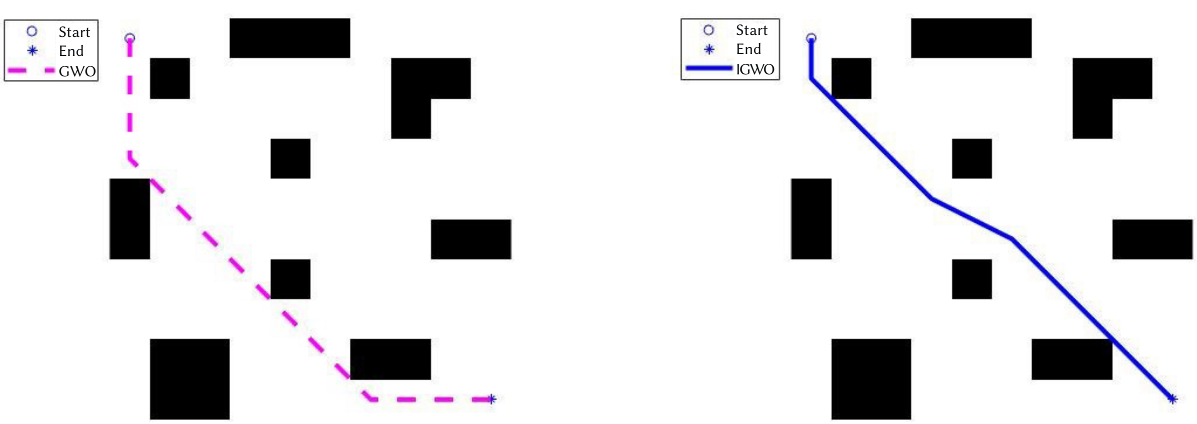

(a) The results of the GWO algorithm.

(b) The results of the improved GWO algorithm.

Fig. 8. Path planning results.

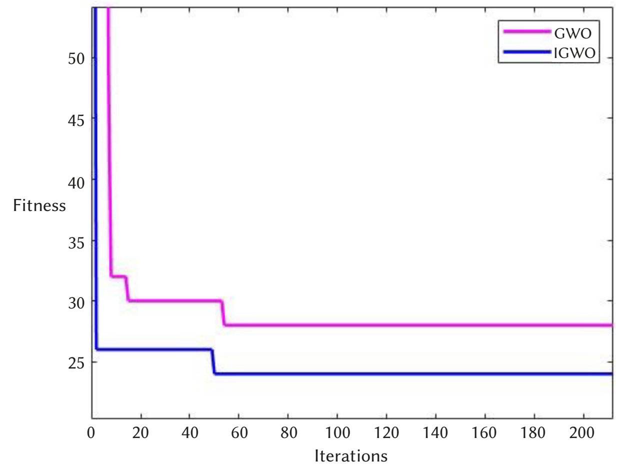

Fig. 9. Convergence curves of the algorithms..

In order to avoid the chance of the experiment, another comparison experiment was conducted on the map with higher precision between them, and the result is shown in Fig. 10, the experimental result of the improved algorithm is reduced from 82 to 48 in the total distance of the target path, whose effect is significant. Also the convergence rate is more stable that still higher than the original GWO algorithm.

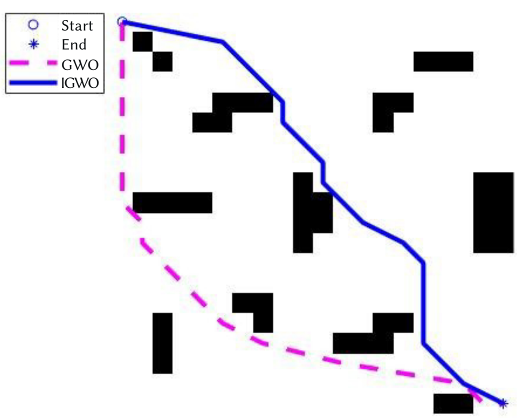

(a) The results of the algorithms.

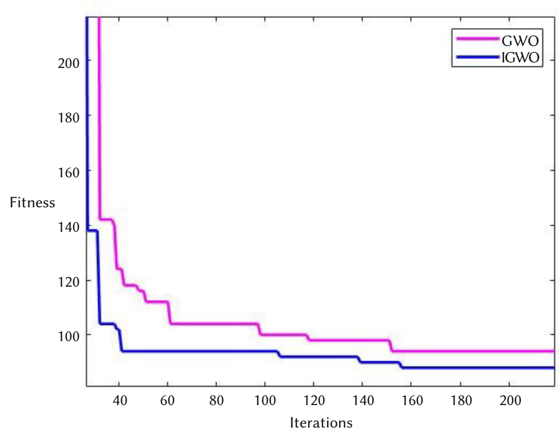

(b) Convergence curves of the algorithms.

Fig. 10. Path planning results in map with different precisions.

Based on this, by defining the start point and destination, the flight path of UAV is planned. More detailed and specific comparison experiments are conducted later on map models with precision of 15, 20, 25 and 30 respectively, as well as making a comparison of the convergence rate. Besides, the experiments of Simulated Annealing algorithm and Genetic algorithm were added to compare the path planning effect of the related methods to prove the superiority of the improved GWO algorithm. The experimental results of the four different methods for UAV path planning are shown in Fig. 11, and the convergence curve of each algorithm is shown in Fig. 12. The comparison data of each algorithm are shown in Table II, Table III, Table IV and Table V.

TABLE II. Comparison of the Results of Each Algorithm(Precision=15)

Algorithm	Total Paths	Whether to avoid obstacles
IGWO	22	Y
GWO	24	Y
SA	28	Y
GA	22	Y

TABLE III. Comparison of the Results of Each Algorithm(Precision=20)

Algorithm	Total Paths	Whether to avoid obstacles
IGWO	40	Y
GWO	48	Y
SA	48	Y
GA	42	Y

TABLE IV. Comparison of the Results of Each Algorithm(Precision=25)

Algorithm	Total Paths	Whether to avoid obstacles
IGWO	50	Y
GWO	70	Y
SA	56	Y
GA	56	Y

TABLE V. Comparison of the Results of Each Algorithm(Precision=30)

Algorithm	Total Paths	Whether to avoid obstacles
IGWO	64	Y
GWO	106	Y
SA	112	Y
GA	66	Y

Fig. 11 visualizes the path planning results of the UAV for various methods on map models with different precisions. As shown in Table II, III, IV and V, the path planning effect demonstrated by the Improved Grey Wolf Optimization algorithm will be better than that of the simple heuristic algorithm. On maps with different precisions, several types of methods completely avoid obstacles in the map, but in terms of path length index, the designed combined algorithm can better match the specific map and related environment to achieve smaller total path distance and reduce UAV flight cost. The improved GWO algorithm improves the metrics of the basic GWO algorithm in path planning, reducing the total target distance consumption by 8.3%, 16.7%, 28.6%, and 39.6% on the map models with accuracies of 15, 20, 25 and 30 respectively, compared to the previous algorithm according to the total target path distance data from the tables.

It can be known that swarm intelligence algorithms are always updated towards the current optimal result in the process of optimization, so the search result of UAV path is always the best target value in current stage, and finally the best path is obtained cumulatively. From the Fig. (a) and (b) in Fig.11, it is obvious that when there are many possibilities in the space, once the convergence ability of the algorithm is too strong, such as the GWO algorithm, it will lead to that in one stage, optimization falls into local optimum. If the algorithm does not have the ability to jump out of local optimum, it will lead to the overall poor flight path, trajectory deviation or even failure of the finally planned UAV. Therefore, an effective and reasonable adjustment is very important for the planning problem.

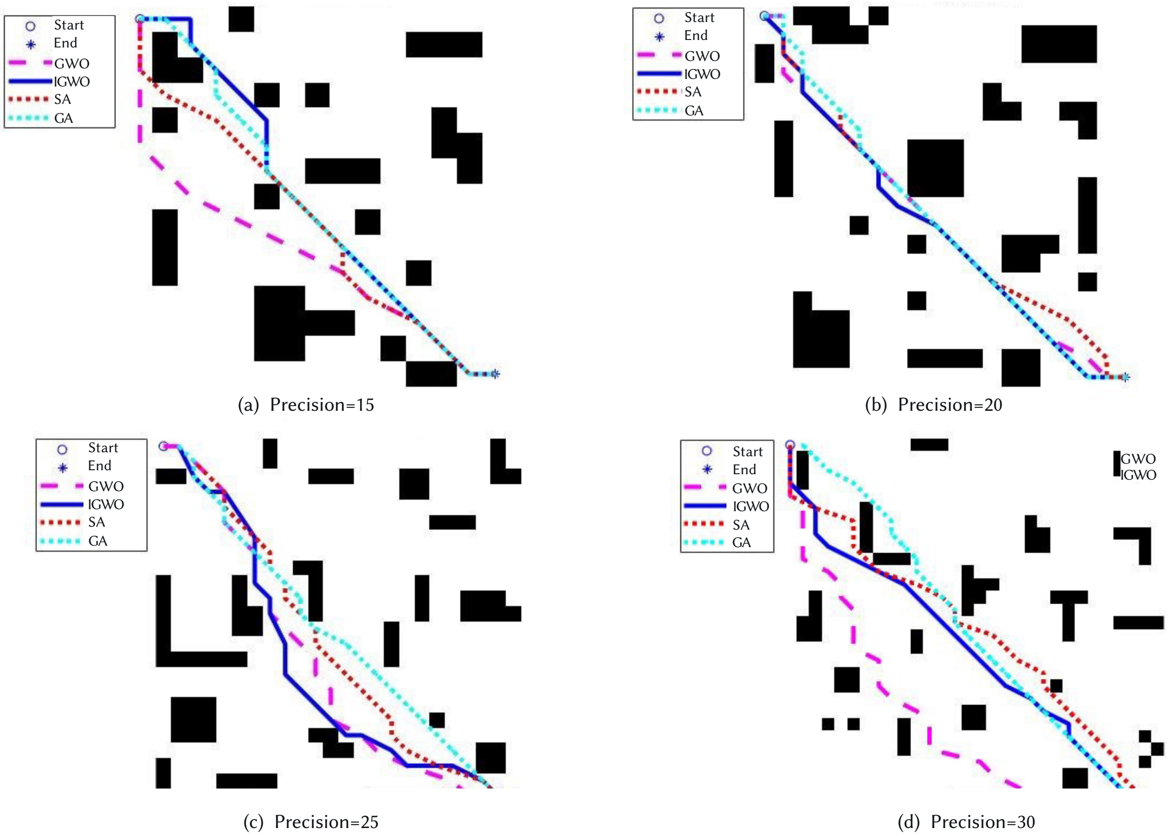

(a) Precision=15 (b) Precision=20

(c) Precision=25 (d) Precision=30

Fig. 11. Path planning results in map with different precisions.

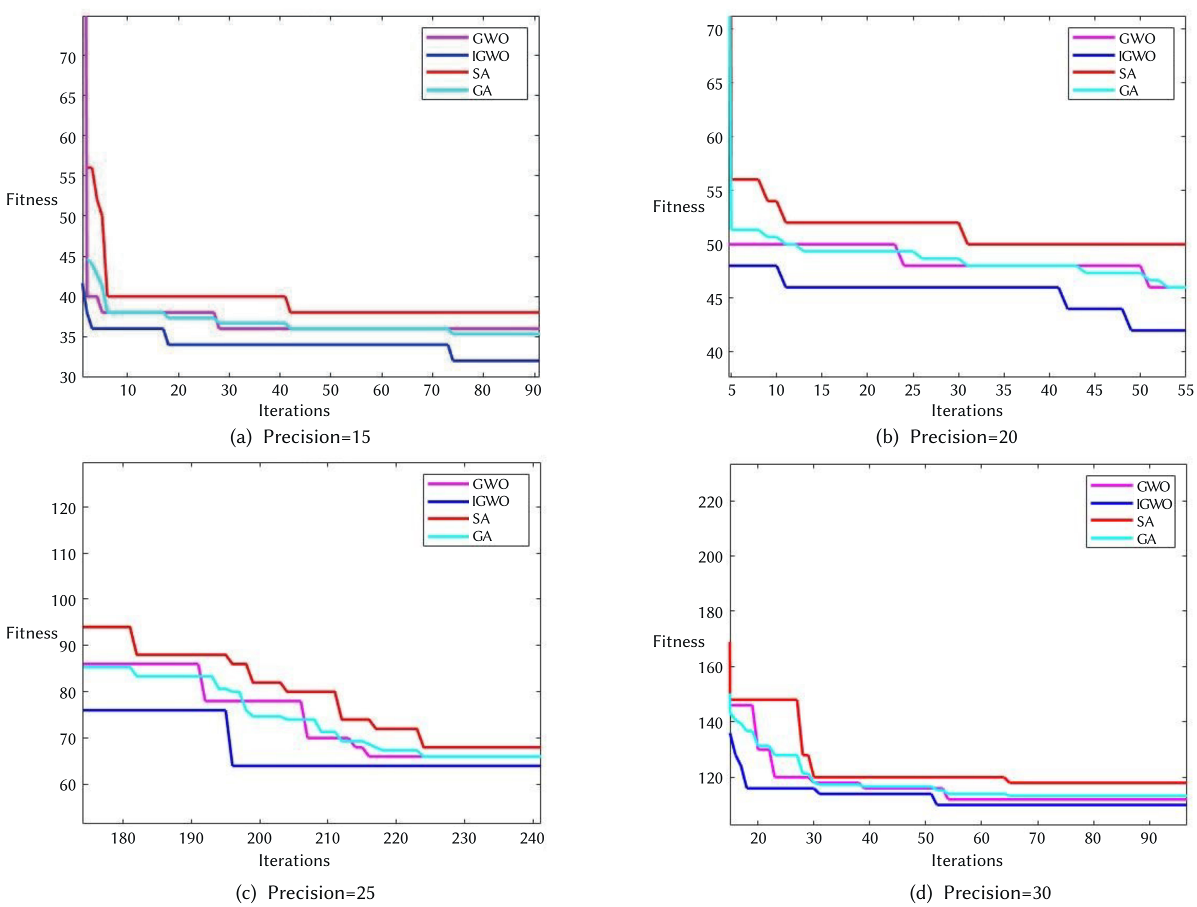

(a) Precision=15 (b) Precision=20

(c) Precision=25 (d) Precision=30

Fig. 12. Convergence curves in map with different precisions.

Furthermore, the improvement of the exponential decay of the convergence factor of the GWO algorithm, shown in Fig. 12, accelerates the speed of the algorithm search convergence and improves the efficiency of path planning. The improved GWO algorithm is significantly better than the original GWO algorithm in terms of convergence rate, and also has greater superiority than some other swarm intelligence algorithms such as Simulated Annealing algorithm and Genetic Algorithm, no matter on which precision of map model. Compared with some other search algorithms, the algorithm is more suitable for UAV path point finding in the UAV path planning problem.

Thus it is experimentally verified that the introduction of the Simulated Annealing algorithm's probabilistic leap out of local optimum in the Grey Wolf Optimization algorithm can improve the performance of the basic Grey Wolf Optimization algorithm in path planning. Therefore, compared with other methods in the experiment, it can be seen that the improved method can not only maintain a high search rate, but also get better search results.

V. Conclusion

The work of this paper is to solve the path planning problem of UAVs for crop pest monitoring in agricultural fields. The improved Grey Wolf Optimization algorithm is used to perform optimal path planning while avoiding collisions between UAVs and obstacles during flight. It can be seen from the simulation experiments that the designed algorithm is more effective than some swarm intelligence methods. The adjustment of the convergence factor speeds up the convergence rate, and the property of probabilistic sudden leap of the Simulated Annealing algorithm introduced in the algorithm mechanism avoids to a certain extent the defect that the Grey Wolf Optimization algorithm falls into local optimum too early.

For the Grey Wolf Optimization algorithm to consider, due to its simplicity and efficiency, the algorithm has been successfully applied in many fields, in terms of the improvement of the Grey Wolf Optimization algorithm, in addition to the grey wolf population diversity can also be improved, better diversity can effectively improve the search efficiency of the algorithm and improve the planning performance; it can also improve its search mechanism, the Grey Wolf Optimization algorithm uses the adaptation value of A,C and a to balance the algorithm ability, easy to fall into local optimum, it can also consider introducing new search strategies to make up for the algorithm deficiency.

In the current context, the Grey Wolf Optimization algorithm can still be used in other fields and has broad application prospects.

Acknowledgment

We would like to thank the editors and reviewers in advance for their comments in helping us improve the quality of this paper. This work was supported by the National Natural Science Foundation of China under Grant 62072255.

References

[1] G. Tang, C. Tang, C. Claramunt, X. Hu and P. Zhou, "Geometric A-Star Algorithm: An Improved A-Star Algorithm for AGV Path Planning in a Port Environment," in IEEE Access, vol. 9, pp. 59196-59210, 2021, doi: 10.1109/ACCESS.2021.3070054.

[2] Y. Du, X. Zhang and Z. Nie, "A Real-Time Collision Avoidance Strategy in Dynamic Airspace Based on Dynamic Artificial Potential Field Algorithm," in IEEE Access, vol. 7, pp. 169469-169479, 2019, doi: 10.1109/ACCESS.2019.2953946.

[3] W. Huang, K. Sun, J. Qi and J. Ning, "Optimal Allocation of Dynamic Var Sources Using the Voronoi Diagram Method Integrating Linear Programing," in IEEE Transactions on Power Systems, vol. 32, no. 6, pp. 4644-4655, Nov. 2017, doi: 10.1109/TPWRS.2017.2681459.

[4] R. Zou and S. Bhattacharya, "On Optimal Pursuit Trajectories for Visibility-Based Target-Tracking Game," in IEEE Transactions on Robotics, vol. 35, no. 2, pp. 449-465, April 2019, doi: 10.1109/TRO.2018.2882747.

[5] L. Chen, Y. Shan, W. Tian, B. Li and D. Cao, "A Fast and Efficient Double-Tree RRT*-Like Sampling-Based Planner Applying on Mobile Robotic Systems," in IEEE/ASME Transactions on Mechatronics, vol. 23, no. 6, pp. 2568-2578, Dec. 2018, doi: 10.1109/TMECH.2018.2821767.

[6] D. Dev Misra, K. K. Sarma, U. Bhattacharjee, P. K. Goswami and N. Mastorakis, "Optimal Routing in the 5G Ultra Dense Small Cell Network using GA, PSO and Hybrid PSO-GA Evolutionary Algorithms," 2020 24th International Conference on Circuits, Systems, Communications and Computers (CSCC), 2020, pp. 39-44, doi: 10.1109/CSCC49995.2020.00016.

[7] R. M. C. Santiago, A. L. De Ocampo, A. T. Ubando, A. A. Bandala and E. P. Dadios, "Path planning for mobile robots using genetic algorithm and probabilistic roadmap," 2017 IEEE 9th International Conference on Humanoid, Nanotechnology, Information Technology, Communication and Control, Environment and Management (HNICEM), 2017, pp. 1-5, doi: 10.1109/HNICEM.2017.8269498.

[8] P. Hu, S. Chen, H. Huang, G. Zhang and L. Liu, "Improved Alpha-Guided Grey Wolf Optimizer," in IEEE Access, vol. 7, pp. 5421-5437, 2019, doi: 10.1109/ACCESS.2018.2889816.

[9] S. N. Ghorpade, M. Zennaro and B. S. Chaudhari, "GWO Model for Optimal Localization of IoT-Enabled Sensor Nodes in Smart Parking Systems," in IEEE Transactions on Intelligent Transportation Systems, vol. 22, no. 2, pp. 1217-1224, Feb. 2021, doi: 10.1109/TITS.2020.2964604.

[10] F. Ge, K. Li, W. Xu and Y. Wang, "Path Planning of UAV for Oilfield Inspection Based on Improved Grey Wolf Optimization Algorithm," 2019 Chinese Control and Decision Conference (CCDC), 2019, pp. 3666-3671, doi: 10.1109/CCDC.2019.8833455.

[11] L. Guo, Q. Xie, X. Huang and T. Chen, "Time difference of arrival passive location algorithm based on grey wolf optimization," 2017 3rd IEEE International Conference on Computer and Communications (ICCC), 2017, pp. 877-881, doi: 10.1109/CompComm.2017.8322669.

[12] Y. Gu and N. Liu, "An Adaptive Grey Wolf Algorithm Based on Population System and Bacterial Foraging Algorithm," 2020 IEEE International Conference on Artificial Intelligence and Computer Applications (ICAICA), 2020, pp. 744-748, doi: 10.1109/ICAICA50127.2020.9182707.

[13] S. Lee and S. B. Kim, "Parallel Simulated Annealing with a Greedy Algorithm for Bayesian Network Structure Learning," in IEEE Transactions on Knowledge and Data Engineering, vol. 32, no. 6, pp. 1157-1166, 1 June 2020, doi: 10.1109/TKDE.2019.2899096.

[14] R. Li and M. Chen, "Flight control law evaluation for UAV based on simulated annealing algorithm," Proceedings of the 32nd Chinese Control Conference, 2013, pp. 8697-8702.

[15] H. Daryanavard and A. Harifi, "UAV Path Planning for Data Gathering of IoT Nodes: Ant Colony or Simulated Annealing Optimization," 2019 3rd International Conference on Internet of Things and Applications (IoT), 2019, pp. 1-4, doi: 10.1109/IICITA.2019.8808834.

[16] J. Su et al., "Aerial Visual Perception in Smart Farming: Field Study of Wheat Yellow Rust Monitoring," in IEEE Transactions on Industrial Informatics, vol. 17, no. 3, pp. 2242-2249, March 2021, doi: 10.1109/TII.2020.2979237.

[17] Y. Mao, M. Chen, X. Wei and B. Chen, "Obstacle Recognition and Avoidance for UAVs Under Resource-Constrained Environments," in IEEE Access, vol. 8, pp. 169408-169422, 2020, doi: 10.1109/ACCESS.2020.3020632.

[18] B. Guo, H. Dai, Z. Li and W. Huang, "Efficient Planar Surface-Based 3D Mapping Method for Mobile Robots Using Stereo Vision," in IEEE Access, vol. 7, pp. 73593-73601, 2019, doi: 10.1109/ACCESS.2019.2920511.

[19] C. Picard and J. Schiffmann, "Realistic Constrained Multiobjective Optimization Benchmark Problems from Design," in IEEE Transactions on Evolutionary Computation, vol. 25, no. 2, pp. 234-246, April 2021, doi: 10.1109/TEVC.2020.3020046.

[20] Z. Li, V. Tam and L. K. Yeung, "An Adaptive Multi-Population Optimization Algorithm for Global Continuous Optimization," in IEEE Access, vol. 9, pp. 19960-19989, 2021, doi: 10.1109/ACCESS.2021.3054636.

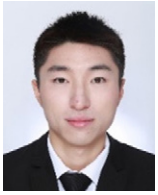

Qun Ding

Qun Ding is currently working as a researcher for the Jiangsu Key Laboratory of Big Data Security & Intelligent Processing, Nanjing, China. His research interests include swarm intelligent optimization. He has won two provincial competition awards, and ranked the forefront of the municipal algorithm competition. He won several scholarships during university. He is going to pursue his master's degree major in Software Engineering in Nanjing University of Posts & Telecommunications, Nanjing, China.

Xiaolong Xu

Xiaolong Xu is currently a professor in the School of Computer Science, Nanjing University of Posts & Telecommunications, Nanjing, China. He is also working for the Jiangsu Key Laboratory of Big Data Security & Intelligent Processing. He received the B.E. in computer and its applications, M.E. in computer software and theories and Ph.D. degree in communications and information systems, in 1999, 2002 and 2008, respectively. He is a senior member of China Computer Federation. He teaches graduate courses and conducts research in areas of Artificial Intelligence, Cloud Computing, Big Data and Novel Network Computing Technologies. As the leader of project teams, he has successfully completed a number of high-level research projects, including the projects sponsored by the National Science Fund of China. He has published more than 100 Journal and conference papers as the first or corresponding author and 5 books. He is authorized 52 patents by the State Intellectual Property Office of China as the first inventor. He was rated as excellent young professor of Jiangsu Province in 2014, selected as the high-level creative talents of Jiangsu province in 2015, and won the title of outstanding expert in the area of computer science and technology.

Electromiographic Signal Processing Using Embedded Artificial Intelligence: An Adaptive Filtering Approach

Daniel Proaño-Guevara[1]*, Xiomara Blanco Valencia[2], Paul D. Rosero-Montalvo[3], Diego H. Peluffo-Ordóñez[4,5]*

[1] Instituto Superior Técnico – Universidade de Lisboa, (Portugal)
[2] Universidad Internacional de La Rioja, Logroño (Spain)
[3] Computer Science department, IT University of Copenhagen, (Denmark)
[4] Modeling, Simulation and Data Analysis (MSDA) Research Program, Mohammed VI Polytechnic University, (Morocco)
[5] Faculty of Engineering, Corporación Universitaria Autónoma de Nariño, Pasto, (Colombia)

Received 26 July 2022 | Accepted 9 August 2022 | Published 18 August 2022

Abstract

In recent times, Artificial Intelligence (AI) has become ubiquitous in technological fields, mainly due to its ability to perform computations in distributed systems or the cloud. Nevertheless, for some applications -as the case of EMG signal processing- it may be highly advisable or even mandatory an on-the-edge processing, i.e., an embedded processing methodology. On the other hand, sEMG signals have been traditionally processed using LTI techniques for simplicity in computing. However, making this strong assumption leads to information loss and spurious results. Considering the current advances in silicon technology and increasing computer power, it is possible to process these biosignals with AI-based techniques correctly. This paper presents an embedded-processing-based adaptive filtering system (here termed edge AI) being an outstanding alternative in contrast to a sensor-computer- actuator system and a classical digital signal processor (DSP) device. Specifically, a PYNQ-Z1 embedded system is used. For experimental purposes, three methodologies on similar processing scenarios are compared. The results show that the edge AI methodology is superior to benchmark approaches by reducing the processing time compared to classical DSPs and general standards while maintaining the signal integrity and processing it, considering that the EMG system is not LTI. Likewise, due to the nature of the proposed architecture, handling information exhibits no leakages. Findings suggest that edge computing is suitable for EMG signal processing when an on-device analysis is required.

Keywords

Adaptive Filters, Artificial Intelligence On-The-Edge (Edge AI), Digital Signal Processor (DSP), Electromyography (EMG), Embedded Processing, Intelligent Processing, Online Processing.

DOI: 10.9781/ijimai.2022.08.009

I. Introduction

Biomedical signal processing and proper filtering are critical for designing intelligent prosthesis, neurorehabilitation, and clinical diagnosis [1], [2]. In this regard, assisting people with physical disabilities is one of the main concerns, as it directly impacts activities of daily living (ADLs) and thus the quality of life [3]–[8]. The electromyogram (EMG) is one of the most studied biosignals in the medical and engineering fields [9]. EMG signals are generated by physiological variations in the state of the muscle fiber membranes, i.e., muscle contractions [10]–[12]. Electromyography is a technique for evaluating the generation, recording, and analyzing of muscle signals [11], [13]. Therefore, it is necessary to understand how EMG evaluates muscle activation to process and interpret it correctly [14]. EMG signals are compound biomedical signals because they are generated by a spatiotemporal interferential summation of action potentials [1], [15]. Thus, EMG is considered a pseudo-stochastic, non-stationary, linear signal [1], [14], [15], with a time-varying or dynamic model being the most suitable approach to analyze it [16].

* Corresponding author.

E-mail addresses: daniel.proano@sdas-group.com (D. Proaño), diego.peluffo@sdas-group.com (D. Peluffo).

There are two main types of EMG analysis [11]: neurological and kinesiological. On the one hand, the neurological analysis evaluates the response of a muscle to external electrical stimulation under static conditions. On the other hand, the kinesiological analysis evaluates neuromuscular activation during voluntary movements. For example, kinesiological protocols may assess muscle activity during postural tasks and functional exercises under a rehabilitation or training program.

According to the type of electrodes used for signal recording, there are two kinds of EMG: intramuscular EMG and surface EMG. Intramuscular EMG is an invasive technique that uses a monopolar needle electrode to detect a subject's motor unit potential (MUP). Meanwhile, surface EMG records muscle activity using at least a pair of electrodes on the skin surface. The latter method is the most commonly used to monitor voluntary contractions for kinesiological studies [12], [13]. Finally, EMG is also classified according to the topographic anatomical location of the muscle group being analyzed [13], [17].

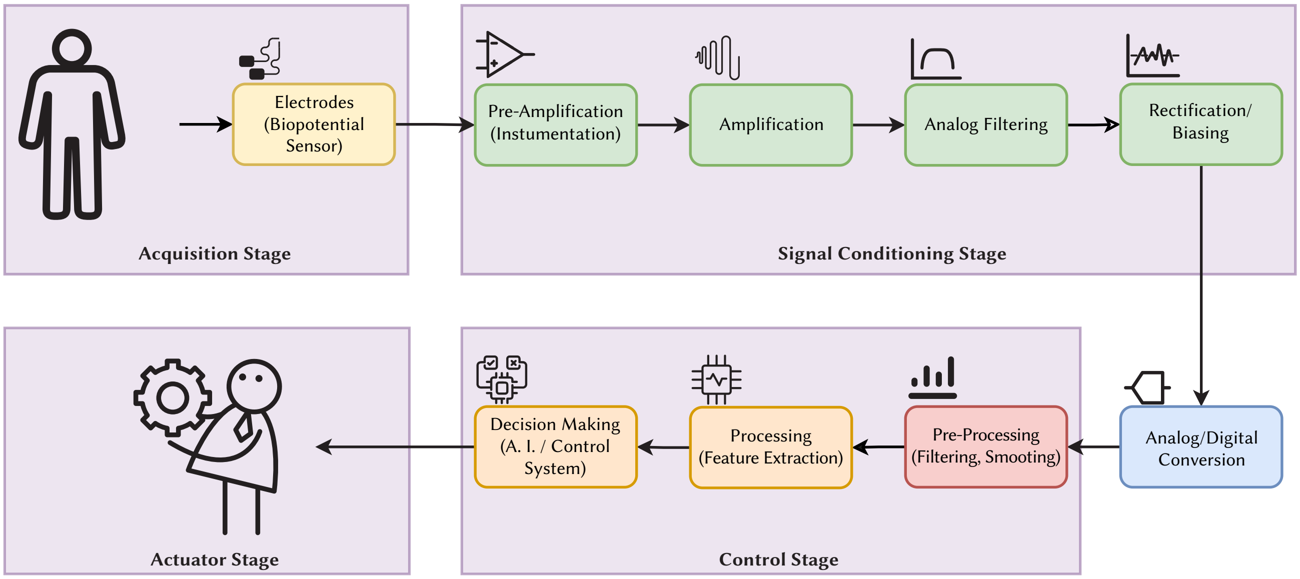

Fig. 1. Biopotential sensing and processing stages.

Kinesiological surface electromyography (KSEMG) is widely used as a **study and evaluation tool** [11] for biomechanics [18], diagnosis [19], [20], rehabilitation research [21], user-prosthesis interfaces [9], [12], [22] and human-machine interfaces for several devices [23]. Thus, this study focuses on the KSEMG analysis.

As a result of several groups standardizing EMG signal acquisition processes [24], the SENIAM project (Surface Electromyography for Non-Invasive Assessment of Muscles) began in 1996 to formulate recommendations for studying EMG signals. These recommendations include information on sensor types and location, signal processing, and characteristic curve modeling [24], [25]. Regarding biopotential sensing systems, the main stages are the power supply, pre-amplification with an instrumentation amplifier, analog filtering, rectification, analog-digital conversion, and control [11], [25]–[27].

Raw EMG signals typically vary between a few microvolts and 2-3 millivolts. Therefore, this signal is usually amplified by a minimum gain of 500 with preamplifiers, extending to 1000 when using units with passive leads. Differential amplifiers are used at this stage, allowing differential signals and rejecting common-mode voltages between input terminals and common ground [11], [13]. The frequency range of the EMG signal is between 10Hz to 500Hz [12], [20]. It is recommended to avoid any notch filter as it destroys too much information [11]. The rectification stage reflects all the signals below the baseline average. Rectification facilitates the reading and computational analysis of the data. In the control stage, digital signal processing (DSP) is widely applied in techniques such as signal smoothing, amplitude normalization of the acquired signal, and removal of artifacts. [25], [27]–[30].

For more complex applications, as with prosthetic devices, the control stage is subdivided into different stages: signal filtering and smoothing are the pre-processing components, and feature extraction is the processing step. Later, a classification stage [12], [22], which will be called the decision-making stage in this article, finally passes to an actuating stage [9], [19],[21]–[23].

Fig. 1 shows the biopotential sensing and processing stages and sub-stages. This paper focuses on the pre-processing block, highlighted in red, specifically in the digital filtering of KSEM signals.

Digital signal processing (DSP) is a branch of computer science specializing in a single type of data, signals [31]. DSP consists of mathematics, algorithms, and techniques related to representing, transforming, and manipulating signals and their information after digitization [31], [32]. Unlike the signal processing techniques of analog electronics, DSP techniques guarantee reproducibility and accuracy of results, recognizing them as superior and more reliable in certain circumstances than their analog counterparts [33].

Intelligent signal processing (ISP) uses machine learning and other 'smart' techniques to extract as much information as possible from the received signal data -in the case of EMG signals, information can be extracted through proper characterization stages as studied in [34], [35]. Classical signal processing methods are robust and straightforward tools that work incomparably with mathematical models that are linear, stationary, and Gaussian. However, real systems are non-linear, with erratic or impulsive statistical structures that can vary over time. Minimal signal or noise-structure changes can lead to qualitative changes in how classical processing systems filter noise or maintain stability [36]. Adaptive filtering is an *Online Learning* technique. It trains its parameters while acquiring information, unlike machine learning which usually trains on the entire dataset or at least a mini-batch of data. Adaptive filtering can be considered an Artificial Intelligence technique since it seeks to minimize an error signal using stochastic gradient descent (SGD) and falls into the field of 'Computer Perception.' It has become one of the most efficient methods for acquiring physiological signals [37]. One approach for denoising is the adaptive noise cancellation of EMG signals, which uses an external noise source loosely related to the noise implicit in the EMG signal. For this task, filtering algorithms such as Kalman Filter, LMS (Least Mean Squares), RLS (Recursive-Least-Squares), Wiener, UFIR (Finite Impulse Response), Gaussian, bee colony algorithms, and Bayesian, among others, have been implemented [38]–[44].

The RLS filtering algorithm seeks to minimize the sum of squares of the differences between the desired signal and the filter output, updating iteratively as new information is acquired. This algorithm solves least squares estimation recursively [43], [45]–[48]. Few works have been found on edge intelligent EMG signal processing (on the embedded system). Diniz and Limem [45], [46] perform traditional digital acquisition and filtering processes using a general-purpose GPU 'NVidia Jetson' as a shared device. They implement machine learning and decision-making algorithms, but there is no evidence of intelligent signal processing per se.

The scientific community is focused on pattern recognition and classification in prosthetic devices and recognizes that the variability in acquired SEMG signals between test subjects is significant [3], [6],

[49], [50]. Furthermore, the literature review has shown that the digital signal processing techniques used on EMG in embedded systems are for LTI systems [1], [14], [27]–[30],[51], [52]. Since EMG signals are pseudo-stochastic (therefore time-varying), these techniques are not the most suitable.

Therefore, using adaptive filtering algorithms in an embedded system to eliminate noise in sEMG signals is proposed as a scalable system for multiple users, reducing the time and complexity of system calibration. This approach respects the non-linear characteristics of the biologically-originated system preserving the information without substantial distortion and adaptability to a varying noise source; besides, it allows the filtering system to be used in multiple applications without significant modifications. This paper introduces an adaptive filtering system implemented on an embedded system (Edge AI) that uses a simulated white noise source as the target signal to be removed. To contrast and validate the model, an FIR filter is also implemented using classical DSP techniques (LTI) and the same adaptive filtering system but implemented in a sensor-computer-actuator system.

The results show that the embedded processing system achieves a similar filtering quality and performance as the sensor-computer-actuator system. Some of the essential advantages of the embedded system are eliminating any networking interfaces, guaranteeing the security of the acquired data, no latency, and no loss of communication between the computing device and the sensors and actuators.

The rest of this manuscript is organized as follows: Section II shows the hardware and the comparison approach used to validate the presented approach. Afterward, section III details the dataset used, the performance metrics, the benchmark methods and a comparison with previously published literature, and the experiment description that outlines the approaches used in this paper. Subsequently, section IV analyzes the results obtained in each of the benchmarks and the presented approach and discusses the authors' findings. Finally, section V concludes the article and draws ideas for further research.

II. Materials and Methods

A. Materials - Hardware & Testbench Architecture

The embedded system for processing is a PYNQ-Z1; it uses a ZYNQ-7000 SoC from XILINX composed of an ARM Cortex-A9 and programmable logic cells of the Artix-7 family. It works with a Linux-based operating system running Python notebooks as an interface medium.

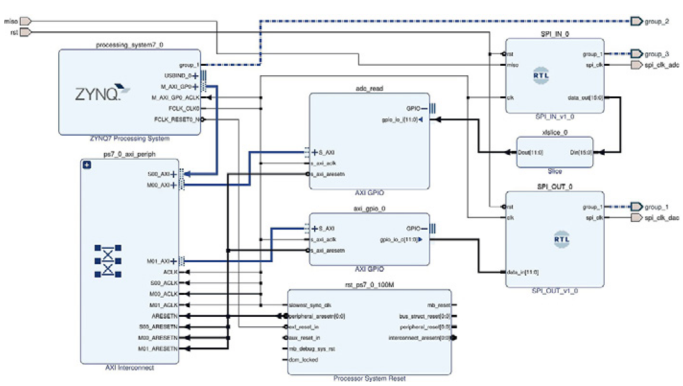

Fig. 2. Block diagram defining the behavior of the acquisition system.

On the one hand, the system incorporates a Digilent's PMOD AD1 module as a signal reading system, incorporating an AD7476 analog-to-digital converter (ADC). This converter has a maximum output rate of 1 MSPS at a resolution of 12 bits. On the other hand, the system uses a Digilent's PMOD DA2 module as a signal reconstruction system since it incorporates a DAC121S101 digital to analog converter (DAC). This converter has a maximum output rate of 1 MSPS at a resolution of 12 bits. Timing diagrams describe the communication of these systems. Thus, it is necessary to decode these protocols and implement them in HDL, using finite state machines (FSM) to model the required behaviors. All hardware blocks are linked together and interfaced with the ARM processor, completing the description of the real-time processing architecture. Fig. 2 shows the final result.

Digilent Analog Discovery 2's function generator recreates the EMG signals and is used to analyze the frequency and measure the parameters needed. The waveform's information comes from the public database [53], further described in A. Finally, Fig. 3 presents the architecture used in the experiment.

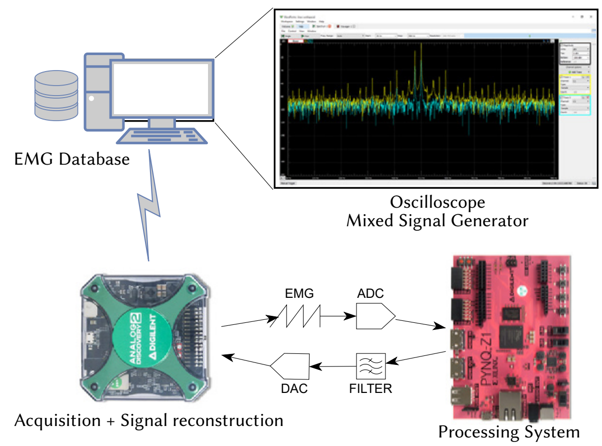

Fig. 3. Processing system architecture.

B. Comparison Approach

The test scenario of the three processing systems is designed based on the methodology presented in Fig. 4. The first scenario consists of a system architecture using classical DSP. In contrast, the second scenario consists of an embedded processing system, an adaptive RLS filter in a horizontal structure. Finally, scenario three involves processing using a sensor-computer-actuator system and wireless communication protocols. A common comparison framework for the three scenarios is set, where spectrograms, signal means, processing times, and SNR are analyzed.

The evaluation metrics for the test scenarios compare input and output signal averages, the time lag associated with the processing time, an analysis of the spectrogram, and the SNR of the signals. Finally, the evaluation metrics are contrasted between the three groups to determine the most suitable architecture for the EMG signal filtering tasks. The evaluation and testbench is further explained in B and C.

III. Experimental Setup

A. Dataset Description

The dataset "ISRMYO-I: A DATABASE FOR SEMG-BASED HAND GESTURE RECOGNITION" [53] consists of sEMG signals recorded for different hand gestures. The database follows an organization as raw EMG, the unprocessed recorded signals, and train and test, which are the relevant data to train a classifier model. This database recorded 16 channels of the forearm's sEMG with a multichannel sleeve sensor, firstly used for hand motion classification. The raw database was acquired with a sampling frequency of 1 kHz, and 12 Bits of resolution [54].

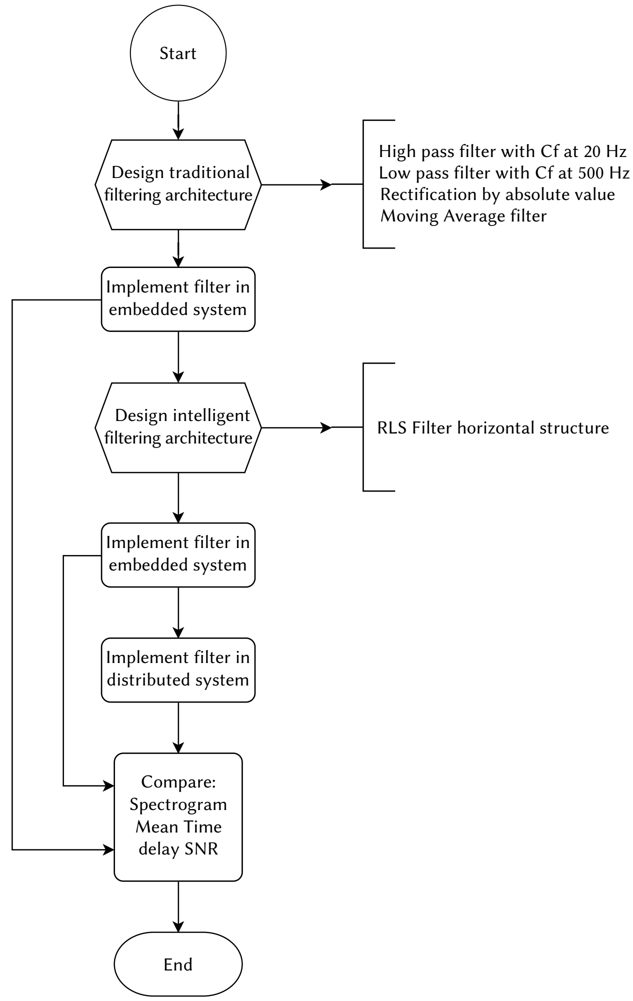

Fig. 4. Design and testing methodology for classical, intelligent embedded, and intelligent sensor-actuator-computer DSP processing paradigms.

The information used for reconstructing the sEMG signal comes from one subject. The maximum buffer memory (4096 points) for the arbitrary signal generator was selected to reconstruct the signal. The signal is then rescaled to 3 Vpp and a mean offset of 1.5 V.

B. Performance Metrics

One of the performance metrics used is the Signal-to-noise ratio SNR. According to [55] it is described as (1):

$$SNR = 10\log\left(\frac{\sum_{n=1}^{N} f(n)^2}{\sum_{n=1}^{N}\left[f(n)-\hat{f}(n)\right]^2}\right) \quad (1)$$

where, $f(n)$ is a signal containing noise, $\hat{f}(n)$ is the denoised signal, and N is the length of the signal.

The SNR compares the desired signal level to the noise level or the noisy signal. SNR is defined as the ratio of signal power to the noise power, and a ratio greater than 0 dB indicates more signal than noise.

Another metric used is the processing delay. It compares an inputted sinusoidal signal with the system's output and measures the time difference between the zero-crossing point of both signals.

C. Benchmark Methods

The benchmark methods considered for this work only analyze the filtering features.

The database authors [53] apply a DRMS (differential root mean square) processing to multiple channels. There is no single-channel processing and thus no possible benchmark comparations with this approach.

[56] states a resampling of the database to 1000 Hz and a band-pass filtering between 3 Hz to 300 Hz. No filtering architecture or metrics are presented.

[3] applies a 20-order 50 Hz comb filter to remove the power interference from the data. A db5 wavelet basis function of three layers threshold noise reduction is used, achieving an 8.8151 SNR.

Three different testbench scenarios are set to validate the proposed approach properly while taking the processing time, mean shifting, and SNR as a metric.

1. A classical DSP, where the embedded system performs all the computations, is set for the first comparison point with the characteristics taken from [27]:
    - A high-pass filter with a cutoff frequency of 20 Hz
    - Low-pass filter with a cutoff frequency of 500 Hz
    - Rectification with the sample absolute value
    - Smoothing through a moving average filter
2. The second approach is a real-time RLS filtering architecture with a sensor-computer-actuator paradigm. In this approach, the embedded system is used to acquire the sample, send it through Wi-Fi to a computer where it is filtered, and then wirelessly received and reconstructed.
3. The proposed approach, the one to be compared, eliminates the networking structure and external processing device to embed the computation.

D. Experiment Description

As described in the benchmark methods, the experimentation is composed of three tests, one implementing a classical DSP system and another as a sensor-computer-actuator system, where the sensor and the actuator communicate wirelessly with the computer through TCP-IP sockets, and finally, the embedded processing system.

The classical DSP processing system consists of a band-pass filter between 20 and 500 Hz in a horizontal FIR structure of 61 taps to facilitate the process and operation in real-time. The results of the FIR filter are then passed through an averaging filter with a window of 20 taps, from which its absolute value is previously obtained by way of rectification. This structure is implemented in the PYNQ embedded system.

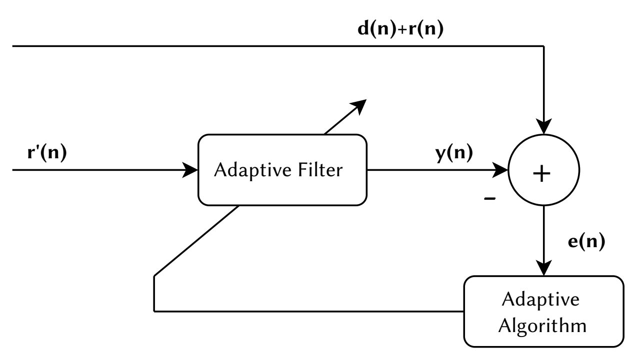

Fig. 5. Noise cancellation structure using adaptive filters.

The same filtering architecture is used for the sensor-computer-actuator system and the embedded AI processing system. A linear FIR and RLS filter structure is used, which will allow real-time learning of variations of the noise. Fig. 5 presents the adaptive noise cancellation structure. In this architecture, the input to the filter is the modeled signal or noise measurement $r'(n)$, and the desired signal is the acquired signal (desired signal added with noise) $d(n) + r(n)$. Therefore, the filter's output would be the noise model, and the output $e(n)$ corresponds to the filtered signal. The model of the signal to be removed by the filtering structure is considered white noise. The simulation of a SEMG baseline, which would be the desired signal to be removed, is highly complicated because of the number of hyperparameters and is computationally expensive. Therefore, this model is avoided for online applications.

Fig. 6 shows the architecture of a horizontal RLS adaptive filter, which can process in real-time the acquired data, allowing online learning of the acquired data, thus adjusting to the circumstances in which the structure is being used. This architecture is similar to a neural unit of a perceptron since, in the forward step, it summates the multiplications of the inputs by their weights $\Sigma_k X(k) * W(k)$. Subsequently, it compares it with the desired signal $d(k)$ and generates an error signal $\epsilon(k)$. Finally, the error signal is backpropagated through the structure with an algorithm based on stochastic gradient descent (SGD).

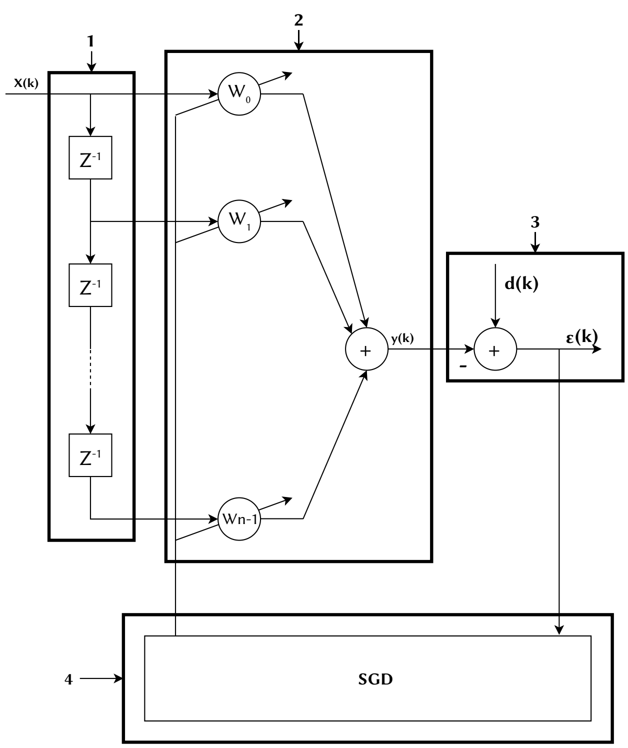

Fig. 6. Intelligent sEMG filtering algorithm for embedded processing. 1- Shows the delay taps of the filter, 2- presents the forward pass of the information, 3- corresponds to the error computation, and 4- is the SGD-based backpropagation algorithm.

IV. Results and Discussion

For the description of the results, the related tests and measurements will be presented, taking into account the signals in the same contextual frame, their spectrograms, and a propagation delay analysis analyzed with pure sinusoidal signals.

A. Results of Classical DSP

Fig. 7 and Fig. 8 show that the algorithm works as soon as it is started, without needing waiting times.

Fig. 9 shows the original signal, filtered by DSP, and the superposition of both signals in an acquisition period of 4 minutes, at a sampling frequency of 4 kHz.

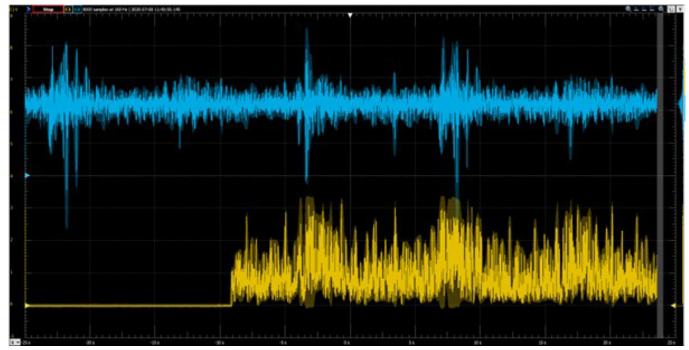

Fig. 7. Start of acquisition with traditional DSP, original signal [blue] and filtered signal [yellow], the horizontal axis represents time, while the vertical axis represents the amplitude in volts of the measured signal.

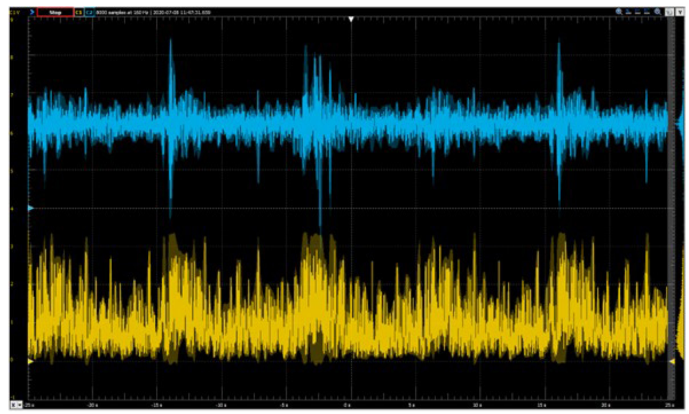

Fig. 8. Regular operation of traditional DSP, original signal (in blue) and filtered signal (in yellow), the horizontal axis represents time, while the vertical axis represents the amplitude in volts of the measured signal.

The visual analysis of the signals shows a radical change in the waveform, rectifying the impulses and leading it to oscillate from the 0 baseline without the additive component that moves the oscillation line, as in the original signal. The average of the original signal is 2.1908V, and the filtered signal is 0.9419V, which verifies what was described above. As for the spectra analysis, they can be observed in Fig. 10 and Fig. 11.

The high-frequency component of the signal is removed from the spectrograms, while the low-frequency component is distorted.

B. Results of Sensor-Computer-Actuator System

Fig. 12 and Fig. 13 show that the algorithm needs a minimum time to start working. Initially, the signal shows considerable noise, and it is impossible to identify the original signal, and after some time, it can be seen that the filtering effects are more noticeable, showing the adaptability of the filter.

Fig. 14 shows the original signal, filtered by the sensor-computer-actuator system, and the superposition of both signals in an acquisition period of 4 minutes, at a sampling frequency of 4kHz.

In addition, if a visual analysis is made, the signals appear similarly. The change is not radical given the noise source; the original signal's average is 2.193V, and the filtered signal is 2.175V, which shows that they maintain their characteristics to a large extent. It should be emphasized that in Fig. 20. errors are observed in the data communication reflected both in the wave's shape and information gaps in the spectrogram. The loss of information jeopardizes the integrity of the filtering process, as these are critical data that should not be lost.

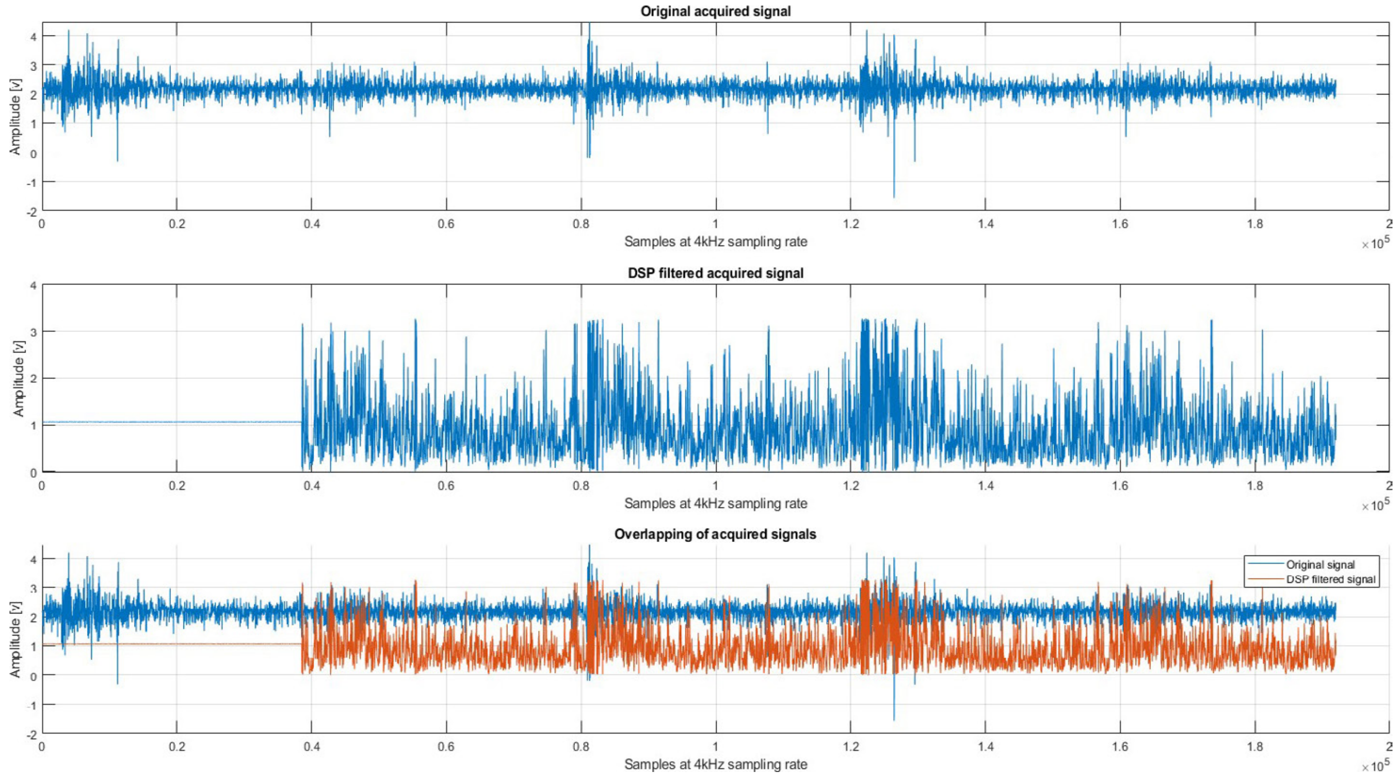

Fig. 9. Original signal vs filtered signal using traditional DSP.

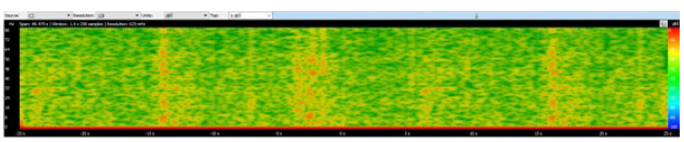

Fig. 10. Spectrogram of the original signal in a traditional DSP context. The horizontal axis represents time, while the vertical axis represents the frequency in Hz of the measured signal.

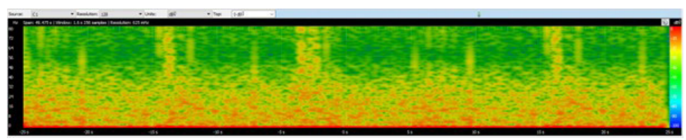

Fig. 11. Spectrogram of the filtered signal in a traditional DSP context. The horizontal axis represents time, while the vertical axis represents the frequency in Hz of the measured signal.

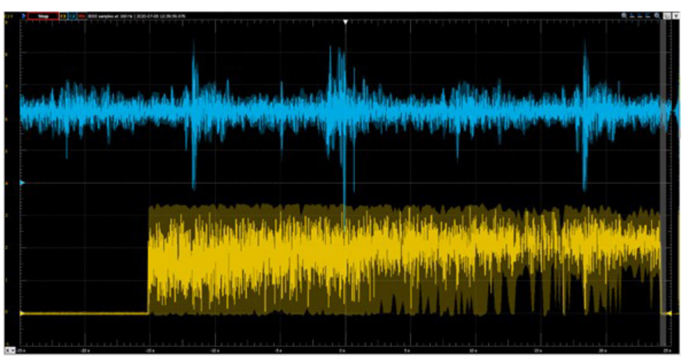

Fig. 12. Start of acquisition with the sensor-computer-actuator system: original signal [blue] and filtered signal [yellow]. The horizontal axis represents time, while the vertical axis represents the amplitude in volts of the measured signal.

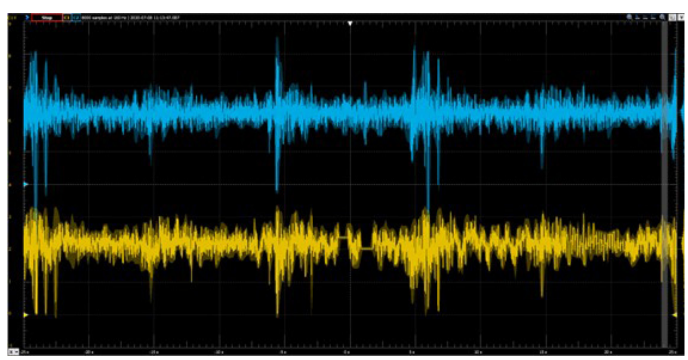

Fig. 13. Normal operation of the sensor-computer-actuator system: original signal [blue] and filtered signal [yellow]. The horizontal axis represents time, while the vertical axis represents the amplitude in volts of the measured signal.

The spectrogram analysis can be observed in Fig. 15 and Fig. 16.

No significant change can be seen comparing the spectrograms, except for the blurring effect in the impulsive peaks, regularizing the signal, and the concentration of the frequency components in the low bands.

C. Results of Embedded Processing

Fig. 17 and Fig. 18 show that the algorithm needs a minimum time to start working. Initially, the signal shows more noise than the original signal, and after some time, the filtering effects are more noticeable.

Fig. 19 shows the original signal, filtered by the on-the-edge system, and the superposition of both signals in an acquisition period of 4 minutes, at a sampling frequency of 4kHz.

The visual analysis of the signals shows that they maintain a remarkable similarity. The change is not radical, given the noise source. The average of the original signal is 2.192V, and the filtered signal is 2.173V, which shows that they maintain their characteristics.

As for the spectra analysis, they can be observed in Fig. 20 and Fig. 21.

The spectrogram comparison does not show much change, except for the blurring effect on the impulsive peaks, regularizing the signal.

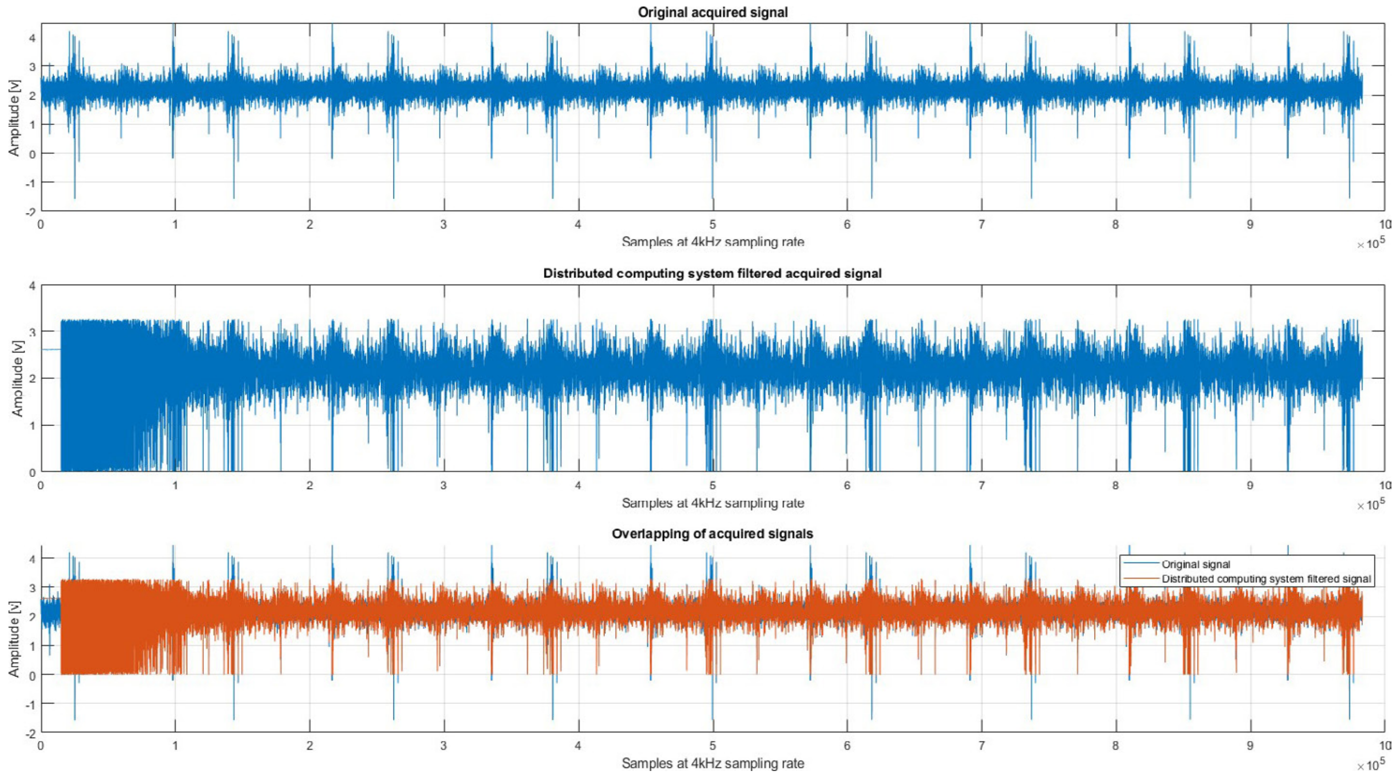

Fig. 14. Original signal vs filtered signal using the sensor-computer-actuator system.

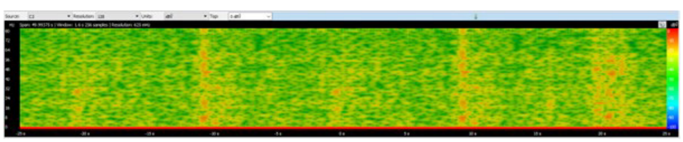

Fig. 15. Spectrogram of the original signal in the context of a distributed computing system. The horizontal axis represents time, while the vertical axis represents the frequency in Hz of the measured signal.

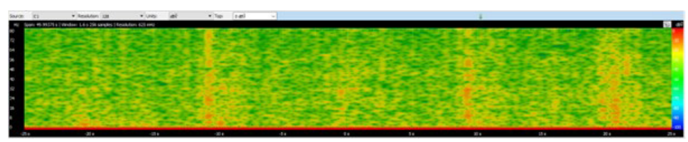

Fig. 16. Spectrogram of the filtered signal in the context of a distributed computing system. The horizontal axis represents time, while the vertical axis represents the frequency in Hz of the measured signal.

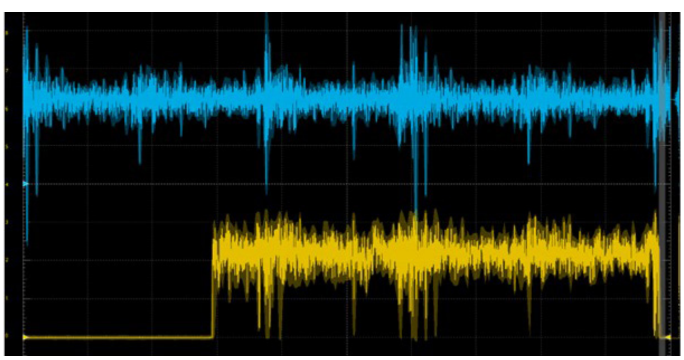

Fig. 17. Start of acquisition with embedded processing: original signal [blue] and filtered signal [yellow]. The horizontal axis represents time, while the vertical axis represents the amplitude in volts of the measured signal.

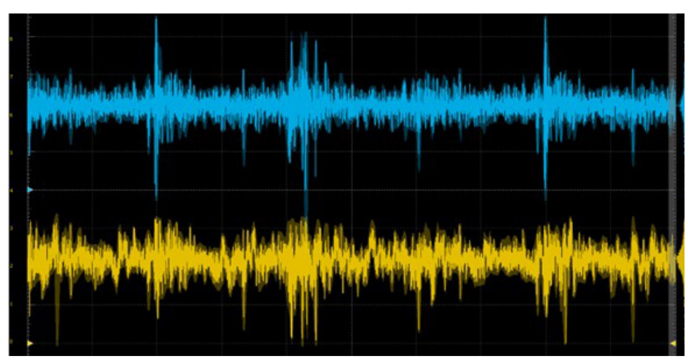

Fig. 18. Regular operation with embedded processing: original signal [blue] and filtered signal [yellow]. The horizontal axis represents time, while the vertical axis represents the amplitude in volts of the measured signal.

D. Results Analysis

Fig. 22 shows the signal-to-noise ratio of the DSP, sensor-computer-actuator, and embedded systems. This measure analyzes the filtering quality of the signals by removing a noise signal, which is a white noise type generated artificially. Both the convergence points of the embedded processing system and the sensor-computer-actuator system are highlighted -the convergence delay is also depicted for the latter-.

Table I shows the comparative results of the filtering paradigms. The fastest processing system is the sensor-computer-actuator system. In contrast, the embedded system exhibits processing times close to those of the distributed system, and the classic DSP system is considerably slower than the others. The mean shift in the sensor-computer-actuator and embedded processing systems is minimal. Meanwhile, the classical DSP system strongly changes the signal's nature, which is evident from the mean shift. The only filtering system that does not come into action when the system is turned on is the sensor-computer-actuator system, which needs a calibration and algorithm adaptation time.

Regarding the use of resources, the best is the DSP system, as it needs only one signal source, the SEMG acquisition source. However, in addition to the SEMG signal source, sensor-computer-actuator

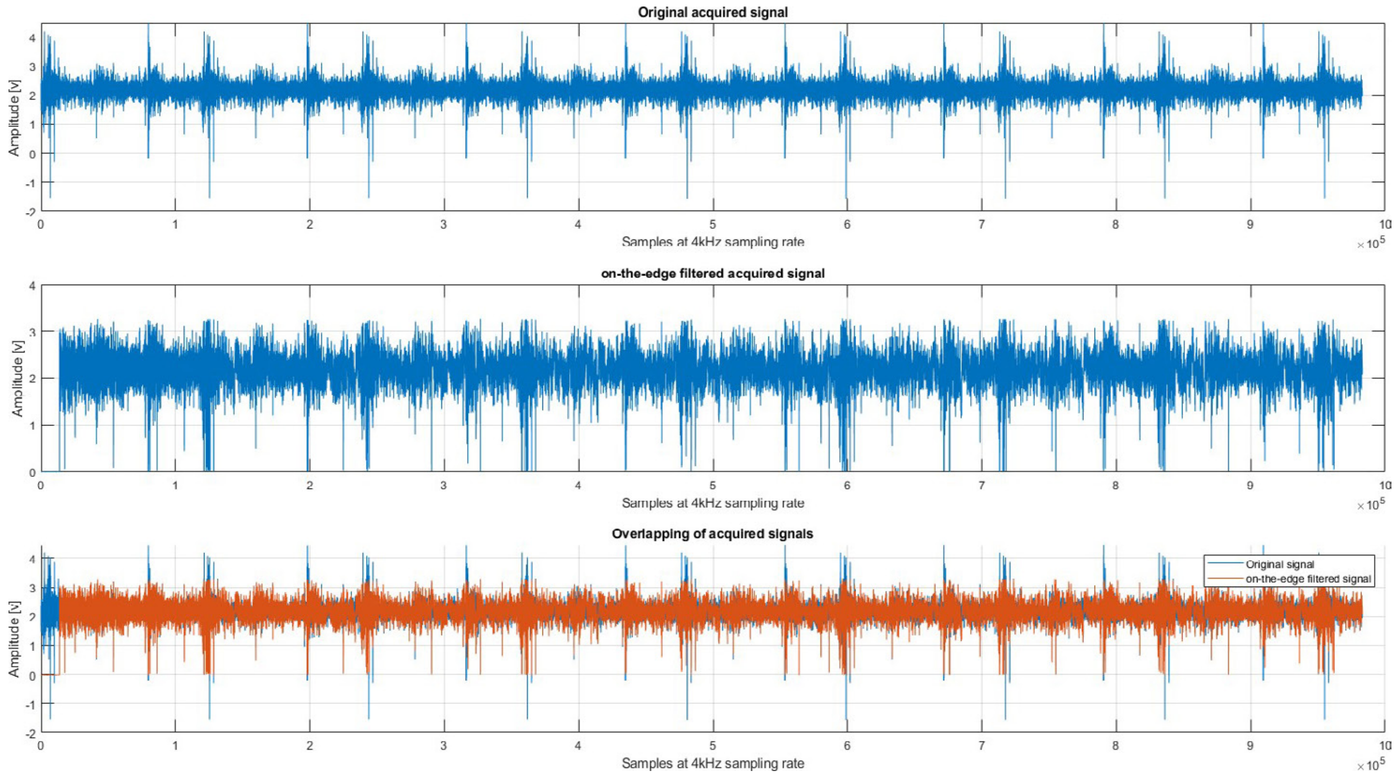

Fig. 19. Original signal vs filtered signal using an embedded system.

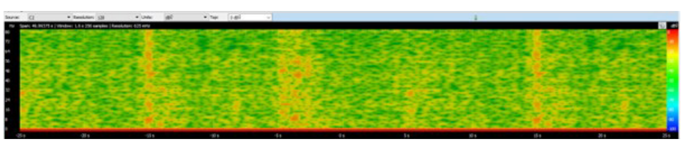

Fig. 20. Embedded processing-driven spectrogram of the original signal. The horizontal axis represents time, while the vertical axis represents the frequency in Hz of the measured signal. Source.

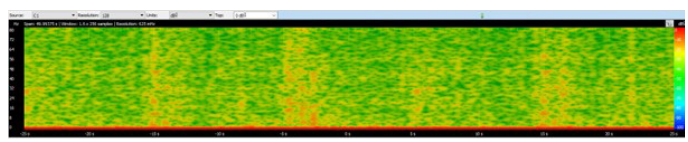

Fig. 21. Embedded processing-driven spectrogram of filtered signal. The horizontal axis represents time, while the vertical axis represents the frequency in Hz of the measured signal Source.

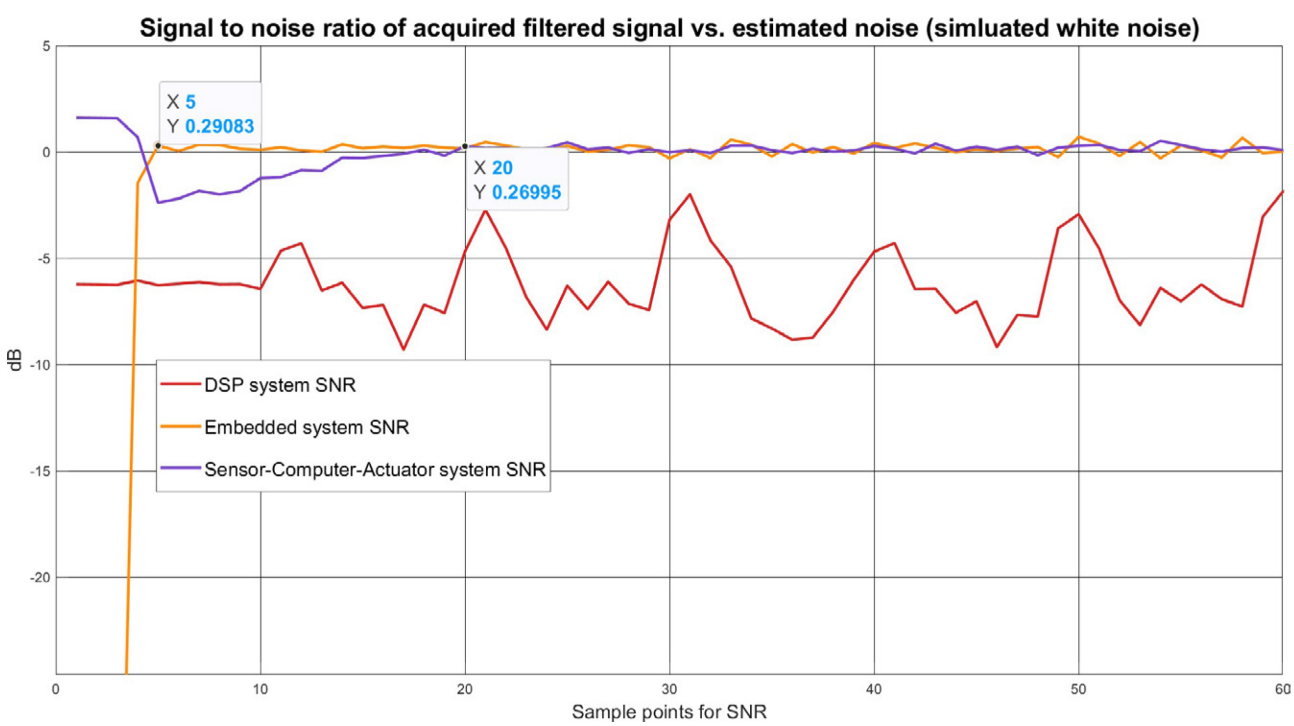

Fig. 22. SNR comparison of analyzed signals. In red is the SNR of the DSP system, in orange is the SNR of the embedded system, and in purple is the SNR of the sensor-computer-actuator system.

TABLE I. Comparative Results of Filtering Paradigms

	DSP	**Sensor - Computer - Actuator**	**Embedded System**
Processing Time	36.43 ms	2.573 ms	3.822 ms
Mean Shift	1.248 V	18 mV	19 mV
Immediate Action	Yes	No	Yes
Resources	One signal source	Two signal sorurces, network interface, PC	Two signal sources
SNR Mean	-6.321 db	0.11124 dB	0.15125 dB

and embedded processing systems need a second signal source to acquire noise. Therefore, the system that consumes the most physical resources is the distributed one, which requires a network interface and a high-capacity computer capable of executing the calculations involved in this processing.

The signal-to-noise ratio (SNR) determines the filtering quality, comparing the power of the filtered signal with the power of the noisy signal, which, in this case, is a simulated white noise signal. The results show that both the embedded processing and sensor-computer-actuator systems improve the signal, even if it is minimal. Meanwhile, the traditional DSP system does not fulfill the task of eliminating this type of noise, resulting in an average SNR of -6,321 dB. Again, Fig. 22 shows that the convergence speed of the distributed computing system is lower than that of the on-the-edge system.

E. Discussion

The results and measurements presented in the previous sections show that, although the sensor-computer-actuator processing is the fastest, it is more unstable, generating losses of information when the buffers of the communication socket are saturated. In addition, it requires more hardware equipment due to implementing a wireless communication system based on Wi-Fi. An intermediary is needed in the network structure connected to the Internet, which affects the security of the transmitted data. Nevertheless, a computer with good characteristics can adequately perform all the calculation and communication processes.

Regarding the traditional DSP system, it is the most widely used to date because of the relative simplicity of its implementation and the fact that it does not require modeling or acquisition of the signal noise to be removed. These features allow the processing system to act on its own. Furthermore, the algorithms presented in this paper can be optimized using C language or even by building hardware modules in HDL that can be implemented in the FPGA part of the embedded system—radically accelerating the computational speed of the system.

Although the processing delay is about 70 % in the embedded processing system, it is still much faster than the traditional DSP processing system. It implies a good use of hardware and software resources with the great advantage of adaptability to the noise sources that a surface EMG signal may suffer, which may change over time in amplitude and nature.

The embedded processing methodology is the cheapest and most efficient online learning technique in terms of resources since it eliminates the entire network interface of the distributed system. It has an adequate processing time, much shorter than DSP (showing a significant improvement in this area) and slightly longer than the sensor-computer-actuator system. It allows immediate action in terms of processing while reducing the external computational load that can be a problem when dealing with EMG signals.

V. Final Remarks

The processing and filtering of EMG signals are crucial for using these signals in prosthetic-device control processes or medical diagnostics. Traditionally, rigid filtering structures based on DSP have been used, although it does not acknowledge the non-LTI characteristics of the EMG. Subsequently, for more complex processes respecting the intrinsic characteristics of the system, all the information to be processed is sent to a discrete computing unit with which they usually communicate wirelessly. Therefore, addressing an integral processing methodology embedded in the device is appropriate because of the technological advances in the miniaturization of silicon processing systems and their increased computational capacity. Furthermore, embedded processing implies that the intelligent processing algorithms and decision-making are implemented on-device, eliminating discrete computing systems and substantially improving the processing that traditional LTI DSP techniques offer.

Objective comparison is made between the traditional DSP system, the discrete processing system, and the embedded processing system using the same device and the same database reconstructed by a function generator. The spectrograms of the signals, the delays due to the processing, and the signal-to-noise ratio are evaluated. The intelligent filtering algorithm is an adaptive RLS filter to which a simulated white noise signal is introduced as a noise source.

It was not found in the literature review any contribution to the implementation of adaptive filters for sEMG in an embedded system. Most of them use distributed computation systems in MATLAB. The most significant contribution of this paper is introducing a real-time implementation of adaptive filtering algorithms respecting the non-LTI characteristics of the EMG signals.

Given the current technological availability, it is appropriate and even advisable to perform intelligent data processing on-device. Even if a distributed processing system is still necessary for further processing, embedding processing blocks is advisable. It will reduce the computational load by receiving helpful information and not only raw data. Embedding intelligent processing blocks in the acquisition device will allow building more complex processing architectures and signal usage techniques, offering better results to end-users.

Therefore, intelligent embedded (edge AI) processing of electromyographic signals is more effective than traditional hardware processing. Embedding the processing is more effective because the time delay between signals is shorter than in a sensor-computer-actuator system. Suppose the noise interfering with the desired signal is properly characterized or acquired with secondary sensors. In that case, it can provide highly relevant information without considerable changes in the frequency and temporal nature of the electromyographic signals. On the other hand, considering the current state of technology, applying embedded artificial intelligence techniques is justified since they reduce the computational load suffered by other devices and allow the development of architectures with greater scalability. Furthermore, the autonomy of processing between the intelligent nodes that make up an acquisition system can be considered relevant. Even the total autonomy of each sensor is possible and does not require an auxiliary computing system or auxiliary conditioning of the signals to carry out the decision-making process.

Acknowledgments

The authors acknowledges the valuable support given by the SDAS Research Group (https://sdas-group.com/ –Accesed on: 11-Jul-2022).

References

[1] R. M. Rangayyan, *Biomedical Signal Analysis.* IEEE Press, 2nd ed., 2015.

[2] R. Singh, N. Rajpal, R. Mehta, "An empiric analysis of wavelet-based feature extraction on deep learning and machine learning algorithms for arrhythmia classification," *International Journal of Interactive Multimedia and Artificial Intelligence*, 2021, doi: 10.9781/ijimai.2020.11.005.

[3] C. Li, G. Li, G. Jiang, D. Chen, H. Liu, "Surface emg data aggregation processing for intelligent prosthetic action recognition," *Neural Computing and Applications*, vol. 32, pp. 16795–16806, 11 2020, doi: 10.1007/S00521- 018-3909-Z/TABLES/4.

[4] G. Li, O. W. Samuel, C. Lin, M. G. Asogbon, P. Fang, P. O. Idowu, "Realizing efficient emg-based prosthetic control strategy," *Advances in Experimental Medicine and Biology*, vol. 1101, pp. 149–166, 2019, doi: 10.1007/978- 981-13-2050-7_6.

[5] D. Proaño-Guevara, J. Procel-Feijóo, J. Zhingre- Balcazar, L. Serpa-Andrade, "Biomimetical arm prosthesis: A new proposal," vol. 590, 2018, pp. 549– 558, Springer International Publishing.

[6] L. Resnik, H. H. Huang, A. Winslow, D. L. Crouch, Zhang, N. Wolk, "Evaluation of emg pattern recognition for upper limb prosthesis control: A case study in comparison with direct myoelectric control," *Journal of NeuroEngineering and Rehabilitation*, vol. 15, pp. 1–13, 3 2018, doi: 10.1186/S12984-018-0361- 3/FIGURES/3.

[7] J. Ribeiro, F. Mota, T. Cavalcante, I. Nogueira, V. Gondim, V. Albuquerque, A. Alexandria, "Analysis of man-machine interfaces in upper-limb prosthesis: A review," *Robotics 2019, Vol. 8, Page 16*, vol. 8, p. 16, 2 2019, doi: 10.3390/ROBOTICS8010016.

[8] Y. Li, J. Deng, Q. Wu, Y. Wang, "Eye-tracking signals based affective classification employing deep gradient convolutional neural networks," *International Journal of Interactive Multimedia and Artificial Intelligence*, vol. 7, 2021, doi: 10.9781/ijimai.2021.06.002.

[9] J. M. Fajardo, O. Gomez, F. Prieto, "Emg hand gesture classification using handcrafted and deep features," *Biomedical Signal Processing and Control*, vol. 63, p. 102210, 1 2021, doi: 10.1016/J.BSPC.2020.102210.

[10] J. V. Basmajian, C. J. D. Luca, *Muscles alive : their functions revealed by electromyography.* Williams & Wilkins, 1985.

[11] P. Konrad, *The abc of emg.* 2005.

[12] C. Tepe, M. C. Demir, "The effects of the number of channels and gyroscopic data on the classification performance in emg data acquired by myo armband," *Journal of Computational Science*, vol. 51, p. 101348, 4 2021, doi: 10.1016/J.JOCS.2021.101348.

[13] J. Kimura, *Electrodiagnosis in Diseases of Nerve and Muscle: Principles and Practice.* Oxford University Press, 4 ed., 2013.

[14] R. Merletti, D. Farina, *Surface Electromyography: Physiology, Engineering and Applications.* Wiley-IEEE Press, 4 2016.

[15] S. Cerutti, C. Marchesi, *Advanced Methods of Biomedical Signal Processing.* IEEE Press, 2011.

[16] K. A. Wheeler, H. Shimada, D. K. Kumar, S. P. Arjunan, "A semg model with experimentally based simulation parameters," *2010 Annual International Conference of the IEEE Engineering in Medicine and Biology Society, EMBC'10*, pp. 4258–4261, 2010, doi: 10.1109/IEMBS.2010.5627175.

[17] K. L. Moore, A. F. Dalley, A. M. R. Agur, *Clinically oriented anatomy.* Wolters Kluwer Health/Lippincott Williams & Wilkins, 2014.

[18] M. Yaserifar, A. S. Oliveira, "Surface emg variability while running on grass, concrete and treadmill," *Journal of Electromyography and Kinesiology*, vol. 62, p. 102624, 2 2022, doi: 10.1016/J.JELEKIN.2021.102624.

[19] J. W. Lee, M. J. Shin, M. H. Jang, W. B. Jeong, S. J. Ahn, "Two-stage binary classifier for neuromuscular disorders using surface electromyography feature extraction and selection," *Medical Engineering & Physics*, vol. 98, pp. 65–72, 12 2021, doi: 10.1016/J.MEDENGPHY.2021.10.012.

[20] T. Lulic-Kuryllo, F. Negro, N. Jiang, C. R. Dickerson, "Standard bipolar surface emg estimations mischaracterize pectoralis major activity in commonly performed tasks," *Journal of Electromyography and Kinesiology*, vol. 56, p. 102509, 2 2021, doi: 10.1016/J.JELEKIN.2020.102509.

[21] M. M. Yassin, A. M. Saber, M. N. Saad, A. M. Said, A. M. Khalifa, "Developing a low-cost, smart, handheld electromyography biofeedback system for telerehabilitation with clinical evaluation," *Medicine in Novel Technology and Devices*, vol. 10, p. 100056, 6 2021, doi: 10.1016/J.MEDNTD.2020.100056.

[22] L. E. Sánchez-Velasco, M. Arias-Montiel, E. Guzmán- Ramírez, E. Lugo-González, "A low-cost emg- controlled anthropomorphic robotic hand for power and precision grasp," *Biocybernetics and Biomedical Engineering*, vol. 40, pp. 221–237, 1 2020, doi: 10.1016/J.BBE.2019.10.002.

[23] E. Noboa, M. Rácz, L. Szucs, P. Galambos, G. Márton, Eigner, "Development of an emg based svm supported control solution for the platypous education mobile robot using mindrove headset," *IFAC-PapersOnLine*, vol. 54, pp. 304–309, 1 2021, doi: 10.1016/J.IFACOL.2021.10.273.

[24] H. J. Hermens, B. Freriks, C. Disselhorst-Klug, G. Rau, "Development of recommendations for semg sensors and sensor placement procedures," *Journal of Electromyography and Kinesiology*, vol. 10, pp. 361–374, 10 2000, doi: 10.1016/S1050-6411(00)00027-4.

[25] D. Stegeman, H. Hermens, "Standards for surface electromyography: The european project surface emg for non-invasive assessment of muscles (seniam)," *SENIAM*, pp. 108–112, 2007.

[26] A. Pashaei, M. R. Yazdchi, H. R. Marateb, "Designing a low-noise, high-resolution, and portable four channel acquisition system for recording surface electromyographic signal.," *Journal of medical signals and sensors*, vol. 5, pp. 245–52, 2015.

[27] T. Roland, S. Amsuess, M. F. Russold, W. Baumgartner, "Ultra-low-power digital filtering for insulated emg sensing," *Sensors (Switzerland)*, vol. 19, pp. 1–24, 2019, doi: 10.3390/s19040959.

[28] L. Rozaqi, A. Nugroho, K. H. Sanjaya, A. I. Simbolon, "Design of analog and digital filter of electromyography," *Proceeding - 2019 International Conference on Sustainable Energy Engineering and Application: Innovative Technology Toward Energy Resilience, ICSEEA 2019*, pp. 186–192, 2019, doi: 10.1109/ICSEEA47812.2019.8938645.

[29] A. K. Sahu, A. K. Sahu, "A review on different filter design techniques and topologies for bio- potential signal acquisition systems," *Proceedings of the 3rd International Conference on Communication and Electronics Systems, ICCES 2018*, pp. 934–937, 2018, doi: 10.1109/CESYS.2018.8723912.

[30] H. Tankisi, D. Burke, L. Cui, M. de Carvalho, S. Kuwabara, S. D. Nandedkar, S. Rutkove, E. Stålberg, M. J. van Putten, A. Fuglsang-Frederiksen, "Standards of instrumentation of emg," *Clinical Neurophysiology*, vol. 131, pp. 243–258, 2020, doi: 10.1016/j.clinph.2019.07.025.

[31] S. W. Smith, *The scientist and engineer's guide to digital signal processing.* California Technical Publishing, 2nd ed., 1997.

[32] A. Oppenheim, R. Schafer, J. Buck, *Discrete-Time Signal Processing.* Prentice Hall Press, 2nd ed., 1998.

[33] R. Woods, J. McAllister, G. Lightbody, Y. Yi, *FPGA- Based Implementation of Signal Processing Systems.* Wiley, 10 2008.

[34] A. Viveros-Melo, L. Lasso-Arciniegas, J. A. Salazar- Castro, D. H. Peluffo-Ordóñez, M. A. Becerra, A. E. Castro-Ospina, E. J. Revelo-Fuelagán, "Exploration of Characterization and Classification Techniques for Movement Identification from EMG Signals: Preliminary Results," in *Communications in Computer and Information Science*, 2018, pp. 139–149, doi: 10.1007/978-3-319-98998-3_11.

[35] L. Lasso-Arciniegas, A. Viveros-Melo, J. A. Salazar- Castro, M. A. Becerra, A. E. Castro-Ospina, E. J. Revelo-Fuelagán, D. H. Peluffo-Ordóñez, "Movement Identification in EMG Signals Using Machine Learning: A Comparative Study," in *Lecture Notes in Computer Science (including subseries Lecture Notes in Artificial Intelligence and Lecture Notes in Bioinformatics)*, 2018, pp. 368–375, doi: 10.1007/978-3-030-01132-1_42.

[36] S. Haykin, B. Kosko, *Intelligent Signal Processing.* IEEE Press, 12 2001.

[37] C. S. Palacios, S. L. Romero, "Calibración automática en filtros adaptativos para el procesamiento de señales emg," *Revista Iberoamericana de Automatica e Informatica Industrial*, vol. 16, pp. 1–6, 2011.

[38] I. F. Ghalyan, Z. M. Abouelenin, V. Kapila, "Gaussian filtering of emg signals for improved hand gesture classification," *2018 IEEE Signal Processing in Medicine and Biology Symposium, SPMB 2018 - Proceedings*, pp. 1– 6, 2019, doi: 10.1109/SPMB.2018.8615596.

[39] M. Z. Jamal, D. H. Lee, D. J. Hyun, "Real time adaptive filter based emg signal processing and instrumentation scheme for robust signal acquisition using dry emg electrodes," *2019 16th International Conference on Ubiquitous Robots, UR 2019*, pp. 683–688, 2019, doi: 10.1109/URAI.2019.8768662.

[40] S. Márquez-Figueroa, Y. S. Shmaliy, O. Ibarra- Manzano, "Optimal extraction of emg signal envelope and artifacts removal assuming colored measurement noise," *Biomedical Signal Processing and Control*, vol. 57, p. 101679, 2020, doi: 10.1016/j.bspc.2019.101679.

[41] L. L. Menegaldo, "Real-time muscle state estimation from emg signals

during isometric contractions using kalman filters," *Biological Cybernetics*, vol. 111, pp. 335– 346, 2017, doi: 10.1007/s00422-017-0724-z.

[42] P. Okoniewski, S. Kocon, J. Piskorowski, "Linear time-varying multi-notch fir filter for fast emg measurements," *2018 23rd International Conference on Methods and Models in Automation and Robotics, MMAR 2018*, pp. 634–637, 2018, doi: 10.1109/MMAR.2018.8486122.

[43] A. R. Verma, Y. Singh, B. Gupta, "Adaptive filtering method for emg signal using bounded range artificial bee colony algorithm," *Biomedical Engineering Letters*, vol. 8, pp. 231–238, 2018, doi: 10.1007/s13534-017-0056-x.

[44] T. Yu, K. Akhmadeev, E. L. Carpentier, Y. Aoustin, D. Farina, "On-line recursive decomposition of intramuscular emg signals using gpu-implemented bayesian filtering.," *IEEE transactions on bio-medical engineering*, 2019, doi: 10.1109/TBME.2019.2948397.

[45] P. S. R. Diniz, *Adaptive Filtering*. Springer US, 2008.

[46] M. Limem, M. A. Hamdi, M. A. Maaref, "Denoising uterine emg signals using lms and rls adaptive algorithms," 3 2016, pp. 273–276, IEEE.

[47] A. C. Mugdha, F. S. Rawnaque, M. U. Ahmed, "A study of recursive least squares (rls) adaptive filter algorithm in noise removal from ecg signals," 6 2015, pp. 1–6, IEEE.

[48] P. Singh, K. Bhole, A. Sharma, "Adaptive filtration techniques for impulsive noise removal from ecg," 12 2017, pp. 1–4, IEEE.

[49] M. R. Ahmed, R. Halder, M. Uddin, P. C. Mondal, A. K. Karmaker, "Prosthetic arm control using electromyography (emg) signal," *2018 International Conference on Advancement in Electrical and Electronic Engineering, ICAEEE 2018*, 2 2019, doi: 10.1109/ICAEEE.2018.8642968.

[50] K. T. Kim, S. Park, T. H. Lim, S. J. Lee, "Upper- limb electromyogram classification of reaching- to-grasping tasks based on convolutional neural networks for control of a prosthetic hand," *Frontiers in Neuroscience*, vol. 15, p. 1311, 10 2021, doi: 10.3389/FNINS.2021.733359/BIBTEX.

[51] G. M. Hägg, B. Melin, R. Kadefors, "Applications in ergonomics," 2005. doi: 10.1002/0471678384.ch13.

[52] Y. H. Hsueh, C. Yin, Y. H. Chen, "Hardware system for real-time emg signal acquisition and separation processing during electrical stimulation," *Journal of Medical Systems*, vol. 39, 2015, doi: 10.1007/s10916-015- 0267-6.

[53] D. Z. Yinfeng Fang, "Isrmyo-i: A database for semg- based hand gesture recognition," 2018. [Online]. Available: https://dx.doi.org/10.21227/H26Q26, doi: 10.21227/H26Q26.

[54] Y. Fang, H. Liu, G. Li, X. Zhu, "A multichannel surface EMG system for hand motion recognition," *International Journal of Humanoid Robotics*, vol. 12, p. 1550011, may 2015, doi: 10.1142/s0219843615500115.

[55] Q. Ai, Q. Liu, W. Meng, S. Q. Xie, "Neuromuscular signal acquisition and processing," in *Advanced Rehabilitative Technology*, Elsevier, 2018, pp. 33–66, doi: 10.1016/b978-0-12-814597-5.00003-5.

[56] M. Sharma, N. Gaddam, T. Umesh, A. Murthy, P. K. Ghosh, "A comparative study of different EMG features for acoustics-to-EMG mapping," in *Interspeech 2021*, aug 2021, ISCA.

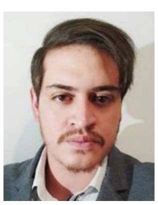

Daniel Proaño-Guevara

Daniel received his B.Eng. degree in electronics engineering from the Universidad Politécnica Salesiana, Ecuador, 2019, his M.Sc. in artificial intelligence from Universidad Internacional de La Rioja UNIR, Spain, 2020, and he is currently studying his M.Eng. in electronics engineering from the Instituto Superior Técnico-Universidade de Lisboa, Portugal. His research interest includes intelligent digital signal processing, artificial intelligence, embedded systems design, FPGA, and biomedical engineering. Currently, he is a research assistant at the SDAS group.

Xiomara Blanco Valencia

She is originally from Bogotá, Colombia; she studied for her System Engineering degree at the University of Santander in Bucaramanga and then moved to Salamanca, Spain, where she studied for her master's degree and PhD in Artificial Intelligence at the University of Salamanca. She is currently working as Professor at the Department of Computer Science at Universidad Internacional de La Rioja, Spain. In addition, she is a member of the Smart Data Analysis Systems Group SDAS Group. Her research interests include Artificial Intelligence, Soft computing, Recommender systems for health and Natural Language Processing.

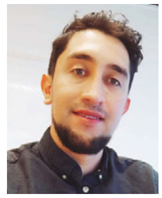

Paul D. Rosero-Montalvo

He is a Post. Doc at IT University of Copenhagen (ITU) in Denmark since June 2021. His research focuses on emerging microcontrollers to run machine learning models in decentralized networks. Earlier, He was a research assistant professor in the Applied Science Department at the Universidad Tecnica del Norte (UTN), Ecuador, for seven years. At the same time, he was a part-time lecturer in the TI Department at Instituto Tecnologico 17 de Julio, Ecuador. He received his Ph.D. from the University of Salamanca in Spain in November 2020, where Prof. Vivian Lopez-Batista advised him. He has a master's degree in Data Management systems from Universidad de las Fuerzas Armadas ESPE, Ecuador (2018), and an Engineering degree in Electronics and Telecommunications from UTN (2013).

Diego H. Peluffo-Ordóñez

He was born in Pasto - Colombia in 1986. He received his degree in electronic engineering, Master's in industrial automation and PhD in engineering from the Universidad Nacional de Colombia, Manizales - Colombia, in 2008, 2010 and 2013, respectively. In 2012, he undertook his doctoral internship at KU Leuven - Belgium.From 2013 to 2014, he worked as a post-doc at Université Catholique de Louvain at Louvain la-Neuve - Belgium. From 2014 to 2015, he worked as a lecturer at Universidad Cooperativa de Colombia - Pasto.From 2015 to 2017, he worked as a researcher/professor at Universidad Técnica del Norte - Ecuador. From 2017 to 2020, he worked as a researcher/professor at Yachay Tech - Ecuador. From 2020 to 2022, he worked as a Consultant/Curriculum Author at deeplearning.ai. Currently, he is working as an assistant professor at the Modeling, Simulation and Data Analysis (MSDA) Research Program from Mohammed VI Polytechnic University - Morocco. He works as a Master's thesis advisor with the Artificial Intelligence Master's program from Universidad Internacional de La Rioja (UNIR) - Spain. He is the founder and head of the SDAS Research Group. As well, he works as an invited lecturer and an external researcher at Corporación Universitaria Autónoma de Nariño - Pasto, Colombia, and is a member of SEDMATEC Research Group. Also, he is an external collaborator at Writing Lab from Tecnológico de Monterrey - Mexico. As well, he is an external supervisor of PhD programs at Universidad de Granada - Spain, Universitat Politècnica de València - Spain,and Universidad Nacional de La Plata - Argentina.He has served as an organizing committee member (general chair, session chair, competitions chair) as well as a keynote speaker in several conferences. Also, he has served as a guest editor for the Computers and Electrical Engineering Journal. His main research interests are kernel-based and spectral methods for data clustering and dimensionality reduction. The scope of his topics of interest encompasses complex high-dimensional data, signal, image and video analysis for medical and industry applications.

Improvement in Quality of Service Against Doppelganger Attacks for Connected Network

Deepak Choudhary*, Roop Pahuja

Instrumentation and Control Department, Dr B.R Ambedkar National Institute of Technology, Jalandhar (India)

Received 29 October 2021 | Accepted 13 June 2022 | Published 2 August 2022

Abstract

Because they are in a high-risk location, remote sensors are vulnerable to malicious ambushes. A doppelganger attack, in which a malicious hub impersonates a legitimate network junction and then attempts to take control of the entire network, is one of the deadliest types of ambushes. Because remote sensor networks are portable, hub doppelganger ambushes are particularly ineffective in astute wellness contexts. Keeping the framework safe from hostile hubs is critical because the information in intelligent health frameworks is so sensitive. This paper developed a new Steering Convention for Vitality Effective Systems (SC-VFS) technique for detecting doppelganger attacks in IoT-based intelligent health applications such as a green corridor for transplant pushback. This method's main advantage is that it improves vitality proficiency, a critical constraint in WSN frameworks. To emphasize the suggested scheme's execution, latency, remaining vitality, throughput, vitality effectiveness, and blunder rate are all used. To see how proper the underutilized technique is compared to the existing Half Breed Multi-Level Clustering (HMLC) computation. The suggested approach yields latency of 0.63ms and 0.6ms, respectively, when using dead hubs and keeping a strategic distance from doppelganger assault. Furthermore, during the 2500 cycles, the suggested system achieves the highest remaining vitality of 49.5J.

Keywords

CHANNEL(CH), Doppelganger, Remote-Configuration, Steering Protocol, Security, Security and Vitality Expertise Transportation Systems, Web of Things.

DOI: 10.9781/ijimai.2022.08.003

I. Introduction

Inaccessible detection, health care, climate forecasting, security, and surveillance are just a few of the applications that have recently seen widespread use of remote sensor systems. The value of these hub shifts is dependent on the junction's size, the type and length of the battery used, the junction's life cycle, the weight of the sensor, and other factors [1]. The WSN can be classified into three groups. A primary type is a level arrangement. The second type could be based on clusters, and the third could be organized at various levels. The most challenging problem in remote sensor networks (WSN) is parcel directing [2]. The person sensor hub sends data bundles to the group controller hub via Bluetooth. The provenance of the guiding is crucial, especially in the vicinity of hostile hubs. The development of energy-efficient forms is another pressing issue [3]. Because the hubs are usually blocked off once installed in primary remote locations, replacing the batteries can be a time-consuming process. As a result, steering conventions must be created so that they consume the least amount of energy possible. Because they provide stack adjusting focus points while consuming the least energy, clustering directing techniques are widely used in package delivery [4]. The placement of assaults is the next major challenge in WSN frameworks. WSN sensors are the most vulnerable to outside attacks. As a result, recognizing abnormal behavior is critical in determining how close these ambushes are.

* Corresponding author.

E-mail address: engg_deepak@yahoo.com

Three different approaches can be used to detect distorted behavior in WSN frameworks [5]. The primary arrangement entails the application of data mining techniques. Machine learning algorithms are used in the current method. The final plan employs clustering techniques. WSN attacks include wormholes, black holes, listening quietly attacks, doppelganger attacks, and Sybil attacks. Lack of plan judgment and sincerity are the main deterrents to these attacks [6]. WSN sensor hubs are distinguished by their dynamic and self-organizing nature. As a result, verifying sensor hubs could be a difficult task. As a result, any malicious hub can quickly access the system without proper authentication. In addition, the vitality constraint makes verification extremely challenging [7]. Sticking is a type of attack in which adversarial hubs broadcast massive amounts of signals simultaneously due to a decision to ultimately compromise the remote detector network's security [8]. Another common type of ambush is the Sybil ambush. During this type of attack, the virulent hub uses the identities of the network's legitimate hubs to determine a large number of malicious shoppers to send to the network's head. With this type of attack, the location of all poisonous centres remains constant [9]. Doppelganger attacks are also common among WSNs. One malicious hub creates duplicate counterparts with the same ID to encourage the WSN. There are two methods for detecting doppelganger ambushes. These strategies make use of both centralized and localized sites [10]. This study presents an utterly unique technique for distinguishing doppelganger assaults in remote detector systems.

II. Related Work

For detective work on doppelganger assaults, [11] devised a multi-level crossover location approach. The chance hypothesis plan was used to support the instructed technique. During the initial setup, the abnormal behavior of the device junctions was identified. The battery levels of the junctions were then checked in the following step. All different hubs within the organization were aware of the proximity of doppelganger hubs during the last step. [12] devised a novel Sybil Observe Improved Privacy-Aware Savvy upbeat technique for Sybil ambushes in remote sensing systems for detective work. Sybil's death was announced in three stages. The leading organization was the first step. Secure communication was the first stage, and Sybil hub differentiating proof was the last. The device hub's neighbourhood information was used. [13] devised a method for investigating Sybil's attacks. The instructed convention enabled communication between the cluster's device hubs. The strategy was created specifically to aid in administering quality confinement in remote device systems. [14] unquestionable a method of dealing with a denial-of-sleep ambush This system was made using the Hopfield neural organize framework, which was created by combining the firefly calculation with the Hopfield neural organize framework. To detect denial-of-sleep attacks, the moveable plunge technique was combined with the neural arrangement. [15] provided a visual representation of the various techniques for detective work doppelganger hub attacks mentioned in the article. For comparison, each theoretical and informative study was provided. The difficulties and obstacles of detective work doppelganger attacks in remote device systems were discussed in this study. [16] devised a new method for detecting low-rate profit dissent attacks in remote device systems. This convention was made possible by the Hilbert Huang change. The non-linear activity flag data was analyzed and used to distinguish low-rate denial-of-service attacks. [17] Indisputable associate degree RSA-based technique for denial-of-sleep attacks in detective work. This paper proposes a novel associate degree interconnected structure supported by convention. This study used the RSA scientific discipline technique to ensure that the hubs stayed in the energy-saving mode. This system resulted in significant energy savings. For detective work, man-in-the-middle attacks, [18] recommended using an intermission finding approach in remote device systems. Signature action checking was commonly used to identify the attack, which employed three distinct methods. The situation and block plots, the categorization conspiracies, and the framework inquiry plot were among these plots. To distinguish profit-risk rejection, [19] used standard reliance estimators. This innovation was created for remote sensing element systems based on the Internet of Things (IoT). The method began with the creation of knowledge and progressed to incorporating placement. After the enclosed placement, the highlighted age arrived. Finally, datasets were used in the framework's development and analysis. [20] used deep learning to distinguish profit attacks during this case; lightweight confirmation procedures were used. The 0.5 breeds protect remote sensing systems (WSNs) from doppelganger attacks. A multi-level copy discovery strategy that used a crossover approach was created using various-stages bunch computation. The HMLC strategy is based on a three-stage location framework, with the first evaluating abnormal transportable hub movement at intervals of the zone (DZ), the second (battery health and pseudo irregular), and the third (battery check and pseudo irregular) being the most important (educates alternative systems virtually copy). The method's adequacy is indicated by security features such as a false negative, asset, coordinated universal time, organized capability, and site delay. According to the counselled calculation, the HMLC strategy is capable of detecting and neutralizing the counterpart's obstructive manoeuvres. Wrongdoing is on the rise, and frameworks must change to keep up. It's common knowledge that transmission should be protected by thorough screening at each restraint point.

III. Energy Proficient Wireless Sensor Network

Intelligent health care frameworks in intelligent transportation systems are becoming increasingly common. IoT sensors are being used to provide period assistance to a wide range of patients. These sensors collect treatment knowledge from patients and send it to the cloud via various remote association strategies. The data is then saved, analyzed, and distributed to UN agencies that provide health care to the community. This study aimed to create a secure and dependable Web-based solution that relied on WSNs to move information between supply and destination junctions in a highly safe and cost-effective manner. The data from the person sensing element is also stored on the server and once verified. It should be sent to the appropriate location. As a result, secure knowledge sharing is crucial for connected network monitoring platforms. WSN security and knowledge assurance are two types of security imperatives.

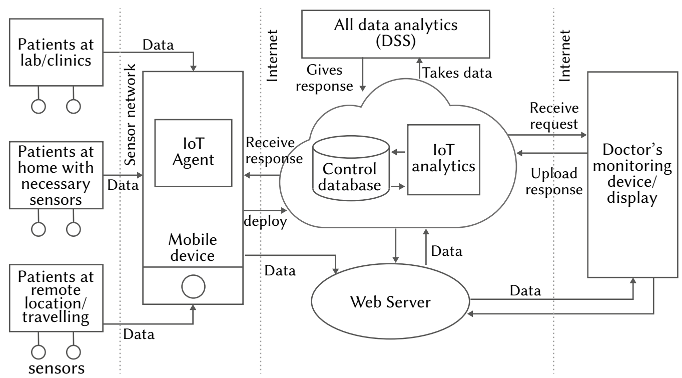

Fig. 1. Block Diagram of Connected Networks.

The IoT care system, on the other hand, is depicted in Fig. 1. The management unit is in charge of overseeing knowledge gathering and exchange. The data is then sent to the cloud over a long-distance medium, such as a Wi-Fi network or a 3G/4G network. Cloud data is communicated with servers during this time to determine their capability. Furthermore, information units are used to store this data temporarily? The information is sent from the servers to the healthcare framework. The recommended method assumes that the WSN display is identical, with N distant device hubs. Even though their location and arrangement are different from neighbour hubs throughout the T time, the prompt technique accepts the arbitrary waypoint show for all single hub quality. In the case of a mounted battery, the framework should replace dead hubs with modern moveable hubs to perform competent WSN activities such as police work information and knowledge transfer. Furthermore, every CHANNEL has agreed to establish each police work hub through mercantilism and deliver information packets containing investigation knowledge (e.g., battery, key, area, ID) to any or all CHANNELS. WSN hubs are always created clusters, with each cluster having its CH. Because CHANNEL can send information, link with other CHANNELS, and prepare information before transmission, the duty of doppelganger location in WSNs is determined by CHANNEL capability. As a result, selecting a conveyable hub that can meet the on-top criterion is critical. This research expects the following highlights for curve-based cluster preparation:

1. To perform the tasks, the CHANNEL should be required to have a high battery level.
2. A CHANNEL should be explicit in a WSN for high-level network and coverage.
3. The chosen CH should be placed near the Stating terminal during preparation.
4. The CH is time-stamped for the chosen space interim.

In an Associate in Nursing IoT-based WSN, clusters are managed in R-radius rings. In general, cluster methodology is used in a very WSN to extend the network's life. It uses sustaining and assembling techniques for CHANNEL selection at every stage of the discovery process. As a result, the tasks of CH are handled by a single distant device hub. The rest of the hub's functions, on the other hand, are incapacity of group allies. CH establishes contact with hub personnel and relays information to the Starting Terminal. It is divided into two parts: structure and adjustment—cluster and CH are provided in the first stage. The hubs have total control over the CH. The allotted CH sends the message due to the mistreatment of the SC-VFS computation. Moveable hubs select the conglomeration controller using the rigid Gotten Flag Quality Sign. The CH creates a Time Division Multiple Access position file for its hubs and assigns a time-defined house to each hub after gathering information and communicating with the cluster. The instant stage begins when you select the cluster and CH. By spreading openings in proportion to the amount, device hubs establish steady-state associations with CH. Moveable hubs, on the other hand, are dormant. CH can begin transferring knowledge to BS once all data from all coupled junctions has been gathered. The majority of previous work on WSN transmittal for leap scope has supported a direct-route arrangement bend. In some cases, a rule-based layout reduces the difficulty and leads to the most efficient resolution. Examine the circumstances in which a rule-based transmission fails for the primary time stress, indicating the need for a spiral-dependent mode.

A. Doppelganger Assault in Remote Sensor Arrangement

A wireless device network is vulnerable to various threats (WSN). The doppelganger attack is a popular type of attack. As a result, it employs villain device junctions that resemble natural device junctions and do not employ proper authorization mechanisms; as a result, this type of attack is difficult to detect. As a result of the fact that energy may be a significant constraint in IoT systems, developing methods to detect doppelganger attacks, as well as the mistreatment of even the tiniest amount of energy, could be a significant challenge.

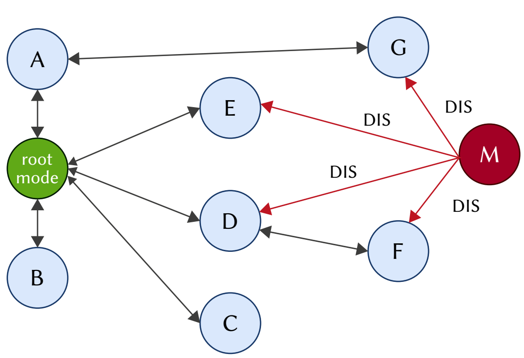

Fig. 2. Shows a Doppelganger Attack on a Wireless Sensor Network.

Fig 2. depicts a doppelganger assault in a very remote detector configuration for a Destination-oriented Coordinated Non-cyclic Chart (DODAG) design. Take a look at **A**pple, **B**ag, **C**atch, **D**rag, **E**ject, **F**ast, and **G**rade, all real-life hubs. Within the arrangement, unused risky hub M duplicates hub B. In a very Direction-Oriented Directed Acyclic Graph (DODAG) system, the hubs may be composition-independent and arrange themselves according to the desired values. This practicality allows nefarious hubs to quickly join the DODAG tree without requiring any authorization strategies. They'll simply imitate a variety of different hubs in various locations. The malicious hub M deduces the layout of the DODAG tree and connects at the first step. During the first stage, the intrepid hub M sends a DODAG knowledge Requesting (DIS) impact message to all or any of its cousins. During this communication, hub B's doppelganger identity is hidden. All other hubs in the arrangement acknowledge hub M in the third step by generating a DODAG knowledge Protest (DIO) management report. In the next stage, the current DODAG topology is rebuilt part M, and data is transmitted while the malicious hub M is displayed. During this method, the remote sensor's hub M organizes a doppelganger ambush.

B. Levels of Doppelganger Assault Discovery in WSNs

In remote detector systems for doppelganger assaults, there are three degrees of location. Any level of discovery could be used to transform an assaulted arrangement into a warranted doppelganger assault-free arrangement. The potency of a doppelganger assault determines the speed with which a harmful activity may begin within the organization. By obtaining the complete information from the memory of a hacked detector junction, including key, character, and communication knowledge, among other things, associate degree admonitory understands the constraints imposed by the detector junction's unsupervised nature. An adviser could most likely duplicate the confiscated moveable hub and re-deploy it to the organization of the targeted site. The message will then use this hacked versatile hub to display and change the various functions.

As a result, it'll be hazardous if the doppelganger hub isn't discovered soon. Fig..3 depicts the degrees of doppelganger assault detection in WSN. At the first level, repeat observation is completed. At this level, group controller hubs (CH) are used to track how frequently moveable hub teams occur.

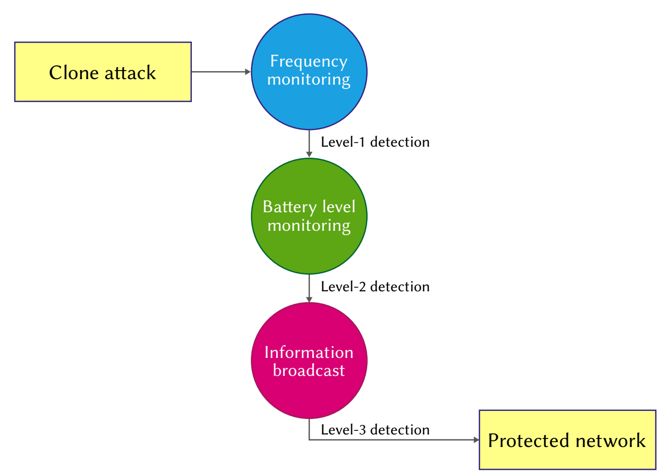

Fig. 3. WSN Doppelganger Attack Detection Levels.

A doppelganger hub is detected if the worth of this repeat is less than a certain threshold. As a result, CH hubs detect doppelganger attacks at the most basic level. The battery levels of the hubs are verified and compared during level-2 discovery. Original hubs have lower battery levels than Doppelganger hubs. This frequently occurs since doppelganger hubs do not appear to be delivered until the first hubs are sent.

Furthermore, the doppelganger hubs have increased battery capacity, allowing for fully organized capture. If two hubs have the same key, the battery level in level-2 discovery is compared in this manner. The secret word is entered, and the hub with the highest battery level is used. The hub is considered a doppelganger junction if the watchword is incorrect.

The CH hubs relay information from the doppelganger hub to the level-3 website's bottom station (BS). The doppelganger hub sends all information to the bottom station. The doppelganger hub will travel around the organization in various clusters. To prevent this, the Bachelor of Science distributes knowledge from the doppelganger junction to various cluster pioneers at the same time.

This doppelganger detection method is used at level three when the organization has completed three steps of positioning and is no longer vulnerable to doppelganger attacks.

C. Steering Convention for Vitality Effective Systems (SC-VFS)

The recommended steering convention aims to increase vitality production. The most disadvantage of the WSN structure is its lack of life. As a result, to differentiate doppelganger assaults, the computation should be designed to be energy economical. Consequently, the planned SC-VFS computation is employed as a guiding convention for steering knowledge using live hubs whereas avoiding doppelganger hub assaults with the smallest {amount} amount of vitality usage. This computation is given in Calculation one. Calculation one is split into three steps. The setup stage happens throughout the primary part. The hub determination stage is the moment step, whereas the consistent stage is the third. The recommended steering convention is meant to extend vitality productivity. The most disadvantage of the WSN structure is its restricted vitality. As a result, to spot doppelganger attacks, the computation should be designed so that it's energy production.

Consequently, the recommended SC-VFS computation is employed as a steering convention for guiding knowledge victimization live hubs while avoiding doppelganger hub attacks with very little energy consumption. This Computation is given in Calculation-1. The primary calculation is split into three components. The setup stage happens throughout the primary part. The hub determination stage is the opening, followed by the steady-state determination stage.

D. SC-VFS Computation

This study created the use of a real-world WSN hub vitality usage demonstration. The presentation considers info coding, transmission management usage, and increased handling capabilities. We tend to study the results of neutering clusters live on the management usage of a CH hub that has been unmarked in the previous analysis. Moreover, compression operations' speed is considered, supported by the affiliation of the made information. It's {an effect an impact an impression a bearing a management a sway} on a CH junction's transmission control dispersion since a CH junction's vitality request show is inaccurate, leading to organize overhead. To the most effective of my data, no preceding distributions have sufficiently cared for this time. Victimization is the advised approach. We tend to compute the vitality distribution of the group controller to work out the entire quantity of vitality saved. Assume that there are T sensors during a configuration. Assume there are n clusters in total. T/n refers to the quality range of hubs per cluster. Every cluster has T/n-1 hubs and a group controller. We tend to assume that every one of those hubs is distributed equally during a PQ-squared space. Contemplate the plunge hub, denoted by the letter atomic number 50. This hub is ready up in the following ways: (X_{SN}, Y_{SN}). contemplate the subsequent scenario: the sender imparts the signal with c. the entire vitality for using the signals to broadcast by sender is indicated at that point by the equation (1):

$$ES_t^{B,D} = B * ES^1{}_t + B * \lambda * D^{\sigma} \quad (1)$$

Here, $ES_t^{B,D}$ describes the significant quantity utilized for different levels of energy by the sender in causation the indictive signal, Number of bits 'B' over a distance D, describes the number of bits within the communicated indicative signal, $ES^1{}_t$ describes the quantity of energy exhausted by the disseminator in transmitting one bit, describes the kind of connected vehicles in between the group controller and additionally the plunge junction, constitutes the whole distance between the group controller and additionally, the plunge junction and additionally the 'r' describes the promulgating factors. the whole energy spent by the receiver junction for the reception of B bits over a distance D is given by the equation (2):

$$ES_r^{B,D} = B * ES^1{}_r \quad (2)$$

Here, $ES_r^{B,D}$ describes the number of energies spent by the receiver inflicting the message B bits over a distance D, constitutes the number of bits at intervals the transmitted message, and $ES^1{}_t$ describes the number of energies spent by the receiver in receiving one bit. the number of energies spent by the group controller for the uploading of the identical signals to any or all the junctions within the network is given by the equation (3):

$$ES_{CH} = ps * ES^1{}_{CH} + ps * \lambda * D^2 \quad (3)$$

Here, ES_{CH} tells the number of strength spent by the group controller for disturbing the same signals to any or all the hubs within the network, ps constitutes the box size within the circulate the disturbing signals, $\lambda-$ tells the kind of channel in between the group controller and also the plunge junction and D tells the whole distance between the group controller and also the plunge junction. $ES^1{}_{CH}$ the number of energies spent by the plunge junction in gathering the distributed signals that are circulated by the group controller is described by the equation (4):

$$ES_s = ps * ES^1{}_s \quad (4)$$

Here, ES_S is the utilized strength by the plunge junction in catching the distributed signals circulated by the group controller, ps constitutes the box size within the circulate the disturbing signals, $ES^1{}_S$ tells utilized strength by the plunge junction for disturbing one pack. The number of utilized strengths by group controller for obtaining the details boxes from different hubs of the controller is described by the equation (5):

$$ES_{CH}{}^{nodes} = ps * ES^1{}_{CH} * (Total/Number - 1) \quad (5)$$

Where $ES_{CH}{}^{nodes}$ is the utilized strength needed for the group controller for accepting information from group hubs, ps constitutes the box size within the circulate the disturbing signals, $ES^1{}_{CH}$ tells utilized strength by the plunge junction for disturbing one pack and $(Total/Number - 1)$ is the total range of junctions in every cluster excluding the cluster controller.

The average distance in between the group controller and the sole junctions present in that specific section is given by the equation (6):

$$ES_{CH}{}^{nodes} = \frac{(1/2\pi)*(P*Q)}{(T/N-1)} \quad (6)$$

Where $ES_{CH}{}^{nodes}$ is the average distance between the group controller and the sole junctions present in that specific group, $(P*Q)$ is the total area of the junction distribution and $(T/N - 1)$ is the total range of junctions in every cluster excluding the cluster controller. The total energy drained by the group controller is given by the equation (7):

$$ED_{CH} = ps * ES^1{}_{CH} * (T/N - 1) + ps * \lambda * D^2 \quad (7)$$

ED_{CH} is the total energy radiating by the group controller, ps describes the box value, $ES^1{}_{CH}$ describes the amount of energy required by the group controller junction in receiving a sole section and $(T/N - 1)$ is the total number of junctions in each group excluding the group controller, describes the type of channel in between the group controller and the plunge junction and D describes the total distance between the group controller and the plunge junction. The total energy radiating by the individual member of the cluster is given by the equation (8):

$$ED_{node} = \frac{B*ES^1{}_{node}+B*\lambda*D^{\sigma}}{(T/N-1)} \quad (8)$$

Here, ED_{node} describes the total energy drained by the individual member of the cluster, B describes the number of bits in the message sent by each junction, $ES^1{}_{node}$ is utilized strength used for one-bit information sent, λ describes the type of channel in between the group controller and the plunge junction, D describes the total distance between the group controller and the plunge junction and the σ describes the propagation constant. Thus, the total energy conserved using the proposed algorithm is given by the equation (9):

$$E_{saved} = ED_{CH} - ED_{node} \tag{9}$$

Where E_{saved} is the total energy stored using the proposed algorithm, ED_{CH} is the total energy drained by the group controller, and ED_{node} describes the total energy drained by the individual member of the cluster. It is also represented by the equation (10):

$$E_{saved} = \left[ps * ES^1{}_{CH} * \left(\frac{T}{N} - 1\right) + ps * \lambda * D^2\right] - \left[\frac{B * ES^1{}_{node} + B * \lambda * D^\sigma}{\left(\frac{T}{N} - 1\right)}\right] \tag{10}$$

Algorithm with Calculation:1

/* ***Discovered Stage*** */

1. *formatting of n clusters*
2. *for i=1: n*
   a. *cypher means a position of the cluster as Mi*
      i. *For j=1: ki /* ki refers to a range of junctions within the cluster i */*
      ii. *cypher distance of every junction from the cluster means position as dij*
   b. *end for*
3. *determine initial group controller as ICHi*
4. *turn out the TDMA schedule*
5. *Transfer the group controller and TDMA schedule to every junction*
6. *end for /* Junction choice part */*
7. *for r=1: R /* R refers to a range of rounds */*
   a. *for i=1: n*
      i. *For a=1: Ai /* Ai refers to a range of alive junctions */*
      ii. *cypher the residual energy*
      iii. *Send the residual energy data*
   b. end for

/* ***Steady-state part*** */

8. *for i=1: n*
   a. *for j=1: I /*ki refers to a range of junctions within the cluster i */*
   b. *cypher alive junction with the highest energy as W1*
   c. *cypher alive junction with second highest energy as W2*
   d. *end for*
9. *Send W1 and W2 to every junction within the cluster*
10. *The doppelganger threat is detected average between W1 and W2 abnormal situation*
11. *Impulsive threshold stetted worth by letter (ζ)*
12. *letter (ζ) describes doppelganger removal*
13. *Re-compute the group controller supported W1 and W2*
14. *cypher higher than steps until Connected Networks finish*
15. *end for*

The whole energy saved is given by Fig. 4.

IV. Validation of Performance

This section contains many MATLAB 2018 program results. The search situation necessitates using MATLAB laptop code as a communication and remote device tool repository. The MATLAB program was designed to replicate the subsequent discoveries and graphs. To protect Wireless networks from doppelganger attacks, the quick SC-VFS computation evaluates victimization's many characteristics such as latency, leftover vitality, work rate, vitality effectiveness, and inaccuracy. WSN productivity for the IoT network

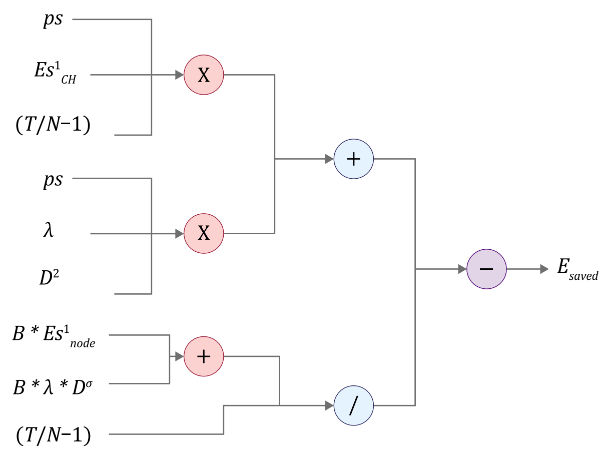

Fig. 4. Energy saved using proposed SC-VFS Computation.

is also boosted by group position safe leading conventions. SC-VFS has the potential to be a powerful clustering-based leadership system. Every circle, cluster and CH are chosen at random. When selecting CHs, the additional power of the device hubs is overlooked. WSN hubs with lower remaining vitality are also chosen, which impacts the setup process. The planned method evaluates critical viewpoints labelled as true or false positives. A true positive could be a doppelganger who was successfully identified; an untrue positive could be a doppelganger who was not identified. Bit by bit, the counselled risk recreation is administered. All of the doppelganger location aggregation occurred on time. Its worth indicates that as the amount is carried, real positives increase. The primary step is to obtain permission and distinguish between proof of abnormalities at cluster to characterize the hazard discovered due to the planned technique containing multiple steps to find doppelgangers. It is considered repeatable to calculate the speed of similitude of the outputs at entirely different times with ambiguous input values. The CHs can ensure alternative Centre points that they must be elite because of the CH for this cycle based on their choice. To complete this task, each CH Centre can use the advised technique to deliver an acceptable hail to the opposite Centre. Every CH Centre, every support Centre decides whether or not to assist in a startup and supports the focused movement of the message equipped by the bachelor's degree. The group controller is chosen based on flag escalated premise due to the prompt response implementing the contemporary to a physical phenomenon. This indicates that not all WSN hubs are included in the cluster formation method. When the CHs provide total distributing controlled data, the hub closest to the CH decides to link the bunch, during which the CH provides the hubs with the most straightforward flag. After deciding which CHANNEL can link the gather, every hub closer to the CH should notify the CH that it has joined the gather as an organizing element. Every hub closer to the CH sends an entry bundle (JN-Request) to the CH of their choice, along with each junction's and thus the CH's IDs. The transmission of vital moveable hubs in the web of things systems is depicted in Fig. 5. This diagram introduces eleven hubs that are of high quality. The letter BS designates the bottom station hub. Despite a wide range of curve-based preparation options, most recently generated inquiries have focused on causing straight structure. A large-scale array of remote sensors has been transmitted for the first time. As a result, the device transmission process is divided into two stages:

1. Identifying the leading device areas on the curve,
2. Establishing a proper arrangement curve

Because of the unusual arrangement, it's difficult to persuade the proper configuration bent. We usually look for the ideal situation to react to your address. This resulted in such a long bend in response to the question, and it was planned as a way for winning device transmission once the usage bend is separate steady, and still as a way for productive and correct device setup once it isn't. Fig. 6 shows the location of fifty hubs within the unique WSN structure. A 250-meter hub run is contained within a single quadrant. Hub one is the transmittal base station, while Hub two is the collection base station. The data bundles are sent from Hub one to Hub two. The data transmission pathways are depicted in Fig. 5. One of the WSN constraints is the energy consumption of reversible battery device hubs, which has an impact on the overall system's lifespan and, as a result, their use in various traffic and surveillance-transport sectors, as well as traffic-environmental reasons. Predicting how long something will last in natural applications is one of the most challenging aspects of delivering.

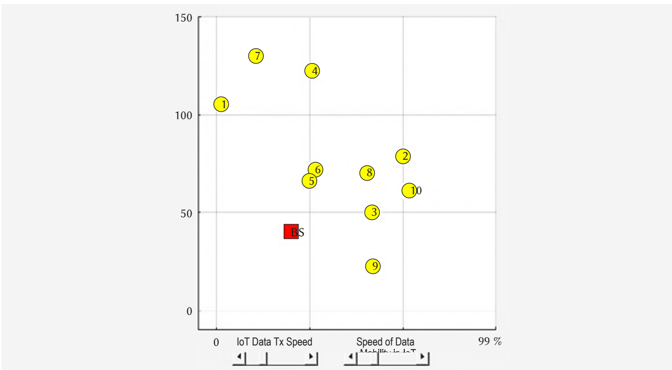

Fig. 5. Straightforward quality junctions for Connected Networks.

Lifetime addresses how to reduce device hub power usage by prolonging the time until one of the device hubs reaches the end of its life cycle. The well-being and natural suggestions are investigated to carry out the check. Finding device hub locations that improve scope and continuity is quite challenging under these circumstances. WSN has the most in-depth understanding of the situation. Because device setup and battery replacement are both resource-intensive, deploying WSN with as few sensors as possible while maintaining scope and continuity is critical.

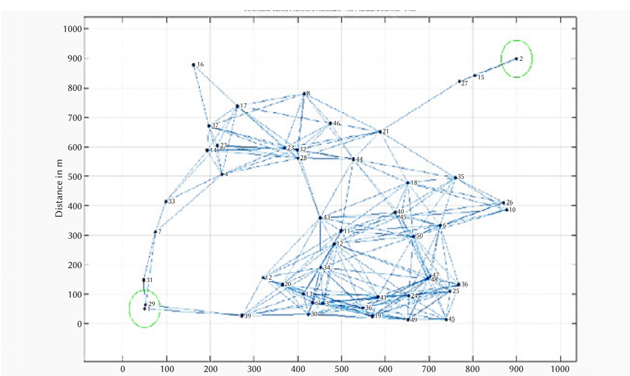

Fig. 6. Junction varying environment in Connected Networks.

The IoT guiding route with a flexibility path pair is shown in Fig. 7. There are two options for non-mandatory courses, as this example demonstrates. The total number of bounces in this scenario is eight. The Base Station Transponder sends out a total of 4736 packages. A total of four hubs have perished due to the doppelganger assault. By changing the doppelganger assault to '1 -> 29 -> 7 -> 4 -> 22 -> 21 -> 27 -> 2', the directing hubs were located. Flexible hubs send the total number of messages during a linked network. If hubs receive and transmit data through messages, the total communication overhead in a WSN is one N, and CH should dispatch every message. The counselled technique has a lower overhead than earlier methods. This often occurs because the possible hypothesis plan is developed on a cluster, and each hub must provide information to CH. The number of totally utilized hubs is also proportional to O(N).

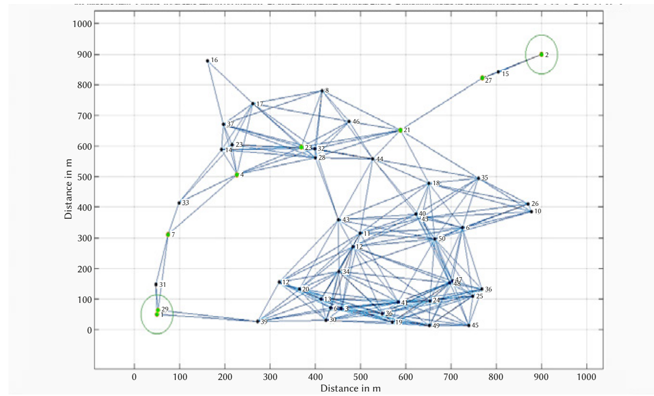

Fig. 7. Selective Route-2 in Web of things.

The CH has its claim line for a comparable estimate, including data from all participating (i.e. N) hubs. As a result, as previously stated, the capability overhead for checking battery voltage is O(N); nevertheless, the capability overhead for a variety of esteems is O (1). (i.e., one signifies the settled total of checks). Consequently, the calculable capability overhead of the suggested technique is O. (N). The CH and hubs are switched off until broadcasting time is available to conserve electricity. The CH organization should be imposed on any hub that will be causing knowledge. When non-CH hubs are latched, they transmit information to the CH, which gathers it and sends it to the BS. As a consequence of the most effective strategy"> the greatest way to share information is to reduce organize expectancy; one knowledge transmission process may reduce hub vitality utilization. As a result, a method of lo wering takeaway using a single bounce, multi-hop, and composite organizing style is shown. The IoT steering route with flexibility path four is shown in Fig. 8. There are four options for non-mandatory courses, as seen in this example. The BS-Transponder receives and transmits a total of 5368 bundles. Consequently, a larger number of packets are sent more quickly in this situation. The doppelganger assault has claimed the lives of twenty-seven hubs. By retaining a strategic distance from the doppelganger assault, the steering hubs were revealed to be '1 -> 39 -> 3 -> 11 -> 18 -> 21 -> 27 -> 2'.

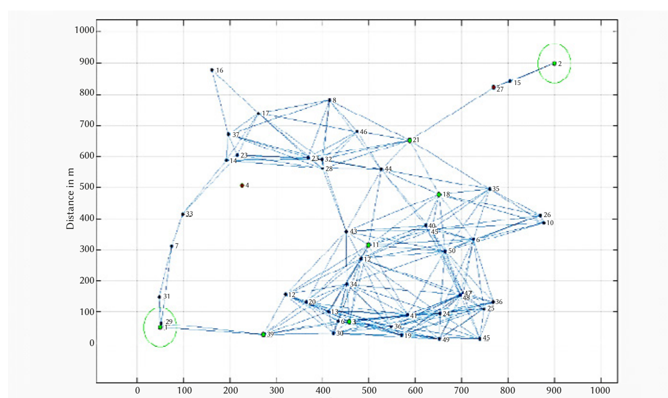

Fig. 8. Selective Route-4 in Web of things.

With dead hubs, the proposed SC-VFS approach achieves still another highly nickel-and-dime delay. By avoiding doppelganger attacks, the proposed approach achieves the least delay. For a fifty hubs victimization doppelganger attack with twenty dead hubs and ten dead hubs, respectively, the latency is 1.1ms and 0.9ms. With dead hubs, our HMLC strategy achieves latencies of 0.85ms and 0.81ms and retains a strategic distance from doppelganger assaults. The proposed approach produces a temporal delay of zero.63ms and 0.6ms, respectively, with no dead hubs and no doppelganger attack. Victimization is another critical factor to consider; the preferred strategy for doppelganger localization is liveliness since counselling requires some management to degree and directs the WSN.

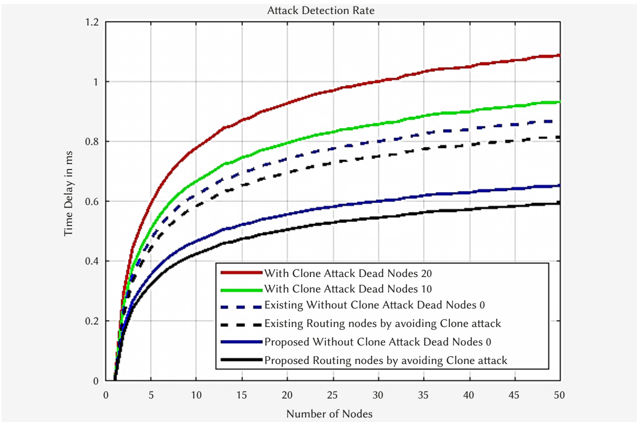

Fig. 9. Time latency for Different Junctions.

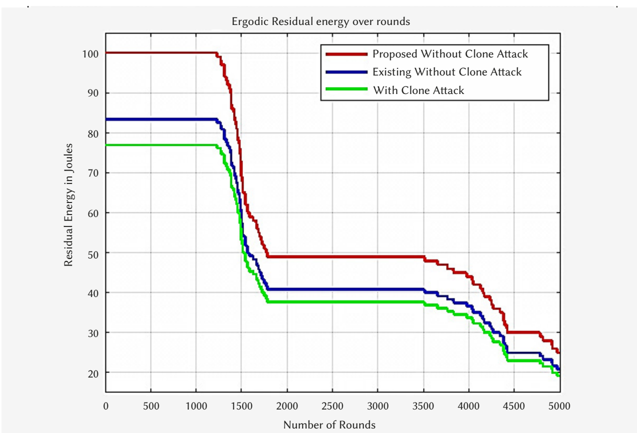

Fig. 10. Strength of Residual Vs Round Junctions.

Because the number of cycles will rise, Fig. 10 displays residual vitality changes. With doppelganger attack, the inflated vitality is about 38.2 J for 2500 rounds. The HMLC approach's increased vitality for an analogous 2500 rounds is forty.8J. For the 2500 cycles, the recommended approach produces the maximum remaining vitality of 49.5 J. As a result, we learn that the intended approach has the least remaining viability.

Outturn is another crucial statistic for evaluating the productivity of a guiding framework. Will expanding the number of generating packages available at the supply hub result in output growth? On the other hand, more prominent groups may induce more excellent bundle formation rates. Consider a 100-joint setup. If there are five clusters and each cluster has an increment of 30 distant hubs, the estimated handling time for a hub to talk its information to a group controller associate degree log is analogous to 19- or 21 openings under the intended approach. If the phantom effectiveness/efficacy is four packets per second, one cycle will take at least 30/6 = 5-seconds to complete. Fig. 11 depicts the variance in output as a function of the number of device hubs.

The relationship between vitality efficiency and the number of device hubs is shown in Fig. 12. With a doppelganger assault, the vitality productivity for fifty hubs is almost 150.33 Mbps/Hz. Using the display HMLC calculation, the energy efficiency for an analogous fifty hubs is 281.4 Mbps/Hz. For the fifty hubs, the proposed Computation has the highest vitality effectiveness of 401.3 Mbps/Hz. As a result, we learn that the suggested computation takes into account a cow vitality potency.

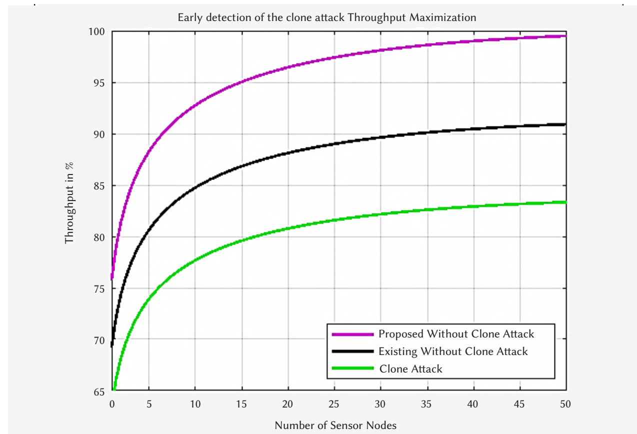

Fig. 11. Outcome of the Proposed Algorithm on Junctions.

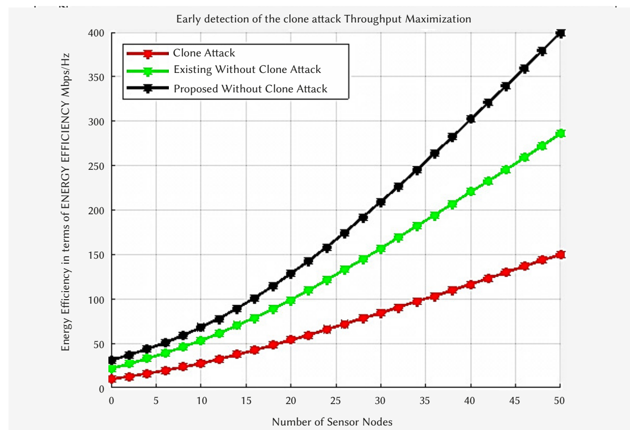

Fig. 12. Energy Variation vs No. of Connected Devices.

As seen in Fig.13, the error rate varies depending on the number of device hubs. Because the number of device hubs rises, the error rate decreases. For a total of five device hubs, the display HMLC approach has a 0.06 slip rate. The intended solution has a 0.043% slip rate for an equal five hubs. The display and recommended frameworks blunder rates were 0.27, and 0.21, respectively, for ten hubs.

As a result, the error rate associated with the proposed framework is the lowest. As seen in Fig. 13, the error rate varies depending on the number of device hubs. Because the number of device hubs rises, the error rate decreases. For a total of five device hubs, the display HMLC approach has a 0.06 slip rate. The intended technique has a 0.043 slip rate for an equivalent five hubs. The display and recommended frameworks had blunder rates of 0.27 and 0.21, respectively, for 10-hubs. As a result, the error rate associated with the proposed framework is the lowest.

A. Benefits of the Planned Methodology

To begin with, the intended strategy offers the benefit of police investigation doppelganger attacks promptly. The suggested approach reduces time by having a lightweight structure that uses less energy. Another crucial advantage is that the aggressor is isolated from the organization, which prevents the aggressor from becoming intrusive with the organization's operations.

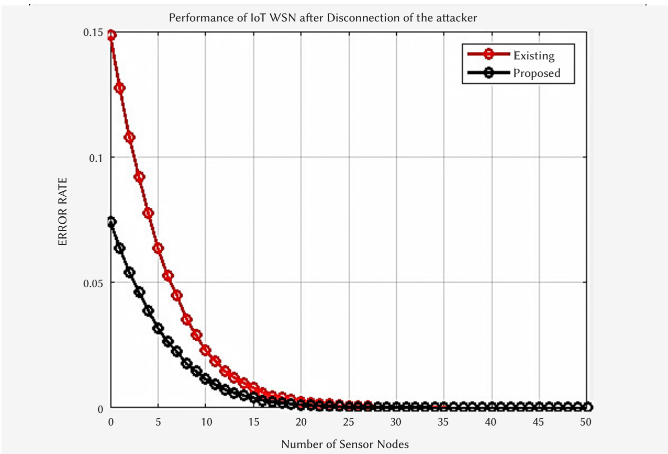

Fig. 13. Accuracy Rate.

V. Conclusion

We provide a novel approach for police investigation doppelganger attacks in remote sensing systems during this work. The various levels of doppelganger ambush detection were outlined. The 3 stages were: repeat checking, battery level detection, and information broadcast. Moreover, SC-VFS was designed for the vibrant -structured steering of bundles information related to connected networks of vehicles applications. The suggested approach was divided into 3 stages: setup, hub choosing, and consistent state. The framework was tested with fifty hubs placed randomly in places. In 2 items, the guiding way was determined: moveable path two and moveable path four. The urged Computation had the very best vitality effectiveness of 401.3 Mbps/Hz for the 50 hubs. Moreover, over 10 hubs, the blunder rate for the conventional HMLC method, and the up-to-date SC-VFS strategy were committed to being 0.27 and 0.21, majorly. Consequently, the recommended approach obtained better vitality efficacy while having an all-time low error rate.

Funding: Not applicable.

Conflicts of interest Statement: Not applicable.

References

[1] E.F.A. Elsmany, M.A. Omar, T.C. Wan, A.A. Altahir, EESRA: energy efficient scalable routing algorithm for wireless sensor networks, IEEE-Institute of Electrical and Electronics Engineers Access 7 96974–96983, 2019.

[2] W. Zhang, D. Han, K. C. Li and F. I. Massetto, "Wireless sensor network intrusion detection system based on MK-ELM," *Soft Computing*, vol. 24, no. 16, pp. 12361–12374, 2020.

[3] M. Adil, M. A. Almaiah, A. O. Alsayed, and O. Almomani, "An anonymous channel categorization scheme of edge junctions to detect jamming attacks in wireless sensor networks," *Sensors (Switzerland)*, vol. 20, no. 8, pp. 1–19, 2020.

[4] J. John, P. Rodrigues, "Multi-objective HSDE Algorithm for Energy-Aware Group controller Selection in WSN," *Journal of Networking and Communnication Systems*, vol. 2, no. 3, pp. 20–29, 2019.

[5] S. Aljawarneh, M. Aldwairi, M.B. Yassein, "Anomaly-based intrusion detection system through feature selection analysis and building hybrid efficient model," Journal of Computer Science, vol. 25, pp. 152–160, 2018.

[6] N. T. Tam, T. Q. Tuan, H. T. T. Binh, A. Swami, "Multifactorial evolutionary optimization for maximizing data aggregation tree lifetime in wireless sensor networks," in *Artificial Intelligence and Machine Learning for Multi-Domain Operations Applications,* volume-II, pp.114-130. 2020.

[7] M. Safaldin, M. Otair and L. Abualigah, "Improved binary gray wolf optimizer and SVM for intrusion detection system in wireless sensor networks," *Journal of Ambient Intelligent and Humanized Computing*, vol. 12, no. 2, pp. 1559–1576, 2021

[8] A. Mazinani, S.M. Mazinani, M. Mirzaie, "FMCR-CT: an energy-efficient fuzzy multi cluster based routing with a constant threshold in wireless sensor network," *Alexgdenra Engeerring Journal*, vol. 58, pp. 127–141, 2019.

[9] Z. Wang, C. Zhou, Y. Liu, "Efficient Hybrid Detection of Junction Replication Attacks in Mobile Sensor Networks," *Mobile Information Systems*, pp. 1-13, 2017.

[10] I. Qasemzadeh Kolagar, H. Haj Seyyed Javadi, M. Anzani, "Hypercube bivariatebased key management for wireless sensor networks," *Journal of Science of Networking*, vol. 28, no. 3, pp. 273-285, 2017.

[11] Q. Yu, L. Jibin, L. Jiang, "An improved ARIMA-based traffic anomaly detection algorithm for wireless sensor networks," *International Journal of Distributed Sensor Networks*, vol. 12, no. 1, 2016.

[12] D. Tian et al, "A microbial inspired routing protocol for VANETs,'' *IEEE Journal of Internet Things,* vol. 5, no. 4, pp. 2293-2303, 2018.

[13] K. Stepien, A.P. Poniszewska-Maranda, "Security Measures in Vehicular Ad-Hoc Networks on the Example of Bogus and Sybil Attacks," *Advanced Information Networking and Applications*, vol. 1151, Springer, Cham. pp. 419–430, 2020.

[14] R. Fotohi and S. Firoozi Bari, "A novel countermeasure technique to protect WSN against denial-of-sleep attacks using firefly and Hopfield neural network (HNN) algorithms," *Journal of Supercomputing*, vol. 76, no. 9, pp. 6860–6886, 2020

[15] M. Numan, "A Systematic Review on Doppelganger Junction Detection in Static Wireless Sensor Networks," *IEEE Access,* vol. 8, pp. 65450–65461, 2020.

[16] C. Hongsong, M. Caixia, F. Zhongchuan and C. H. Lee, "Novel LDoS attack detection by spark-assisted correlation analysis approach in wireless sensor network," *IET Information Security,* vol. 14, no. 4, pp. 452–458, 2020.

[17] J. Cui, L. Wei, J. Zhang, et al., "An efficient message-authentication scheme based on edge computing for vehicular ad hoc networks,"*IEEE-Transction. on Intelligent Transportation Systems*, 1–12, 2018.

[18] A. Boualouache, S. Senouci, and S. Moussaoui, "A Survey on Pseudonym Changing Strategies for Vehicular Ad-Hoc Networks," *IEEE Communications Surveys & Tutorials, vol. 20, no. 1,* pp. 770–790, 2018.

[19] R. W. van der Heijden, S. Dietzel, T. Leinmüller and F. Kargl, "Survey on Misbehavior Detection in Cooperative Intelligent Transportation Systems," in *IEEE Communications Surveys & Tutorials*, vol. 21, no. 1, pp. 779-811, Firstquarter 2019, doi: 10.1109/COMST.2018.2873088.

[20] M. Ikeda, L. Barolli, "Performance of optimized link state routing protocol for video streaming application in vehicular ad-hoc networks cloud computing," *Concurrency and Computation Practice and Experience,* vol. 27, no. 8, pp. 2054–2063, 2015.

Deepak Choudhary

Mr. Deepak Choudhary Ph.D. Research Scholar at the NITJ having the 15-years of the teaching experience and nine years of experience in industry. He has published the many papers in SCI and SCIE journals and International conferences. His area of internet is WSN and IoT application in WASNET, MANET AND HYBRID WBAN and VANET APPLICATIONS ON IOT USING DL AND ML Techniques. His recent research is focused on anomaly detection in the intelligent transportation system.

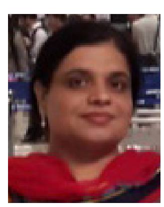

Roop Pahuja

Dr Roop Pahuja working as Associate Professor in NIT, having more than 20 years of experience in Teaching, her area of interests is in VI-Applications and wireless network, Image Processing & Machine Learning.

A Security Situation Awareness Approach for IoT Software Chain Based on Markov Game Model

Xudong Zhu[1], Honggao Deng[2] *

[1] Wuxi Vocational Institute of Arts & Technology (China)
[2] Guilin University of Electronic Technology (China)

Received 13 December 2021 | Accepted 13 June 2022 | Published 1 August 2022

Abstract

Since Internet of Things (IoT) has been widely used in our daily life nowadays, it is regarded as a promising and popular application of the Internet, and has attracted more and more attention. However, IoT is also suffered by some security problems which seriously affect the implementation of IoT system. Similar to traditional software, IoT software is always threated by many vulnerabilities, thus how to evaluate the security situation of IoT software chain becomes a basic requirement. In this paper, A framework of security situation awareness for IoT software chain is proposed, which mainly includes two processes: IoT security situation classification based on support vector machine and security situation awareness based on Markov game model. The proposed method firstly constructs a classification model using support vector machine (IoT) to automatically evaluates the security situation of IoT software chain. Based on the situation classification, we further proposed to adopt Markov model to simulate and predict the next behaviors of participants that involved in IoT system. Additionally, we have designed and developed a security situation awareness system for IoT software chain, the developed system supports the detection of typical IoT vulnerabilities and inherits more than 20 vulnerability detection methods, which shows great potential in IoT system protection.

Keywords

Internet of Things, Markov Game Model, Security Situation Awareness, SVM, Vulnerability Detection.

DOI: 10.9781/ijimai.2022.08.002

I. Introduction

With the wide application of the Internet and the continuous development of information technology, Internet and software are heavily involved in our daily lives [1], [2]. However, simple informatization and technologies can no longer satisfy people's requirements [3], [4], [5], so that the Internet of Things (IoT) has emerged at this historic moment [6], [7].

As the extension of the Internet, IoT cannot be separated from the support of the software chain [8], [9], and with the continuous development of the software chain, its security problems have become increasingly severe [10]. In a complex environment, the software chain (refers to an IoT software system that is composed of a series of firmware, device drivers, system software and application software) has become the focus of IoT security [1], [6]. Especially in battlefield environment, the security of the IoT software chain can often affect the evolution of a war, and even determine its outcome [11], [12].

The security situation awareness [13], [14], [15] is built on an effective vulnerability classification method and some mature dynamic security enhancement technologies. Security situation awareness is regarded as a process of cognition of the system security status [13]. There are some commonly used technologies to support this process, including the fusion processing of original data measured from the system [16], the extraction of the background status and activity semantics [17], the identification of various network activities and abnormalities [18]. According to the above methods, the system's security status could be greatly learned. However, for IoT software chain, these works could not be simply implemented due to the complexity of the IoT environment [7], [19], [20]. An IoT system always accessed by many devices of different types. they may use different communication protocols, different information formats and have different behaviors. Apparently, it is very hard to summarize and analyze a large amount of collected information, so that the security situation awareness for IoT system is a challenging and worthwhile topic [21], [22], [23].

In this paper, we propose to implement Markov game model [24], [25], [26] with support vector machine (SVM) [27], [28], [29] to realize the security situation awareness of the IoT software chain, aim at analyzing and understanding the security-related elements of IoT software system, thus to perceive current security status and predict future security situation. The Markov game model is established by game theory, and has been long implemented in network security. Markov game model simulates the possible behaviors and analyze the rewards of the behaviors to address the attack defense problem, thus obtaining optimal strategy. Different as the Markov game model implementation in network security, IoT software chain contains many real device nodes. To be specific, it is to detect, extract, understand, evaluate, and predict the security elements that affect the IoT software chain. Note that the "situation" reflects the possible development tendency and complex software environments which formed by the interaction of various system conditions, rather than a certain system

* Corresponding author.

E-mail addresses: zhuxudong08@126.com (X. Zhu), 32465448@qq.com (H. Deng).

condition or phenomenon. Commonly, the situation consists of two parts, one is the "state", which refers to the overall current status quo, obtained by evaluating the information and incidents, thus determining the authenticity, type, characteristic and hazard of an attack. Another part is "tendency", which to the overall development trend. We conduct an in-depth analysis of the attack incidents within a unit of time to find out the various stages and steps of an attack. With the Markov game model, many behaviors in the IoT network could be greatly quantified, thus to select the best solution according to established rules, so that the evolution trend of both the offensive and defensive could be predicted, thereby improving the security of the IoT software chain.

The main contribution of our research is twofold:

(1) We have proposed an IoT security situation awareness method within two parts. We first utilize SVM to classify multiple security situations. And then, based on the security classification method, we have further proposed to use Markov game model to simulate three participants and predict their next behaviors in IoT system.

(2) The proposed two methods above are integrated to develop a useable system to perceive the security situation of the IoT software chain and provide guidance.

The remainder of this paper is organized following: The research background and the related work of security situation awareness is presented in Section II. Section III serves to introduce the framework of the proposed method, and detail the specific process of 1) IoT security situation classification based on support vector machine and 2) security situation awareness based on Markov game model. Additionally, Section III also describes the module designs and deployment. The experiments and results are discussed in Section VI. Finally, we have the conclusion in Section V.

II. Background and Related Work

The security issues of the IoT have received extensive attention from the research community and have been resolved at different levels. Yang et al. [30] investigated the security and privacy issues of the IoT and they emphasized the limitations of applying security in IoT devices. Also, they summarized the classification of IoT attacks (such as physical attacks, remote attacks, local attacks, etc.). Moreover, they analyze different levels of IoT security issues and propose corresponding solutions. Kumar et al. [31] discussed the security issues at each layer of the IoT three-tier architecture, and investigated most of the security flaws, which are caused by various communication technologies used in wireless sensor networks. In order to ensure that only legitimate users are controlled and authorized, Kalam et al. [32] proposed an authorized access model as a security framework for IoT. However, current research on IoT security does not pay enough attention to software chain. Since IoT is more vulnerable to attacks, especially in a confrontational environment. Therefore, the security threats detection, threats addressing, and security strengthen for IoT software chain matter significantly nowadays.

The concept of cyberspace situation awareness was first proposed by Bass et al. [33], and they had pointed out that "fusion-based network situation awareness" will surely become the discovery of the development of network management. After that, Endsley et al. [34] gave a definition of the network security situation, believing that it includes acquiring, understanding and displaying of security elements which significantly influence on network situation, and future trends prediction, in a large-scale network environment. Franke et al. [35] regarded cyber security situation awareness as a subset of situation awareness, which mainly focuses on network security according to IDS alerts and vulnerability information. Network security situation awareness commonly applies some situation awareness methods to network security [36], enabling personnel to have a macro grasp of the security status of the entire network in a dynamically changing environment, and to provide decision-making support for senior managers.

Current researches [14], [37], [38] on cyber security situation awareness mainly focus on three levels, including situation perception, situation comprehension, and situation projection. Situation awareness identifies all activities in a system (including attack activities) and their features and characteristics. The related methods can be roughly classified into two categories according to whether prior knowledge is used. For situation understanding [39], it identifies attack activities and their characteristics. Additionally, by analyzing the semantics relationships of attack activities, situation understanding could infer the attacker's intentions. Currently, situation understanding mainly starts from two aspects [39], that is, attack behavior prediction and attack purpose understanding. The purpose of situation projection is to assess the hazard and the potential threats that have appeared to the managed network based on the identified attack activities. Current researches [40], [41] commonly concentrate upon knowledge-based reasoning situation projection, situation projection based on statistical analysis and gray-scale theoretical situation projection.

There are still many challenges to the network security situation awareness [42], such as the fusion of massive heterogeneous measurement data, activity identification under incomplete information conditions, semantic calculation of network activities, visualization of network situation, and network security collaboration of situation awareness etc.

III. Approach

In a complex environment, changes in the IoT software chain at any time may affect the entire security situation. In this paper, we propose an IoT security situation awareness technology based on the Markov game model with support vector machine (SVM). By assessing the current state of the IoT software chain and evaluating participants' behaviors, the proposed approach can provide useful guidance for users.

A. Framework

The framework of our method is shown in Fig. 1, includes two main procedures: IoT security situation classification based on support vector machine and security situation awareness based on Markov game model.

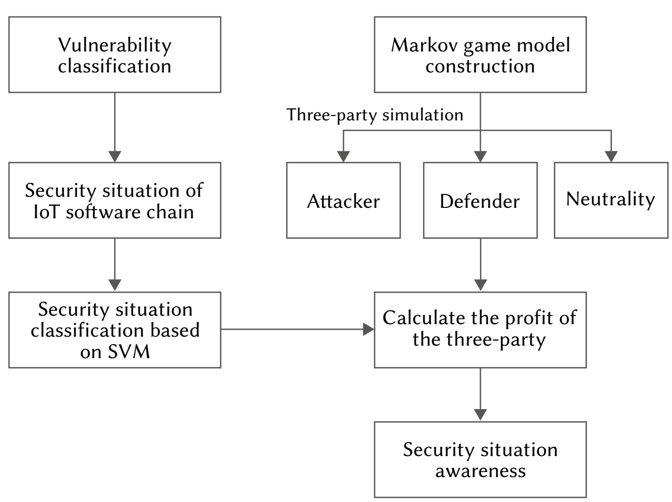

Fig. 1. Framework of the proposed method.

Commonly, there are often three objects in the game model, namely "attacker", "defender", and "user". The attacker's purpose is to attack the vulnerability of the system and cause the IoT system to malfunction or even destroy. While the defender implements reinforcement schemes to improve system security and reduce the damage caused by potential threats. For users, they are about the status of the IoT system.

We firstly construct a classifier to automatically classify the security situation based on SVM. After that, in the simulation game, we record the state of the IoT software chain at different times. At the same time, we calculate the probability of what actions the participants may take, based on the state changes caused by different behaviors. Finally, we calculate the benefits of the three parties in the game under different strategies. After completing the above steps, the Markov game model can be constructed to learn threats to the IoT systems, thus the defenders can draw up the best reinforcement scheme.

B. IoT Security Situation Classification Based on Support Vector Machine

1. Security Situation Classification

The IoT security situation classification is constructed based on vulnerabilities analysis of the IoT software chain. Specifically, we first conduct an in-depth analysis of the threats or vulnerabilities in IoT software chain, and classify them into some categories. After that, by referring to the national response plan for public emergencies, the security of the IoT software chain is classified into 5 levels according to the characteristics, hazards, and the status changes of the vulnerabilities in a IoT software chain. For convenience, the security situation of IoT software chain is quantitative described ranging from 0 to 1. The detailed classification is shown in Table I.

TABLE I. Classification of IoT Security Situation

Security score	Security level	Description
0.0~0.2	safe	The entire software chain is operating normally, no threat behavior that beyond perception, no severe vulnerabilities.
0.2~0.4	mild danger	The overall operation of the software chain is slightly affected by a few vulnerabilities, the malicious behaviors are a little active.
0.4~0.6	danger	The software chain is affected, with some security vulnerabilities in a higher threat level. And it has a high possibility that causes major damage.
0.6~0.8	severe danger	A large scale of serious attack has been found in the software chain, along with many security vulnerabilities, and the malicious behaviors are active.
0.8~1	extreme danger	The software chain has been severely damaged, malicious attacks are very active, which could cause a variety of service interruptions and endanger critical infrastructure.

2. SVM Implementation

To better realize the security situation awareness of IoT software chain, the SVM is additionally adopted in our method. In practice, we utilize SVM to classify the security level of security situations under different cases (different vulnerabilities and threats). The specific process is shown in Fig. 2.

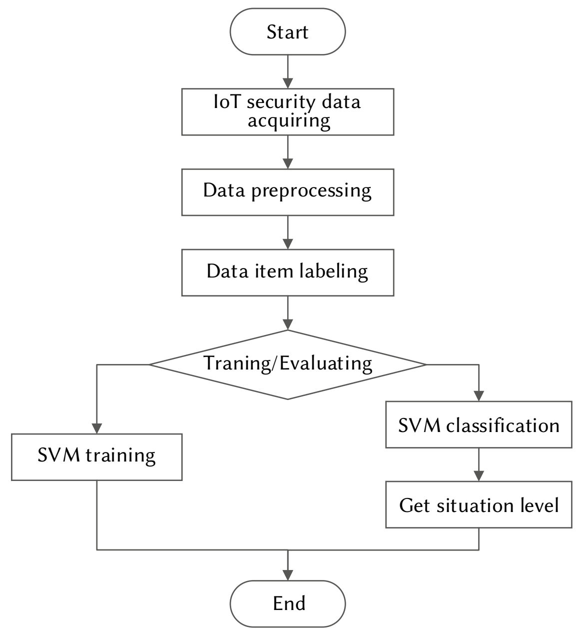

Fig. 2. The SVM implementation in IoT security situation classification.

The guided information for IoT security situation awareness is acquired from Snort's intrusion detection system, firewall and X-Scan vulnerabilities, which are detailed as follows.

Snort data item. Snort is a real-time traffic analysis tool based on libpcap, which can effectively record IP data packets. The acquired data are: activity, protocol, source, destination address, destination port, generation time of alarm and alarm level, etc.

Firewall data item. The firewall can record the network communication between internal and external networks, and effectively protecting the internal network. The acquired data are: source and destination addresses, destination ports, protocol type, duration, sent bytes, received bytes, and behavior, etc.

X-Scan data items. X-Scan mainly performs vulnerability scanning and security level assessment. The following data are acquired by scanning the specified IP, that is, the type and version of operating system, port status, port BANNER, CGI vulnerability, IIS vulnerability, and RPC vulnerability etc.

Due to the complexity of the IoT software chain, the acquired data may be complex or have diverse characteristics. Therefore, the following indexes are added below to better determine the security situation of IoT system.

Continuous alarm time. Suppose that at time t the alarm is alerted, and suspended until $t+n$ time, the continuous alarm time is defined as Equation(1):

$$\mathrm{IP\_}n = \sum_{i=1}^{n} D_i^S \cup D_i^f \cup D_i^x \tag{1}$$

where n is a continuous time interval, D_i^S is the alarm information captured by Snort at time i, D_i^f represents the operational alarm behavior captured by the firewall at time i, and D_i^x is the vulnerability alarm information captured by X-Scan at time i. The addressing range of n is $[0, +\infty]$, if on alarm is captured, n is set as 0.

Vulnerability risk value. Suppose that in a fixed time period s, the sequence of vulnerabilities captured from the detection is $L = \{L_1, L_2, L_3, \dots, L_n\}$, and the risk that the vulnerability may be exploited in s is $T = \{T_1, T_2, T_3, \dots, T_n\}$, then the vulnerability risk value is defined as:

$$\mathrm{T_n} = \sum_{i=1}^{m} L_n | W_i \tag{2}$$

where m is the amount of network data captured, and W_i is the damage level of vulnerability form L_n in the captured network data.

For convenience, we normalize all the above training data to [0,1], using the following formula:

$$\mathrm{F}(i) = \begin{cases} \frac{D_i}{100}, D_i < 100 \\ 1, D_i \geq 100 \end{cases} \tag{3}$$

where D_i is the captured data.

Based on the preprocessed data, the SVM can be easily adopted to realize the IoT security situation classification with gaussian kernel function. But a simple two class model cannot meet our requirement because the security situation level is classified into 5 levels in our approach. Hence, we adopt a one-against-one strategy for the implementation. To be specific, we utilize multiple two-class SVM classifiers for every two levels respectively and get the corresponding score. Finally, the level of IoT security situation will be classified according to the sum score.

In summary, the classification of IoT security situation with SVM mainly includes three procedures: security data acquiring, data preprocessing and the training and classification of SVM. The algorithm description is given as Algorithm 1.

Algorithm 1. IoT security situation classification with SVM

Inputs. IoT security data

Output. The level of IoT security situation.

1. Acquire the security data from IoT software chain;
2. Preprocess the acquired data;
3. Obtain the needed data item and index value;
4. *Classify the IoT security situation using SVM;*
5. Output the security level of IoT system.

C. Security Situation Awareness Based on Markov Game Model

1. Construction of the Markov Game Model

The Markov game model is built on the game theory and Markov decision process (MDP). The former refers to the theory of how to make decisions under the interaction of multiple participants, while the latter is to make decision from the available behavior set based on the observed information (or state). Although the next state may be random, but the state transition is traceable according to Markov probability. Simply, the next state is only related to the current moment. In our approach, we have fully considered the impact of the behaviors of both attackers and defenders, and adopted the two-role Markov game analysis for security assessment, so that the potential threats can be dynamically analyzed.

Here, we list the basic components of Markov game model as following:

Participants. Participants are classified into three camps, that is, attacker, defender and user. The attacker conducts malicious attacks to make the IoT software chain disabled, while the defender implements security reinforcement solutions to reduce the vulnerability of the system, thereby improving the security of the IoT software chain. The user only uses the equipment, but does not care about the security issues.

Situation space. All possible situations in the IoT software chain constitute the situation space.

Behavior space. The behavior space is constituted by all the possible behaviors of the three participants.

Transition probability. With the evolution (caused by participants' behaviors) of IoT system, the situation is constantly changing. According to the transitions and the security evaluation of the IoT system, all participants may choose corresponding behaviors from the behavior space, with a probability.

Reward function. It refers the gains of all participants. Since the purpose of the attacker is to cause maximum damage to the system, its reward is expressed in terms of damage to the system; The purpose of the defender is to enhance the security of IoT system, the reward is expressed by the damage that the administrator can reduce after taking security actions; For users, their requirement is to get sufficient network resources, so the reward is expressed by the degree of utilization of system services.

2. The Markov Game Process

The game process means that all participants select a behavior from the behavior space according to the current state of the system, and then the system transfers to a new state. Subsequently, the participants need to make decisions based on the new state. This process is repeated until the preset condition is satisfied. In other words, at any time, for a certain threat, the three participants choose the corresponding behavior and get their rewards.

At a given moment and for a certain threat t, the three participants choose their own behavior strategy, and get their rewards, respectively. In our method, the reward that each part will obtain is described as a reward function. The purpose of each participant is to maximize the reward function, this process is quantitatively described as:

$$\mathrm{TPN}(t, k) = \{S_i(k), e_j(k)\} \tag{4}$$

where $S_i(k)$ is the state of the i-th propagation node at time k; $e_j(k)$ is the state of the j-th propagation path at time k. Simply, $\mathrm{TPN}(t, k+1)$ is the system state at time $k+1$, and the state change of the system follows the Markov rule. For attackers, they need to analyze which type of t belongs and consider that how to utilize this threat could get the most reward. Then, they could adopt some malicious behaviors. For the defensive side, the administrator's implementation of security measures on node i will bring about two impacts: 1) reducing the damage of threats t that affect the IoT software chain. 2) reducing the impact on system availability, that is, the impact of security plan on the availability of node i, which is described as:

$$V_s(S_i(k)) = \Delta\rho_{ai} \cdot value_{ai} \tag{5}$$

where $\Delta\rho_{ai}$ is the number of changes in node utilization performance, measured by the node utilization value before the security enhancement is implemented and the after value; and $value_{ai}$ represents the availability of node i. For users, their reward is measured by the sum of the use ratio of N nodes and the amount of M utilization path.

For example, suppose that there are 4 nodes in the IoT software chain, and the threat's propagation path is shown in Fig. 3. Initially, at time k, only node 1 detects the threat, and the system situation danger level reaches mild danger. Subsequently, at k+1 time, the threat spreads to node 3. So that the defender implements a reinforcement plan for node 3 according to the transmission route. If the reinforcement fails, node 3 is successfully infected and the system situation level reaches general danger. Otherwise, node 3 is not infected, and the system

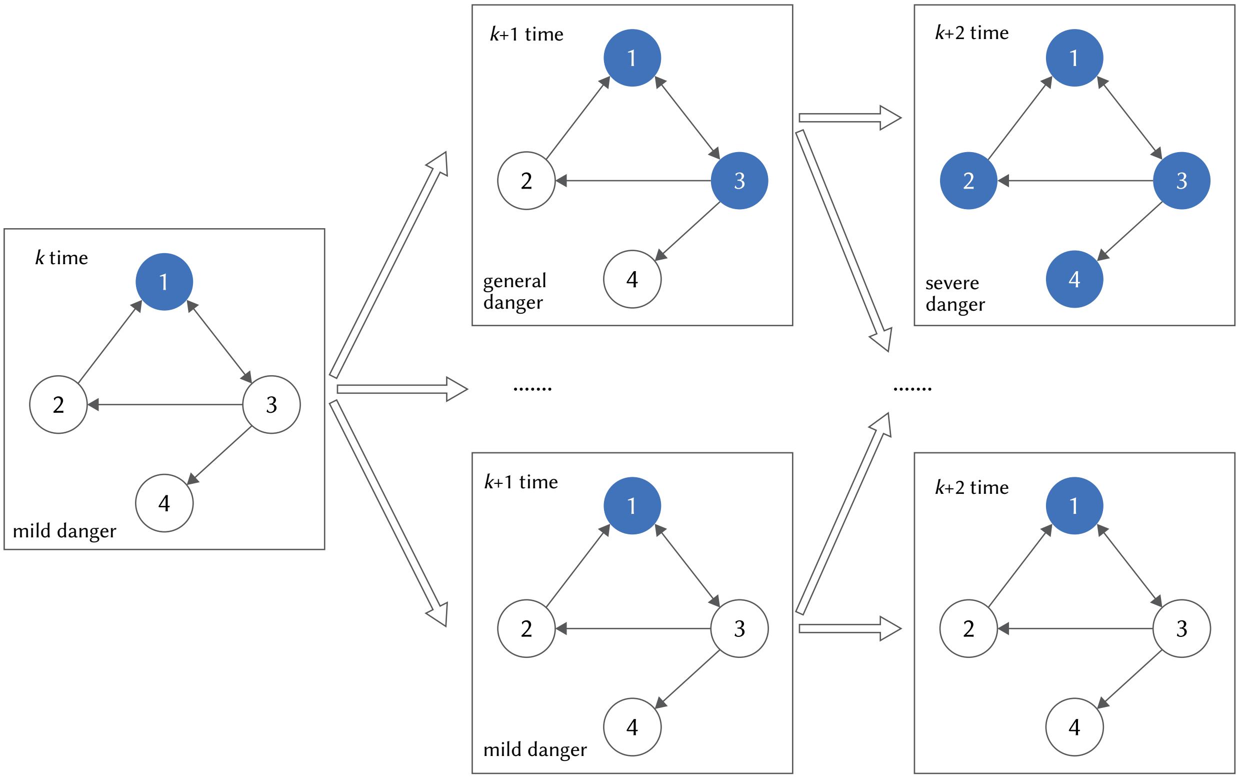

Fig. 3. The Markov game process.

situation level is still in mild danger. At k+2 time, under the case that node 3 is successfully infected, the threat continues to spread to nodes 2 and 4. At this time, if the defender chooses to reinforce node 1 but the reinforcement fails, the entire IoT software chain is completely infected, with a severely dangerous system situation. The defender needs to consider whether to turn off the system. If node 3 is safe, the defender only needs to implement reinforcement plan on node 1. If it succeeds, the entire system is in a safe condition.

Finally, the system constantly evolutes as the above process. For a finite-step (K-step) game process, from time k to time k+K, the states in different times forms a tree structure, and each path from the root node to the leaf node is a possible evolution, with the total rewards of all participants.

In summary, the IoT security situation awareness mainly includes three procedures: data processing, threat propagation network construction and IoT security evaluation based on Markov game model. The process is given as Algorithm 2.

Algorithm 2. IoT security situation awareness based on Markov game model.

Inputs. IoT security data

Output. The IoT security situation.

1. Preprocess the IoT security data;
2. Construct the threat propagation network for each threat t based on the security information;
3. According to the threat propagation network, construct a Markov game model for t, and the security situation of t is calculated;
4. Analyze the best reinforcement plan for the defender to deal with the threat of t;
5. Sum up the damage of all threats, and evaluate the overall security situation of the IoT software chain based on different requirements.

D. Module Designs and Deployment

1. Framework

In this paper, we design a practical system of the security situation awareness for IoT software chain as shown in Fig. 4. The system consists of a database, an interface for users and 5 main modules, including data acquisition module, situation analysis module, situation assessment module, security enhancement module and situation prediction module. We will detail these main modules below.

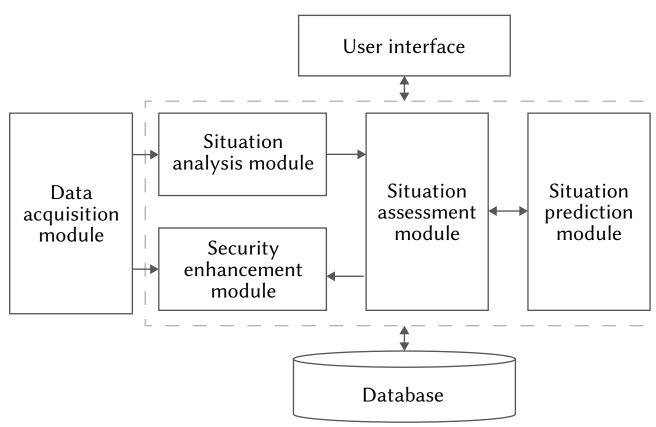

Fig. 4. Framework of the proposed system.

2. Data Acquisition Module

The data acquisition module obtains various data such as the status of the IoT system, the security threats faced and other security-related data through some automatic tools in the IoT software chain. These data will be stored in the database, and the invalid data will be cleaned up regularly.

3. Situation Analysis Module

The situation analysis module is actually a process of analyzing and standardizing the collected data. This is because the obtained data from the data acquisition module cannot be directly used as the input of subsequent modules. This module uses such as standardized analysis, redundancy detection, and conflict detection methods to analyze the original data, thus obtaining a standardized data set.

4. Situation Assessment Module

After getting standardized data, these data will be input to our proposed SVM-based security situation classification method to conduct security situation assessment by 1) analyzing the data from the situation analysis module 2) and the security situation awareness technology based on the Markov game model. Therefore, the security situation of the IoT system can be quantitatively described.

5. Situation Prediction Module

The situation prediction module adopts a situation prediction algorithm, based on the current security situation and the threats faced from the IoT system. Then it analyzes the law of changes in the situation, thus to predicts the tendency of the security situation of the IoT software chain.

6. Security Enhancement Module

The purpose of security enhancement module is to generate the reasonable security reinforcement plan for users. According to the predicted security situation tendency, and analyzing the weakest node of the IoT software chain, this module finally provides a reinforcement plan to advice the administrator to improve the security of the system.

IV. Implementation and Results

A. Running Environment

We have deployed our system with two proposed methods on a computer equipped with i7 CPU in 3.8GHz, RAM 32-GB, the used operation system is Window 11 Home.

B. Results and Analysis

Based on the above proposed methods, we have developed a security situation awareness system for IoT software chain. To evaluate the effectiveness of our approach, we deployed the system on a complex project and monitor the attacks on the IoT software chain of the target project. The detailed security information is shown in Table II.

In practice, our system supports the detection of typical IoT vulnerabilities and inherits more than 20 vulnerability detection methods, so that it can effectively detect various vulnerabilities and realize the security situation awareness.

C. Threat to Validity

At present, the proposed security situation awareness system for IoT software chain is still in preliminary exploration. Here, we discuss the threat to validity to our work.

Since the acquired security data are from different ways, we have normalized these data into a suitable format that can be used by SVM. But this process involves manual effort, which means, it may bring in some risks of human mistakes.

The second threat is that we need to choose a kernel function for SVM classification, different kernel function may produce different outcomes. We still need to learn how to reasonably choose a suitable kernel function.

Additionally, in our experiment, the used data set is too small, which directly affects the experimental outcomes and maybe not sufficient to provide convincing evaluation. We will look for some large-scale data set and conduct corresponding evaluations in the future.

TABLE II. Security Information Under Evaluation

Type of vulnerability	Attack description	CWE ID	Number of test cases
Time-related vulnerability	Race condition attack	366	38
	Competitive hazard attack	364	20
Environment-related vulnerability	Usage after memory is released	416	522
	Type obfuscation attack	400	904
	Uninitialized conditions	176	83
	Buffer overflow	457	981
	Other types	121	909
Security designing flaw	Other types	464	80
Hardware vulnerabilities	Other types	506	160
Memory-related vulnerability	Integer overflow	369	904
Logical-related vulnerabilities	Other types	404	626
Digital-related vulnerability	Uninitialized conditions	459	38
	Buffer overflow	122	920
Trigger vulnerability	Other types	510	72
	Type obfuscation attack	681	56
	Uninitialized conditions	665	316
	Buffer overflow	680	938

V. Conclusion and Future Work

The security of the IoT software chain no doubt affects the activities of the entire IoT system, especially in a complex environment. To provide more useful information for administrators and enhance the security of IoT system, in this paper, we have proposed a security situation awareness method for IoT software chain, and construct a Markov game model to simulate behaviors of attackers, defensives and users in the complex IoT application environment. Then the obtained security information is used to calculate the gains and losses of the three participants in the game, thus to evaluate the current security situation IoT system and predict the security situation in next stage. In order to improve the practical effect of the proposed security situation awareness, the SVM is adopted to pre-classify the security situation of the IoT system. Additionally, we have designed and implemented an IoT security situation awareness system that integrates 5 modules with different functions.

In fact, the current work still needs to be expanded. For example, we use SVM to classify the security situation, at this stage, introducing other more advanced models (such as neural network) can improve the classification accuracy and further improving the effectiveness of the proposed method.

References

[1] Perera C , Zaslavsky A , Christen P , et al. "Context Aware Computing for The Internet of Things: A Survey," *IEEE Communications Surveys & Tutorials*, 2014, 16(1):414-454.

[2] Heath T , Bizer C . "Linked Data: Evolving the Web into a Global Data Space," *Molecular Ecology*, 2011, 11(2):670–684.

[3] Malaiya R K, Kwon D, Kim J, et al. "An empirical evaluation of deep learning for network anomaly detection," *International Conference on Computing, Networking and Communications (ICNC). IEEE*, 2018: 893-898.

[4] Chen X Z , Zheng Q H , Guan X H , et al. "Quantitative Hierarchical Threat Evaluation Model for Network Security," *Journal of Software*, 2006, 17(4):885-897.

[5] Macqueen J . "Some Methods for Classification and Analysis of MultiVariate Observations," *Proc of Berkeley Symposium on Mathematical Statistics & Probability*. 1965.

[6] Li S , Xu L D , Zhao S . "Applications of Internet of Things: A Survey," *Information Systems Frontiers*, 2015, 17(2):243-259.

[7] D Miorandi, Sicari S , Pellegrini F D , et al. "Internet of things: Vision, applications and research challenges," *Ad Hoc Networks*, 2012, 10(7):1497-1516.

[8] Wang X , Liu W . "Research on Air Traffic Control Automatic System Software Reliability Based on Markov Chain," *Physics Procedia*, 2012, 24:1601-1606.

[9] Wang L Z , Zhang S S , Tao Q K . "A software-reuse-oriented agile supply chain model based on software agent," *Journal of Computer Research and Development*, 2002, 39(2):153-158.

[10] Cui J , Wang L , X Zhao, et al. "Towards predictive analysis of android vulnerability using statistical codes and machine learning for IoT applications," *Computer Communications*, 2020, 155(Apr.):125-131.

[11] Zanella A , Bui N , Castellani A , et al. "Internet of Things for Smart Cities," *IEEE Internet of Things Journal*, 2014, 1(1):22-32.

[12] Granjal J , Monteiro E , Silva J S . "Security for the Internet of Things: A Survey of Existing Protocols and Open Research Issues," *IEEE Communications Surveys & Tutorials*, 2015, 17(3):1294-1312.

[13] Sanchez-Arias G , Garcia C G , G-Bustelo B . "Midgar: Study of communications security among Smart Objects using a platform of heterogeneous devices for the Internet of Things," *Future Generation Computer Systems*, 2017, 74(SEP.):444-466..

[14] Webb J , Ahmad A , Maynard S B , et al. "A Situation Awareness Model for Information Security Risk Management," *Computers & Security*, 2014, 44(2):1-15.

[15] Zhang D , He Q . "Security Situation Awareness Method for Smart Grid," *International Core Journal of Engineering*, 2020, 6(5):49-55.

[16] Lei Z , Wu X . Wu, X.: "An edge-guided image interpolation algorithm via directional filtering and data fusion," *IEEE Transactions on Image Processing*, 2006, 15(8):2226-2238.

[17] Dey A , Mohammad F , Ahmed S , et al. "Anomaly Detection in Crowded Scene by Pedestrians Behaviour Extraction using Long Short Term Method: A Comprehensive Study," *International Journal of Education and Management Engineering*, 2019, 9(1):51-63.

[18] Wilks P , English M J . "A system for rapid identification of respiratory abnormalities using a neural network," *Medical Engineering & Physics*, 1995, 17(7):551-555.

[19] He W , Yan G , Xu L D . "Developing Vehicular Data Cloud Services in the IoT Environment," *IEEE Transactions on Industrial Informatics*, 2014, 10(2):1587-1595.

[20] Park N , Kim M , Bang H C . "Symmetric Key-Based Authentication and the Session Key Agreement Scheme in IoT Environment," *Lecture Notes in Electrical Engineering*, 2015, 330:379-384

[21] Weber R H . "Internet of Things – New security and privacy challenges," *Computer Law & Security Review the International Journal of Technology & Practice*, 2010, 26(1):23-30.

[22] D Guinard, Trifa V , Karnouskos S , et al. "Interacting with the SOA-Based Internet of Things: Discovery, Query, Selection, and On-Demand Provisioning of Web Services," *IEEE Transactions on Services Computing*, 2010, 3(3):223-235.

[23] Sicari S , Rizzardi A , Grieco L A , et al. "Security, privacy and trust in Internet of Things: The road ahead," *Computer Networks*, 2015, 76(jan.15):146-164.

[24] Jia R , Ding Y . "Nonzero-sum non-stationary discounted Markov game model," *Mathematical Methods of Operations Research*, 2000, 52(2):265-270.

[25] Lei C , Zhang H Q , Wan L M , et al. "Incomplete Information Markov Game Theoretic Approach to Strategy Generation for Moving Target Defense," *Computer Communications*, 2018, 116(JAN.):184-199.

[26] Hu H , Hu C , Yao S . Decision Model of Optimal Active Response for Network Security Using Partial Observable Markov Game[J]. *Hsi-An Chiao Tung Ta Hsueh/Journal of Xi'an Jiaotong University*, 2011, 45(4):18-24.

[27] Cauwenberghs G , Poggio T . "Incremental and Decremental Support Vector Machine Learning," *Advances in neural information processing systems*, 2001, 13(5):409-412.

[28] Amari S , Wu S . "Improving support vector machine classifiers by modifying kernel functions," *Neural Networks*, 1999, 12(6):783-789.

[29] Zien A , G Rätsch, Mika S , et al. "Engineering support vector machine kernels that recognize translation initiation sites," *Bioinformatics*, 2000, 16(9):799-807.

[30] Yang Y , Wu L , Yin G , et al. "A Survey on Security and Privacy Issues in Internet-of-Things," *Internet of Things Journal, IEEE*, 2017, 4(5):1250-1258.

[31] Sathishkumar J , Patel D R . "A Survey on Internet of Things: Security and Privacy Issues," *International Journal of Computer Applications*, 2014, 90(11):20-26.

[32] Bouij-Pasquier I , Kalam A , Ouahman A A , et al. "A Security Framework for Internet of Things," *Springer, Cham*, 2015.

[33] Bass T . "Intrusion Detection Systems & Multisensor Data Fusion: Creating Cyberspace Situation Awareness," *CiteSeer*, 2000.

[34] Endsley, Mica R . "Measurement of Situation Awareness in Dynamic Systems," *Human Factors*, 1995, 37(1):65-84.

[35] Franke N , Hippel E V . "The Case of Apache Security Software," *Social Science Electronic Publishing*.

[36] Kou G , Wang S , Tang G . "Research on Key Technologies of Network Security Situation Awareness for Attack Tracking Prediction," *Chinese Journal of Electronics*, 2019, 28(001):162-171.

[37] Zhylin A , Hudyncev M , Litvinov M . "Functional model of cybersecurity situation center," *Collection Information technology and security*, 2018, 6(2):51-67.

[38] Lakhno V , Akhmetov B , Korchenko A , et al. "Development of a decision support system based on expert evaluation for the situation center of transport cybersecurity," *Journal of Theoretical and Applied Information Technology*, 2018, 96(14):4530-4540.

[39] Chen S , Jian Z , Huang Y , et al. "Autonomous driving: cognitive construction and situation understanding," *Science China Information Sciences*, 2019, 62(008):1-27.

[40] Kourti T . "Abnormal situation detection and projection methods—industrial applications. October 28–29, 2003. Hamilton, Ontario, Canada," *Chemometrics & Intelligent Laboratory Systems*, 2005, 76(2):215-220.

[41] Lewis L , Jakobson G , Buford J . "Enabling cyber situation awareness, impact assessment, and situation projection," *Military Communications Conference. IEEE*, 2008.

[42] Lin P , Chen Y . "Network Security Situation Assessment Based on Text SimHash in Big Data Environment," *International Journal of Network Security*, 2019, 21(4):699-708.

Xudong Zhu

Xudong Zhu is currently working as an Associate Professor for the Wuxi Vocational Institute of Arts & Technology, Wuxi, China. His research interests include software engineering and Internet of things.

Honggao Deng

Honggao Deng is currently working as a researcher for the Guilin University of Electronic Technology, Guilin, China. His research interests include software engineering and communication and Information System.

STAIBT: Blockchain and CP-ABE Empowered Secure and Trusted Agricultural IoT Blockchain Terminal

Guofeng Zhang[1*], Xiao Chen[2], Lei Zhang[3], Bin Feng[1*], Xuchao Guo[4], Jingyun Liang[5], Yanan Zhang[6]

[1] School of Information Science and Technology, Taishan University, Taian Shandong (China)
[2] School of Economics and Management, Taishan University, Taian Shandong (China)
[3] Shandong Academy of Macroeconomic Research, Jinan Shandong (China)
[4] College of Information and Electrical Engineering, China Agricultural University, Beijing (China)
[5] Laboratory of Quality and Safety Risk Assessment for Agro-Products of the Ministry of Agriculture (Jinan), Institute of Quality Standard and Testing Technology for Agro-Products, Shandong Academy of Agricultural Sciences, Jinan Shandong (China)
[6] School of Information Science and Engineering, University of Jinan, Jinan Shandong (China)

Received 14 December 2021 | Accepted 25 April 2022 | Published 28 July 2022

Abstract

The integration of agricultural Internet of Things (IoT) and blockchain has become the key technology of precision agriculture. How to protect data privacy and security from data source is one of the difficult issues in agricultural IoT research. This work integrates cryptography, blockchain and Interplanetary File System(IPFS) technologies, and proposes a general IoT blockchain terminal system architecture, which strongly supports the integration of the IoT and blockchain technology. This research innovatively designed a fine-grained and flexible terminal data access control scheme based on the ciphertext-policy attribute-based encryption(CP-ABE) algorithm. Based on CP-ABE and DES algorithms, a hybrid data encryption scheme is designed to realize 1-to-N encrypted data sharing. A "horizontal + vertical" IoT data segmentation scheme under blockchain technology is proposed to realize the classified release of different types of data on the blockchain. The experimental results show that the design scheme can ensure data access control security, privacy data confidentiality, and data high-availability security. This solution significantly reduces the complexity of key management, can realize efficient sharing of encrypted data, flexibly set access control strategies, and has the ability to store large data files in the agricultural IoT.

Keywords

Agricultural Internet Of Things, Blockchain, Ciphertext-Policy Attribute-Based Encryption(CP-ABE), Data Security, Privacy Protection.

DOI: 10.9781/ijimai.2022.07.004

I. Introduction

As the key technology of agricultural informatization, agricultural IoT has made enough and outstanding achievements all over the world. Nevertheless, the traditional agricultural IoT that uses a centralized storage architecture is facing problems such as data privacy leakage, data tampering, data untrusted and so on. The decentralization, non-tampering and traceability of blockchain provide new technologies and new ideas for the development of agricultural informatization and IoT, making it rapidly become an important technology in many applications of precision agriculture [1].

On the whole, the integrated application of blockchain and IoT technology has become a new research hotspot in the field of agricultural information. As a distributed ledger, each node of blockchain stores complete ledger data. How to ensure the security and privacy of the data stored in the ledger is a topic that cannot be bypassed by the research and application of blockchain technology. Unauthorized access to IoT devices can cause serious privacy and security issues, and has become a major challenge hindering the widespread adoption of IoT technology [2]. Agricultural IoT terminal is an important source of agricultural data, and its privacy protection and access control are very important for the data security management of the whole life cycle of Agricultural IoT. How to protect the privacy and security of agricultural data from the data source is the starting point and goal of this research.

This work is dedicated to the technical integration of blockchain and IoT. Through the introduction of cryptography technology, we design a data encryption and access control scheme suitable for IoT terminals, and finally design a secure and trusted agricultural IoT blockchain terminal. The main contributions of this paper are as follows:

1. A system architecture of a universal IoT blockchain terminal based on cryptography, blockchain and IPFS technology is proposed. It inherits the advantages of the traditional Internet of Things terminal, and at the same time has the technical characteristics of directly acting as a blockchain and IPFS node. Make it an effective carrier for the integrated application of blockchain and the Internet of Things.

* Corresponding author.

E-mail addresses: binfeng@tsu.edu.cn (Bin Feng), zhangguofeng@tsu.edu.cn (Guofeng Zhang).

2. Based on the ciphertext-policy attribute-based encryption(CP-ABE) algorithm, a fine-grained and flexible terminal data access control scheme is designed. The innovative use of the IoT terminal as an effective means of data access control realizes the binding of data access control and data collection equipment. At the same time, the experimental results show that the scheme will not affect the storage efficiency of blockchain data.
3. A hybrid data encryption scheme is designed. With the help of the fine-grained access control scheme designed in this paper, it can not only realize 1-to-N encrypted data sharing, but also significantly reduce the complexity of key management.
4. A "horizontal + vertical" segmentation plan for IoT data is proposed.Combining the hybrid data encryption scheme and IPFS storage proposed in this paper, it realizes the efficient storage, security and trusted fine-grained authorized access of IoT data.

The following organizational structure of this paper is: Section II summarizes the related works of this work; section III briefly introduces the two key technologies used in this paper; section IV designs and proposes the architecture, data access control, data segmentation and privacy protection schemes of the secure and trusted agricultural Internet of Things data terminal, and further introduces the algorithm designed in this paper; section V describes the experiment. According to the experimental results, the advantages of this design scheme are systematically analyzed from two aspects of security and performance; section VI gives the conclusion of this paper.

II. Related Works

A. Blockchain and Agricultural IoT

Recent studies have conducted a comprehensive investigation on the blockchain and the IoT in precision agriculture, and proposed a new blockchain model [1]. The security of equipment in precision agriculture is a key issue of the IoT, and the integration of blockchain and IoT technology can provide a new solution to this problem [2]. The agricultural IoT is more vulnerable to attacks than other industrial scenarios. Based on the blockchain and IoT technology, a new identity verification and key management scheme is designed, called AKMS-AgriIoT [3], in which encryption and verification are made by the General Satellite Service (GSS) is completed and submitted to the blockchain system. The use of limited-function sensing devices in the IoT as a reliable data source for the blockchain has been studied, and it is believed that the integration of blockchain and IoT can be applied to the agricultural production process [4]. In the process of pre production and post production of agriculture, through the integration of blockchain, smart contracts and IoT devices, trust has been established between all parties and a fully automated process has been completed [5]. The traditional fish farm system and the Hyperledger Fabric blockchain can perform Integration [6], the device client uses embedded hardware such as Raspberry Pi and Arduino to communicate with the traditional fish farm system and the blockchain. As a super node [7], Raspberry Pi 3B can safely process and aggregate field data and push it to the blockchain ledger. In precision agriculture applications, it is believed that every IoT node can interact with the ledger and directly record data on the ledger [7]. In the agricultural supply chain system, the Fabric with IPFS is used. It can effectively promote the construction of quality traceability system of agricultural products supply chain [8]. The design of agricultural product supply chain scheme based on blockchain should ensure that data encryption storage is safe and reliable, the transaction records can be traced, queried and appealed, and private data is owned by each participant [9].

It can be seen that blockchain and agricultural IoT have been widely studied from theory to technology. However, the above research in agricultural IoT focuses on the integration of the two, and there is no clear scheme for data sharing, access control and privacy protection in blockchain. In particular, how to realize data privacy protection and access control on the device side of the IoT is the starting point and goal of this paper.

B. Blockchain Data Sharing and Access Control

Hyperledger blockchain is dedicated to providing brand new solutions for data security and privacy protection [10],[11]. A Secure and Reliable Traceability System for Agricultural Products Powered by Permissioned BlockChain Technology is proposed, and the fine-grained authorized access and agricultural product quality and safety traceability mechanism under the CP-ABE algorithm is discussed [12]. HyperLedger fabric has been used in the pharmaceutical traceability system [13]. Jemel et al. [14] and Huang Sui et al. [15] discussed data sharing methods based on blockchain and CP-ABE technology. Wang Xiuli et al. [16] proposed data access control and sharing model using ABE for fine-grained access control and secure sharing. Based on ABAC and blockchain, Zhang et al. [17] use access trees to configure access policies to enable fine-grained authorized access to IoT devices. However, the IoT devices need to use the blockchain proxy node to interact with the blockchain ledger, and there is a risk of data being tampered with at the collection end.

C. Block Data Encryption and Privacy Protection

Data confidentiality is a prerequisite for ensuring data security. The security of block (ledger) data is mainly guaranteed by encrypting transaction data with encryption algorithm, and its access rights should also be considered. CP-ABE algorithm has been used in blockchain system to realize flexible data authorization access [18]. To support more flexible public key generation, Sahai and Waters [19] first proposed an Attribute-based Encryption (ABE) scheme, which uses a set of attributes rather than a unique identifier to identify the identity. ABE is a kind of fine-grained 1-to-N encryption scheme.

Further research has proposed the key-policy Attribute-based Encryption (KP-ABE) [20] and the ciphertext-policy Attribute-based Encryption (CP-ABE) [21]. KP-ABE embeds the policy into the encryption key and the attributes into the ciphertext. CP-ABE embeds the policy into the ciphertext and the attributes into the user key. The common feature of both is that the encryption and decryption of data are bound to the access policy, and only when the attributes in the attribute set can satisfy the access structure can the data be decrypted . Fine-grained access control can be achieved while retaining cryptographic control. However, the application scenarios of the two are different. The KP-ABE scheme stores the encrypted ciphertext on the server.It assigns a specific access policy to the user when access is granted, commonly used for paid video sites, log encryption management,etc. In the CP-ABE scheme, as long as it has corresponding attributes and satisfies its logical relationship, ciphertext data can be automatically decrypted, which is more suitable for one-time encryption and multiple authorized private data sharing, such as encrypted data sharing in cloud storage.

Symmetric encryption system has the characteristics of fast speed and shared keys between encryption and decryption parties. Although it can also be used for blockchain data encryption, with the increasing complexity of business transactions between organizations and the dynamic change of the number of organizations, key distribution and management will become more and more complex. Moreover, there will be problems such as key leakage and multiple encryption.

In view of the above analysis, this article uses the CP-ABE algorithm and the symmetric encryption DES algorithm to design a hybrid encryption scheme suitable for IoT terminals. It can encrypt sensitive data collected by IoT terminals and perform flexible access control on data on the chain. While ensuring data security, the complexity of key management is further reduced.

III. Preliminaries

A. CP-ABE

The data in the blockchain ledger is shared to the all nodes of blockchain, and is easily accessed illegally. The CP-ABE scheme sets access control policies based on data attributes and is used for data encryption. Anyone who has the attributes in the access control policy and satisfies the logical relationship can decrypt the data. Because it doesn't care about specific users at all, it has more flexibility in access control. Therefore, this paper introduces the CP-ABE algorithm to guarantee data confidentiality and authorized access control of the data sharer. It realizes the unification of ownership and control of data in blockchain.

The CP-ABE encryption algorithm [21] composed of five basic algorithms, including Setup, Encrypt, KeyGen, Decrypt and Delegate. Among them, CT = Encrypt (PK, M, T) is the encryption algorithm, which can encrypt the plaintext message M under the public key PK and the access control tree T into ciphertext CT, the specific as in (1).

$$CT = (T, \check{C}, C, \forall y \epsilon Y : C_y, C'_y) \tag{1}$$

$$\check{C} = Me(g,g)^{as} \tag{2}$$

$$C = h^s \tag{3}$$

$$C_y = g^{q_y(0)} \tag{4}$$

$$C'_y = H(att(y))^{q_y(0)} \tag{5}$$

Here, the parameters α, s are random, and g is the generator of the bilinear group of prime order. Let G1 and G2 be two multiplicative cyclic groups of prime order p,g be a generator of G1 and e be a bilinear map e : G1 × G1 ⟶ G2.

The parameters y is the leaf node of access structure T,q_y is a polynomial for each node y in the tree T . The ciphertext CT is constructed by T, which is the tree access structure. The function att(x) is defined only when x is a leaf node and represents the attribute associated with the leaf node x in T.

The decryption function is DecryptNode (CT, SK, x), defined as in (6).

$$DecryptNode(CT, SK, x) = \frac{e(D_i, C_x)}{e(D'_i, C'_x)} = \frac{e(g^r \cdot H(i)^{r_i}, h^{q_x(0)})}{e(g^{r_i}, H(i)^{q_x(0)})} \tag{6}$$

$$DecryptNode(CT, SK, x) = e(g,g)^{r q_x(0)} \tag{7}$$

Here, SK is a private, which is associated with a set of S attributes, and a node x from T.

For the explanation of other parameters, refer to the literature [21]. However, the above two formulas and the parameters T and attr(x) show that attributes are the essential for data encryption and decryption and access control in the CP-ABE algorithm. It determines the flexibility of the access control policy and who can decrypt the ciphertext data.

B. IPFS

InterPlanetary File System (IPFS) is a point-to-point distributed file system, a network transmission protocol designed by Juan Benet and open source management by Protocol Labs, which can provide permanent and distributed storage of files. Integrating the technical advantages of P2P, Git, BitTorrent, Kademlia, Self-certifying File System (SFS) and Web, it can provide a simple interface similar to HTTP Web. Its distributed storage technology can be perfectly matched with blockchain technology to boost the ability of the blockchain system to store large files. For example, IPFS integrated with blockchain technology for agricultural products supply chain traceability system [22].

IV. The Proposed Schemes and Algorithms

A. System Architecture of a IoT Blockchain Terminal

This paper is focused on the protection of agricultural IoT data security and access control. With the empowerment of blockchain and cryptography technology, a universal secure and trusted agricultural IoT blockchain terminal is designed. Its architecture is shown in Fig. 1.

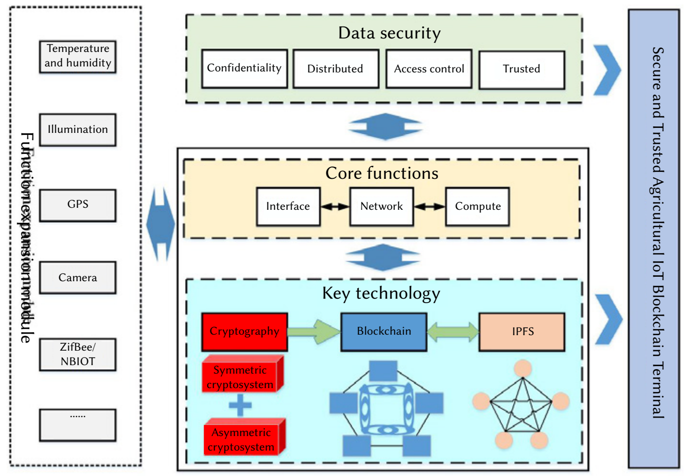

Fig. 1. General secure and trusted agricultural IoT blockchain terminal architecture.

This architecture is still based on traditional embedded technology and has a wealth of functional expansion interfaces to facilitate the access of sensors and expansion modules. From a functional and technical point of view, this system uses blockchain and IPFS technology to realize distributed storage of collected data. With the help of symmetric encryption and asymmetric encryption mechanisms, it can protect data privacy, set flexible access control, and finally provide secure and trusted IoT data collection service. Its typical feature is that the terminal integrates blockchain, IPFS, cryptography and embedded systems, and can be used as a gateway to the agricultural IoT, providing raw data directly on the chain at the collection end, protecting data security from the source.

Deploying the blockchain and IPFS system directly in the terminal system puts forward certain requirements for embedded hardware and software. The data segmentation and encryption algorithm designed in this paper belongs to a part of the terminal embedded software. It interacts with blockchain and IPFS to realize the uplink release of encrypted data. As an ARM-based microcomputer motherboard, the Raspberry Pi has almost all the basic functions of a PC, making it one of the best choices for the integration of IoT terminals and blockchain. This paper will also be based on the Raspberry Pi 4B development board for experimental verification. In view of the limited storage capacity of the embedded system, the terminal device may not store the complete blockchain ledger data, but is only used to publish the data.

B. Terminal Data Access Control Scheme

1. Terminal Registration

This paper regards the IoT terminal as an access control object. First, the terminal must be registered and connected to the network. The administrator sets the private data encryption key, terminal number, attributes and related parameters for the terminal. These parameters constitute a unique file for the device to collect. Data access control is called an access control file.

2. Fine-Grained Access Control Algorithm

The core function of Agricultural IoT system is to automatically perceive and obtain the process data of the three stages before, during and after agricultural production. This work is mainly completed automatically by the IoT terminal, and the continuous data presents typical dynamic and serialization characteristics. All the collected data include the serial number, name and other key information of the IoT terminal. Obviously, the access control of IoT data can also be transformed into the access control of IoT terminals. In this paper, the serial number and other key information of the IoT terminal and the key of data encryption are written into a unique file to set a flexible and fine-grained access control policy for the terminal. Therefore, this file is named device access control file. The access control policy of the file can be expressed in the form of access tree, as shown in Fig. 2.

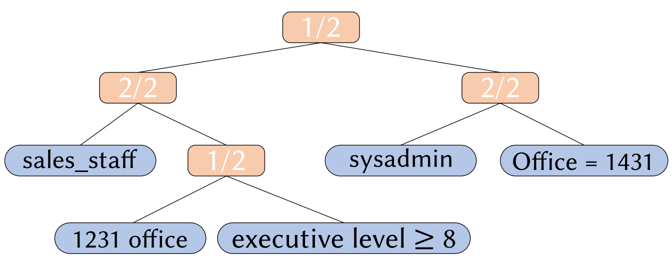

Fig. 2. Access tree model.

Fig. 2 shows an access control tree model. This is an example of setting access control policies on the basis of employee attributes. The logical meaning of the access control tree is as follows.

1. Employees with sysadmin attribute in 1431 office.
2. Sales staff with execution level greater than or equal to 8, in 1231 office.

This paper realizes one-time encryption and n-time sharing of data. When the access user has the attributes in the access tree and can meet its logical relationship, the secret data can be decrypted correctly.

3. Access Control Smart Contract

We create an access control file for each terminal, which contains the key and access control policy used by the terminal for data encryption. To protect the data privacy of the file and to perform flexible access control, encryption is performed using the CP-ABE algorithm. However, please note that the CP-ABE ciphertext of this file will take up more storage space than the plaintext. The specific amount occupied is related to the number of data attributes used for encryption. Obviously, this is not conducive to the on-chain storage of the file. Therefore, this paper uses IPFS for file storage, meanwhile, publishes the hash value in IPFS through the authorized access control smart contract. The name of the designed access control smart contract is auth, which includes the design of the access control structure and the related operation functions of access control.

```
// AuthSet describes authset details of what makes up a simple
   authset
  type AuthSet struct {
    ID          string     'json:"ID"'
    Terminal    string     'json:"terminal"'
    Authinfo    string     'json:"authinfo"'
  }
```

According to the above analysis, the access control file of each device corresponds to the access control data, including the Terminal number and the access control authentication information Authinfo. In the follow-up experiments of this paper, in order to facilitate the experiment, Authinfo is mainly used to store the key information encrypted by the device, which will be introduced in section V.B.

C. Privacy Data Segmentation and Encryption Scheme

1. Data Segmentation

The secure and trusted agricultural IoT blockchain terminal can collect different data in agricultural production scenarios, such as data such as temperature, humidity, and light in agricultural greenhouses, fields, and other production environments, as well as video, voice, and image data. To ensure the performance of the blockchain system, data segmentation technology is adopted to segment the above data, and a " horizontal + vertical " IoT data segmentation scheme is designed. Specifically:

First, the horizontal data segmentation. The IoT data is divided into structured data and unstructured data. Generally speaking, structured data is relatively standardized, occupies less storage space, and can be stored on the blockchain normally. Unstructured data occupies more storage space. Therefore, it needs to be stored with the help of IPFS file system, which can not be affected by file size.

Secondly, vertical data segmentation. Separate private data and public data in structured data. Separate the sensitive and private data on the blockchain and perform encryption processing to better ensure data privacy.

Through the data segmentation technology, the classified storage of structured data and unstructured data, and the classified processing of sensitive data and public data are realized, making the data collected by safe and trusted terminals more standardized and clear.

2. Privacy Data Encryption

The symmetric encryption system has the advantage of fast speed. Under the premise of ensuring the security of the key, it can fully meet the confidentiality requirements of the data on the blockchain. This paper uses the DES symmetric encryption algorithm to encrypt the private data on the blockchain and the unstructured private data stored in IPFS. As the key for the symmetric encryption algorithm, the key is stored in the access control policy file. Only users with access rights to the device can decrypt the key, thereby ensuring the security of private data.

Therefore, a hybrid encryption scheme is constructed by CP-ABE and DES algorithms, combined with data segmentation technology, which can protect data confidentiality and achieve fine-grained authorized access to data. Among them, the data segmentation and privacy data encryption scheme process is shown in Fig. 3.

3. Data Publish Smart Contract

The data collected by a secure and trusted IoT blockchain terminal needs to be published on the blockchain with the help of a blockchain smart contract. The data publish smart contract defines the structure of the data set. At the same time, it defines operation functions such as the initialization of the ledger, the creation of data sets, and the query.

```
type DataSet struct {
    ID          string     'json:"ID"'
    Terminal    string     'json:"terminal"'
    User        string     'json:"user"'
    Airtemp     float32    'json:"airtemp"'
    Airhumi     int        'json:"airhumi"'
    Illu        int        'json:"illu"'
    Gps         string     'json:"gps"'
}
```

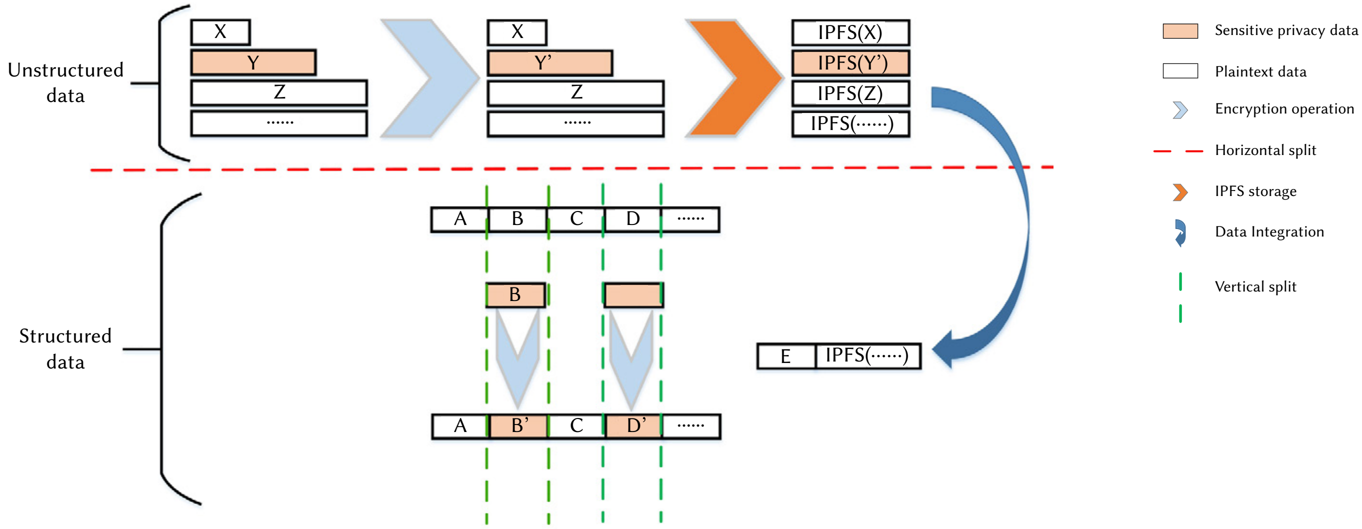

Fig. 3. The data segmentation and privacy data encryption scheme process.

This paper takes the greenhouse environment data of the agricultural IoT system as an example, and designs a data set DataSet, where ID is used to represent the data number, Terminal represents the number of the terminal, User represents the user number, Airtemp represents the air temperature, and Airhumi represents the air humidity, Illu means light intensity, Gps means the current coordinates of the device. In section V, this smart contract will be experimentally verified.

4. Proposed Algorithm

According to the above design scheme, this work designs the terminal security registration algorithm, block data access control algorithm and secure trusted data encryption uplink algorithm. Algorithm 1 and algorithm 2 show the pseudo codes of the latter two algorithms respectively.

The terminal security registration algorithm is to construct an access control policy, which determines the flexibility and accuracy of data sharing. The symbolic variables are shown in Table I.

Algorithm 1: Block data access control algorithm

```
Input: Block data retrieval conditions, user private key
Output: Query result data of the ledger
begin:
  BlockData = ChaincodeQuery (sect, retrieval conditions);
  if (Does it contain ciphertext data?)
    AuData= ChaincodeQuery(auth,Terminal number);
    ct_acfile =IPFS_Get(AuData.authinfo);
    acfile=Cpabe-dec(ct_acfile,user private key);
  if (Has the decryption succeeded?)
    DES_Decrypt (BlockData.ciphertext, acfile.TelKey);
    return the complete data after decryption;
  else
    return BlockData containing ciphertext;
  else
  return BlockData;
end
```

Algorithm 2: Secure trusted data encryption uplink algorithm

```
Input: Data collected by Agriculture IoT terminals, Encryption key
Output: Secure and trusted blockdata under privacy protection
begin:
  StData, UstData=HorizontalDatasplit(Data);
  SensitiveCheck(StData,UstData);
  if (Is unstructured data?)
    if (Is sensitive data?)
      Ciphertext = DES_Encryption(UstData.StData);
      UstFile = CreateCiphertext_file(Ciphertext);
    else
      UstFile = CreateCiphertext_file(UstData);
    H(UstFile) = IPFS_add(UstFile);
    upData = DataMerge(Terminal number,H(UstFile));
    ChainCodeInvoke = (sect,upData);
  else
    PData, SData = VerticalDataSplit(StData);
    While (Is sensitive data encrypted?) do
      Ciphertext[] = DES_Encryption(SData);
  upData = DataMerge(PData, Ciphertext[]);
  ChainCodeInvoke = (sect,upData);
end
```

TABLE I. Symbolic Variables

Variable name	Meaning
Tid	Terminal identifier or number
A	Attributes set
TK	Terminal data encryption key
Acf	Access control file
Acf'	Ciphertext of access control file
H	The identification of the ciphertext of the access control file in IPFS
D	Terminal attributes and data
UD	Data that needs to be stored on the chain
S	Terminal security registration smart contract

$$CreatAC\_File(Tid, A, TK) \rightarrow Acf \tag{8}$$

The *CreateAC_File* function generates an access control policy based on attributes, and generates an access control file based on terminal parameters.

$$Cpabe\_enc(Acf, TK) \rightarrow Acf' \tag{9}$$

The *Cpabe_enc* function performs CP-ABE encryption on the access control file.

$$IPFS\_add(Acf') \rightarrow H \tag{10}$$

The *IPFS_add* function uploads the ciphertext access control file to the IPFS system and receives the hash value of the file H, that is, the unique identification of the file.

$$DataMerge(Tid, D, H) \rightarrow UD \tag{11}$$

The DataMerge integrates the terminal number and the file's hash into the chaindata.

$$ChainCodeInvoke(UD, S) \tag{12}$$

Finally, auth chaincode is called to publish the chaindata on the blockchain.

In Algorithm 1, when there is a ciphertext in the blockdata that the user queries, and it is determined that the ciphertext needs to be decrypted, it will go to the IPFS to retrieve the access control file of the terminal. The IPFS file downloaded by the IPFS_Get function needs to be decrypted by Cpabe_dec. Only when the current user attribute (private key) meets the access control strategies can the decryption succeed. After the decryption is successful, the DES algorithm key for encrypting the terminal data is obtained.The key cannot be decrypted without access control privileges, thereby protecting the user's data privacy.

The core of Algorithm 2 is data segmentation. HorizontalDatasplit divides data into structured and unstructured data, and VerticalDataSplit divides structured data into public data and sensitive data. Then perform data encryption and data integration depended on the split results and the sensitivity of the data, and finally publish it on the blockchain. The classification and hierarchical processing of data are realized to ensure the privacy and security of data.

V. Experiments

In this section, we simulate the experimental results and analyze of the proposed scheme.

A. Materials and Environment

The hardware experiment environment in this paper includes secure and trusted terminal nodes and PC nodes. The safe and trusted terminal node uses the Raspberry Pi Pi 4B development board, 8GB of memory, 64GB of storage, integrated temperature and humidity sensor DHT11, GPS module, and light sensor BH1750FVI, as shown in Fig. 4.

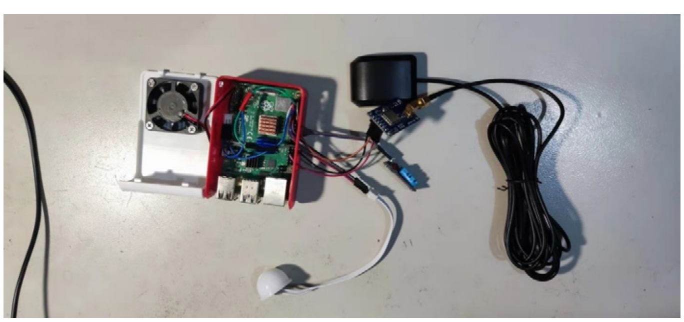

Fig. 4. Secure and trusted agricultural IoT blockchain terminal.

The software system of the terminal is: x64 Ubuntu Server 20.04 LTS operating system, HyperLedger Fabric 2.1.0 blockchain platform, and the node data collection and encryption and decryption programs are developed in C language. The open source CP-ABE algorithm is used in the experiment [23]. In order to test the access control and data encryption designed in this paper, a blockchain network including 1 Orderer node and 2 Peer nodes was built in the Raspberry Pi system, as shown in Fig. 5. Among them, Peer nodes belong to organization 1 and organization 2, and the development of smart contracts adopts the Golang language.

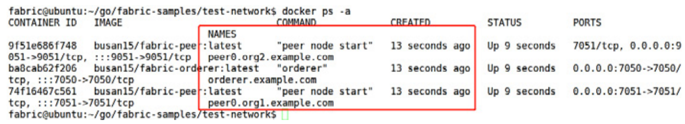

```
fabric@ubuntu:~/go/fabric-samples/test-network$ docker ps -a
CONTAINER ID   IMAGE                          COMMAND              CREATED          STATUS         PORTS
                                      NAMES
9f51e686f748   busan15/fabric-peer:latest     "peer node start"    13 seconds ago   Up 9 seconds   7051/tcp, 0.0.0.0:9
051->9051/tcp, :::9051->9051/tcp      peer0.org2.example.com
ba8cab62f206   busan15/fabric-orderer:latest  "orderer"            13 seconds ago   Up 9 seconds   0.0.0.0:7050->7050/
tcp, :::7050->7050/tcp                orderer.example.com
74f16467c561   busan15/fabric-peer:latest     "peer node start"    13 seconds ago   Up 9 seconds   0.0.0.0:7051->7051/
tcp, :::7051->7051/tcp                peer0.org1.example.com
fabric@ubuntu:~/go/fabric-samples/test-network$
```

Fig. 5. Blockchain network process.

B. Data Access Control Policy Experiment

1. Data Access Control Policy Encryption

In this experiment, there are three employees in the IoT data center, administrators Sara and LeBron, sales staff Kevin, and the system assigns private keys to them based on key attributes such as their identities and positions. Specifically, Sara and LeBron both have sysadmin attributes, but Sara is in the office of 1431 and LeBron is in the 1531 office. Kevin has the sales_staff attribute, has an employee level of 7, and is in the 1231 office.

The number of the secure and trusted blockchain terminal in the experiment is T0000001, and its key of private data encryption is 123456, the name of the designed data access control policy file is T0000001.txt, and the content is "Congratulations. The key of T00000001 is 123456". According to Fig. 2 in Section IV.B, set a data access control policy for it, and perform CP-ABE encryption. Therefore, the encryption command is:

cpabe_enc pub_key T0000001.txt (sysadmin and office=1431) or (sales_staff and (executive_level ≥ 8or office = 1231))

After encryption, the T0000001.txt.cpabe file will be created. The content is the ciphertext of T0000001.txt, as well as the attributes and access control policies that can correctly decrypt the file, so as to ensure the confidentiality of the data and flexible access control.

2. Access Control File Operation

The IPFS file system generates a unique hash value while storing the data access control file T0000001.txt.cpabe, as shown in Fig. 6. This hash value is called and the access control smart contract auth is published on the blockchain, thereby realizing the access control file on the blockchain. The data visitor can retrieve the hash value of the access control file with terminal number T0000001 in IPFS by calling the smart contract, as shown in Fig. 7, obtain the file locally through the IPFS interface or command, and then rename it to the terminal number, as shown in Fig. 8.

Fig. 9 shows the process of access control policy verification. For LeBron, even though he has sysadmin attributes, he is not in the 1431 office, so he cannot decrypt the access control file to get the key, and he cannot obtain the private data collected by the terminal, but can only see the non-sensitive data. On the contrary, although Kevin's level is not enough, he is in the 1231 office and has the sales_staff attribute, so he can correctly decrypt the access control file and obtain the encryption key of the terminal T0000001 from the file content as 123456. There is no doubt that Sara can also decrypt the key.

```
fabric@fabric:~/cp-abe/cpabe-0.11$ ipfs add T0000001.txt.cpabe
added QmPkunmPDeUkXhoyRQZVByijussECL19dB1vuETNJPWK3c T0000001.txt.cpabe
 2.99 KiB / 2.99 KiB [==========================================================] 100.00%
fabric@fabric:~/cp-abe/cpabe-0.11$
```

Fig. 6. Access control file upload to IPFS system.

```
sectAuth.c,9 输入参数=[00000001 T0000001 QmPkunmPDeUkXhoyRQZVByijussECL19dB1vuETNJPWK
3c]
sectAuth.c,11 开始数据发布上链=[00000001 T0000001 QmPkunmPDeUkXhoyRQZVByijussECL19dB1
vuETNJPWK3c]
sectAuth.c,14 cCmd=[peer chaincode invoke -o localhost:7050 --ordererTLSHostnameOverr
ide orderer.example.com --tls --cafile /home/fabric/go/src/github.com/hyperledger/fab
ric-samples/test-network/organizations/ordererOrganizations/example.com/orderers/orde
rer.example.com/msp/tlscacerts/tlsca.example.com-cert.pem -C mychannel -n auth --peer
Addresses localhost:7051 --tlsRootCertFiles /home/fabric/go/src/github.com/hyperledge
r/fabric-samples/test-network/organizations/peerOrganizations/org1.example.com/peers/
peer0.org1.example.com/tls/ca.crt --peerAddresses localhost:9051 --tlsRootCertFiles /
home/fabric/go/src/github.com/hyperledger/fabric-samples/test-network/organizations/p
eerOrganizations/org2.example.com/peers/peer0.org2.example.com/tls/ca.crt -c '{"funct
ion":"AddAuthSet","Args":["00000001","T0000001","QmPkunmPDeUkXhoyRQZVByijussECL19dB1v
uETNJPWK3c"]}']
2021-12-14 15:42:16.668 UTC [chaincodeCmd] chaincodeInvokeOrQuery -> INFO 001 Chainco
de invoke successful. result: status:200
fabric@fabric:~/go/src/github.com/hyperledger/fabric-samples/des_fabric$ peer chaincode query -C mychann
el -n auth -c '{"Args":["GetAllAuthsets"]}'
[{"ID":"00000000","terminal":"T0000001","authinfo":"Encryption key under cp abe encryption"},{"ID":"0000
0001","terminal":"T0000001","authinfo":"QmPkunmPDeUkXhoyRQZVByijussECL19dB1vuETNJPWK3c"}]
fabric@fabric:~/go/src/github.com/hyperledger/fabric-samples/des_fabric$
```

Fig. 7. Publish access control files on the blockchain.

```
fabric@fabric:~/go/bin$ ipfs get QmPkunmPDeUkXhoyRQZVByijussECL19dB1vuETNJPWK3c
Saving file(s) to QmPkunmPDeUkXhoyRQZVByijussECL19dB1vuETNJPWK3c
 2.99 KiB / 2.99 KiB [====================================================] 100.00% 0s
fabric@fabric:~/go/bin$ cp QmPkunmPDeUkXhoyRQZVByijussECL19dB1vuETNJPWK3c T0000001.txt
fabric@fabric:~/go/bin$ ls QmPkunmPDeUkXhoyRQZVByijussECL19dB1vuETNJPWK3c T0000001.txt
QmPkunmPDeUkXhoyRQZVByijussECL19dB1vuETNJPWK3c  T0000001.txt
```

Fig. 8. Download the access control file from the IPFS system.

```
fabric@fabric:~/cp-abe/cpabe-0.11$ cpabe-dec pub_key lebron_priv_key T0000001.txt.cpa
be
cannot decrypt, attributes in key do not satisfy policy
fabric@fabric:~/cp-abe/cpabe-0.11$ cpabe-dec pub_key kevin_priv_key T0000001.txt.cpab
e
fabric@fabric:~/cp-abe/cpabe-0.11$ ls -ltr T0000001.txt*
-rw-rw-r-- 1 fabric fabric 49 Dec 12 17:56 T0000001.txt
fabric@fabric:~/cp-abe/cpabe-0.11$ cat T0000001.txt
Congratulations. The key of T00000001 is 123456
fabric@fabric:~/cp-abe/cpabe-0.11$
```

Fig. 9. Access control policy verification.

The experimental results have shown that the scheme designed can realize the fine-grained authorized access of data encryption keys, thereby realizing one-time encryption and multiple sharing, and reducing the complexity of key management.

C. Private Data Encryption Experiment

In this experiment, the trusted terminal can collect the five parameters of air temperature, air humidity, light intensity, and GPS, and publish it on the blockchain together with the terminal number T000001 and user information Test0001. In order to protect the privacy of the data owner, the data on the chain can be sliced into sensitive data and public data. Among them, sensitive data is encrypted using encryption algorithms, and the ciphertext is published, so as to realize data desensitization and protect user privacy.

```
sectUpload.c,14 输入明文参数=[00000001 T0000001 Test0001 36.5 74]
sectUpload.c,19 开始对隐私信息[T0000001] [T0000001]进行加密...
sectUpload.c,30 加密后隐私信息[T0000001] [73A7080A12291355].END.
sectUpload.c,33 开始数据发布上链=[00000001 73A7080A12291355 Test0001 36.5 74 1220 ,204700,A,34
03.868,N,11709.432,W,001.9,336.9,170698,013.6,E*6E]
sectUpload.c,36 cCmd=[peer chaincode invoke -o localhost:7050 --ordererTLSHostnameOverride ord
erer.example.com --tls --cafile /home/fabric/go/src/github.com/hyperledger/fabric-samples/test
-network/organizations/ordererOrganizations/example.com/orderers/orderer.example.com/msp/tlsca
certs/tlsca.example.com-cert.pem -C mychannel -n sect --peerAddresses localhost:7051 --tlsRoot
CertFiles /home/fabric/go/src/github.com/hyperledger/fabric-samples/test-network/organizations
/peerOrganizations/org1.example.com/peers/peer0.org1.example.com/tls/ca.crt --peerAddresses lo
calhost:9051 --tlsRootCertFiles /home/fabric/go/src/github.com/hyperledger/fabric-samples/test
-network/organizations/peerOrganizations/org2.example.com/peers/peer0.org2.example.com/tls/ca.
crt -c '{"function":"AddDataSet","Args":["00000001","73A7080A12291355","Test0001","36.5","74",
"1220",",204700,A,3403.868,N,11709.432,W,001.9,336.9,170698,013.6,E*6E"]}']
2021-12-14 16:11:01.348 UTC [chaincodeCmd] chaincodeInvokeOrQuery -> INFO 001 Chaincode invoke
 successful. result: status:200
```

Fig. 10. Publish private data encryption on the blockchain.

Fig. 10 shows the above-mentioned data segmentation, data encryption, and publishing process. In the experiment, the user ID T00000001 in the data is divided into sensitive data by using the data segmentation technology. It is encrypted by DES encryption algorithm with key 123456, and the ciphertext 73a708a12291355 is calculated. By calling the AddDataSet function in the sect smart contract, the sensitive data and public data are published on the blockchain together, and the response code "200" indicates that the data publish is successful.

D. Encrypted Data Storage Space Experiment

The CP-ABE encryption operation will cause the ciphertext data to occupy more storage space. In order to verify the influence of CP-ABE encryption operation on the storage space of ciphertext data, three experiments are designed in this section. details as follows:

Experiment 1. Perform CP-ABE encryption on plaintext data with file sizes of 49b, 98b, 147b, and 196b. The encryption attributes and access control policy is "(sysadmin and office=1431) or (sales_staff and (executive_level ≥ 8 or office = 1231))". The storage space occupied by ciphertext and plaintext is shown in Table II.

TABLE II. Experiment 1 Storage Space Occupation Results

Plaintext size (bit)	Increment size (bit)	Cipher-text (bit)	Increment (bit)	Additional (bit)
49	-	3066	-	3017
98	49	3114	48	3016
147	49	3162	48	3015
196	49	3162	48	3014

Experiment 2. Perform CP-ABE encryption on plaintext data with file sizes of 49b, 98b, 147b, and 196b. The encryption attributes and access control policy is "(sysadmin and office=1431)". The storage space occupied by ciphertext and plaintext is shown in Table III.

TABLE III. Experiment 2 Storage Space Occupation Results

Plaintext size (bit)	Increment size (bit)	Cipher-text (bit)	Increment (bit)	Additional (bit)
49	-	921	-	872
98	49	969	48	871
147	49	3162	48	3015
196	49	3162	48	3014

Experiment 3. Perform CP-ABE encryption on "libmultipath.so.0" files with a file size of 384848b, respectively, using encryption attributes and access control policy A, namely "(sysadmin and office=1431) or (sales_staff and (executive_level ≥ 8 or office = 1231))" and B, namely "(sysadmin and office=1431)". The storage space occupied by ciphertext and plaintext is shown in Table IV.

TABLE IV. Experiment 3 Storage Space Occupation Results

Plaintext size (bit)	Access control policy	Cipher-text (bit)	Additional (bit)
384848	A	387866	3018
384848	B	385721	873

The results of Experiment 1 show that with the same encryption attributes and access control policy, the space occupied by the ciphertext is positively correlated with the space occupied by the plaintext. For example, when the plaintext space increases by 49, the ciphertext space increases by 48 in response. The results of Experiment 1 and Experiment 2 jointly show that for the same plaintext data, the space occupied by the ciphertext is positively related to the encryption attributes and access control policies adopted. For example, the data of 49b adopts two different access control policies, which occupy 3018b, 872b of storage space.

More importantly, the additional ciphertext storage space caused by encryption attributes and access control policies is fixed. The results of Experiment 3 proved the above point, such as encryption attributes and access control policy A will increase the storage of 3018b, and B will increase the storage of 873b. It should be noted that the amount of space added in Table II and Table III differs from the amount of space added in Table IV by a few bits, which is mainly caused by the line breaks in the plaintext data in the experiment. From an order of magnitude point of view, the amount of increase is the same, as shown in Fig. 11.

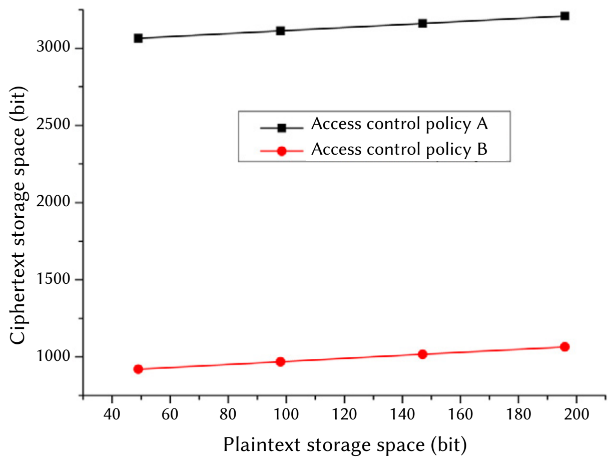

Fig. 11. The ciphertext storage space of different access control policies.

It is seen that when selecting encryption attributes and setting access control policies, to avoid occupying additional blockchain data storage space, the following three basic principles should be adhered to.

1. Choose as few encryption attributes as possible.
2. Configure access control policies as streamlined as possible.
3. For ciphertext data with large storage space, direct storage on the chain will take up too much space, and the IPFS system can be borrowed to relieve the pressure on blockchain storage.

E. Security Analysis

1. Data Access Control Policy Security

As described in section V.B, the access control right of the data collected by the security terminal is decided by the data access control policy file of the device. The CP-ABE encryption algorithm ensures that only users whose attributes and policies match exactly can decrypt the control policy file. In the scenario of consortium blockchain identity authentication and attributes issued by an authority, illegal users cannot steal confidential information. Meanwhile, the data access control file of the secure and trusted terminal can be dynamically adjusted according to the situation, such as changing the encryption key, updating the access control policy, etc., thereby ensuring the dynamic security of data access control.

2. Confidentiality of Private Data

This paper proposes a hybrid encryption scheme. The private data is encrypted with symmetric encryption algorithm, the key and device access control file are encrypted with CP-ABE algorithm, and strict access control strategy is set, which provides double insurance for the confidentiality of private data. As in section V.C, through data segmentation and private data encryption, the ciphertext is stored on the chain, which ensures the confidentiality of data under distributed data storage. The encryption key is stored in the access control policy file and encrypted based on CP-ABE algorithm, in this way, the data owner can better control the access authority of the data.

3. High Availability of Data

Both IPFS and blockchain adopt the principle of distributed technology, and the data collected by the IoT terminal is directly linked to the distributed storage. The technical characteristics of both determine the high availability of the system under single point or multi-point failure, and effectively improve the overall usability of the system.

4. Data Non-repudiation

In order to share data, publishers and users of data need to encrypt or decrypt twice, while encryption and decryption based on CP-ABE requires the support of user data attributes and logical relationship, i.e. access control policies. Therefore, the operation of data by both sides is undeniable and technically mutual trust. Specifically, distributed storage based on Fabric and IPFS ensures that data publishers cannot reject data on the blockchain. The adopted CP-ABE encryption algorithm ensures that data users obtain access rights through their own private key, and the operation of the key is undeniable. It solves the problems of data security and mutual trust in Agricultural IoT, and lays a foundation for the application of safe and reliable agricultural IoT data terminal in agricultural product quality and safety traceability system.

5. Anti-security Attack

The IoT often uses wireless communication for data transmission. If the private data is not encrypted, it can be easily eavesdropped by hackers. The privacy protection scheme proposed in this paper can resist eavesdropping attacks. At the same time, this paper encrypts the encryption key twice, which can effectively resist the plaintext key disclosure attack. For conventional IoT applications, data unauthorized access is the most common security attack or hidden danger. Using CP-ABE encryption algorithm to set fine-grained access control policies for data can effectively resist data unauthorized access attacks.

F. Performance Analysis

1. The Complexity of Key Management Is Significantly Reduced

The CP-ABE and DES hybrid encryption scheme designed in this paper realizes one-time encryption by users and flexible sharing among multiple users, which significantly reduces the complexity of key management in a symmetric cryptosystem. According to cryptographic theory, in a symmetric encryption system, if n users need to agree on a security key with each other, the number of keys required is n(n-1)/2. In this paper, the CP-ABE encryption algorithm is used to control access to the data encryption key. With n users participating, an access control policy is set for each user, that is, there are n decryption keys in total. Is the worst case. Therefore, the key management complexity is reduced from n(n-1)/2 to n.

2. Efficient and Flexible Access Control Policies

Data segmentation technology and CP-ABE encryption technology can protect data confidentiality and flexible access control, but the CP-ABE solution stores attributes and access control policies in ciphertext, which will increase the amount of ciphertext storage. It can be seen from Table II that when the access control policy A is used for encryption, the encrypted ciphertext of 49-bit plaintext data will become 3066 bits, which is 62.57 times the original. However, when the IPFS system is used to store it, the handle in the IPFS is stored on the blockchain, no matter how large the ciphertext data itself is, it will only occupy 46 bits of storage space.

According to the comparison data of IPFS storage space and ciphertext storage space shown in Fig. 12, taking the storage of 384848-bit files as an example, replacing the 387866-bit ciphertext storage with 46 bits will save 99.99% of the storage space. Obviously, this provides a new solution for setting more flexible and complex access control policies, while ensuring the efficiency of data storage.

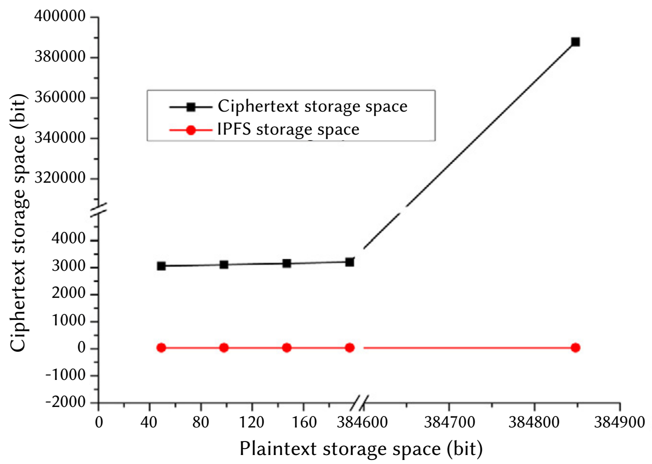

Fig. 12. Comparison of IPFS and ciphertext storage space.

3. It Has the Ability to Store and Expand the Big Data File of the Agricultural IoT

The agricultural IoT data includes not only the structured data of the experiment in this paper, but also unstructured data such as video, image, voice, GIS, etc. With the help of the IPFS file system, the corresponding smart contract can be developed to safely upload the above data to the chain.

VI. Conclusion

This paper studies the technical integration of agricultural IoT and blockchain, and designs a secure and trusted agricultural IoT blockchain terminal. With the help of CP-ABE and DES encryption algorithms, an access control and hybrid encryption scheme is designed to assure the security and authorized access control of data on the blockchain. Taking the data collection of the agricultural IoT production link as an example, the data segmentation, data encryption and access control scheme designed is verified. Through experimental verification, the terminal designed in this paper can be directly used as a node of the blockchain and IPFS to realize the release of collected data and the upload of files. However, the application scenarios of the agricultural IoT cover multiple links of agricultural production before, during and after production. The design of this system still needs to be continuously optimized according to specific business scenarios, which is also the main research direction of this work in the future. On the whole, the agricultural IoT blockchain terminal designed is a typical representative of the integrated application of blockchain and IoT technology, and has important research significance and application value.

Acknowledgment

This work was supported by the Project of Shandong Provincial Natural Science Foundation under Grant No.ZR2021QF056, Key R&D Program of Shandong Province (soft science project) under Grant No.2021RKL02002, Shandong social science planning and research project under Grant No.21CSDJ43, National Natural Science Foundation of China under Grant No. 62071320, Shandong federation of social sciences under Grant No. 2021-YYGL-32, and Tai'an Science and Technology Innovation Development Project under Grant No. 2020NS080.

References

[1] M. Torky, A. E. Hassanein, "Integrating blockchain and the internet of things in precision agriculture: Analysis, opportunities, and challenges," *Computers and Electronics in Agriculture*, vol. 178, p. 105476, 2020, doi: 10.1016/j.compag.2020.105476.

[2] S. Raveena, A. S. Edward, "Secure b-iot based smart agriculture–a brief review," in *Journal of Physics: Conference Series*, vol. 1964, 2021, p. 042006, IOP Publishing.

[3] B. Bera, A. Vangala, A. K. Das, P. Lorenz, M. K. Khan, "Private blockchain-envisioned drones-assisted authentication scheme in iot-enabled agricultural environment," *Computer Standards & Interfaces*, vol. 80, p. 103567, 2022, doi: 10.1016/j.csi.2021.103567.

[4] M. Pincheira, M. Vecchio, R. Giaffreda, S. S. Kanhere, "Cost-effective iot devices as trustworthy data sources for a blockchain-based water management system in precision agriculture," *Computers and Electronics in Agriculture*, vol. 180, p. 105889, 2021, doi: 10.1016/j.compag.2020.105889.

[5] T. H. Pranto, A. A. Noman, A. Mahmud, A. K. M. B. Haque, "Blockchain and smart contract for iot enabled smart agriculture," *PeerJ Computer Science*, vol. 7, p. e407, 2021, doi: 10.7717/peerj-cs.407.

[6] L. Hang, I. Ullah, D. Kim, "A secure fish farm platform based on blockchain for agriculture data integrity," *Computers and Electronics in Agriculture*, vol. 170, p. 105251, 2020, doi: 10.1016/j.compag.2020.105251.

[7] O. Lamtzidis, D. Pettas, J. Gialelis, "A novel combination of distributed ledger technologies on internet of things: Use case on precision agriculture," *Applied System Innovation*, vol. 2, no. 3, p. 30, 2019.

[8] W. Keke, C. Zhide, X. Jian, "Efficient traceability system for quality and safety of agricultural products based on consortium blockchain," *Journal of Computer Applications*, vol. 39, no. 8, p. 2438, 2019.

[9] Y. Li'na, Z. Guofeng, J. Jingdun, G. Wanlin, Z. Ganghong, T. Sha, "Modern agricultural product supply chain based on block chain technology," *Nongye Jixie Xuebao/Transactions of the Chinese Society for Agricultural Machinery*, vol. 48, pp. 387–393, 2017.

[10] S. Namasudra, G. C. Deka, P. Johri, M. Hosseinpour, A. H. Gandomi, "The revolution of blockchain: State-of-the-art and research challenges," *Archives of Computational Methods in Engineering*, vol. 28, no. 3, pp. 1497–1515, 2021.

[11] A. A. Khan, M. Uddin, A. A. Shaikh, A. A. Laghari, A. E. Rajput, "Mf-ledger: Blockchain hyperledger sawtooth-enabled novel and secure multimedia chain of custody forensic investigation architecture," *IEEE Access*, vol. 9, pp. 103637–103650, 2021, doi: 10.1109/ACCESS.2021.3099037.

[12] G. Zhang, X. Chen, B. Feng, J. Wen, "Research on a safe and reliable agricultural product traceability system driven by permissioned blockchain technology," in *The International Conference on Image, Vision and Intelligent Systems (ICIVIS 2021)*, 2022, pp. 955–966, Springer.

[13] M. Uddin, "Blockchain medledger: Hyperledger fabric enabled drug traceability system for counterfeit drugs in pharmaceutical industry," *International Journal of Pharmaceutics*, vol. 597, p. 120235, 2021.

[14] M. Jemel, A. Serhrouchni, "Decentralized access control mechanism with temporal dimension based on blockchain," in *14th IEEE International Conference on Ebusiness Engineering, ICEBE 2017, Shanghai, China, November 4-6, 2017*, 2017, pp. 177–182, IEEE Computer Society.

[15] Z. Zhang, X. Ren, "Data security sharing method based on CP-ABE and blockchain," *Journal of Intelligent & Fuzzy Systems*,vol. 40, no. 2, pp. 2193–2203, 2021, doi: 10.3233/JIFS-189318.

[16] X. Wang, X. Jiang, Y. Li, "Model for data access control and sharing based on blockchain," *Ruan Jian Xue Bao/Journal of Software*, vol. 30, no. 6, pp. 1661–1669, 2019.

[17] Y. Zhang, B. Li, B. Liu, J. Wu, Y. Wang, X. Yang, "An attribute-based collaborative access control scheme using blockchain for iot devices," *Electronics*, vol. 9, no. 2, p. 285, 2020.

[18] G. Zhang, X. Chen, B. Feng, X. Guo, X. Hao, H. Ren, C. Dong, Y. Zhang, "BCST-APTS: blockchain and CP-ABE empowered data supervision, sharing, and privacy protection scheme for secure and trusted agricultural product traceability system," *Security and Communication Networks*, vol. 2022, pp. 2958963:1–2958963:11, 2022, doi: 10.1155/2022/2958963.

[19] A. Sahai, B. Waters, "Fuzzy identity-based encryption," in *International Conference on Theory & Applications of Cryptographic TechniquesAnnual*, 2005, pp. 457–473, Springer.

[20] V. Goyal, O. Pandey, A. Sahai, B. Waters, "Attribute- based encryption

for fine-grained access control of encrypted data," in *Proceedings of the 13th ACM Conference on Computer and Communications Security, CCS 2006, Alexandria, VA, USA, October 30 - November 3, 2006*, 2006, pp. 89–98, ACM.
[21] J. Bethencourt, A. Sahai, B. Waters, "Ciphertext-policy attribute-based encryption," in *2007 IEEE symposium on security and privacy (SP'07)*, 2007, pp. 321–334, IEEE.
[22] L. Zhang, W. Zeng, Z. Jin, Y. Su, H. Chen, "A research on traceability technology of agricultural products supply chain based on blockchain and ipfs," *Security and Communication Networks*, vol. 2021, 2021.
[23] B. W. John Bethencourt, Amit Sahai, "Ciphertext- policy attribute-based encryption," *[Online]*, vol. 2021, 2021.

Guofeng Zhang

He was born in June 1986. He graduated from China Agricultural University with a doctor's degree in 2020 and North China University of technology with a master's degree in 2013. At present, he works in Taishan University and is now a lecturer. The main research fields are blockchain, Internet of things, information security, etc.

Xiao Chen

She was born in October 1986 and graduated from China Agricultural University with a master's degree in 2012. Since 2012, she has been working in Taishan University and is now a lecturer. At present, the main research directions are digital economy and blockchain technology.

Lei Zhang

He was born in June 1983, graduated from East China Normal University in Shanghai 2009, with a master's degree. I have been working in Shandong Academy of Macroeconomic Research since 2010.Now I am the deputy director of the investment and Financing Policy Research Institute.My main research directions are digital economy, industrial economy, etc. I have published 1 monograph, 12 journal articles, presided over and completed 4 provincial social science projects, and won 6 provincial awards such as the provincial social science outstanding achievement award.

Bin Feng

He received the BS degree in Computer Science and Technology in 2002 from the LiaoCheng University, Shandong, China, and the MS degree in software engineering in 2006 from the Dalian University of Technology, Dalian, China. He has been an assistant in TaiShan University among 2002–2004. He is currently a full engineer of Computer Science at Dalian University of Technology, Dalian, China, since 2006. Since 2011, he is currently pursuing his PhD degree in computer software and theory from the Dalian University of Technology, Dalian, China. His research interests include data hiding, image processing, network and information security.

Xuchao Guo

He received Bachelor degree in Computer Science in 2015 and his Master's degree in 2018 from Shandong Agricultural University, China. He is currently Ph.D. student in the College of Information and Electrical Engineering, China Agricultural University, China. He is mainly engaged in natural language processing and knowledge graph. His research interests include: deep learning, natural language processing, computer vision, complex network analysis.

Jingyun Liang

She graduated from Shandong University in 2005 with a master's degree in Applied Chemistry. She worked in Shandong Agricultural University from 2005 to 2011 and has worked in the Institute of agricultural quality standards and testing technology of Shandong Academy of Agricultural Sciences since 2011. The main research direction is the analysis and risk assessment of toxins and pesticide residues in agricultural products. Presided over one sub project of the national risk assessment project and two projects of Shandong Provincial Department of science and technology, published 5 SCI papers and applied for more than 10 invention patents.

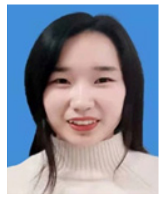

Yanan Zhang

She was born in Heze, Shandong, China, in 1997.She is currently pursuing a master's degree, Majored in electronic information in School of Information Science and Engineering, Jinan University, Jinan, Shandong, China. From 2020 to 2022, She has been researching on blockchain techniques, especially on fabric. Her research interests include blockchain data security, privacy protection.

Variational Learning for the Inverted Beta-Liouville Mixture Model and Its Application to Text Categorization

Yongfa Ling[1], Wenbo Guan[2], Qiang Ruan[3], Heping Song[4]*, Yuping Lai[5]

[1] School of Artificial Intelligence, Hezhou University, Hezhou (China)
[2] Institute of Information Engineering, CAS, Beijing (China)
[3] DigApis Information Security Technology Co., Ltd., Nantong, Jiangsu (China)
[4] School of Computer Science and Communication Engineering, Jiangsu University, Zhenjiang (China)
[5] School of Cyberspace Security, Beijing University of Posts and Telecommunications, Beijing (China)

Received 24 November 2021 | Accepted 22 June 2022 | Published 10 August 2022

Abstract

The finite invert Beta-Liouville mixture model (IBLMM) has recently gained some attention due to its positive data modeling capability. Under the conventional variational inference (VI) framework, the analytically tractable solution to the optimization of the variational posterior distribution cannot be obtained, since the variational object function involves evaluation of intractable moments. With the recently proposed extended variational inference (EVI) framework, a new function is proposed to replace the original variational object function in order to avoid intractable moment computation, so that the analytically tractable solution of the IBLMM can be derived in an effective way. The good performance of the proposed approach is demonstrated by experiments with both synthesized data and a real-world application namely text categorization.

Keywords

Bayesian Inference, Extended Variational Inference, Inverted Beta-Liouville Distribution, Mixture Model, Text Categorization.

DOI: 10.9781/ijimai.2022.08.006

I. Introduction

Positive data arise naturally in many real-world applications, such as object clustering [1], scene categorization [2], image segmentation [3], and object detection [4]. During the last decade, many non-Gaussian mixture models, e.g., the finite inverted Dirichlet mixture model (IDMM) [5], [6], the finite generalized inverted Dirichlet mixture model (GIDMM) [7], the finite generalized Gamma mixture model (GGaMM) [3] and the finite inverted Beta-Liouville mixture model (IBLMM) [8], were proposed to model and analyze positive data due to their powerful modeling capabilities. Among these mixture models, the IBLMM is one of the most popular approaches for modeling univariate and multivariate positive data. For example, the IBLMM is shown to be very flexible and powerful in analyzing and clustering text documents [8], therefore, modeling positive data with the IBLMM is well-motivated.

The major task in modeling the data with the finite mixture models is the learning of the model parameters, which refers to both estimating the model parameters and determining the number of components (i.e., the model complexity). A variety of approaches can be applied to address this problem, such as the expectation maximization (EM) algorithm [9], the Markov chain Monte Carlo (MCMC) [10], the expectation propagation (EP) [11] and the variational inference (VI) [12]. Among these approaches, the VI has been the most popular method. Much of its popularity is due to the fact that it may scale well to large applications. The main idea behind the VI is to find a approximate distribution for the intractable real posterior distribution by minimizing the Kullback-Leibler (KL) divergence of these two distributions. This is equivalent to maximizing the evidence lower bound (ELBO), which is also known as the variational objective function. Unfortunately, it is infeasible to obtain an analytical solution to the VI for many non-Gaussian mixtures, such as the IDMM, the GIDMM, the GGaMM and the IBLMM, since some computationally intractable moments exist in the ELBO. This problem can be solved by the recently proposed extended variational inference (EVI)[13]. The main idea behind the EVI framework is that the optimal solutions can be obtained by means of maximizing a lower bound of the ELBO. This bound can be obtained by introducing some tractable approximations to the original objective function.

Motivated by the powerful modeling capability of the IBLMM and the excellent performance achieved by the EVI framework, the EVI framework is applied to learn the IBLMM. The major contributions of this work can be summarized as follows. First, the analytical solution within the EVI framework for the IBLMM is derived. In this framework, the estimated values of all the involved parameters and the number of components can be simultaneously obtained. Second, the proposed approach is used in an important real-world application namely text categorization. Synthesized and real data evaluations demonstrate the good performance of the model trained by the proposed approach.

The reminder of this paper is organized as follows. In Section II, a brief review of the IBLMM is given. In Section III, the Bayesian learning algorithm with the EVI is derived. The experimental results on synthesized and real datasets are reported in Section IV. Finally, some conclusions are drawn in Section V.

* Corresponding author.

E-mail address: songhp@ujs.edu.cn (H. Song).

II. Preliminaries

A brief overview of the IBLMM is given first in this section. Then, a complete Bayesian framework for this model is presented.

A. Finite Inverted Beta-Liouville Mixture Model

If a D-dimensional random vector $\mathrm{x} = [x_1, \dots x_D]^T$ contains positive values, the underlying distribution of x can be modeled by the inverted Beta-Liouville (IBL) distribution. The probability density function (PDF) of the IBL distribution is given by [14]

$$p(\mathbf{x} \mid \boldsymbol{\alpha}, u, v) = \frac{\Gamma(\sum_{d=1}^{D}\alpha_d)\Gamma(u+v)}{\Gamma(u)\Gamma(v)} \prod_{d=1}^{D} \frac{x_d^{\alpha_d - 1}}{\Gamma(\alpha_d)} \times \left(\sum_{d=1}^{D} x_d\right)^{u - \sum_{d=1}^{D}\alpha_d} \left(1 + \sum_{d=1}^{D} x_d\right)^{-(u+v)} \quad (1)$$

where $\boldsymbol{\alpha} = [\alpha_1, \dots, \alpha_D]^{\mathrm{T}}$, $\Gamma(\cdot)$ is the Gamma function defined as $\Gamma(a) = \int_0^{\infty} t^{a-1} e^{-t} dt$.

To model the multimodality of the observed data $\boldsymbol{X} = [\boldsymbol{x}_1, \dots, \boldsymbol{x}_N]$, the mixture modeling technique [15] is used to construct the IBLMM with the PDF as follows

$$p(\mathbf{X} \mid \boldsymbol{\Lambda}, \mathbf{u}, \mathbf{v}, \boldsymbol{\pi}) = \prod_{n=1}^{N} \sum_{m=1}^{M} \pi_m \, p(\mathbf{x_n} \mid \boldsymbol{\alpha}_m, u_m, v_m) \quad (2)$$

where M is the number of components, $\boldsymbol{\pi} = [\pi_m, \dots, \pi_M]^{\mathrm{T}}$ is the mixing weights, $\boldsymbol{\Lambda} = [\boldsymbol{\alpha}_1, \dots, \boldsymbol{\alpha}_M]$, $\boldsymbol{u} = [u_1, \dots, u_M]^{\mathrm{T}}$ and $\boldsymbol{v} = [v_1, \dots, v_M]^{\mathrm{T}}$ denote the parameter matrices.

B. Bayesian Framework for IBLMM

It is convenient to turn the mixture model in (2) into a latent variable model. For each vector $\boldsymbol{x}_n$, a latent vector variable $\boldsymbol{z}_n = [\mathrm{z}_{n1}, \dots, \mathrm{z}_{nM}]^{\mathrm{T}}$ is assigned, such that $\mathrm{z}_{nM} \in \{0,1\}$, $\sum_{m=1}^{M} \mathrm{z}_{nM} = 1$ and $\mathrm{z}_{nM} = 1$ if $\boldsymbol{x}_n$ is drawn from the mth component and 0 otherwise. Then, the latent variable model of IBLMM can be written as

$$p(\mathbf{Z} \mid \boldsymbol{\pi}) = \prod_{n=1}^{N} \prod_{m=1}^{M} \pi_m^{z_{nm}} \quad (3)$$

$$p(\mathbf{X}, \mathbf{Z} \mid \boldsymbol{\Lambda}, \mathbf{u}, \mathbf{v}) = \prod_{n=1}^{N} \prod_{m=1}^{M} p\left(\mathbf{x}_n \mid \boldsymbol{\alpha}_m, u_m, v_m\right)^{z_{nm}} \quad (4)$$

where $\boldsymbol{Z} = [\boldsymbol{z}_1, \dots, \boldsymbol{z}_M]^{\mathrm{T}}$.

To formulate a full Bayesian mixture model, the conjugate priors on parameters $\boldsymbol{\Lambda}$, $\boldsymbol{u}$, $\boldsymbol{v}$, and $\boldsymbol{\pi}$ have to be designated as follows:

$$p(\boldsymbol{\Lambda}) = \mathcal{G}(\boldsymbol{\Lambda} \mid \mathbf{g}, \mathbf{h}) = \prod_{m=1}^{M} \prod_{d=1}^{D} \mathcal{G}\left(\alpha_{md} \mid g_{md}, h_{md}\right) \quad (5)$$

$$p(\mathbf{u}) = \mathcal{G}(\mathbf{u} \mid \mathbf{s}, \mathbf{t}) = \prod_{m=1}^{M} \mathcal{G}\left(u_m \mid s_m, t_m\right) \quad (6)$$

$$p(\mathbf{v}) = \mathcal{G}(\mathbf{v} \mid \mathbf{p}, \mathbf{q}) = \prod_{m=1}^{M} \mathcal{G}\left(v_m \mid p_m, q_m\right) \quad (7)$$

$$p(\boldsymbol{\pi}) = \mathrm{Dir}(\boldsymbol{\pi} \mid \mathbf{c}) = \frac{\Gamma(\sum_{m=1}^{M} c_m)}{\prod_{m=1}^{M} \Gamma(c_m)} \prod_{m=1}^{M} \pi_m^{c_m - 1} \quad (8)$$

where $\boldsymbol{g} = \{g_{md}\}$, $\boldsymbol{h} = \{h_{md}\}$, $\boldsymbol{s} = \{s_m\}$, $\boldsymbol{t} = \{t_m\}$, $\boldsymbol{p} = \{p_m\}$, $\boldsymbol{q} = \{q_m\}$, $\boldsymbol{c} = \{c_m\}$, $\mathcal{G}(\cdot)$ and $\mathrm{Dir}(\cdot)$ denote the Gamma distribution and the Dirichlet distribution, respectively.

Following the Bayes' theorem and combining (3), (4), (5), (6), (7) and (8), the joint distribution of the observation $\boldsymbol{X}$ and all the random variables $\boldsymbol{\Theta} = \{\boldsymbol{Z}, \boldsymbol{\Lambda}, \boldsymbol{u}, \boldsymbol{v}, \boldsymbol{\pi}\}$ is given by:

$$p(\mathbf{X}, \boldsymbol{\Theta}) = p(\mathbf{X}, \mathbf{Z} \mid \boldsymbol{\Lambda}, \mathbf{u}, \mathbf{v}) p(\mathbf{Z} \mid \boldsymbol{\pi}) p(\boldsymbol{\pi}) p(\boldsymbol{\Theta}) p(\mathbf{u}) p(\mathbf{v}) \quad (9)$$

this equation has illustrated the relations of all the random variables entailed in the Baysian estimation of IBLMM. $\boldsymbol{Z}$ is the latent variable that indicates from which component the data is generated. π is the weight of each component. The other letters are the parameters of each IBLM.

III. Learning the Model

A. Extended Variational Inference

The VI framework [12] is commonly employed to estimate the parameters and determine the optimal number of components of the mixture models. The major goal is to find an approximate distribution $q(\boldsymbol{\Theta})$ for the true posterior distribution $p(\boldsymbol{\Theta} \mid \boldsymbol{X})$. The optimal $q(\boldsymbol{\Theta})$ can be obtained by maximizing the ELBO as follows:

$$\mathcal{L}(q) = \langle \ln p(\mathbf{X}, \boldsymbol{\Theta}) \rangle_q - \langle \ln q(\boldsymbol{\Theta}) \rangle_q \quad (10)$$

where $\langle \cdot \rangle_q$ denotes the expectation regarding the distribution q. Note that the $\mathcal{L}(q)$ is not analytically tractable for most of the non-Gaussian mixture models, such as the IDMM, the GIDMM, the GGaMM and the IBLMM, as (9) involves intractable moments. The recently proposed EVI framework [13] offers an effective way to proposed EVI framework [13] offers an effective way to framework is that if a "helping function" $\widetilde{p}(\mathbf{X\Theta})$, which satisfies the constraint $\mathrm{E}_q[\ln p(\mathbf{X}, \boldsymbol{\Theta})] \geq \mathrm{E}_q[\ln \widetilde{p}(\mathbf{X}, \boldsymbol{\Theta})]$, can satisfies the constraint $\mathrm{E}_q[\ln p(\mathbf{X}, \boldsymbol{\Theta})] \geq \mathrm{E}_q[\ln \widetilde{p}(\mathbf{X}, \boldsymbol{\Theta})]$, can be found, then the optimal solutions can be reached $\mathcal{L}(q)$. This bound is given by

$$\mathcal{L}(q) \geq \widetilde{\mathcal{L}}(q) = \mathrm{E}_q[\ln \widetilde{p}(\mathbf{X}, \boldsymbol{\Theta})] - \mathrm{E}_q[q(\boldsymbol{\Theta})] \quad (11)$$

To formulate a computationally tractable expression for the $\widetilde{\mathcal{L}}(q)$, the simplest approach called the mean-field approach is adopted which factorizes the $q(\boldsymbol{\Theta})$ as follows

$$q(\boldsymbol{\Theta}) = \prod_{n=1}^{N} \prod_{m=1}^{M} q\left(z_{nm}\right) \prod_{m=1}^{M} \prod_{d=1}^{D} q\left(\alpha_{md}\right) \times \prod_{m=1}^{M} [q(u_m) q(v_m) q(\pi_m)] \quad (12)$$

Then, the optimal form of $q(\Theta_k)$, denoted by $q^*(\Theta_k)$ in this case, is given by

$$\ln q_k^*(\Theta_k) = \langle \ln \widetilde{p}(\mathbf{X}, \Theta) \rangle_{s \neq k} + \mathrm{Cst} \quad (13)$$

where $\langle \cdot \rangle_{s \neq k}$ denotes the expectation regards all factors $q_s(\Theta_s)$ except for $s = k$ and "Cst" denotes a normalizing constant. In the EVI framework, all factors $q_s(\Theta_s)$ are need to be initiate first and then each factor is updated by updating the hyper-parameters.

B. Variational Distribution

This section details how (13) is applied to compute the variational factors. Note that the EVI is essentially iterative, since it represents a distribution factor applying knowledge about other factors. Following the principles of the EVI framework, the expectation of the joint distribution's logarithm is first calculated as

$$\begin{aligned}\langle \ln p(\mathbf{X},\mathbf{\Theta})\rangle &= \sum_{n=1}^{N}\sum_{m=1}^{M}\langle z_{nm}\rangle\{\langle \ln \pi_m\rangle + \mathcal{R}_m + \mathcal{F}_m \\ &+ \sum_{d=1}^{D}(\langle\alpha_{md}\rangle - 1)\ln x_{nd} + \ln\left(\sum_{d=1}^{D}x_{nd}\right)(\langle u_m\rangle \\ &- \sum_{d=1}^{D}\langle\alpha_{md}\rangle\Bigg) - (\langle u_m\rangle + \langle v_m\rangle)\ln\left(1+\sum_{d=1}^{D}x_{nd}\right)\Bigg\} \\ &+ \sum_{m=1}^{M}\sum_{d=1}^{D}[(g_{md}-1)\langle\ln\alpha_{md}\rangle - h_{md}\langle\alpha_{md}\rangle] \\ &+ \sum_{m=1}^{M}[(s_m - 1)\langle\ln u_m\rangle - t_m\langle u_m\rangle] \\ &+ \sum_{m=1}^{M}[(p_m - 1)\langle\ln v_m\rangle - q_m\langle v_m\rangle] \\ &+ \sum_{m=1}^{M}(c_m - 1)\langle\ln\pi_m\rangle + \text{Cst}\end{aligned} \tag{14}$$

where $\mathcal{R}_m = \left\langle \ln\frac{\Gamma(\sum_{d=1}^{D}\alpha_{md})}{\prod_{d=1}^{D}\Gamma(\alpha_{md})}\right\rangle$, $\mathcal{F}_m = \left\langle \ln\frac{\Gamma(u_m+v_m)}{\Gamma(u_m)\Gamma(v_m)}\right\rangle$. It is noteworthy that (14) is not available in a closed form because it includes the intractable moments $\mathcal{R}_m, \mathcal{F}_m$. Following the principles of the aforementioned EVI framework, two "helping functions" $\widetilde{\mathcal{R}}_m, \widetilde{\mathcal{F}}_m$, satisfying $\mathcal{R}_m \geq \widetilde{\mathcal{R}}_m$, $\mathcal{F}_m \geq \widetilde{\mathcal{F}}_m$, respectively have to be found. According to [16], $\widetilde{\mathcal{R}}_m$ and $\widetilde{\mathcal{F}}_m$ are obtained as follows:

$$\begin{aligned}\widetilde{\mathcal{R}}_m &= \ln\frac{\Gamma(\sum_{d=1}^{D}\bar{\alpha}_{md})}{\prod_{d=1}^{D}\Gamma(\bar{\alpha}_{md})} + \sum_{d=1}^{D}\left[\Psi\left(\sum_{k=1}^{D}\bar{\alpha}_{mk}\right) - \Psi(\bar{\alpha}_{md})\right] \\ &\times[\langle\ln\alpha_{md}\rangle - \ln\bar{\alpha}_{md}]\bar{\alpha}_{md}\end{aligned} \tag{15}$$

$$\begin{aligned}\widetilde{\mathcal{F}}_m &= \ln\frac{\Gamma(\bar{u}_m+\bar{v}_m)}{\Gamma(\bar{u}_m)\Gamma(\bar{v}_m)} + [\Psi(\bar{u}_m+\bar{v}_m) - \Psi(\bar{u}_m)] \\ &\times(\langle\ln u_m\rangle - \ln\bar{u}_m)\bar{u}_m + [\Psi(\bar{u}_m+\bar{v}_m) - \Psi(\bar{v}_m)] \\ &\times(\langle\ln v_m\rangle - \ln\bar{v}_m)\bar{v}_m,\end{aligned} \tag{16}$$

where

$$\begin{aligned}\bar{\alpha}_{md} &= \langle\alpha_{md}\rangle, \bar{u}_m = \langle u_m\rangle \\ \bar{v}_m &= \langle v_m\rangle, \Psi(a) = \frac{\partial\ln\Gamma(a)}{\partial a}\end{aligned} \tag{17}$$

Insert (15) and (16) into (14) then a lower bound to $\langle \ln p(\boldsymbol{X},\boldsymbol{\Theta})\rangle$ is obtained as

$$\begin{aligned}\langle \ln\tilde{p}(\mathbf{X},\mathbf{\Theta})\rangle &= \sum_{n=1}^{N}\sum_{m=1}^{M}\langle z_{nm}\rangle\{\langle\ln\pi_m\rangle + \widetilde{\mathcal{R}}_m + \widetilde{\mathcal{F}}_m \\ &+ \sum_{d=1}^{D}(\langle\alpha_{md}\rangle - 1)\ln x_{nd} + \ln\left(\sum_{d=1}^{D}x_{nd}\right) \\ &\times\left(\langle u_m\rangle - \sum_{d=1}^{D}\langle\alpha_{md}\rangle\right) - (\langle u_m\rangle + \langle v_m\rangle) \\ &\times\ln\left(1+\sum_{d=1}^{D}x_{nd}\right)\Bigg\} + \sum_{m=1}^{M}\sum_{d=1}^{D}[(g_{md}-1) \\ &\times\langle\ln\alpha_{md}\rangle - h_{md}\langle\alpha_{md}\rangle] \\ &+ \sum_{m=1}^{M}[(s_m-1)\langle\ln u_m\rangle - t_m\langle u_m\rangle] \\ &+ \sum_{m=1}^{M}[(p_m-1)\langle\ln v_m\rangle - q_m\langle v_m\rangle] \\ &+ \sum_{m=1}^{M}(c_m-1)\langle\ln\pi_m\rangle + \text{Cst.}\end{aligned} \tag{18}$$

Now, $\boldsymbol{\alpha}$, $\boldsymbol{u}$, and $\boldsymbol{v}$ are the i. i. d. variables. Details about solving the optimal variational factors using (13) is given as follows.

1. $q^*(\boldsymbol{Z})$: Including all terms that do not depend upon z_{nm} into a constant term, the equation (19) is obtained as follows

$$\ln q^*(z_{nm}) = \sum_{n=1}^{N}\sum_{m=1}^{M} z_{nm}\ln\rho_{nm} + \text{Cst} \tag{19}$$

where

$$\begin{aligned}\ln\rho_{nm} &= \ln\pi_m + \widetilde{\mathcal{R}}_m + \widetilde{\mathcal{F}}_m + \sum_{d=1}^{D}(\bar{\alpha}_{md} - 1)\ln x_{nd} \\ &+ \left(\bar{u}_m - \sum_{d=1}^{D}\bar{\alpha}_{md}\right)\ln\left(\sum_{d=1}^{D}x_{nd}\right) \\ &-(\bar{u}_m + \bar{v}_m)\ln\left(1+\sum_{d=1}^{D}x_{nd}\right)\end{aligned} \tag{20}$$

Taking exponential of both sides of (19), $q^*(\boldsymbol{Z})$ is recognized to be a categorical density

$$q^*(\mathbf{Z}) = \prod_{n=1}^{N}\prod_{m=1}^{M} r_{nm}^{z_{nm}} \tag{21}$$

where

$$r_{nm} = \frac{\rho_{nm}}{\sum_{m=1}^{M}\rho_{nm}} \tag{22}$$

where r_{nm} are nonnegative and have a unit sum.

2. $q^*(\boldsymbol{\Lambda})$: Absorbing any terms independent of $\boldsymbol{\alpha}_{md}$ into the additive constant results in

$$\ln q^*(\alpha_{md}) = (g^*_{md} - 1)\ln\alpha_{md} - h^*_{md}\alpha_{md} + \text{Cst} \tag{23}$$

where g^*_{md} and h^*_{md} are defined by

$$g^*_{md} = g_{md} + \left[\Psi\left(\sum_{k=1}^{D}\bar{\alpha}_{md}\right) - \Psi(\bar{\alpha}_{md})\right]\bar{\alpha}_{md}\sum_{n=1}^{N}\langle z_{nm}\rangle \tag{24}$$

$$h^*_{md} = h_{md} - \sum_{n=1}^{N}\langle z_{nm}\rangle\left[\ln x_{nd} - \ln\left(\sum_{d=1}^{D}x_{nd}\right)\right] \tag{25}$$

Taking the exponential of both sides of (23), the equation (26) is obtained as follows

$$q^*(\mathbf{\Lambda}) = \prod_{m=1}^{M}\prod_{d=1}^{D}\mathcal{G}(\alpha_{md} \mid g^*_{md}, h^*_{md}) \tag{26}$$

3. $q^*(\boldsymbol{u})$: Any terms which are independent of u_m will be absorbed into the additive constant as

$$\ln q^*(u_m) = (s^*_m - 1)\ln u_m - t^*_{md}u_m + \text{Cst} \tag{27}$$

where s^*_m and t^*_m are given by

$$s^*_m = s_m + [\Psi(\bar{u}_m + \bar{v}_m) - \Psi(\bar{u}_m)]\bar{u}_m\sum_{n=1}^{N}\langle z_{nm}\rangle \tag{28}$$

$$t^*_m = t_m - \sum_{n=1}^{N}\langle z_{nm}\rangle\left[\ln\left(\sum_{d=1}^{D}x_{nd}\right) - \ln\left(1+\sum_{d=1}^{D}x_{nd}\right)\right] \tag{29}$$

Taking the exponential of both sides of (27), the equation (30) is obtained as follows

$$q(\mathbf{u}) = \prod_{m=1}^{M}\mathcal{G}(u_m \mid s^*_m, t^*_m) \tag{30}$$

4. $q^*(\boldsymbol{v})$: Considering the derivation of the update equation for the factor , the logarithm of the optimized factor is given by

$$\ln q^*(v_m) = (p_m^* - 1)\ln v_m - q_{md}^* v_m + \mathrm{Cst} \tag{31}$$

where

$$p_m^* = p_m + [\Psi(\bar{u}_m + \bar{v}_m) - \Psi(\bar{v}_m)]\bar{v}_m \sum_{n=1}^{N} \langle z_{nm} \rangle \tag{32}$$

$$q_m^* = q_m + \sum_{n=1}^{N} \langle z_{nm} \rangle \ln\left(1 + \sum_{d=1}^{D} x_{nd}\right) \tag{33}$$

It is obvious that (31) has a similar form as to the logarithm of the Gamma prior density. Similarly, the equation (34) is obtained as follows

$$q^*(\mathbf{v}) = \prod_{m=1}^{M} \mathcal{G}(v_m \mid p_m^*, q_m^*) \tag{34}$$

5. $q^*(\boldsymbol{\pi})$: Keeping only terms that have a functional dependence on π_m, the equation (35) is obtained as follows

$$\ln q^*(\pi_m) = (c_m^* - 1)\ln \pi_m + \mathrm{Cst} \tag{35}$$

where

$$c_m^* = \sum_{n=1}^{N} \langle z_{nm} \rangle + c_m \tag{36}$$

Taking the exponential of both sides of (35), the equation (37) is obtained as follows

$$p(\boldsymbol{\pi}) = \mathrm{Dir}(\boldsymbol{\pi} \mid \mathbf{c}^*) = \frac{\Gamma(\sum_{m=1}^{M} c_m^*)}{\prod_{m=1}^{M} \Gamma(c_m^*)} \prod_{m=1}^{M} \pi_m^{c_m^* - 1} \tag{37}$$

All the expected values in the above equations are evaluated by

$$\bar{\alpha}_{md} = \frac{g_{md}^*}{h_{md}^*}, \langle \ln \alpha_{md} \rangle = \Psi(g_{md}^*) - \ln(h_{md}^*) \tag{38}$$

$$\bar{u}_m = \frac{s_m^*}{t_m^*}, \langle \ln u_m \rangle = \Psi(s_m^*) - \ln(t_m^*) \tag{39}$$

$$\bar{v}_m = \frac{p_m^*}{q_m^*}, \langle \ln v_m \rangle = \Psi(p_m^*) - \ln(q_m^*) \tag{40}$$

$$\langle z_{nm} \rangle = r_{nm}, \langle \pi_m \rangle = \frac{c_m^*}{\sum_{m=1}^{M} c_m^*}$$
$$\langle \ln \pi_m \rangle = \Psi(c_m^*) - \Psi\left(\sum_{m=1}^{M} c_m^*\right) \tag{41}$$

C. Full Variational Learning Algorithm

With the above obtained variational factors in hand, it is straightforward to evaluate the lower bound (11) for this model. In practice, it is useful to be able to monitor the bound during the re-estimation in order to test for convergence. The lower bound (11) is given by

$$\tilde{\mathcal{L}}(q) = \langle \ln \tilde{p}(\mathbf{X}, \boldsymbol{\Theta}) \rangle - \langle \ln q^*(\mathbf{Z}) \rangle - \langle \ln q^*(\boldsymbol{\Lambda}) \rangle - \langle \ln q^*(\mathbf{u}) \rangle - \langle \ln q^*(\mathbf{v}) \rangle - \langle \ln q^*(\boldsymbol{\pi}) \rangle \tag{42}$$

where $\langle \ln \tilde{p}(\mathbf{X}, \boldsymbol{\Theta}) \rangle$ is computed using (18). The other terms in the bound are easily evaluated to give the following results:

$$\langle \ln q^*(\mathbf{Z}) \rangle = \sum_{n=1}^{N} \sum_{m=1}^{M} r_{nm} \ln r_{nm} \tag{43}$$

$$\langle \ln q^*(\boldsymbol{\Lambda}) \rangle = \sum_{m=1}^{M} \sum_{d=1}^{D} [g_{md}^* \ln h_{md}^* - \ln \Gamma(g_{md}^*) + (g_{md}^* - 1)\langle \ln \alpha_{md} \rangle - h_{md}^* \langle \alpha_{md} \rangle] \tag{44}$$

$$\langle \ln q^*(\mathbf{u}) \rangle = \sum_{m=1}^{M} [s_m^* \ln t_m^* - \ln \Gamma(s_m^*) + (s_m^* - 1)\langle \ln u_m \rangle - t_m^* \langle u_m \rangle] \tag{45}$$

$$\langle \ln q^*(\mathbf{v}) \rangle = \sum_{m=1}^{M} [p_m^* \ln q_m^* - \ln \Gamma(p_m^*) + (p_m^* - 1)\langle \ln v_m \rangle - q_m^* \langle v_m \rangle] \tag{46}$$

$$\langle \ln q^*(\boldsymbol{\pi}) \rangle = \ln \frac{\Gamma(\sum_{m=1}^{M} c_m^*)}{\prod_{m=1}^{M} \Gamma(c_m^*)} + \sum_{m=1}^{M} (c_m^* - 1)\langle \ln \pi_m \rangle \tag{47}$$

The analytically tractable solution for Bayesian estimation of the IBLMM can be obtained in a similar way to the conventional EM algorithm. This inference algorithm is summarized in the Algorithm 1.

Algorithm 1. Algorithm for EVI-based Bayesian IBLMM

1. Set the initial values of M, g_{md}, h_{md}, s_m, t_m, p_m, q_m, c_m.
2. Initialize r_{nm} by K-Means algorithm
3. **repeat**
4. The variational E-step: Update $q^*(\boldsymbol{Z})$ according to (21).
5. The variational M-step: Update $q^*(\boldsymbol{\Lambda})$, $q^*(\boldsymbol{u})$, $q^*(\boldsymbol{v})$ and $q^*(\boldsymbol{\pi})$ according to (26), (30), (34), and (37), respectively.
6. **until** Stop criterion is reached.
7. Determine the best number of components M via annihilating the components with mixing weights $\pi_m \leq 10^{-5}$.

IV. Experiments and Results

In this section, the proposed variational method refered to as EVI-IBLMM is validated through both synthesized datasets and real datasets. The goal of the synthesized dataset validation is to investigate the accuracy of the EVI-IBLMM algorithm in terms of parameter estimation and model selection. The goal of the real dataset validation is to compare the EVI-IBLMM to three other methods: the IDMM applying the EVI technique (EVI-IDMM) [6], the GIDMM applying the EVI technique (EVI-GIDMM) [13] and the GaMM applying the EVI technique (EVI-GaMM) [4]. To provide broad noninformative prior distributions, we set the hyperparameters of the prior distribution as $g_{md} = s_m = p_m = 1$, $h_{md} = t_m = q_m = 0.1$, $c_m = 0.001$, and initialize the number of components with large value (15 in this paper). The initial values of r_{nm} are obtained using the K-means algorithm. Note that this specific selection was based on our experiments and was found to be convenient and effective in our case. When the EVI-IBLMM algorithm stops, the posterior means are taken as the parameter estimates in the IBLMM.

A. Synthesized Data Validation

The performance of the proposed EVI-IBLMM in terms of estimation and determination through quantitative analysis on four 2-D synthesized datasets is first evaluated, which are generated from four known IBLMMs with different parameters. It is worth noting that the selection of $D = 2$ is purely for ease of representation. Table I shows the actual parameters for the four IBLMMs. The initial number of components for each dataset are set to double amounts of the actual number of components with equal mixture weights. The average estimated parameters of the four generated datasets over 20 runs of

TABLE I. True Values of the Parameters in the IBLMM Applied to Generate the Four Synthesized Datasets

Dataset	m	α_{m1}	α_{m2}	u_m	v_m	π_m
A	1	12.00	24.00	8.50	12.50	0.400
	2	21.00	15.00	18.00	5.00	0.600
B	1	12.00	24.00	8.50	12.50	0.200
	2	21.00	15.00	18.00	5.00	0.300
	3	18.50	8.00	4.00	16.50	0.500
C	1	12.00	21.00	8.50	12.50	0.100
	2	21.00	35.00	18.00	5.00	0.200
	3	32.00	28.00	4.00	16.50	0.300
	4	2.00	18.00	24.00	8.00	0.400
D	1	21.00	6.00	18.00	24.00	0.100
	2	2.00	28.00	8.00	15.00	0.200
	3	18.00	68.00	24.00	16.00	0.250
	4	76.00	8.00	4.00	18.00	0.300
	5	2.00	4.00	4.00	12.00	0.150

TABLE II. The Mean of the Estimated Parameters for the Synthesized Datasets Over 20 Runs of the EVI-IBLMM Algorithm

Dataset	N_m	m	$\hat{\alpha}_{m1}$	$\hat{\alpha}_{m2}$	$\hat{u}_m$	$\hat{v}_m$	$\hat{\pi}_m$
A	200	1	11.99	23.95	8.56	12.51	0.400
	300	2	21.27	15.20	18.10	5.00	0.600
B	120	1	11.31	22.59	8.50	12.54	0.200
	180	2	20.81	14.93	18.50	5.13	0.300
	300	3	18.30	8.01	4.18	17.09	0.500
C	80	1	12.46	21.64	9.20	14.12	0.098
	160	2	19.84	33.52	18.30	5.08	0.202
	240	3	30.68	26.81	4.07	16.76	0.300
	320	4	2.00	18.12	24.32	8.21	0.400
D	100	1	22.26	6.42	17.70	23.46	0.103
	200	2	1.98	27.09	7.80	15.03	0.201
	250	3	16.61	64.69	23.79	15.82	0.253
	300	4	73.02	7.48	4.04	18.10	0.302
	150	5	2.32	4.14	3.98	12.11	0.141

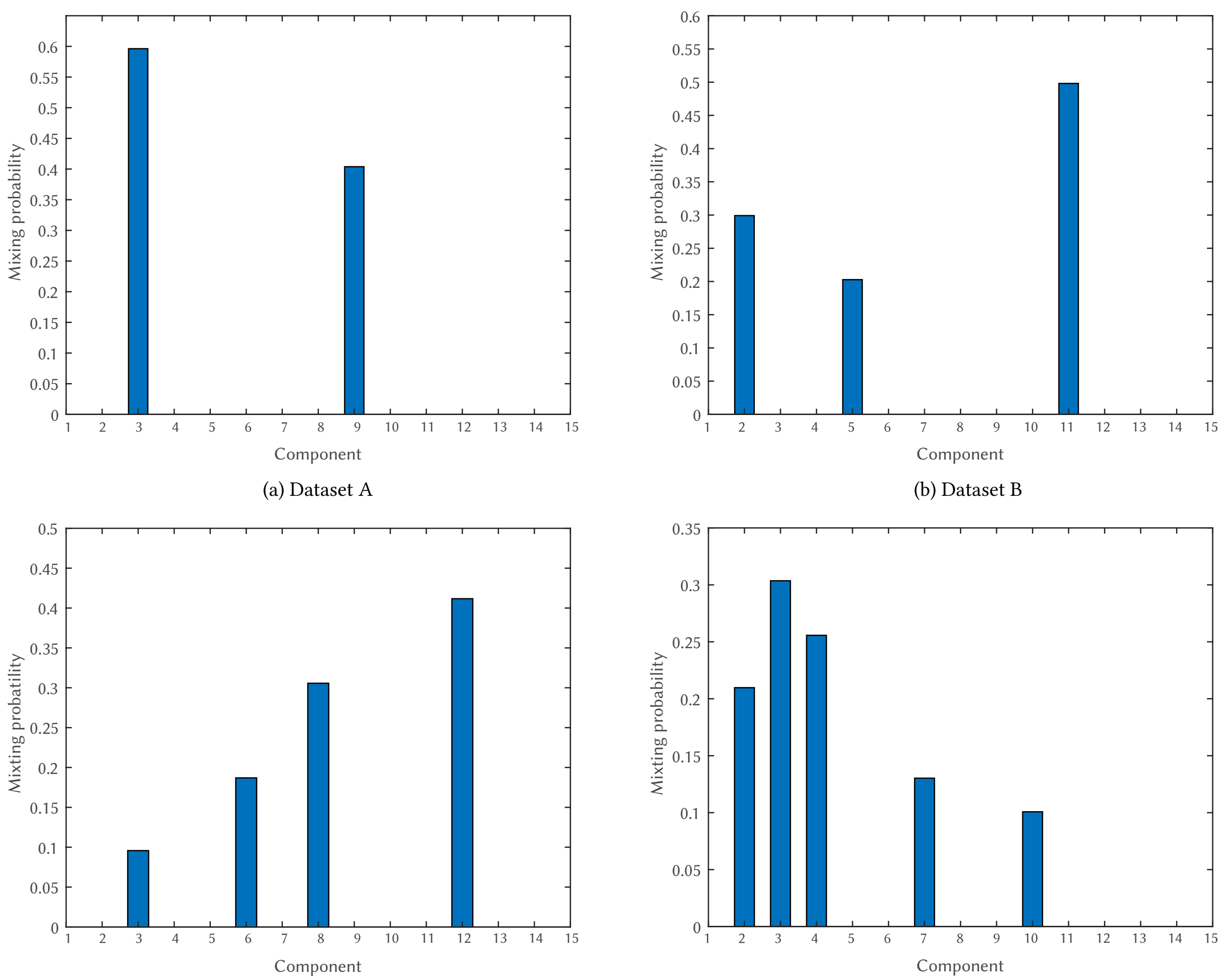

(a) Dataset A
(b) Dataset B
(c) Dataset C
(d) Dataset D

Fig. 1. Estimated mixing probabilities of components for the synthesized datasets. (a) Dataset A. (b) Dataset B. (c) Dataset C. (d) Dataset D.

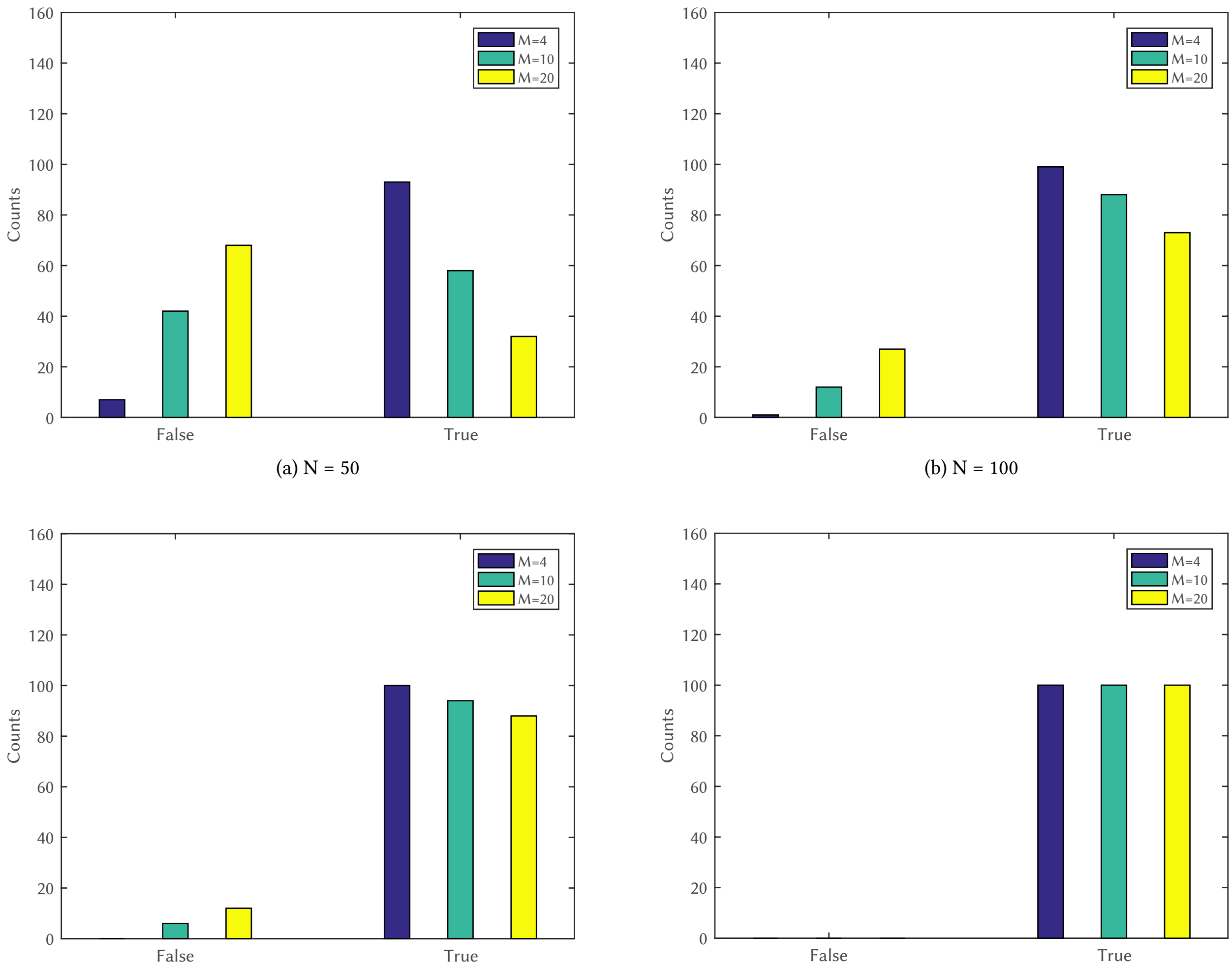

(a) N = 50 (b) N = 100

(c) N = 200 (d) N = 500

Fig. 2. The counts of the estimated number of components over 100 runs of simulations based on dataset A. M denotes the initial number of components and N denotes the sample size.

simulations are reported in Table II. According to these results, the proposed EVI-IBLMM algorithm is capable of accurately estimating both the parameters and the mixing weights of the IBLMM. Next, the model selection capability of the EVI-IBLMM algorithm is investigated. When the initial number of components is larger than the true one, the EVI-IBLMM algorithm is capable of forcing some of the mixing weights to approach zero. These components make little contribution to the model, thus they can be eliminated. The EVI-IBLMM algorithm is initiated with a mixture of many components (15 in this paper) and equal mixture weights. Fig. 1 shows the estimated mixture weights of each component for the different generated datasets after convergence. According to these results, it can be clearly observed that the EVI-IBLMM algorithm is able to effectively determine the model complexity. Then, the effect of initial number of components upon the resulting model complexity is investigated. Based on dataset A, Fig. 2 shows the effect of initial number of components on the resulting model complexity over 100 runs of simulations. In Fig. 2, “True” donates that the model has correctly converged to the initial number of components and “False” means that the model does not have the same componets number with the initial ones after training. According to the results shown in this picture, the EVI-IBLMM algorithm is capable of identifying the accurate number of components regardless of whether the sample size is small or large. Moreover, as the sample size gets larger, the effect of the initial number of components gets more insignificant. Finally, the convergence of the EVI-IBLMM algorithm is investigated. Fig. 3 shows the value of the variational objective function in each iteration. According to this figure, it is clear that the variational objective function is always increasing during iterations, thus the convergence is demonstrated.

B. Text Categorization

Text categorization refers to the task of automatically assigning unlabeled text documents into predefined categories. During the past few decades, this task has attracted considerable attention from researchers due to many reasons, such as the hug amount of digital documents that are easily available and the increasing demand to organize, store, and retrieve these documents accurately and efficiently. Efficient text categorization are beneficial for many applications, such as document processing and visualization [17], digital information search [18], and information retrieval [19]. This problem is challenging and different statistical methods were proposed and applied in the past. Although different, most of the proposed techniques addressed this problem as following: First, a set of labeled text documents which belong to a certain number of classes are given to train the model. In our experiment, the data that has the same label is used to train one IBLMM, after training, the number of IBLMM is equal to the number of categories; Second, a new unobserved text is assigned to the category with the highest similarity regarding its content by the model.

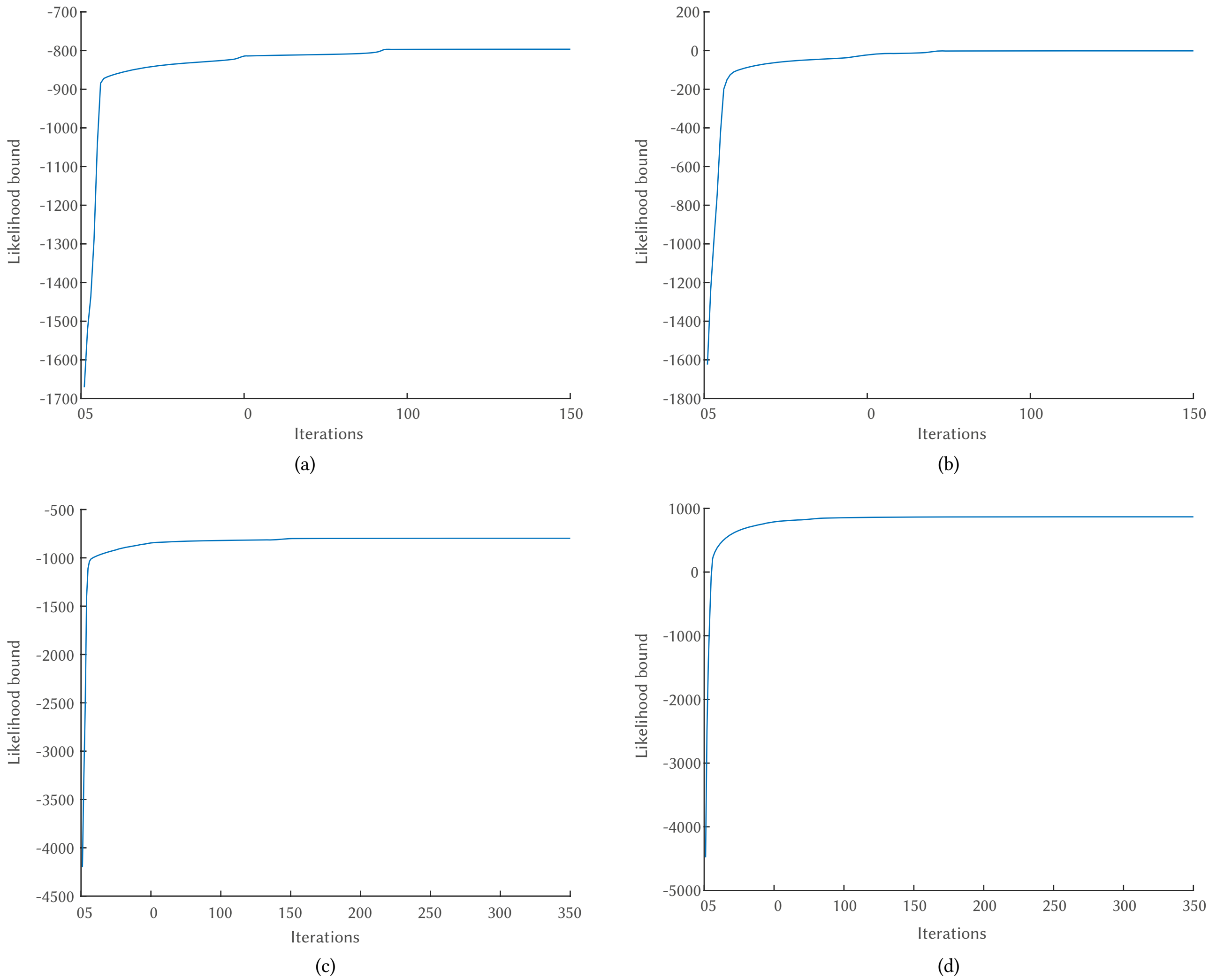

Fig. 3. Convergence of the proposed EVI-IBLMM algorithm for the different synthesized datasets. (a) Dataset A. (b) Dataset B. (c) Dataset C. (d) Dataset D.

TABLE III. Comparisons of Text Categorization Accuracies (in %) and Runtime (in S) Obtained by Different Approaches

Dataset	Method	EVI-IBLMM	EVI-GIDMM	EVI-IDMM	EVI-GaMM
WebKB	Accuracy	**90.36**	89.27	89.91	89.03
	Runtime	0.66	0.61	0.59	0.39
20Newsgroup	Accuracy	**81.11**	79.82	80.20	78.86
	Runtime	4.85	5.35	3.84	0.71

The text categorization experiment with the proposed EVI-IBLMM in our paper is conducted by using two extensively applied text collections: WebKB [20] and 20Newsgroup[1]. The WebKB dataset is composed of four categories: course, faculty, project and student, with a total of 4,199 documents. The 20Newsgroups dataset contains 13,998 newsgroup documents evenly distributed on 20 categories. Each of these categories is 30 times randomly divided into two separate halves, one half for training and the other half for testing. Following [21], the Porter's stemming [22] is applied to reduce the words to their basic forms. In the pre-processing step, the words that occur less than 3 times or are shorter than 2 in length are eliminated, which results in the representation of each document by a positive vector. The vectors in the different training sets are then modeled by the IBLMM trained by the algorithm in the previous section. Finally, each document vector is categorized to a given category according to the well-known Bayes classification rule.

[1] http://kdd.ics.uci.edu/databases/20newsgroups/20newsgroups.html

Three referred methods, namely EVI-based Bayesian GIDMM [13] (EVI-GIDMM), EVI-based Bayesian IDMM (EVI-IDMM) [6] and EVI-based Bayesian Gamma mixture model (EVI-GaMM) [4] are also used to the aforementioned task. Table III shows the mean results of the tested methods in terms of categorization accuracy and training time over 20 runs. Fig. 4 illustrates the categorization accuracies obtained by different methods. Based on these results, it can be found that the proposed EVI-IBLMM has the best categorization accuracy (%) among all the referred mixture-based approaches for the task of text categorization. Moreover, to investigate more insights for the EVI-IBLMM algorithm, the EVI-IBLMM is further compared with deep neural networks (DNNs) on the text categorization task. The fully connected (FC) neural networks with different numbers (i. *e*., *l*) of

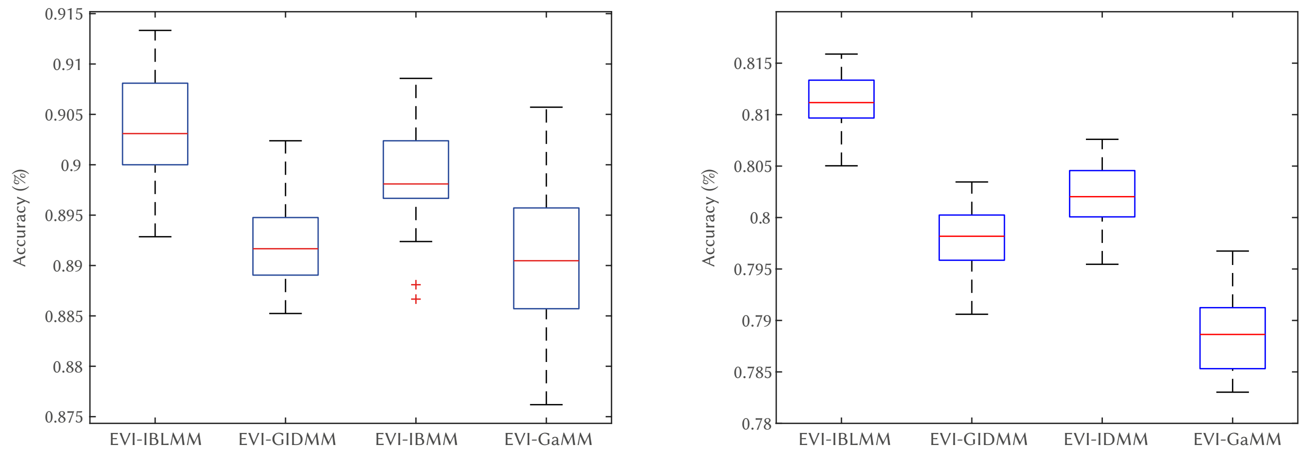

(a) WebKB

(b) 20Newsgroup

Fig. 4. Boxplots for comparisons of the categorization accuracies' distributions for the WebKB and the 20Newsgroup datasets.

hidden layers are used. The extracted feature vectors for the WebKB and 20Newsgroup datasets are used as inputs, respectively. These feature vectors are named as shallow feature vectors. The is set as 1,2 , and 4 , respectively and the number of nodes in each hidden layer is the same as the dimension of the shallow features. Table IV shows the comparison of categorization accuracies and training time of different FC neural networks and the proposed EVI-IBLMM algorithm on both WebKB and 20Newsgroup datasets. According to these results, it can be found that the proposed method significantly decreases training time compared to the FC neural networks. Although the proposed approach cannot outperform the DNNs, it can effectively model the features extracted and obtain proper classification accuracies on the two datasets, which can explicitly show the effectiveness of the proposed method.

V. Conclusions

In this paper, an efficient attractive EVI algorithm for the inverted Beta-Liouville mixture model is proposed. Different from the traditional EM algorithm and MCMC algorithm, this algorithm is able to automatically and simultaneously determine all the model's parameters and the optimal number of components, which can prevent the problem of over-fitting. Besides, the proposed algorithm can converge in a short time, and therefore, it has a relatively high efficiency. The good performance of the proposed method is experimentally demonstrated through both synthetic datasets and real datasets which are generated from a real-world application namely text categorization. A future work can be devoted to investigate how to combine a feature selection criterion with the model selection in a unified Bayesian framework or to extend the IBLMM to the infinite case applying some nonparametric Bayesian methods.

Acknowledgment

This work was supported by the General Project of Science and Technology Plan of Beijing Municipal Commission of Education (No. KM201910009014) and the National Natural Science Foundation of China (Grant No. 62172193).

References

[1] M. A. Mashrgy, T. Bdiri, N. Bouguila, "Robust simultaneous positive data clustering and unsupervised feature selection using generalized inverted dirichlet mixture models," *Knowledge-Based Systems*, vol. 59, no. 2, pp. 182-195, 2014.

[2] T. Bdiri, N. Bouguila, "Variational bayesian inference for infinite generalized inverted dirichlet mixtures with feature selection and its application to clustering," *Applied Intelligence*, vol. 40, pp. 507-525, 2016.

[3] C. Liu, H. Li, K. Fu, F. Zhang, M. Datcu, W. J. Emerye, "Bayesian estimation of generalized gamma mixture model based on variational em algorithm," *Pattern Recognition*, vol. 87, pp. 269-284, 2019.

[4] Y. Lai, H. Cao, L. Luo, Y. Zhang, F. Bi, X. Gui, Y. Ping, "Extended variational inference for gamma mixture model in positive vectors modeling," *Neurocomputing*, vol. 432, pp. 145-158, 2021.

[5] T. Bdiri, N. Bouguila, "Positive vectors clustering using inverted dirichlet finite mixture models," *Expert Systems with Applications*, vol. 39, no. 2, pp. 1869-1882, 2012.

[6] Y. Lai, Y. Ping, W. He, B. Wang, J. Wang, X. Zhang, "Variational bayesian inference for finite inverted dirichlet mixture model and its application to object detection," *Chinese Journal of Electronics*, vol. 27, no. 3, pp. 603-610, 2018.

[7] S. Bourouis, M. A. Mashrgy, N. Bouguila, "Bayesian learning of finite generalized inverted dirichlet mixtures: Application to object classification and forgery detection," *Expert Systems with Applications*, vol. 41, no. 5, pp. 2329-2336, 2014.

[8] C. Hu, W. Fan, J. Du, N. Bouguila, "A novel statistical approach for clustering positive data based on finite inverted beta-liouville mixture models," *Neurocomputing*, vol. 333, pp. 110-123, 2019.

[9] Y. Agusta, D. L. Dowe, "Unsupervised learning of gamma mixture models using minimum message length," in *Proceedings of the 3rd IASTED international multi-conference artificial intelligence and applications*, 2003, pp. 457-462.

[10] S. Favaro, Y. W. Teh, "Mcmc for normalized random measure mixture models," *Statistical Science*, vol. 28, no. 3, pp. 335-359, 2013.

[11] T. P. Minka, "Expectation propagation for approximate bayesian inference," in *Proceedings of the Seventeenth Conference on Uncertainty in Artificial Intelligence*, 2001, pp. 362-369.

[12] C. M. Bishop, *Pattern Recognition and Machine Learning* (Information Science and Statistics). New York, NY, USA: Springer-Verlag, 2006.

[13] Z. Ma, J. Xie, Y. Lai, J. Taghia, J. Xue, J. Guo, "Insights into multiple/single lower bound approximation for extended variational inference in non-gaussian structured data modeling," *IEEE Transactions on Neural Network and Learning System*, vol. 31, no. 7, pp. 2240-2254, 2019.

[14] W. Fan, N. Bouguila, "Modeling and clustering positive vectors via nonparametric mixture models of liouville distributions," *IEEE Transactions on Neural Networks and Learning Systems*, vol. 31, no. 9, pp. 3193-3203, 2020.

[15] G. J. McLachlan, D. Peel, *Finite Mixture Models*. Wiley, New York, USA, 2000.

[16] Z. Ma, P. K. Rana, J. Taghia, M. Flierl, A. Leijon, "Bayesian estimation of dirichlet mixture model with variational inference," *Pattern Recognition*, vol. 47, no. 9, pp. 3143-3157, 2014.

[17] H. Strobelt, D. Oelke, C. Rohrdantz, A. Stoffel, D. A. Keim, O. Deussen, "Document cards: A top trumps visualization for documents," *IEEE Transactions on Visualization and Computer Graphics*, vol. 15, no. 6, pp. 1145-1152, 2009.

[18] W. W. Chu, D. B. Johnson, H. Kangarloo, "A medical digital library to support scenario and user-tailored information retrieval," *IEEE Transactions on Information Technology in Biomedicine*, vol. 4, no. 2, pp. 97-107, 2000.

[19] Y. Peng, J. Wang, L. Jiao, "A novel text retrieval algorithm for public crisis cases," *Chinese Journal of Electronics*, vol. 28, no. 4, pp. 712-717,

[20] K. Nigam, A. McCallum, S. Thrun, T. Mitchell, "Learning to classify text from labeled and unlabeled documents," in *Proceedings of the fifteenth national/tenth conference on Artificial intelligence/Innovative applications of artificial intelligence*, 1998, pp. 792-799.

[21] Y. Ping, Y. Zhou, C. Xue, Y. Yang, "Efficient representation of text with multiple perspectives," *The Journal of China Universities of Posts and Telecommunications*, vol. 1, no. 19, pp. 101-111, 2012.

[22] M. Porter, "An algorithm for suffix stripping," *Program*, vol. 14, no. 3, pp. 130-137, 1980.

Yongfa Ling

Yongfa Ling Ph.D, he currently is the assistant to the President of Hezhou University, Dean of the School of Artificial Intelligence (Modern Industry School), His research interests include Wireless Sensor Network and Communication Network Protocol, Compressed Sensing, MAC Mechanism and System Simulation, Collision Decomposition Algorithm, Priority Control Technology.

Wenbo Guan

Wenbo Guan received the bachelor's degree from the Beijing International Studies University and the master's degree from the North China University of Technology, now he is currently pursuing the Ph.D. degree in the Institute of Information Engineering, CAS. His research interests include pattern recognition, machine learning and cyberspace security.

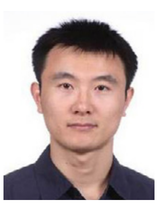

Qiang Ruan

Ruan Qiang, CEO of DigApis Information Security Technology (Jiangsu) Co., Ltd., engaged in cyberspace security research for more than 20 years. His research interests include network attack and defense, industrial Internet security, and vulnerability mining.

Heping Song

Heping Song received the Ph.D. degree in computer application technology from Sun Yat-sen University, Guangzhou, China, in 2011. He is currently a Associate Professor with the Department of Software Engineering, School of Computer Science and Communication Engineering, Jiangsu University, Zhenjiang, China. His current research interests include low-level vision, inverse problems, computer vision and deep learning.

Yuping Lai

Yuping Lai from Beijing University of Posts and Telecommunications, Beijing, China, in 2014. He is currently an associate professor in the School of Cyberspace Security at Beijing University of Posts and Telecommunications, Beijing, China. His research interests include information security, machine learning, and data mining.

Content-Based Hyperspectral Image Compression Using a Multi-Depth Weighted Map With Dynamic Receptive Field Convolution

Shaoming Pan, XiaoLin Gu, Yanwen Chong*, Yuanyuan Guo

The State Key Laboratory of Information Engineering in Surveying, Mapping, and Remote Sensing, Wuhan University, Wuhan 430072 (China)

Received 13 December 2021 | Accepted 21 June 2022 | Published 3 August 2022

Abstract

In content-based image compression, the importance map guides the bit allocation based on its ability to represent the importance of image contents. In this paper, we improve the representational power of importance map using Squeeze-and-Excitation (SE) block, and propose multi-depth structure to reconstruct non-important channel information at low bit rates. Furthermore, Dynamic Receptive Field convolution (DRFc) is introduced to improve the ability of normal convolution to extract edge information, so as to increase the weight of edge content in the importance map and improve the reconstruction quality of edge regions. Results indicate that our proposed method can extract an importance map with clear edges and fewer artifacts so as to provide obvious advantages for bit rate allocation in content-based image compression. Compared with typical compression methods, our proposed method can greatly improve the performance of Peak Signal-to-Noise Ratio (PSNR), structural similarity (SSIM) and spectral angle (SAM) on three public datasets, and can produce a much better visual result with sharp edges and fewer artifacts. As a result, our proposed method reduces the SAM by 42.8% compared to the recently SOTA method to achieve the same low bpp (0.25) on the KAIST dataset.

Keywords

Compression, Dynamic Receptive Field Convolution, Hyperspectral Image, Importance Map, Multi-Depth.

DOI: 10.9781/ijimai.2022.08.004

I. Introduction

Hyperspectral images (HSIs) mainly own two kinds of redundancy, namely spectral similarity and spatial correlation [1]. As a typical 3D image, HSI compression has increasingly received attention in recent years to eliminate these two kinds of redundancy and achieve efficient image storage, transmission and processing [2]-[4].

Traditional lossy compression techniques, such as JPEG [5] and JPEG2000 [6] provide excellent rate-distortion performance for 2D imagery. In order to match the requirements of 3D image compression, a number of 3D compression algorithms including 3D-SPECK [7] and PCA+JPEG2000 [8] arise up for 3D HSI. However, these methods without the consideration of special characteristics of HSI by a direct extension from 2D to 3D may not fully satisfy the requirements of HSI compression [9]-[11], and the spectral fidelity of HSI cannot be guaranteed under the condition of effectively removing the spectral correlation of HSI.

In recent years, several DNNs-based lossy image compression methods [12]-[14] have achieved comparable performance to traditional methods [15],[16]. This is because deep convolutional network (DNNs) not only has good feature extraction ability, but also is good at flexible nonlinear analysis and comprehensive transformation of extracted spatial and spectral characteristics. The core research goal of DNNs-based lossy compression [17]-[19] is to balance compression ratio and the distortion to ensure the image quality [20],[21]. Bit-allocation based on the importance of image content has been effectively adopted in DNNs-based lossy image compression to achieve this goal [22],[23].

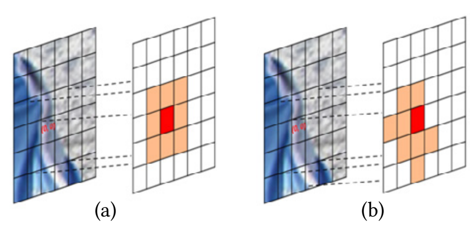

Fig. 1. The convolution is the process of the weighted summation. The red locations denote element to convolve, and the orange positions denote local receptive field to be weighted. (a) 3 × 3 instances of the normal convolution. (b) Our proposed Dynamic Receptive Field convolution (DRFc) with a kernel size of 3 × 3.

However, there are still several challenges in generating an accurate importance map based on the content of the image. An importance map is generally the representations produced by convolutional network that capture the salient contents of the image for bit allocation and compression rate control. In image compression, we usually want the bpp (bits per pixel) to be as small as possible, so a central theme of the importance map research is to search for more powerful representations that capture only the most salient properties of an image.

* Corresponding author.

E-mail address: ywchong@whu.edu.cn

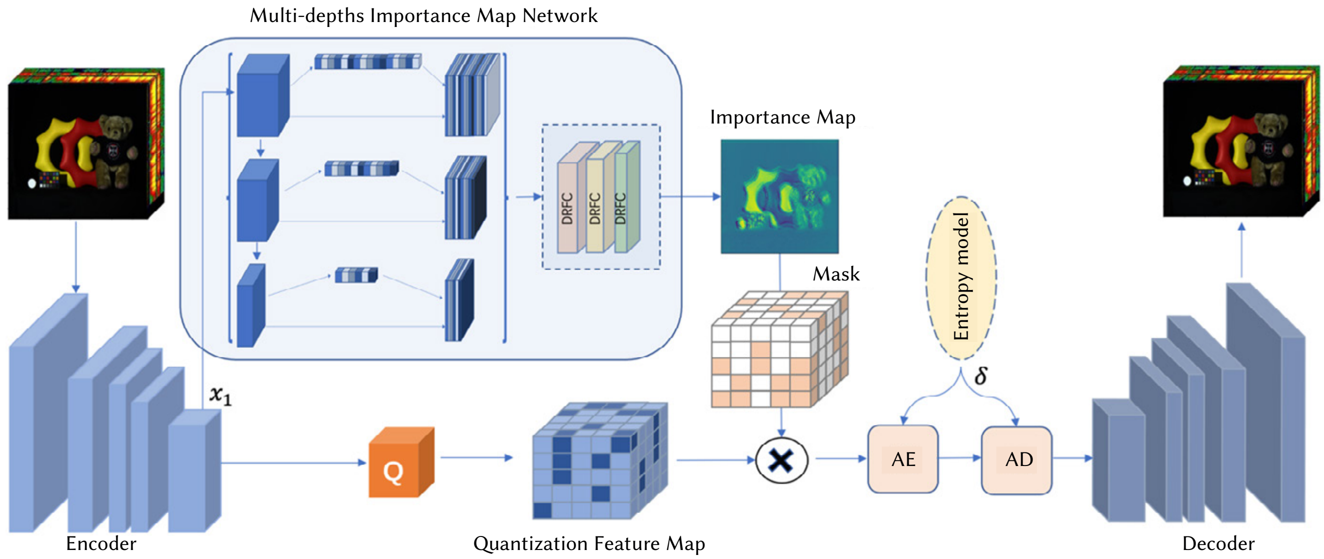

Fig. 2. Illustration of the proposed architecture for content-weighted image compression.

In addition, due to the fixed geometric structure of the convolution operator, as shown in Fig. 1(a), normal convolution has insufficient perception of edges in an image[24], resulting in a smaller value at the edge of the generated important map by CNNs. The larger the value of the importance map, the more bits for the image content are allocated. In this way, fewer bits will be allocated to the edges according to the importance map, and usually are inevitable in producing some visual artifacts, e.g., blurring and blocking in image reconstruction.

In this paper, we proposed a multi-depth importance map (MDIM) with Dynamic Receptive Field Convolution (DRFC) network (MDIMDRF), which is embedded into an encoder-decoder framework to produce an importance map and achieve content-based hyperspectral image compression. First, in our MDIM, we introduced the Squeeze-and-Excitation block(SE-block) to explicitly model the interdependencies between the channels of convolutional features and strengthen feature extraction of CNNs[25], thus improve the representational power of importance map. Since channel-wise information in single-depth importance map (SDIM) leads to excessive loss of non-important channels, and then compression performance often dramatically drops at low bpp, we designed the MDIM based on pyramid decomposition scheme to reconstruct non-important channel information at low bit rate. And then we introduced DRFC to greatly enhance CNNs' capability of extracting edge information. Finally, we replaced normal convolution with DRFc for the last three layers in MDIM and expected to improve the representation ability of important map synthetically.

To sum up, the main issues addressed in this paper are listed as follows:

1. Unlike other methods using simple convolution layers [22],[26]or residual blocks[23],[27] to obtain importance map, we designed MDIM to explicitly model the interdependence between feature channels and improve the representational power of importance map.
2. We reconsidered the guiding role of importance map to rate allocation in coding process, and retained the weak edges and mid-scale textures in the original image by increasing the weight of the regions with sharp edge of importance map.
3. The proposed compression framework can be end-to-end trained, and obtain significantly better results than state-of-the-art (SOTA) methods.

II. Methodology

As shown in Fig. 2, we proposed an end-to-end image compression model, which consists of encoder, MDIMDRF, entropy model, and decoder. Following[12], the encoder network consists of four convolutional layers and three generalized divisive normalization (GDN)[28]layers. The architecture of decoder is symmetric to that of the encoder. The MDIMDRF here can be understood as producing an importance map via MDIM and DRFc to obscure the non-important regions in the image so as to allocate more bits to the important regions.

A. Dynamic Receptive Field Convolution

As shown in Fig. 1(a), when convolving an edge pixel, the normal convolution unit samples the input feature map in a fixed receptive field, causing features to be influenced by irrelevant image content. For our DRFC, as shown in Fig. 1(b), after three steps (details in Fig. 3), we effectively find the $k \times k$ (k is the size of the convolution kernel) pixels with the strongest correlation with the convolution element as its dynamic receptive field.

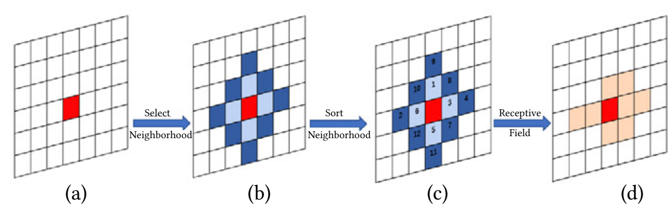

Fig. 3. Illustration of 3 × 3 Dynamic Receptive Field Convolution. The red grids denote pixels for convolution. Grids in light blue are first-order neighbors of the red, Grids in dark blue are second-order neighbors, and Grids in pink are the dynamic receptive field of the red.

For a $k \times k$ normal convolution, a receptive field $\mathcal{R}_{normal}$ (generally a $k \times k$ square grid) is constructed and moved over the input feature map x, with a scheduled step size s, The grid $\mathcal{R}_{normal}$ defines the receptive field size. For example, as shown in Fig. 1(a),

$$\mathcal{R}_{normal} = \{(-1,1), (0,1), \ldots, (0,-1), (1,-1)\} \quad (1)$$

indicates the receptive field for a 3×3 normal convolution.

For each location p_0 on the output feature map y, we summate sampled values weighted by w and have

$$y(p_0) = \sum_{p_n \in \mathcal{R}_{normal}} w(p_n) \cdot x(p_0 + p_n) \quad (2)$$

where p_n enumerates the locations in $\mathcal{R}_{normal}$.

In our Dynamic Receptive Field Convolution, as shown in Fig. 3, we generate an irregular receptive field applying the following steps to the elements for convolution: (1) assemble a fixed-size neighborhood $\mathcal{R}^{o}_{DRFc}$ for each element;(2) sort the neighborhood and create receptive field $\mathcal{R}_{DRFc}$; (3) learn the receptive field representations with CNN. As shown in Fig. 3(b),

$$\mathcal{R}^{o}_{DRFc} = \{(-2,0),(0,-2),(-1,1),\dots,(1,-1),(2,0),(0,2)\} \tag{3}$$

Equation (2) becomes

$$y(p_0) = \sum_{p'_n \in \mathcal{R}_{DRFc}} w(p'_n) \cdot x(p_0 + p'_n) \tag{4}$$

where p'_n enumerates the locations in $\mathcal{R}_{DRFc}$.

TABLE I. ReceptiveField: Create Receptive Field

1. input: Neighborhood $\mathcal{R}^{o}_{DRFc}$ of location p_0, Convolution kernel size k, Moran's Index m
2. output: Receptive Field $\mathcal{R}_{DRFc}$ of p_0
3. Compute an order r of the elements of $\mathcal{R}^{o}_{DRFc}$, subject to
$$\forall p,q \in \mathcal{R}^{o}_{DRFc}: m(p,p_0) < m(q,p_0) \leftrightarrow r(p) < r(q)$$
4. $\mathcal{R}_{DRFc}$ = top k^2 elements in $\mathcal{R}^{o}_{DRFc}$ according to r
5. return $\mathcal{R}_{DRFc}$

Illustrated in Fig. 3, Table I gives the procedures of creating receptive field by imposing an order on the elements $\mathcal{R}^{o}_{DRFc}$ via a correlation measure Moran's Index as

$$\mathrm{m}(p,q) = \frac{\sum_{i=1}^{c} w_{x_p,x_q}(x_{pi}-\overline{x_p})(x_{qi}-\overline{x_q})}{s_{x_p}s_{x_q}\sum_{i=1}^{c} x_{pi}x_{qi}} \tag{5}$$

where x_p, x_q be the vector at location p, q; c is the length of the tensor x_p, x_q; x_{pi}, x_{qi} is the i-th valve of x_p, x_q; w_{x_p,x_q} is the weight of spatial autocorrelation, which is generally the reciprocal of the distance between x_p and x_q; s_{x_p}, s_{x_q} is the variance of x_p, x_q.

The basic idea is to select the points in the adjacency domain in turn that have a high correlation with the center point in turn and apply them to each input channel if and only if they have similar structural roles in two feature maps.

B. Multi-depth Importance Map Network

When we encode an input image, we tend to allocate the bits efficiently according to spatial variant local image content, that is, fewer bits should be allocated to the smooth regions while more bits should be allocated to the regions with more information content, which makes it possible to improve the reconstructed image quality

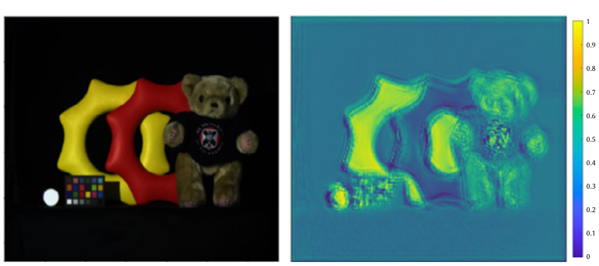

(a) Original image (b) Importance map

Fig. 4. Illustration of Importance map.

while improving the compression ratio. For example, given the image in Fig. 4(a), it is natural to be interested in the teddy bear and two-colored circles, which are called the important regions. It is reasonable to allocate more bits to the teddy bear and two-colored circles and fewer bits to black background.

Thus we first designed a single-depth importance map network(SDIM) of four convolution layers[22] to retain the most important features of the image and generate an importance map to guide the allocation of bits. To improve the representational power of importance map, we strengthen feature extraction of CNNs using SE block[25] via modelling the correlation between feature channels and adjusting the feature map according to the correlation degree. Secondly, in order to compensate the excessive loss of non-important channels caused by channel-wise operation at low bit rate, we adopt a multi-depth importance map network (MDIM) based on pyramid decomposition scheme to reconstruct non-important channel information. As shown in Fig.5, we obtain the sub-importance maps generated by feature maps of different depths respectively, the results of each depth are weighted and summed to produce an importance map.

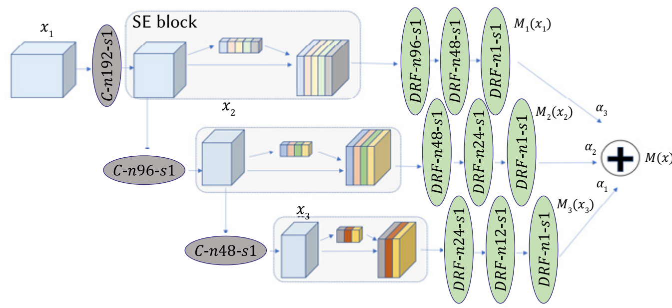

Fig. 5. Illustration of the MDIM's pyramidal decomposition structure with 3 depths. It's noted that "C-n192-s1" represents a CNN layer with 192 filters and a stride of 1 and "DRFC-n96-s1" represents a DRFC layer with 96 filters and a stride of 1 where the normal convolution unit is replaced by Dynamic Receptive Field convolution unit.

Let x_m denotes the input of the m-th layer of MDIM, and also x_1 denotes the original output of encoder. $M_m(x_m)$ represents the output of the m-th layer. In our paper, we sequentially set m to 1, 2, and 3 to individually produce a feature map containing different channel information with only one channel and the same size as the encoder output. The results of each scale are weighted and summed to produce the final importance map $M(x) = \alpha_1 M_1(x_1) + \alpha_2 M_2(x_2) + \alpha_3 M_3(x_3)$. What's more, DRFc instead of normal convolution is used in the last three layers of MDIM to enhance feature extraction of edge pixels, thus increasing the weight of regions with sharp edges or rich textures.

III. Experiments

To evaluate the performance of the proposed compression model, we compared our model with traditional compression methods, i.e., 3D-SPECK[7], PCA+JPEG2000[8], and DNNs-based compression models, i.e., factorized prior[12], hyperprior[29] on different datasets. All DNNs-based experiments are conducted on a server equipped with the NVIDIA GeForce RTX 3090Ti graphics card.

We used three standard HSI datasets to train and test our proposed compression framework: KAIST[30], CAVE[31] and ICVL[32]. KAIST is a high-resolution dataset containing 30 images of size 2704×3376×31, CAVE consists of 28 images of 31×512×512 and ICLR consists of 201 images of 1300×1392×31. A total of 20000 patches with a size of 31×256×256 were sampled from both the original images and their enhancement (such as flipping and rotating at different angles). The data are divided into a training data set, a testing data set and a validation data set. Specifically, 60% of the images were used for training, 20% for testing and 20% for validation. Please note that all the test images are not included in the training dataset. Several original images from KAIST, CAVE and ICLR dataset are shown in Fig. 6, Fig. 7 and Fig. 8, respectively.

Fig. 6. Original image from KAIST.

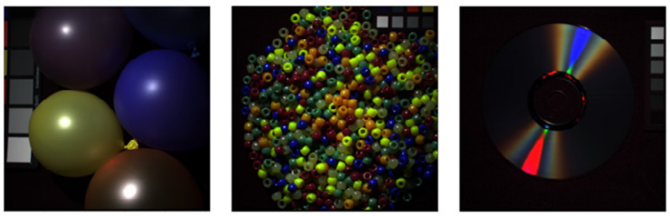

Fig. 7. Original image from CAVE.

Fig. 8. Original image from ICVL.

A. Performance Metrics

To quantitative evaluate the performance of proposed model, we used the following indexes as Peak Signal-to-Noise Ratio (PSNR)[18, 33], Structural Similarity Index Measure (SSIM) [33],[34] and Spectral Angle Mapper (SAM)[35].

1. Peak Signal-to-Noise Ratio

The ratio between the input image and the reconstructed image is known as PSNR. Also, the PSNR is measured based on the Mean Square Error (MSE)[36]. Please note that the PSNR for HSIs in this paper is calculated as in (6),

$$PSNR = \frac{1}{C}\sum_{i=1}^{C} 10log_{10}\left(\frac{p_{max}^2}{MSE}\right) \tag{6}$$

Where p_{max} denotes the maximum value in the i-th band of HSIs, and the unit of PSNR is dB.

2. Structural Similarity Index Measure

It is used to evaluate the distortion between the input image x and the reconstructed image x^*, it can be defined as in (7),

$$SSIM(x, x^*) = \frac{1}{C}\sum_{i=1}^{C}\frac{(2\mu_{x_i}\mu_{x_i^*} + a_1)(2\sigma_{x_i x_i^*} + a_2)}{(\mu_{x_i}^2 + \mu_{x_i^*}^2 + a_1)(\sigma_{x_i}^2 + \sigma_{x_i^*}^2 + a_2)} \tag{7}$$

Where C is the number of bands of input image x, x_i is i-th band of x, and μ_{x_i}, σ_{x_i} are the corresponding mean and variance. a_1, a_2 is constant.

3. Spectral Angle Mapper

The spectrum of each pixel in HSIs is regarded as a high-dimensional vector, and the similarity between the two spectrums is measured by calculating the Angle between the two vectors. Note that a small SAM value indicates less spectral distortion.

B. Training Details and Parameter Settings

Our objective is to minimize the weighted sum of the rate loss and distortion loss, R + λD, where λ governs the trade-off between the two terms. Thus, we trained the model on the batch of size B, and defined the loss function $\mathcal{L}$ of our model on the entire batch:

$$\mathcal{L} = \frac{1}{B}\sum_{i=1}^{B}\{\mathcal{L}_R(c, x^i) + \lambda\mathbb{E}[d(x^i, \circ\widehat{x^i})]\} \tag{8}$$

where c is the code of the input image x^i. $\mathcal{L}_D(c, x^i)$ denotes the rate loss and $d(x^i, \circ\widehat{x^i})$ is the expected difference between the reconstruction $\widehat{x^i}$ and the original image x^i, as measured by Mean Square Error (MSE) in order to be consistent with PCA+JPEG2000[8].

Firstly, we set the weights α_1, α_2, and α_3 in the MDIM to 1/2, 1/4, and 1/4, respectively. During the training process, we set the batch parameter B to 8 and the model is iteratively trained 300 times on the dataset. In addition, the initial learning rate is set to 10^{-4}, and performs stochastic gradient descent[37] using the Adam algorithm[38].

With this setup, we trained a total of 24 separate models: half of the models with MDIM and half without; half of the models with DRFc, and half without; finally, each of these combinations with 6 different values of λ in order to cover a range of rate-distortion tradeoffs.

C. Comparison of Rate–Distortion Performance

In this subsection, we evaluate the performance improvements of the proposed model quantitatively, and rate–distortion curves for different methods on KAIST, CAVE and ICLR datasets are provided in Fig. 9, respectively.

Firstly, we compare the PSNR and SSIM performance of our proposed method with PCA+JPEG2000 and 3D SPEAK as well as the methods proposed in[12, 29].As seen from Fig. 9, our method outperforms traditional methods[7, 8] and DNNs-based methods[12, 29] at a wide range of bpp on three datasets. Although the PSNR and SSIM performance of our method owns only a relatively small advantages on CAVE dataset comparing with factorized prior[12] and hyperprior[29], the corresponding performance improvement is particularly obvious on KAIST and ICLR dataset. This is because the spatial resolution of individual KAIST dataset is almost 35 times higher than that of CAVE dataset and there are 50 times more ICLR training patches than CAVE training patches, larger dataset makes the model more fully trained and the test performance better.

Next, we further compare the SAM performance of different methods based on the work of[35], As seen from Fig. 9, the average rate-distortion curves of SAM show that the proposed method can significantly outperform other methods on three datasets and the SAM performance of our method is still superior to other methods at low bpp on CAVE dataset. For example, compared with factorized prior[12] and hyperprior[29], the SAM of our proposed model is reduced by 0.03 and 0.02 when bpp is 0.25, respectively. A strong explanation is that the importance map network designed in our proposed model takes full account of spectral similarity, and retains spectral characteristic information to the maximum extent.

D. Comparison of Visual Quality

The visual quality comparisons of the reconstructed HSIs in low compression rates for three datasets are provided in Table II. As can be seen from Table II, traditional compression methods such as 3D SPEAK and PCA+JPEG 2000 inevitably produce obvious blurring, ringing in the second and third columns, which can seriously affect the human visual experience. The methods[12, 29] suppress the artifacts effectively, but there are still some blur effects along the edges visible in the fourth and fifth columns. In contrast, our method overcomes the above flaws, and some important edges and textures are well-retained and thus the reconstructed image owns better visual quality due to the bit-allocation guided by the importance map.

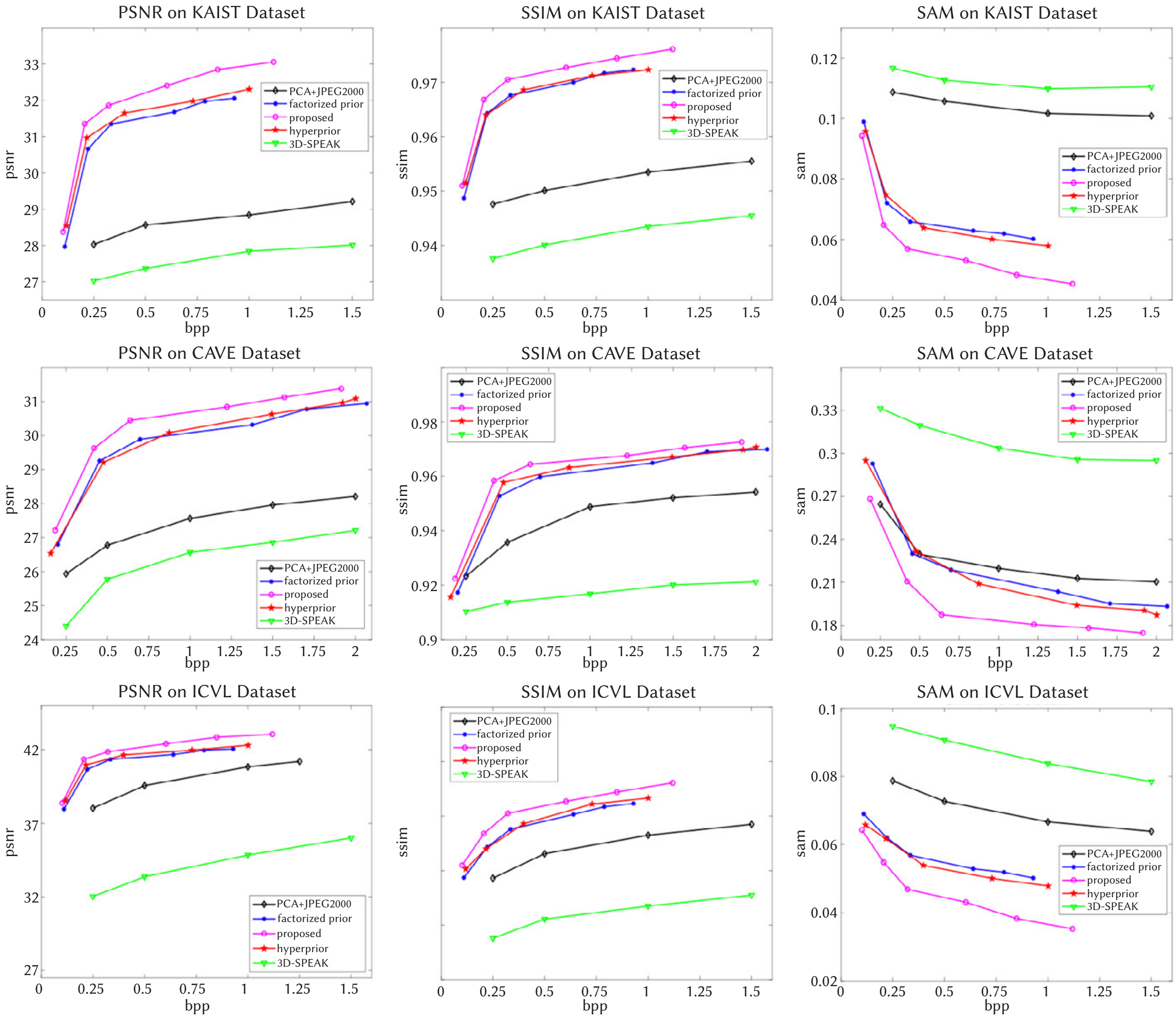

Fig. 9 Comparison of the ratio-distortion curves by different metrics: PSNR, SSIM, and SAM

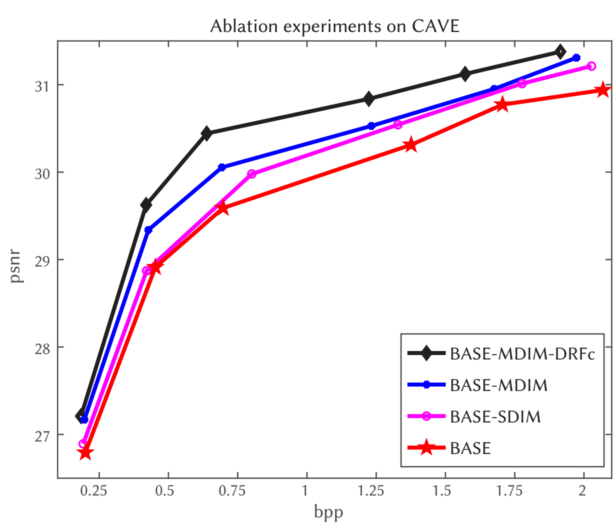

Fig. 10: Illustration of the results of the ablation experiment.

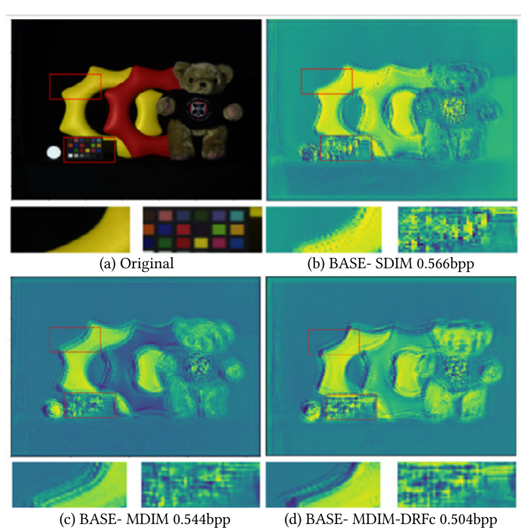

Fig. 11. The important maps obtained by different models. The right color bar shows the palette on the number of bits.

TABLE II. Images Produced By Different Compression Models At Different Compression Rates. All Images Are Visualized With the Same Ordinal Band

KAIST dataset (29,19,9)					
Original image	3D-SPEAK	PCA+JPEG2000	factorized prior	hyperprior	proposed
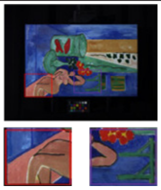	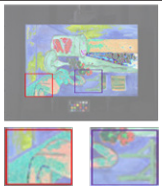	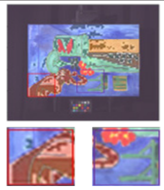	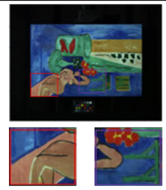	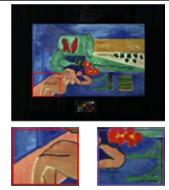	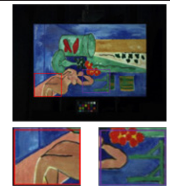
	0.5 bpp PSNR:18.46 SSIM:0.908 SAM:0.430	0.5 bpp PSNR:22.53 SSIM:0.935 SAM:0.263	0.515bpp PSNR:39.43 SSIM:0.982 SAM:0.124	0.543bpp PSNR:40.01 SSIM:0.984 SAM:0.112	0.499bpp PSNR:40.29 SSIM:0.985 SAM:0.102
	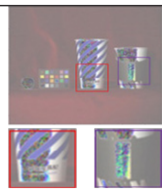		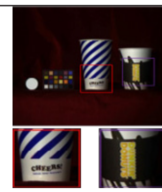	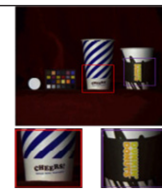	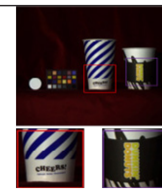
	0.7 bpp PSNR:21.42 SSIM:0.31 SAM:0.72	0.7 bpp PSNR:29.16 SSIM:0.80 SAM:0.42	0.713bpp PSNR:41.94 SSIM:0.992 SAM:0.089	0.748bpp PSNR:43.13 SSIM:0.993 SAM:0.0998	0.676bpp PSNR:44.57 SSIM:0.9946 SAM:0.073
CAVE dataset (24,6,25)					
Original image	3D-SPEAK	PCA+JPEG2000	factorized prior	hyperprior	proposed
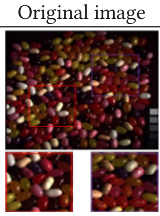	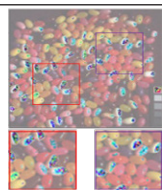		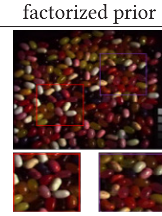		
	0.7 bpp PSNR:23.68 SSIM:0.93 SAM:0.42	0.7 bpp PSNR:28.96 SSIM:0.94 SAM:0.26	0.743bpp PSNR:29.49 SSIM:0.961 SAM:0.210	0.723bpp PSNR:29.13 SSIM:0.958 SAM:0.234	0.711bpp PSNR:29.23 SSIM:0.956 SAM:0.216
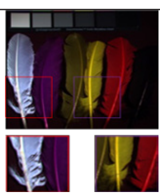	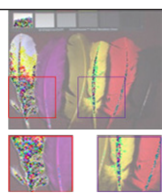				
	0.5bpp PSNR:24.69 SSIM:0.67 SAM:0.76	0.5bpp PSNR:33.16 SSIM:0.84 SAM:0.45	0.565bpp PSNR:31.66 SSIM:0.961 SAM:0.188	0.526bpp PSNR:32.15 SSIM:0.969 SAM:0.179	0.483bpp PSNR:33.14 SSIM:0.975 SAM:0.158
ICVL dataset (29,19,9)					
Original image	3D-SPEAK	PCA+JPEG2000	factorized prior	hyperprior	proposed
					
	0.7bpp PSNR:28.58 SSIM:0.65 SAM:0.07	0.7bpp PSNR:45.41 SSIM:0.993 SAM:0.036	0.737bpp PSNR:53.39 MS-SSIM:0.999 SAM:0.037	0.710bpp PSNR:54.27 MS-SSIM:0.999 SAM:0.035	0.703bpp PSNR:54.48 MS-SSIM:0.999 SAM:0.029
					
	0.5bpp PSNR:26.06 SSIM:0.486 SAM:0.113	0.5bpp PSNR:44.33 SSIM:0.993 SAM:0.056	0.517bpp PSNR:47.81 MS-SSIM:0.999 SAM:0.038	0.539bpp PSNR:50.19 MS-SSIM:0.999 SAM:0.030	0.525bpp PSNR:51.25 MS-SSIM:0.999 SAM:0.026

E. Ablation Experiments

To assess the role of MDIM and DRFc, we trained a baseline model by removing MDIMDRF from our framework. We designed the following four models according to whether the presence of SDIM, MDIM, and DRFc in the architecture: (1) BASE: the baseline model; (2) BASE-SDIM: BASE with SDIM; (3) BASE-MDIM: BASE with MDIM; (4) BASE-MDIM-DRFc: BASE with MDIM and DRFc.

As shown in Fig. 10, at the same bpp, BASE-MDIM-DRFc has the best performance while BASE has the worst performance. BASE-MDIM performs better than BASE-SDIM at low bpp, which proves MDIM's help in reconstructing the non-important channels of convolutional features at low bpp. In Fig. 11, we can observe the blurring artifacts and color distortion in (b) and (c). In contrast, the results in (d) exhibit much clearer and is much more consistent with human visual perception.

IV. Discussion

In our proposed end-to-end compression framework, we design the multi-depths importance map network based on pyramidal decomposition, and produce an importance map to guide bit rates allocation and further compress the code by entropy coding. At the same time, we introduce Dynamic Receptive Field convolution to increase the weight of the importance map in the edge area to solve the distortion caused by insufficient feature representation to edge of normal convolution.

Rate-distortion performance in Fig. 9 clearly shows that our proposed method outperforms conventional and DNNs-based methods at a wide range of bpp. In addition, as shown in Fig. 11, the existence of multi-depth importance map and Dynamic Receptive Field convolution have significant influence on the performance improvement. In addition, to achieve PSNR of 40 and MI-SSIM of 0.95, the average time to encode and decode the image is 49 *ms* and 11 *ms*, running on the GeForce RTX 3090Ti.

V. Conclusion

In this paper, we proposed a content-based compression system for hyperspectral images. In the proposed system, we designed MDIM and DRFc to improve representability of the importance map so as to allocate bits precisely for different contents. Our models can be end-to-end learned on a training set. Experimental results clearly show the superiority of our model in retaining HSI's spectral structure characteristics and extracting edge content, resulting in significant image reconstruction quality.

Acknowledgment

This work was supported by the National Natural Science Foundation of China (Grant Nos. 62072345, 41671382), State Key Laboratory for Information Engineering in Surveying, Mapping and Remote Sensing Special Research Funding. The numerical calculations in this paper have been done on the supercomputing system in the Supercomputing Center of Wuhan University.

References

[1] E. Christophe, C. Mailhes, and P. Duhamel, "Hyperspectral Image Compression: Adapting SPIHT and EZW to Anisotropic 3-D Wavelet Coding," *IEEE Transactions on Image Processing A Publication of the IEEE Signal Processing Society,* vol. 17, no. 12, p. 2334, 2008.

[2] M. E. Paoletti, J. M. Haut, J. Plaza, and A. Plaza, "Deep learning classifiers for hyperspectral imaging: A review," *ISPRS Journal of Photogrammetry and Remote Sensing,* vol. 158, no. Dec., pp. 279-317, 2019.

[3] B. Penna, T. Tillo, E. Magli, and G. Olmo, "Transform Coding Techniques for Lossy Hyperspectral Data Compression," *IEEE Transactions on Geoscience and Remote Sensing,* vol. 45, no. 5, pp. 1408-1421, 2007.

[4] Y. Qu, H. Qi, and C. Kwan, "Unsupervised Sparse Dirichlet-Net for Hyperspectral Image Super-Resolution," in *Conference on Computer Vision and Pattern Recognition*, 2018.

[5] G. K. Wallace, "The JPEG Still Picture Compression Standard."

[6] A. Skodras, C. Christopoulos, and T. Ebrahimi, "The JPEG 2000 still image compression standard," *IEEE Signal Processing Magazine,* vol. 18, no. 5, pp. 36 - 58, 2001.

[7] X. Tang and W. A. Pearlman, "Lossy-To-Lossless Block-Based Compression of Hyperspectral Volumetric Data," in *IEEE*, 2006.

[8] Q. Du and J. E. Fowler, "Hyperspectral Image Compression Using JPEG2000 and Principal Component Analysis," *IEEE Geoscience & Remote Sensing Letters,* vol. 4, no. 2, pp. 201-205, 2007.

[9] H. Ying and G. Liu, "Hyperspectral image lossy-to-lossless compression using the 3D Embedded Zeroblock Coding alogrithm," in *International Workshop on Earth Observation & Remote Sensing Applications*, 2008, pp. 1-6.

[10] A. Karami, S. Beheshti, and M. Yazdi, "Hyperspectral image compression using 3D discrete cosine transform and support vector machine learning," in *International Conference on Information Science*, 2012.

[11] E. Christophe, D. Leger, and C. Mailhes, "Quality criteria benchmark for hyperspectral imagery," *IEEE Transactions on Geoscience and Remote Sensing,* vol. 43, no. 9, pp. 2103-2114, 2005.

[12] J. Ballé, V. Laparra, and E. P. Simoncelli, "End-to-end Optimized Image Compression," 2016.

[13] J. Lee, S. Cho, and S. K. Beack, "Context-adaptive Entropy Model for End-to-end Optimized Image Compression," *arXiv,* 2018.

[14] L. Galteri, L. Seidenari, M. Bertini, and A. Bimbo, "Deep Generative Adversarial Compression Artifact Removal," *IEEE Transactions on Multimedia,* 2017.

[15] H. A. Jawdhari, "Hyperspectral image compression using sparse representations and wavelet transform based spectral decorrelation," 2017.

[16] A. Karami, "Compression of hyperspectral images using discerete wavelet transform and tucker decomposition," *IEEE Journal of Selected Topics in Applied Earth Observations & Remote Sensing,* vol. 5, no. 2, pp. 444-450, 2012.

[17] C. Kwan and J. Larkin, "New Results in Perceptually Lossless Compression of Hyperspectral Images," *Journal of Signal and Information Processing,* vol. 10, no. 3, pp. 96-124, 2019.

[18] L. Theis, W. Shi, A. Cunningham, and F. Huszár, "Lossy Image Compression with Compressive Autoencoders," 2017.

[19] F. Mentzer, E. Agustsson, M. Tschannen, R. Timofte, and L. V. Gool, "Practical Full Resolution Learned Lossless Image Compression," in *2019 IEEE/CVF Conference on Computer Vision and Pattern Recognition (CVPR)*, 2019.

[20] A. Chakrabarti and T. Zickler, "Statistics of real-world hyperspectral images," in *IEEE Conference on Computer Vision & Pattern Recognition*, 2011.

[21] Y. Blau and T. Michaeli, "Rethinking Lossy Compression: The Rate-Distortion-Perception Tradeoff," 2019.

[22] L. Mu, W. Zuo, S. Gu, D. Zhao, and D. Zhang, "Learning Convolutional Networks for Content-weighted Image Compression," 2017.

[23] L. Wu, K. Huang, and H. Shen, "A GAN-based Tunable Image Compression System," 2020.

[24] J. Dai *et al*., "Deformable Convolutional Networks," *IEEE,* 2017.

[25] H. Jie, S. Li, S. Gang, and S. Albanie, "Squeeze-and-Excitation Networks," *IEEE Transactions on Pattern Analysis and Machine Intelligence,* vol. PP, no. 99, 2017.

[26] Z. Cheng, H. Sun, M. Takeuchi, and J. Katto, "Performance Comparison of Convolutional AutoEncoders, Generative Adversarial Networks and Super-Resolution for Image Compression," 2018.

[27] B. Zla, A. Sy, A. Yw, and B. Jza, "Discrimination of the fruits of Amomum tsao-ko according to geographical origin by 2DCOS image with RGB and Resnet image analysis techniques," *Microchemical Journal,* 2021.

[28] J. Ballé, V. Laparra, and E. P. Simoncelli, "Density Modeling of Images using a Generalized Normalization Transformation," *arXiv,* 2015.

[29] J. Ballé, D. Minnen, S. Singh, S. J. Hwang, and N. Johnston, "Variational

image compression with a scale hyperprior," 2018.

[30] I. Choi, M. Kim, D. Gutierrez, D. Jeon, and G. Nam, "High-quality hyperspectral reconstruction using a spectral prior," 2017.

[31] F. Yasuma, T. Mitsunaga, D. Iso, and S. K. Nayar, "Generalized assorted pixel camera: postcapture control of resolution, dynamic range, and spectrum," *IEEE transactions on image processing*, vol. 19, no. 9, pp. 2241-2253, 2010.

[32] K. Yi *et al*., "CLEVRER: CoLlision Events for Video REpresentation and Reasoning," 2019.

[33] F. Mentzer, E. Agustsson, M. Tschannen, R. Timofte, and L. V. Gool, "Conditional Probability Models for Deep Image Compression," in *2018 IEEE/CVF Conference on Computer Vision and Pattern Recognition*, 2018.

[34] G. Toderici *et al*., "Full Resolution Image Compression with Recurrent Neural Networks," *IEEE Computer Society*, 2016.

[35] F. A. Kruse *et al*., "The spectral image processing system (SIPS)—interactive visualization and analysis of imaging spectrometer data," *Remote Sensing of Environment*, 1993.

[36] E. Agustsson, M. Tschannen, F. Mentzer, R. Timofte, and L. V. Gool, "Generative Adversarial Networks for Extreme Learned Image Compression," 2018.

[37] L. Zhou, C. Cai, Y. Gao, S. Su, and J. Wu, "Variational Autoencoder for Low Bit-rate Image Compression," 2018.

[38] D. P. Kingma and J. Ba, "Adam: A method for stochastic optimization," *arXiv preprint arXiv:1412.6980*, 2014.

Shaoming Pan

Shaoming Pan received the B.S. and M.S. degrees from Huazhong University of Science and Technology, China, in 1998, Ph.D. degree from Wuhan University, China. He is an Associate Professor with the State Key Laboratory of Information Engineering in Surveying, Mapping, and Remote Sensing, Wuhan University, Wuhan, China. He is mainly engaged in the research on image processing, multimedia communication and spatial information storage.

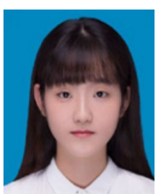

Xiaolin Gu

Xiaolin Gu is currently pursuing the master's degree with the State Key Laboratory of Information Engineering in Surveying, Mapping, and Remote Sensing, Wuhan University, Wuhan, China. Her main research interest is hyperspectral image compression based on neural network.

Yanwen Chong

Yanwen Chong received the B.S. degree from the Qufu Normal University, China, in 1995, M.S. and Ph.D. degrees from Wuhan University, China, in 1998 and 2001. He is a Professor with the State Key Laboratory of Information Engineering in Surveying, Mapping, and Remote Sensing, Wuhan University, Wuhan, China. His research interests include image processing, computer vision and pattern recognition.

Yuanyuan Guo

Yuanyuan Guo is currently pursuing the Ph.D. degree with the State Key Laboratory of Information Engineering in Surveying, Mapping, and Remote Sensing, Wuhan University, Wuhan, China. Her research interests are mainly within the fields of hyperspectral image compression, model-based deep learning.

ED-Dehaze Net: Encoder and Decoder Dehaze Network

Hongqi Zhang[1,2]*, Yixiong Wei[1,2], Hongqiao Zhou[1,2], Qianhao Wu[1,2]

[1] Department of Engineering & Technology Center, No.38 Research Institute of CETC, Hefei 230088 (China)
[2] Anhui Technical Standard Innovation Base (Intelligent Design and Manufacturing, Intelligence Institute, Civil-military Integration), Hefei 230088 (China)

Received 13 December 2021 | Accepted 22 April 2022 | Published 11 August 2022

Abstract

The presence of haze will significantly reduce the quality of images, such as resulting in lower contrast and blurry details. This paper proposes a novel end-to-end dehazing method, called Encoder and Decoder Dehaze Network (ED-Dehaze Net), which contains a Generator and a Discriminator. In particular, the Generator uses an Encoder-Decoder structure to effectively extract the texture and semantic features of hazy images. Between the Encoder and Decoder we use Multi-Scale Convolution Block (MSCB) to enhance the process of feature extraction. The proposed ED-Dehaze Net is trained by combining Adversarial Loss, Perceptual Loss and Smooth L1 Loss. Quantitative and qualitative experimental results showed that our method can obtain the state-of-the-art dehazing performance.

Keywords

Dehaze, Encoder and Decoder Network, Generative Adversarial Networks, Multi-Scale Convolution Block, Loss Function.

DOI: 10.9781/ijimai.2022.08.008

I. Introduction

Images with clear visibility are required for a variety of computer vision tasks, such as object detection and autonomous driving. However, due to the absorption or reflection of light by floating particles contained in the air, images taken in hazy days often suffer from quality degradation. Fig. 1 shows the differences in visual quality on hazy and haze-free scene. The color of objects in a hazy scene is distorted and the visual perception observed by the human eye is reduced.

In order to overcome the degradation of image quality caused by haze, various priority-based [1]–[5] and learning-based [6]–[14] methods have been proposed. The well-known priority-based algorithm proposed by He et al. [1] assumed that at least one channel in the image has very low pixel values. However, the method cannot effectively deal with areas similar to atmospheric light, which results in the sky area or high-brightness objects cannot be accurately dehazed. In addition, the non local color prior proposed by Berman et al. [3] is suitable for the case where the airlight is lower than the scene brightness [11]. Some recent dehazing algorithms use convolutional neural networks to extract image features, which are further used to predict transmission maps and atmospheric light values. Zhang et al. [9] embed the atmospheric scattering model into the dehazing process and design the end-to-end network with dense connections. By combining the convolutional neural network and the physical model, Zhang's method can jointly learn the transmission map, atmospheric light through a one-stage training.

Inspired by the successful application of the GANs in the field of image generation [15]–[19], we propose ED-Dehaze Net, which contains two parts: a Generator and a Discriminator. The predicted haze-free images are generated by the Generator. The Discriminator is responsible for distinguishing the generated images from the real images. In addition, our Generator consists of three submodules: Encoder, Decoder and Multi-Scale Convolution Block. The Generator and Discriminator are trained simultaneously by combining Adversarial loss, Perceptual loss and Smooth L1 loss. In order to prove the effectiveness of the proposed dehazing method, we conduct sufficient experiments on indoor and outdoor dataset. By using the atmospheric scattering model, we synthesize pairs of hazy and haze-free images on the NYU-Depth v2 [20] indoor dataset. In addition, the commonly used benchmark O-HAZE [21] is also used to verify the performance of ED-Dehaze Net in outdoor dehazing task.

Fig. 1. The effect of haze on the visual quality of the real world scene. From left to right: hazy image, dehazed image produced by ED-Dehaze Net, ground truth haze-free image.

Our main contributions are as follows:

(1) We propose a novel Encoder and Decoder Dehaze Network (ED-Dehaze Net), which can effectively remove the haze in the image.
(2) By using Multi-Scale Convolution Block (MSCB), the feature extraction capability of the dehazing network is improved.
(3) We combine Smooth L1 loss and Perceptual loss to train the Generator. And the experimental results show that the proposed ED-Dehaze Net can obtain the state-of-the-art dehazing performance.

* Corresponding author.

E-mail address: ahu0086@163.com

II. Related Work

In this section, we first review the existing dehazing methods for single image. Then, the research of generative adversarial networks will be briefly summarized.

A. Atmosphere Scattering Model

The Atmospheric scattering model [22]–[24] provides a theoretical basis for the research of dehazing algorithms. Meanwhile, the researchers synthesized hazy images data [9], [10] through the atmospheric scattering model, avoiding the expensiveness of real-world data collection. Its formula is as follows:

$$I(x) = J(x)t(x) + A(1 - t(x)) \tag{1}$$

where x represents the position of pixels, and A means the global atmospheric light in the image. $I(x)$ denotes the haze scene, and $J(x)$ is the haze-free image that the dehazing algorithm expects to obtain. $t(x)$ stands for the medium transmission map, which formula is as follows:

$$t(x) = e^{-\beta d(x)} \tag{2}$$

where β and $d(x)$ represent the atmosphere scattering parameter and the scene depth, respectively.

B. Single Image Dehazing

Single image dehazing is a challenging ill-posed problem. Various prior-based and learning-based methods have been proposed for recovering a clear haze-free image from a single hazy image.

Researchers have proposed a variety of hand-crafted prior-based dehazing methods [1]–[5]. He et al. [1] proposed Dark-Channel Prior (DCP) which can estimate the transmission map and remove the haze effectively. Zhu et al. [2] designed Color Attenuation Prior (CAP) and used a linear model to estimate the scene depth. Then, CAP dehazed a single image by combining the atmospheric scattering model. Fattal et al. [4] proposed a local formation model and use it for recovering the scene transmission. Berman et al. [3] assumed that colors of a haze-free image can be well approximated by hundred of distinct colors. By using the assumption of haze-lines, Berman's method could recover both the distance maps and the haze-free images.

With the development of deep learning, some dehazing algorithms [6]–[14] use convolutional neural networks to learn how to remove haze from hazy images. Li et al. [10] designed All-in-One Dehazing Network (AOD-Net) based on a re-formulated atmospheric scattering model without an intermediate parameter estimation process. On the basis of cycleGAN [25], a cycle-consistent dehazing network [7] is proposed, which does not require paired data. Zhang et al. [9] designed Densely Connected Pyramid Dehazing Network (DCPDN), which can jointly learn the transmission map and atmospheric light. By jointly estimating two parameters, DCPDN can reduce system errors significantly. Dong et al. [14] proposed Multi-Scale Boosted Dehazing Network (MSBDN) based on the U-Net architecture. MSBDN proved that boosting strategy can help image dehazing algorithms have more stable performance.

C. Generative Adversarial Networks (GANs)

Goodfellow et al. [26] proposed the original GAN, which contained a generator (G) and a discriminator (D) for data generation. The objective function is calculated as follows:

$$\begin{aligned} L_{GAN} &= \min_G \max_D V(G,D) \\ &= E_{x\sim p_{\text{data}}(x)}[\log D(x)] + E_{z\sim p_z(z)}[\log(1 - D(G(z)))] \end{aligned} \tag{3}$$

where z is the noise variable subject to the distribution $p_z(z)$, and x is sampling from the distribution of real data $p_{data}(x)$.

In the recent years, GANs have been successfully applied in the fields of image super-resolution [15]–[17], image synthesis [18], [19], texture synthesis [27], [28], and image inpainting [29], [30]. Most of GANs contain one or more generators and discriminators, and use min-max optimization to simultaneously optimize the generative model G and the discriminative model D [31].

Inspired by the success of these GANs-based methods for generating high-quality images, we designed an adversarial dehazing network with impressive dehazing performance.

III. ED-Dehaze Net

This section introduces the design details of the proposed ED-Dehaze Net. Section A shows the network structure of the Generator and the Discriminator. The formulas of adversarial loss, smooth L1 loss and perceptual loss are given in Section B, C and D, respectively. Finally, Section E describes the overall loss function used for network optimization.

A. Network Structure

The overall structure of the proposed ED-Dehaze Net is shown in Fig. 2. The hazy image passes through the Generator to remove the haze in the scene and generate a dehazed image. Then, the Discriminator distinguishes the dehazed image from the real haze-free image through the process of adversarial training.

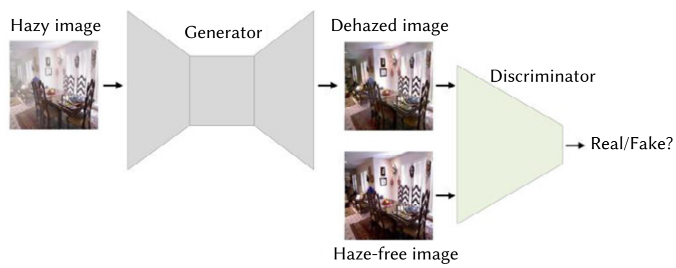

Fig. 2. The overall structure of the ED-Dehaze Net.

The ED-Dehaze Net contains two basic blocks: Convolution Block and Deconvolution Block, as illustrated in Fig. 3. INS stands for Instance Normalization proposed in the paper [32]. RELU is the activation function "Rectified Linear Unit" commonly used in deep neural networks.

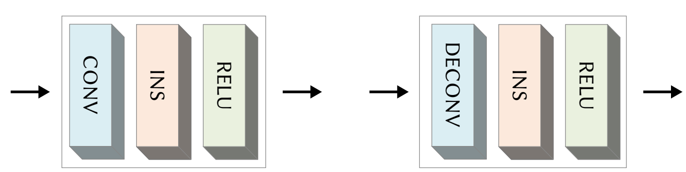

Fig. 3. Convolution Block and Deconvolution Block.

In order to effectively fuse the information of different scales, we design the parallel Multi-Scale Convolution Block (MSCB) as shown in Fig. 4. Each scale of convolution block adopts the Conv Block (shown in Fig. 3) of which 3, 5 and 7 represent convolution kernels of different sizes.

The input feature map first convoluted by Conv-3, Conv-5, Conv-7 to obtain three feature maps with different scale information. Then, the three feature maps are concatenated according to the channel ("Cat" in Fig. 4), and the concatenated 3 map in Fig. 4. Finally, the red feature map and the original input feature map are added ("Add" in Fig. 4). Therefore, the output feature map "OUT" and the input feature map "IN" have exactly the same size.

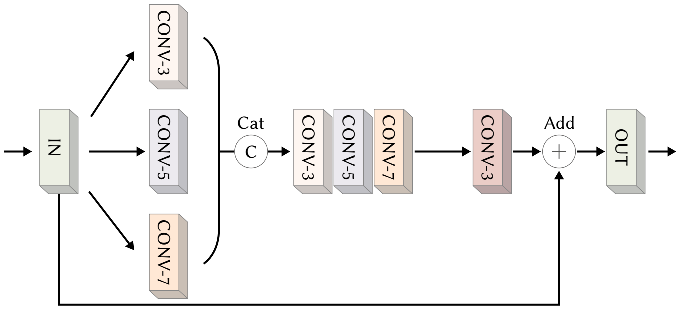

Fig. 4. MSCB: Multi-Scale Conv Block.

The Generator of the ED-Dehaze Net is composed of Encoder, Decoder and multiple MSCBs, as shown in Fig. 5. The dimension of the input image's feature map is reduced during the encoding process to obtain a powerful feature representation. Then, we put the encoded features into MSCBs for enhancing. Finally, the Decoder performs feature decoding to obtain dehazed image of the same size as the original input hazy image.

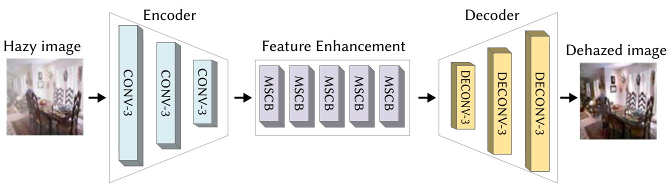

Fig. 5. The Structure of Generator.

The Discriminator shown in Fig. 6 contains multiple Conv-3 blocks, and the stride of all blocks are set to 2. The Discriminator is responsible for distinguishing whether the input images come from the dehazed images of the Generator or the haze-free images of the dataset.

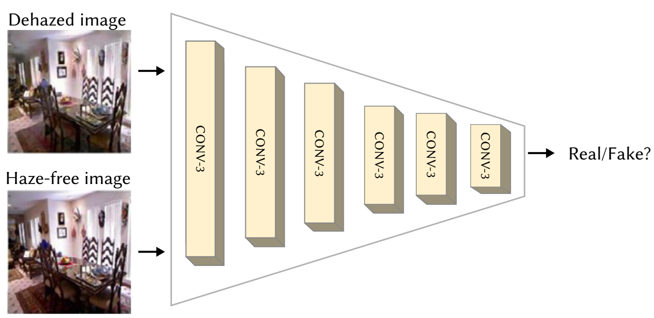

Fig. 6. The Structure of the Discriminator.

B. Adversarial Loss

The Generator and Discriminator are trained simultaneously with adversarial loss. The training purpose of the Generator is to remove the haze in the image to obtain a dehazed image close to the real-world haze-free image. The Discriminator try to judge the input image is a real image or a generated image. The formula for calculating adversarial loss is as follows:

$$L_{\text{adv}} = \min_{G}\max_{D} V(G, D) = E_Y \log\, D(Y) + E_X \log\,(1 - D(G(X))) \tag{4}$$

where $X = \{x_1, x_2, ..., x_m\}$ represents the input hazy images with the batch size of m, $\tilde{Y} = \{\tilde{Y}_1, \tilde{Y}_2, \dots, \tilde{Y}_m\} = G(X)$ means the haze-free images predicted by the Generator. $Y = \{y_1, y_2, ..., y_m\}$ is the real haze-free labels in the dataset.

C. Smooth L1 Loss

The methods used for image dehazing usually adopt L1-norm or L2-norm as objective function during the training process. Girshick et al. [33] proved that Smooth L1 loss is a robust L1 loss which is less sensitive to outliers than the L2 loss. To improve the robustness of the dehazing network, Smooth L1 loss is adopted to optimize the pixel distance between the dehazed image and the real haze-free image, the formulas are as follows:

$$\text{smooth}_{L1}(\delta_i) = \begin{cases} 0.5(y_i - \tilde{y}_i)^2, & \text{if } |y_i - \tilde{y}_i| < 1 \\ |y_i - \tilde{y}_i| - 0.5, & \text{otherwise} \end{cases} \tag{5}$$

$$L_{smo} = \frac{1}{m}\sum_{i=1}^{m} \text{smooth}_{L1}(\delta_i) \tag{6}$$

where $\delta_i = y_i - \tilde{y}_l$ denotes the distance between the dehazed image and the real haze-free image, and m is the number of images.

D. Perceptual Loss

The commonly used pixel-wise objective functions in image reconstruction tasks optimize the network without considering the human visual perceptual quality of the images. By extracting high-level features from the pre-trained convolutional neural network and calculating the semantic distance between the predicted images and the ground truth images, Johnson et al. [34] proposed Perceptual loss, which has been successfully applied in various computer vision tasks [11], [34]–[36]. It has proved that adding perceptual loss on the basis of pixel-wise loss can effectively improve the performance of image reconstruction tasks. We select the first four pooling layers of pre-trained VGG16 [37] (denoted as ψ(•)) for feature extraction. The formula for a single batch is as follows:

$$L_p^k = \frac{1}{m}\sum_{i=1}^{m} \|\psi_k(y_i) - \psi_k(\tilde{y}_i)\|_2 \tag{7}$$

where i represents the i-th input image and k is the k-th pooling layer. And p is the abbreviation of perceptual. After calculating the feature of every single pooling layer, the output of the four pooling layers is added to obtain the Perceptual loss. It can be expressed as following:

$$L_p = \frac{1}{4}\sum_{k=1}^{4} \frac{1}{C_k \times H_k \times W_k} L_p^k \tag{8}$$

where C_k, W_k and H_k represent the number of channels, width and height of the k-th pooling layer, respectively.

E. Overall Loss Function

The overall loss function consists of three parts: Adversarial loss, Perceptual loss, and Smooth L1 loss. As follows:

$$L_{\text{total}} = L_{\text{adv}} + \lambda_{\text{p}} L_{\text{p}} + \lambda_{\text{smo}} L_{\text{smo}} \tag{9}$$

where λ_p and λ_{smo} are the weight of L_p and L_{smo}, respectively.

IV. Experiments Results

Section A gives the parameter settings in the experiment. The descriptions of the synthetic dataset and the real world dataset are in Section B, and the corresponding experimental results are in Section C and D, respectively. To illustrate the effect of Smooth L1 loss and Perceptual loss on the dehazing process, Section E compares the corresponding quantitative metric values by comparing different objective functions. Finally, Section F discusses the improvement of MSCBs on the performance of ED-Dehaze Net.

A. Experiment Setting and Evaluation

All the training images are resized to 256×256 before feeding into the network. The proposed model has been trained on the training dataset and finally the optimal parameters are obtained. The initial learning rate of the Generator and Discriminator are 0.0001 and 0.0004, respectively. After every 2000 iterations, the learning rate is updated to lr = lr × 0.9. The values of λp and λsmo are set to 2 and 10, respectively. Wet use a single NVIDIA GeForce GTX 1080 Ti and the batch size is 4. Adam Optimizer is used to update the gradients during the training process.

We choose Peak Signal-to-Noise Ratio (PSNR) and Structural Similarity Index Measure (SSIM) for evaluation, which are commonly used in the research of image dehazing. Higher values of PSNR and SSIM represent higher image quality. To demonstrate the improvement of the dehazing performance for the proposed ED-Dehaze Net, we compare our method with other state-of-the-art dehazing methods: the Dark-Channel Prior (DCP) proposed by He et al. [1], the Color Attenuation Prior (CAP) proposed by Zhu et al. [2], the cycle-consistency dehazing (cyc-D) network designed by Engin et al. [7], and the All-in-One Dehazing Network (AOD-Net) designed by Li et al. [10].

B. Synthesis Dataset and Real World Dataset

The collection of paired hazy and haze-free images is very time-consuming and expensive. Ancuti et al. [38] synthesized the indoor hazy images dataset based on NYU Depth v2 [20] by the atmospheric scattering model. Here, we use the pipeline proposed by Aucuti for high quality hazy images synthesis. The training set and testing set contain 1149 and 300 pairs of images, respectively. We randomly select the global atmosphere light value from (0.7, 1) for both of them. The atmosphere scattering parameter (denoted as β in Eq. (2)) of the training dataset is set to $\beta \in (1.2, 2.1)$ to simulate hazy images of different densities. By randomly flipping horizontally and vertically, the training set after data augmentation contains 1149 × 3 pairs of images. In order to test the dehazing performance of networks with different density ranges and to ensure the data distribution of the testing set is same as training set, we set the $\beta \in (1.2, 1.5)$, (1.5, 1.8), (1.8, 2.1), and (1.2, 2.1) to get a testing set with 4 density ranges for a total of 300 × 4 pairs of images.

O-HAZE [21] contains 45 pairs of hazy and haze-free images taken in the real world, which the haze is generated by professional machines. We randomly selected 35 pairs as the training set, and the remaining 10 pairs as the testing set.

C. Results on Synthesis Dataset

Table I shows the PSNR/SSIM values obtained on the synthetic dataset by the proposed ED-Dehaze Net and other dehazing algorithms. ED-Dehaze Net outperforms the state-of-the-art methods on both PSNR and SSIM. This indicates that the dehazing images obtained by our method are of higher quality.

TABLE I. PSNR and SSIM Values on Synthesis Dataset

beta	(1.2, 1.5)	(1.5, 1.8)	(1.8, 2.1)	(1.2, 2.1)
DCP	16.314/#0.761	16.212/0.776	15.935/**0.783**	16.346/0.771
CAP	17.422/0.768	17.062/0.723	16.654/0.702	17.175/0.753
cyc-D	17.553/0.657	18.074/0.694	18.263/0.725	17.934/0.766
AOD	18.736/0.782	18.445/**0.788**	17.963/0.779	18.566/0.761
ours	**20.940**/**0.799**	**20.332**/0.784	**19.627**/0.761	**20.264**/**0.781**

The symbol "/" stands for the separation of PSNR and SSIM values.

We randomly select some images from the entire testing set (four ranges of β) to show the visual results. It can be clearly seen in Fig. 7 that the images recovered by the proposed ED-Dehaze Net are closest to the ground truth haze-free images. This proves that the Encoder-Decoder of the Generator can effectively reconstructs the feature information of the image, and removes the haze contained in the scene in an end-to-end manner. The DCP results in a darker color after dehazing, which cannot accurately recover the brightness of the scene. The reason is that DCP relies on priority assumptions and lacks adaptability to different data. The CAP and AOD-Net cannot completely remove the haze in the hazy images. There is still a small amount of haze in the "haze-free" images generated by them, which causes the details and edges of objects in the scenes to be blurred. In addition, the output images of CAP tends to be low-brightness, because its priori assumption of color is not always accurate. The dehazing images generated by cyc-D have obvious color distortion, and it cannot restore the texture information of the image completely.

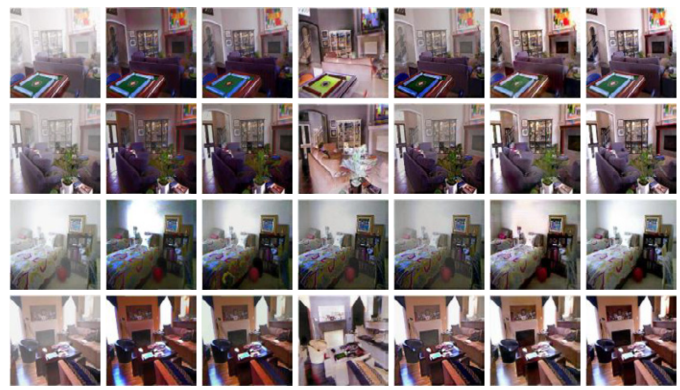

Fig. 7. Visual results on synthesis dataset.

D. Results on O-HAZE

Table II shows the PSNR/SSIM values of the ED-Dehaze Net and other algorithms on the O-HAZE dataset. The quantitative quality of the dehazed images obtained by our method is significantly higher on outdoor scenes. This proves that ED-Dehaze Net can reduce the proportion of noise and restore the structure information of the image.

TABLE II. PSNR and SSIM Values on O-HAZE

Methods	DCP	CAP	AOD	cyc-D	ours
PSNR	16.160	17.078	17.376	19.626	**19.925**
SSIM	0.772	0.792	0.786	0.677	**0.795**

Fig. 8 shows the visual results of various dehazing methods on the O-HAZE dataset. Both DCP and CAP have a phenomenon of color shift and there is still a small amount of haze remaining in the dehazed images, resulting in blurred details. Although AOD-Net uses a convolutional neural network for feature extraction, it does not use multi-scale spatial information like ED-Dehaze Net. So, the AOD-Net can remove the haze in the images, but cannot accurately reconstruct the texture and details. The dehazing images of the cyc-D network has over-smooth, because its unsupervised strategy cannot accurately estimate the density of haze in the image, resulting in excessive dehazing. Meanwhile, Table II shows that the SSIM value of the cyc-D is low, which proves that its excessive dehazing leads to incomplete restoration of the images' structure. Our method can obtain high-quality haze-free images, ensuring that the edge information contained in the images will not be lost.

Fig. 8. Visual results on O-HAZE.

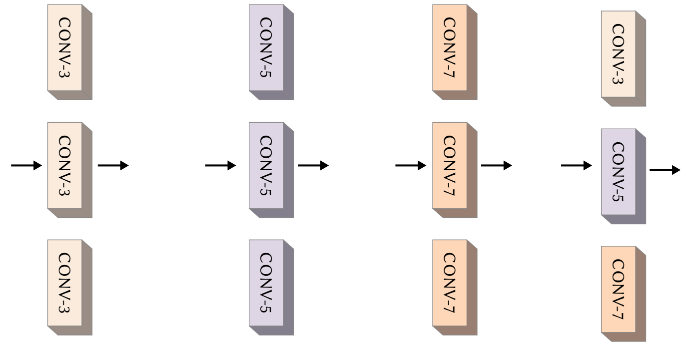

Fig. 9. Comparison with different scales, from left to right: 3 × 3, 5 × 5, 7 × 7 and our multi-scale 3 + 5 + 7.

E. Ablation Study on Loss Function

During the training of the Generator, Smooth L1 loss and Perceptual loss are used to optimize the network. To prove that with the help of Perceptual loss, the network with Smooth L1 loss can generate dehazed images with higher quality. We compare two strategies when choosing loss functions: (a) using Smooth L1 loss alone, and (b) using Smooth L1 loss and Perceptual loss simultaneously. We have not chosen Perceptual loss as the loss function of the Generator alone, because the purpose of Perceptual loss is to measure the distance of features rather than the distance of image pixels. Therefore, the role of Perceptual loss should be an auxiliary of the pixel-wise Smooth L1 loss. Table III lists the ablation experiment results of Smooth L1 loss and Perceptual loss.

TABLE III. Ablation Experiment Results of Smooth L1 Loss and Perceptual Loss

beta	*(1.2, 1.5)*	*(1.5, 1.8)*	*(1.8, 2.1)*	*(1.2, 2.1)*
Smo	19.667/#0.774	19.106/0.724	19.126/0.756	19.644/0.760
L1+ Per	19.821/0.782	19.647/0.781	18.966/**0.772**	20.032/0.774
L2+ Per	19.731/0.748	**20.892**/0.768	19.614/0.758	20.201/0.769
Smo+Per	**20.940**/**0.799**	20.332/**0.784**	**19.627**/0.761	**20.264**/**0.781**

The symbol "/" stands for the separation of PSNR and SSIM values.

The Smo+Per get a higher PSNR/SSIM values than Smo, which means Perceptual loss can help the network generate high-quality dehazed images. In addition, the PSNR/SSIM values obtained by L1 + Per and L2 + Per are lower than Smo + Per. This proves that Smooth L1 loss can optimize the Generator better.

F. Ablation Study on Multi-Scale Convolution Block

The Generator contains multiple Multi-Scale Convolution Blocks (MSCBs) to enhance the process of the feature extraction, so as to obtain better dehazing performance. In order to prove the effectiveness of the multi-scale strategy, we compared the PSNR/SSIM values obtained by a single scale (3 × 3, 5 × 5, 7 × 7) and multiple scales (3 + 5 + 7) as shown in Fig. 9. In order to ensure the fairness of the experiment, all other parameter settings are the same.

The results in Table IV prove that our multi-scale strategy can extract features more effectively. Therefore, ED-Dehaze Net with MSCBs can obtain higher quality dehazed images. For the three single-scale cases (3 × 3, 5 × 5, 7 × 7), the PSNR/SSIM values are very close. This further illustrates that the feature fusion method of multi-scale convolution can enhance the flow of spatial information.

TABLE IV. Ablation Experiment Results of MSCBs

beta	*(1.2, 1.5)*	*(1.5, 1.8)*	*(1.8, 2.1)*	*(1.2, 2.1)*
3 × 3	**21.033**/0.781	19.634/0.792	19.231/0.755	20.132/0.779
5 × 5	19.872/0.796	19.897/0.766	18.998/0.755	19.245/0.773
7 × 7	19.660/0.790	20.226/0.793	19.046/0.758	19.995/0.760
ours	20.940/**0.799**	**20.332**/0.784	**19.627**/**0.761**	**20.264**/**0.781**

Meanwhile, we conduct experiments on the case where the Generator contains only Encoder-Decoder and no MSCBs. The results in Table V show that PSNR and SSIM are very low. The main reason is that the network's capacity and complexity are not sufficient when without MSCBs.

TABLE V. Results With MSCBs and Without MSCBs

beta	*(1.2, 1.5)*	*(1.5, 1.8)*	*(1.8, 2.1)*	*(1.2, 2.1)*
noMSCBs	18.556/0.749	18.673/0.715	17.143/0.729	17.011/0.712
ours	20.940/0.799	20.332/0.784	19.627/0.761	**20.264**/**0.781**

V. Conclusion

This paper proposed an end-to-end dehazing algorithm based on deep learning, called ED-Dehaze Net. The Generator effectively extracted the spatial and texture information of the hazy images by the Encoder-Decoder structure. In order to ensure that the edges and details of the dehazed image are clearly reconstructed, we used Smooth L1 Loss and Perceptual Loss to train the Generator simultaneously. Experiments on synthetic and real world dataset proved that the proposed algorithm can effectively remove the haze in the hazy images.

Acknowledgment

We are very grateful to Dr Jun Zhang and Dr Peng Chen, professors in Anhui University, for their invaluable helps to develop the proposed method and prepare the original manuscript.

References

[1] K. He, J. Sun, X. Tang, "Single image haze removal using dark channel prior," *IEEE Transactions on Pattern Analysis and Machine Intelligence*, vol. 33, pp. 2341-2353, 2010.

[2] Q. Zhu, J. Mai, L. Shao, "A fast single image haze removal algorithm using color attenuation prior," *IEEE Transactions on Image Processing*, vol. 24, pp. 3522 -3533, 2015.

[3] D. Berman, S. Avidan, S. Avidan, "Non-local image dehazing," in *IEEE Conference on Computer Vision and Pattern Recognition*, 2016, pp. 1674 -1682.

[4] R. Fattal, "Dehazing using color-lines," *ACM Transactions on Graphics*, vol. 34, pp. 13, 2014.

[5] G. Meng, Y, Wang, J. Duan, S. Xiang, C. Pan, "Efficient image dehazing with boundary constraint and contextual regularization," in *IEEE International Conference on Computer Vision*, 2013, pp.617-624.

[6] B. Cai, X. Xu, K. Jia, C. Qing, D. Tao, "Dehazenet: An end-to-end system for single image haze removal," *IEEE Transactions on Image Processing*, vol. 25, pp. 5187 -5198, 2016.

[7] D. Engin, A. Genc, H. Kemal Ekenel, "Cycle-dehaze: Enhanced cyclegan for single image dehazing," in *IEEE Conference on Computer Vision and Pattern Recognition Workshops*, 2018, pp. 825 -833.

[8] W. Ren, S. Liu, H. Zhang, J. Pan, X. Cao, M.H. Yang, "Single image dehazing via multi-scale convolutional neural networks," in *European Conference on Computer Vision*, Springer, 2016, pp. 154 -169.

[9] H. Zhang, V.M. Patel, "Densely connected pyramid dehazing network," in *IEEE Conference on Computer Vision and Pattern Recognition*, 2018, pp. 3194 -3203.

[10] B. Li, X. Peng, Z. Wang, J. Xu, D. Feng, "An all-in-one network for dehazing and beyond," 2017, *arXiv*: 1707.06543.

[11] X. Yang, Z. Xu, J. Luo, "Towards perceptual image dehazing by physics-based disentanglement and adversarial training," in *AAAI conference on artificial intelligence*, 2018, pp. 7485 -7492.

[12] X. Qin, Z. Wang, Y. Bai, X. Xie, H. Jia, "Ffa-net: Feature fusion attention network for single image dehazing," 2019 *arXiv*: Computer Vision and Pattern Recognition.

[13] S. Yin, Y. Wang, Y.H. Yang, "A novel residual dense pyramid network for image dehazing," *Entropy*, vol. 21, pp. 1123, 2019.

[14] H. Dong, J. Pan, L. Xiang, Z. Hu, X. Zhang, F. Wang, M.H. Yang, "Multi-scale boosted dehazing network with dense feature fusion," in *IEEE/CVF Conference on Computer Vision and Pattern Recognition* (CVPR), 2020, pp. 2154-2164, doi: 10.1109/CVPR42600.2020.00223.

[15] X. Wang, K. Yu, S. Wu, J. Gu, Y. Liu, C. Dong, Y. Qiao, C. Change Loy, "Esrgan: Enhanced super-resolution generative adversarial networks," in *European Conference on Computer Vision*, 2018, pp. 63 -79.

[16] Y. Yuan, S. Liu, J. Zhang, Y. Zhang, C. Dong, L. Lin, "Unsupervised image super-resolution using cycle-in-cycle generative adversarial networks," in *IEEE Conference on Computer Vision and Pattern Recognition Workshops*, 2018, pp. 701-710.

[17] C. Ledig, L. Theis, F. Huszar, J. Caballero, A. Cunningham, A. Acosta, A. Aitken, A. Tejani, J. Totz, Z. Wang, et al. "Photo-realistic single image superresolution using a generative adversarial network," in *IEEE Conference on Computer Vision and Pattern Recognition*, 2017, pp. 4681 -4690.

[18] R. Huang, S. Zhang, T. Li, R. He, "Beyond face rotation: Global and local perception gan for photorealistic and identity preserving frontal view synthesis," in *International Conference on Computer Vision*, 2017, pp. 2439 -2448.

[19] L. Ma, X. Jia, Q. Sun, B. Schiele, T. Tuytelaars, L. Van Gool, "Pose guided person image generation," in *Neural Information Processing Systems*, 2017, pp. 406-416.

[20] N. Silberman, D. Hoiem, P. Kohli, R. Fergus, "Indoor segmentation and support inference from rgbd images," in *European Conference on Computer Vision*, Springer, 2012, pp. 746 -760.

[21] C.O. Ancuti, C. Ancuti, R. Timofte, C. De Vleeschouwer, "O-haze: a dehazing benchmark with real hazy and haze-free outdoor images," in *Proceedings of the IEEE Conference on Computer Vision and Pattern Recognition Workshops*, 2018, pp. 754-762.

[22] E.J. McCartney, "Optics of the atmosphere: scattering by molecules and particles," New York, John Wiley and Sons, Inc., 1976.

[23] S.K. Nayar, S.G. Narasimhan, "Vision in bad weather," in *IEEE International Conference on Computer Vision*, 1999, pp. 820-827.

[24] S.G. Narasimhan, S.K. Nayar, "Contrast restoration of weather degraded images," *IEEE Transactions on Pattern Analysis and Machine Intelligence*, vol. 25, no. 6, pp. 713 -724, 2003.

[25] J.Y. Zhu, T. Park, P. Isola, A.A. Efros, "Unpaired image-to-image translation using cycle-consistent adversarial networks," in *International Conference on Computer Vision*, 2017, pp. 2223 -2232.

[26] I.J. Goodfellow, J. Pouget-Abadie, M. Mirza, B. Xu, D. Warde-Farley, S. Ozair, A. Courville, Y. Bengio, "Generative adversarial networks," *Advances in Neural Information Processing Systems*, vol. 3, pp. 2672 -2680, 2014.

[27] C. Li, M. Wand, "Precomputed real-time texture synthesis with markovian generative adversarial networks," in *European Conference on Computer Vision*, 2016, pp. 702 -716.

[28] N. Jetchev, U. Bergmann, R. Vollgraf, "Texture synthesis with spatial generative adversarial networks," *arXiv*: 1611.08207, 2016.

[29] R.A. Yeh, C. Chen, T. Yian Lim, A.G. Schwing, M. Hasegawa-Johnson, M.N. Do, "Semantic image inpainting with deep generative models," in *IEEE Conference on Computer Vision and Pattern Recognition*, 2017, pp. 5485 -5493.

[30] J. Yu, Z. Lin, J. Yang, X. Shen, X. Lu, T.S. Huang, "Generative image inpainting with contextual attention," in *IEEE Conference on Computer Vision and Pattern Recognition*, 2018, pp. 5505 -5514.

[31] J. Gui, Z. Sun, Y. Wen, D. Tao, J. Ye, "A review on generative adversarial networks: Algorithms, theory, and applications," *arXiv*: Learning, 2020.

[32] D. Ulyanov, A. Vedaldi, V. Lempitsky, "Instance normalization: The missing ingredient for fast stylization," *arXiv*: Computer Vision and Pattern Recognition, 2016, pp. 1607.08022.

[33] R. Girshick, "Fast R-CNN," in *The IEEE International Conference on Computer Vision* (ICCV), 2015, pp. 1440-1448, doi: 10.1109/ICCV.2015.169.

[34] J. Johnson, A. Alahi, L. Fei-Fei, "Perceptual losses for real-time style transfer and super-resolution," in *European Conference on Computer Vision*, Springer, 2016, pp. 694 -711.

[35] Q. Yang, P. Yan, Y. Zhang, H. Yu, Y. Shi, X. Mou, M.K. Kalra, Y. Zhang, L. Sun, G. Wang, "Low-dose ct image denoising using a generative adversarial network with wasserstein distance and perceptual loss," *IEEE Transactions on Medical Imaging*, vol. 37, pp. 1348 -1357, 2018.

[36] G. Yang, Y. Cao, X. Xing, M. Wei, "Perceptual Loss Based Super-Resolution Reconstruction from Single Magnetic Resonance Imaging," In: X. Sun, Z. Pan, E. Bertino, (eds) Artificial Intelligence and Security. ICAIS 2019. Lecture Notes in Computer Science, vol. 11632, p. 411–424.

[37] K. Simonyan, A. Zisserman, "Very deep convolutional networks for large-scale image recognition," *arXiv*: 1409.1556, 2014.

[38] C. Ancuti, C.O. Ancuti, C. De Vleeschouwer, "D-hazy: A dataset to evaluate quantitatively dehazing algorithms," in *IEEE International Conference on Image Processing*, 2016, pp. 2226-2230.

HongQi Zhang

He is currently chief expert of China Electric Power Group, researcher professor of No. 38 Research Institute of CETC, ISO registered expert, and expert of National Defense Science and Industry Bureau, National Standard Commission, the Ministry of Science and Technology as well as the Ministry of Industry and Information Technology. He leads more than 80 items for the formulation of International, national and industry standards, including 4 international standards, 32 national standards, electronics and machinery industry standards more than 50 items. He won more than 20 provincial-level science and technology awards, including 4 China Standard Innovation Contribution Awards. In 2020, he won the China Standard Innovation Contribution Award, Outstanding Contribution Award; in 2018, he won the China Standard Innovation Contribution Award, with ranking the first order.

Yixiong Wei

He is the senior engineer of No. 38 Research Institute of CETC, and the master supervisor of Chinese Academy of Electrical Sciences. He is long-term engaged in digital cutting-edge technology research, technology breakthrough, application transformation and other works. He presided over the "air 500 Dam Components Assembly Line Intelligent Information Iot" and other projects, as well as the chief designer and other core members to participate in the bureau of Science and technology and other 7 projects. He has obtained 18 patent authorizations, including 1 International Patent Authorization and 6 National Patent Authorizations. He participates in the preparation of 29 standards at various levels, including 1 national standard as the chief editor, 3 industry standards. He has won the first prize of Science and technology progress of Anhui Province, the excellent patent award of China, the first prize of China Quality Association, and the First Prize of science and technology of China Electronic Science and Technology Group, etc.

Zhou Hongqiao

He received the B.S. degree and M.S. degree in the mechanical design manufacture and automation from Wuhan University, Wuhan, China, in 2002 and in 2005, and the Ph.D. degree in mechanical manufacture and automation from Huazhong University of Science and Technology, Wuhan, China, in 2010. He is currently a researcher with the Institute of Electronics Technology, The 38th Research Institute of China Electronics Technology Group Corporation, Hefei, China. He is the author of 8 articles, and 12 national invention patents. He participated in the designation of 2 national standards and 51 military electronic industry standards. His research interests include the designation of electronic industry standards, digital design and manufacturing, enterprise information theory and system integration researches. Dr. Zhou was a recipient of the Second Prize of Anhui Province Science and Technology Progress Award in 2016, and the China Patent Excellence Award in 2017, and the First Prize of China Standard Innovation Contribution Award in 2018.

Wu Qianhao

He was born in Anqing, Anhui, China in 1995. He received the bachelor's degree in the mechanical design manufacture and automation from Anhui University, Hefei, China, in 2017 and the master's degree in transportation engineering from Hefei University of Technology, Hefei, China, in 2020. He is currently a digital design engineer with the Institute of Electronics Technology, The 38th Research Institute of China Electronics Technology Group Corporation, Hefei, China. His research interests include digital twin technology, digital technology and intelligent manufacturing.

A Diverse Domain Generative Adversarial Network for Style Transfer on Face Photographs

Rabia Tahir[1], Keyang Cheng[1]*, Bilal Ahmed Memon[2], Qing Liu[1]

[1] School of Computer Science and Communication Engineering, Jiangsu University, Zhenjiang (China)
[2] Ghulam Ishaq Khan Institute of Engineering Science and Technology Topi, Swabi (Pakistan)

Received 19 December 2021 | Accepted 21 June 2022 | Published 01 August 2022

Abstract

The applications of style transfer on real time photographs are very trending now. This is used in various applications especially in social networking sites such as SnapChat and beauty cameras. A number of style transfer algorithms have been proposed but they are computationally expensive and generate artifacts in output image. Besides, most of research work only focuses on some traditional painting style transfer on real photographs. However, our work is unique as it considers diverse style domains to be transferred on real photographs by using one model. In this paper, we propose a Diverse Domain Generative Adversarial Network (DD-GAN) which performs fast diverse domain style translation on human face images. Our work is highly efficient and focused on applying different attractive and unique painting styles to human photographs while keeping the content preserved after translation. Moreover, we adopt a new loss function in our model and use PReLU activation function which improves and fastens the training procedure and helps in achieving high accuracy rates. Our loss function helps the proposed model in achieving better reconstructed images. The proposed model also occupies less memory space during training. We use various evaluation parameters to inspect the accuracy of our model. The experimental results demonstrate the effectiveness of our method as compared to state-of-the-art results.

Keywords

CycleGAN, Gated-GAN, PReLU, Smooth L1 Loss, Style Transfer.

DOI: 10.9781/ijimai.2022.08.001

I. Introduction

Style transfer means to apply style of an image to another image by keeping the original content the same. Style transfer lies under the category of Image-to-Image translation. Some other examples of Image-to-image translation are transfer from satellite images to Google maps, winters to summers, night to day, etc. [1]. Our work is specifically about applying diverse style transfer from distinct style images to real photographs. These styles can be paintings of artist, animated images or cartoon, sketches etc. There is a limited research work which describes painting style transfer to human faces [2]. Painting style transfer also known as artistic style transfer that means transferring a real photograph into the painting style of some artist [3]. However, painting transfer techniques can be divided into three categories; texture transfer, stroke transfer and section transfer techniques. Texture transfer technique means to follow the texture pattern of painting and then transfer it to the content image. When we apply most of painting transfer techniques to human faces, it results in deformation. Artistic style translation or painting style translation field is facing many issues including appearance of artifacts on generated image. Moreover, if content image contains some organ of human body such as face or head portraits then it is more difficult to perform style translation, because it may destroy structure of the face [4].

* Corresponding author.

E-mail address: kycheng@ujs.edu.cn

Deep learning is getting popular day by day in many social media apps such as DeepArt.io and PRISMA which are most popular examples of deep learning involved in style transfer applications [5]. Therefore, in this work, we propose Diverse Domain Generative Adversarial Network (DD-GAN) for style transfer from famous paintings to human faces. Our model is based on [6], and we aim to perform fast training and better visual results without loss of semantic content. The loss functions used in this model helped to reduce artifacts on generated images. It is faster in training process and generates reconstructed images with preserved content i.e. face. We reduce complexity of the model by using smaller number of residual blocks without sacrificing the accuracy. Furthermore, we use various evaluation parameters to check the efficiency of the proposed model. Hence, our proposed model decreases training time, improves visual results after style translation, generates better reconstructed images is simpler to implement. The main contributions in this work are:

- A novel method DD-GAN is proposed which transfers diverse painting styles to human face photographs.
- A loss function based on SmoothL1 is used in the model that preserves the identity in reconstructed images.
- A simple training strategy and small number of residual blocks enable the model to reduce the training time.

II. Related Work

Style translation is a significant field of computer vision which is being studying from the last two decades [7]. There are many algorithms which were proposed for style translation with different types of deep neural network such as CNN or VGG network. However, a few works encapsulate the significance of Generative Adversarial Networks (GANs) in this field. As our work is related to style transfer with GAN therefore, this section explains some recent work of style transfer with various models of GAN.

A. Generative Adversarial Networks

Generative Adversarial Networks or GANs were proposed in 2014 [8] and brought a revolution in the field of machine learning and computer vision for fake image generation. They are generative models and consist of two parts; Generator and Discriminator. The generator is a generative model which generates fake data similar to the training data while discriminator network detects among real and fake images. The uniqueness of GAN is that both generator and discriminator train simultaneously and improve their performance with time.

GANs use different loss functions such as adversarial loss and cycle consistency loss in order to generate fake data. From 2014 till now, many variants of GAN have been proposed and they are used for various purposes such as image generation, style translation, super-resolution, and text-to-image generation [9]. Many GAN-based methods have been proposed for style translation specifically for multi domain tasks. This work also aims to produce a GAN variant which can perform fast style translation on human photographs. Although GAN and its variants have achieved high accuracy results in style translation tasks but still there are many challenges which are high computational time, need of rich resources, complexity of the model and unstable GAN training. There is need to sort these challenges in new variants of GAN for multi-domain style translation.

B. Image-to-Image Translation

Image-to-Image translation (I2I) methods are of two types; methods with paired data and methods without paired data. Firstly, Isola et al. [10] proposed pix2pix GAN with paired training samples. There are some other examples of I2I methods with paired training data in [11] and [12]. CycleGAN [1], ComboGAN [13], and StarGAN [14] are some examples of image-to-image translation with GAN in an unsupervised way. They performed style translation on multiple domains without paired examples and used as base work for other papers. Our method is also based on CycleGAN because it serves as a general purpose solution for various style translation tasks. In addition, we use transformer module of Gated-GAN to perform multi-domain style translation as CycleGAN requires multiple discriminators and generator module to perform multi-domain style translation. Hu et al. [15] proposed a style transfer model based on CycleGAN and VGG model. However, they used only one GAN structure instead of using two GAN. In order to preserve the semantic content of image, they used VGG network as a feature map. I2I methods have produced improved visualized results in style of various domains but resultant images still contain artifacts and blurriness. Moreover, these methods are unable to preserve the complete identity of the original images especially face. I2I methods need improved loss functions to produce high quality stylized images and reconstructed images with preserved identity.

C. Painting Style Transfer

Painting style transfer or artistic style transfer is another type of image-to-image translation. There are various works which perform artistic style transfer with different deep learning models such as CNN and GAN. Gay et al. [16] proposed a CNN-based style transfer technique which performs style translation on a content image by transferring style of an image. However, this work was computationally expensive which is replaced by recent works [17]-[20]. Zhang and Dana [21] proposed MSG-Net introducing a CoMatch layer in the model for style transfer. This model not only transfers the style to the target image, but also removes the artifacts. They produced better results regarding processing time and visual quality. Most of research is based on different types of style loss function used in style translation. For example, adversarial loss [8], perceptual loss [19], content loss [16], [22]. Huang et al. proposed a brush-based approach that inherits the spirit of the stroke rendering. They transform small patch of images into brushstroke of the target style. Only texture and color are changed while keeping the geometrical shape preserved [23]. The above mentioned methods mostly use common painting style images for style translation. However, a little research work is done which focused on diverse and unique style translation with the help of GAN. Therefore, this article is a contribution in this field. As we consider diverse multiple domains and perform style translation using one GAN model with fast training.

III. Overview of the Proposed Model

We propose Diverse Domain Generative Adversarial Network (DD-GAN) for multi-domain style translation on human photographs. This model specifically focuses on how we can apply different painting styles of artists on human faces and convert them to charming portraits. For this purpose, we adopt an architecture that consists of an encoder, decoder and number of transformers to perform style translation. However, we adopt an efficient training strategy with new loss functions in both generator and discriminator of our model. To stabilize training, we use PReLU in generator and LeakyReLU in discriminator of our model. Moreover, we use Smooth L1 function in reconstruction loss formula. Because Smooth L1 loss function has more benefits over L1 and L2 loss function as it combines advantages of both L1 and L2. Furthermore, it speeds up the training process. This loss function gives better results for reconstructed images as compared to other state-of-the-art methods. Further, we adopt 2D-Instance normalization to speed up the process of stylization. We modify ordinary weight initialization method in discriminator and generator model with Xavier weight initialization method. Our model is simple to adopt yet fasten for diverse style translation on human face photographs. The training time of the proposed model is decreased because small number of residual blocks. Moreover, we use various evaluation metrics to inspect the efficiency of model. For content images, we use Helen dataset as portrait of human. For style images, we use four diverse styles to train our model i.e. wall mural, iconography, painting and Albrecht Durer. All four style images categories are different from each other in terms of texture and pattern. Fig. 1 explains the working of the proposed model. The generator consists of encoder, list of transformers, decoders and instance normalization with PReLU activation function that is used in generator. The encoder contains three convolution layers and the decoder contains four residual blocks. The discriminator model we adopt is commonly used PatchGAN with two loss functions. Details of these components are explained in the next sections.

A. Auto-encoder With Transformers

In DD-GAN, we have a generator G which consists of an encoder E, decoder D and a number of transformers T, and a discriminator D. The number of T depends upon number of styles i.e. you can extend or decrease T based on choice of your style domain. The transformer is basically a number of the residual block and output of encoder (feature maps) is input of the residual block in Transformer T. The residual block consists of a stack of layers and it provides output of a specific layer to any other deep layer in the block. The basic purpose of using the gated transformer is to add multiple styles in a single generator. In our case, we have two domains of images namely; Human face photographs $x_i \epsilon X$ and famous artistic painting images $y_i \epsilon Y_k$ where k means number of style domains. In our case, we set k=4 because there are four diverse domains. There are no paired examples for these two

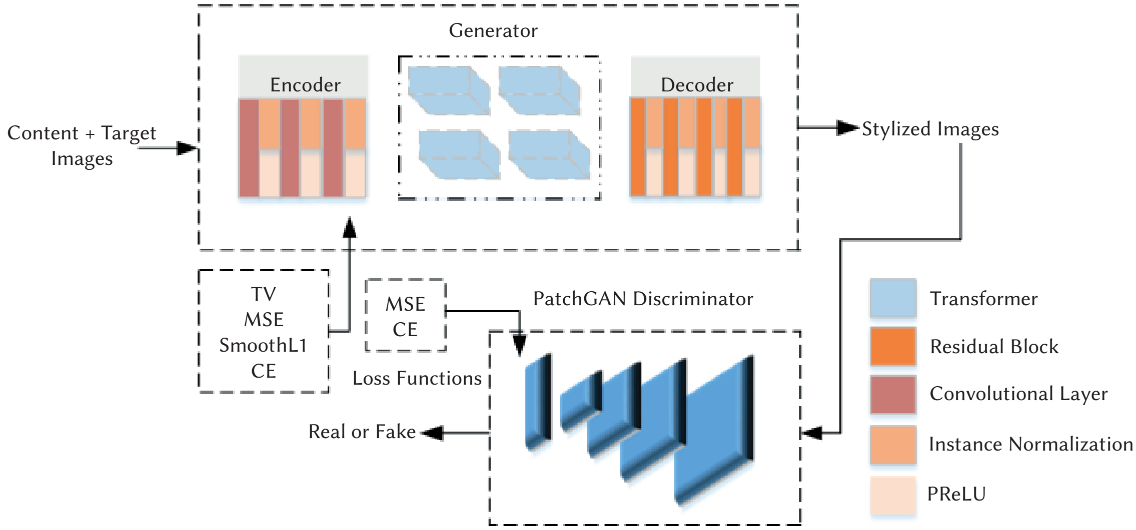

Fig. 1. The architecture of DD-GAN. It consists of an encoder, decoder and four transformers. The discriminator takes the real images and generated images and identifies whether they are real or not.

domains as it is a kind of unsupervised style translation like Cycle-GAN. There are two mapping functions in generator i.e. H and F. The aim of H mapping function is to generate a fake image y by translating painting style to human face photographs i.e. H : x⟶y. Then, we have an inverse mapping function F which converts the translated image back to its original state i.e. F : y⟶x. There is one encoder E in our generator G which encodes the important features of the input image into the feature space E(x) and gives it to Transformer T. This encoder comprises of several convolutional layers, while a convolutional layer is the main component of any deep neural network and comprised of various kernels or filters. The transformer T consists of 1 residual block and the decoder consists of four residual blocks. The transformer T takes the encoded input from encoder and assigns a specific style k to that input. It aims to give an output like G(x, k). The output of these 5 residual blocks is activation T(E(x)). Next, we have a decoder Dco which consists of fractionally strided convolution layers. The purpose of decoder D is to transform the T(E(x)) into output image G(x) i.e. Dco (T(E(x)) = G(x).

B. Discriminator of DD-GAN

The role of discriminator D is to distinguish among real y and fake samples G(x). Therefore, in DD-GAN, we have two separate discriminators D_y and D_x for both mapping functions H and F. The discriminator D_y learns to discriminate real paintings and fake generated painting, while D identifies among real photographs and reconstructed photographs. We train generator with PReLU and discriminator with LeakyReLU which helps to fasten and stabilize the training process. The loss functions in GAN play a very important role for stabilizing training procedure and better quality generation of images. In our model, we use four different loss functions: auto-encoder loss, total variation loss (TV), mean square error (MSE) and cross entropy (CE) loss.

C. Loss Functions

We adopt four loss functions in our model i.e. Mean Square Error (MSE), Smooth L1 reconstruction loss, total variation loss (TV), and cross entropy (CE) loss. First loss function is Least Square Generative Adversarial Network (LSGAN) loss which trains D and G simultaneously like a minimax game [24]. LSGAN can be implemented with the help of Mean Square Error (MSE). LSGAN helps to get non-saturating and smooth gradient in the discriminator D and it is defined as:

$$Loss_{least}=\mathbb{E}_{x\epsilon X}[D(G(X))^2]+\mathbb{E}_{y\epsilon Y}[(D(y)-1)^2] \quad (1)$$

where D(G(x)) means that discriminator is provided a fake input to identify it. And D(y) means that we give the target label to the discriminator to identify among real and fake labels. The second loss function is auto-encoder reconstruction loss which is defined between real input x and reconstructed image $\bar{x}$. We use this loss function by combining both encoder and decoder module i.e. E and Dco. Auto-encoder reconstruction loss reduces the possible mapping function i.e. provides unique solutions and diverse outputs. We use Smooth L1 loss function between reconstructed image and original image and it is defined as:

$$Loss_{rec}=\mathbb{E}_{x\epsilon X}[|| Dco\ \mathbb{E}\ (X)-X ||_{smoothl1}] \quad (2)$$

where Dco is decoder and $\mathbb{E}$ (x) is encoded feature space. And Dco(E(x)) means identical output like input x. Smooth L1 loss function is also known as Huber Loss and it is less prone to outliers as compared to MSE loss function. It is a combination of L1 and L2 loss functions. When training with L2 loss functions, there are chances of gradient exploding. Smooth L1 loss [25] eliminates this limitation and it is defined as:

$$L1_{smooth}(x,y)=\frac{1}{n}\sum_i Z_i \quad (3)$$

where

$$Z_i=\begin{cases}0.5\times(x_i-y_i)^2, & if\ |x_i-y_i|<1\\ |x_i-y_i|-0.5, & if\ |x_i-y_i|\geq 1\end{cases} \quad (4)$$

where x and y contain n different elements and have random shapes. Smooth L1 loss acts like a combination of L1 and L2 losses. When the absolute value is near to zero it acts like L2 loss and when its value is high it acts like L1 loss function. It combines two major benefits of L1 and L2 loss functions which are steady gradients for high values of x and low oscillations for small values of x. With the use of Smooth L1 loss, our model generates reconstructed images with small amount of outliers and fastens the training process. As there are multiple styles in DD-GAN, so the model may get confused between multiple styles. Therefore, we use an auxiliary classifier to discriminate the style categories [6]. To calculate auxiliary classifier loss, we use Cross Entropy loss (CE) to measure the performance of discriminator model whose output is among 1 and 0. It compares the label with discriminator prediction and it is defined as:

$$min_G Loss_{clc}(G)= - \mathbb{E}_{x\epsilon X}[\log C\ (Style=c|G(x, c))] \quad (5)$$

TABLE I. Generative and Discriminative Network of DD-GAN

Encoder	Transformer	Decoder	Discriminator
Conv2d(C=3,F=32, Instance2D,K=7,S=1) PReLU	RB(F=128, Instance2D,K=3,S=2) PReLU	4RB(F=128,Instance2D,K=3,S=2) PReLU	Conv2d(C=3,F=64, Instance2D,K=4,S=2)LeakyReLU
Conv2d(F=64, Instance2D,K=3,S=2) PReLU		ConvT2d(F=128,Instance2D,K=3,S=1/2) PReLU	Conv2d(F=128, Instance2D,K=4,S=2)LeakyReLU
Conv2d(F=128,Instance2D,K=3,S=2) PReLU		ConvT2d(F=64,Instance2D,K=3,S=1/2) PReLU	Conv2d(F=256,Instance2D,K=4,S=2) LeakyReLU
		ConvT2d(F=3.Instance2D,K=7,S=1) tanh	Conv2d(F=512,Instance2D,K=4,S=2) LeakyReLU
			Conv2d(F=1,K=4, S=1)
			Conv2d(nstyles, K=1, S=1)

where c means the index of style collections K i.e. C ϵ 1, 2, 3. . . K. And c is an auxiliary classifier. More details of this loss function can be seen in [6]. The last loss function is total variation regularization loss or TV loss which helps to get smoother generated images i.e. G(x, c). It is defined as [19], [26], [27]:

$$L_{TV}=\sum_{i,j}[\,(G(X)_{i+1,j}-G(X)_{i,j})^2+(G(X)_{i,j+1}-G(X)_{i,j})^2]^{1/2} \quad (6)$$

The overall loss function for generator G is described as:

$$Loss_G\ (total)= Loss_{least}+\alpha L_{TV}+\beta Loss_{clc}+\gamma Loss_{rec} \quad (7)$$

Where α, β, γ are hyper-parameters of weight consistency.

D. PReLU-based Generator

The activation function plays a significant role in neural networks especially in GAN. In most GAN models, we see that ReLU activation is used in the generator while LeakyReLU activation is used in the discriminator. It is popular to use them as activation functions in many neural networks. In any deep learning model, the activation function plays a vital role. Therefore, it is very important to choose a suitable activation function while designing your own model. In our model, we choose Parametric Rectified Linear Unit (PReLU) instead of ReLU activation function in our generator model and LeakyReLU in the discriminator. PReLU adds additional parameters as compared to ReLU. The convergence rate of PReLU is faster as compared to other activation functions such as ReLU and sigmoidal. Therefore, the ultimate purpose of using PReLU activation function in the generator model is to automatically tune the parameters which helps in improving the accuracy rate [28], [29].

E. Network Architecture

We use the network architecture proposed by Chen et al. [6] but with some modifications. In DD-GAN, we have three basic modules named encoder, decoder and transformer. The generator contains three modules named encoder, decoder and transformer. The discriminator is used to identify that the image is real or fake. Table I shows the layers specification of our network. The encoder consists of three layers of Conv2D with instance normalization and PReLU as activation function. Zuo et al. proposed DPGAN [28] to use PReLU in generator while LeakyReLU in discriminator. Therefore, by following it, we are using the same in our model. We use one residual block in Transformer with PReLU and instance normalization. While decoder consists of 4 residual blocks, 2 transpose Conv2D, and 1 Conv2D layer along with PReLU and instance normalization. We reduced the number of residual block from five to four in decoder to make the model less complex and to fasten the training process. We use one up sampling and three down sampling layers in our encoder. We use Markovian Patch GAN architecture for the discriminator because it has a small number of parameters which can applied to various sizes of input [1]. This type of discriminator is effective because it assumes independence among all pixels separately, while these pixels are separated by a patch diameter. The discriminator contains five Con2D layers with instance normalization and LeakyReLU activation function.

F. Instant Normalization and Xaviar Weight Initialization

We use instance normalization in all layers of the encoder, residual block and decoder. Also, we use instance normalization in all layers of discriminator [30]. Replacing batch normalization with instance normalization produces better results especially for style generation tasks. It is better than batch normalization because it independently normalizes all elements of the batch. While training any neural network, the weight initialization is an important step. Too much small weights can lead to vanishing of gradient while too large size weights can lead to explosion of gradient. Xaviar weight initialization [31] method solves this problem by keep the variance same in each layer of the network. Therefore, we use Xaviar weight initialization method because it also gives good performance for style translations tasks [32]. Our model consists of Conv2D layers, therefore we initialize weight with Xaviar normal technique in both generator and discriminator models. As compared to normal weight initialization method, it selects the weight from Gaussian distribution with values zero mean and 1/n variance, where n denotes the number of neurons in input [33].

IV. Datasets and Experiments

A. Datasets

1. Helen Dataset

This paper proposes a model for painting style transfer with diverse domains and five diverse datasets are used for experiments. We use Helen dataset as a content resource. Helen dataset is a famous dataset for facial recognition task. We use images of these datasets as content images in our model. All images in this dataset are portrait images of human faces. This dataset contains 2000 training images and 330 testing images [34]. We use 856 images for training purpose. For style exemplar, we use four different datasets from Kaggle. They are Wall Mural[1], Iconography[2], The Work of Painting[2] and Albrecht_Durer[3].

2. Wall Mural

Mural is a kind of art which is applied directly on some wall, surface or ceiling. Wall Mural is a collection of wall mural painting collected from Kaggle. In this dataset, there are 10,200 images of

[1] https://www.kaggle.com/vbookshelf/art-by-ai-neural-style-transfer

[2] https://www.kaggle.com/thedownhill/art-images-drawings-painting-sculpture-engraving.

[3] https://www.kaggle.com/supratimhaldar/deepartist-identify-artist-from-art/data

human portraits in mural style. The size of images is 400×300 pixels. We take 500 images from this collection as our first style domain.

3. Albrecht Durer

Albrecht_Durer is a collection of a German artist Albrecht Durer (1471-1528). His paintings mostly consist of portraits, water colors and altarpieces. We use 324 images from his collection of drawing and engravings. This collection includes black and white, gray color based engraving drawings of this artist. We use these images as our second domain.

4. Iconography

The Iconography is a collection of icons and works of old Russian applied art, ranging from the artists of 10th to the 18th centuries. We take 500 images from this collection as our third style domain.

5. The Work of Paintings

The Work of Paintings is a collection of Russian Museum's paintings by artists of 18th, 19th and 20th centuries. We take 500 random images from this collection. All images are mostly the self-portrait with dark brown, red and gray texture. These paintings are very colorful, bright and clear in content. Therefore, our total number of images in style training dataset is 1824 while 500 images of Helen as training content. We use 330 images of Helen dataset for testing. Fig. 2 shows all style images that are used in experiments. All categories of painting possess diverse characteristics which can be seen in Fig. 2.

Fig. 2. All four diverse style painting images.

B. Training Strategy

We use batch size of 1 with 120 epochs for trainings. The load size of images is 128×128. The reason of small size of images is to reduce the computational cost. However, for testing phase, we use the original size of images i.e. 256×256 to evaluate the performance. Other details of parameters used in DD-GAN are given in Table II.

TABLE II. Experimental Settings for DD-GAN

Parameters	Value
Epoch	120
Batch size	1
Input size	128 ×128
λ_A	10
Learning rate	0.0002
TV weight	1e-6
No of styles	4
Decay epochs	80
Reconstruction weight	10
β_1 and β_2	0.5 and 0.999

V. Results and Analysis

A. Qualitative Results

Fig. 3 shows qualitative results of DD-GAN with Helen dataset and other four style datasets Wall Mural, Painting, Iconography, Albrecht Durer and reconstructed images. We take human face photographs from Helen dataset as a content image and apply style transfer process on these images after training. We can see the newly generated style transferred images along with reconstructed images. From Fig. 3, we can see that style transfer to iconography and painting images are visually less attractive as compared to Wall mural and Durer images. The reason of this difference is because of dynamic nature of both datasets iconography and painting as both of these datasets contain paintings from different artists. Therefore, it is difficult to train the model. Contrary, Wall Mural and Albrecht Durer are two datasets which contain paintings of one artist and are of same type. Therefore, the resultant images are more appealing and better as compared to the other two datasets. And, reconstructed images are very much similar to the original images because of Smooth L1 loss function.

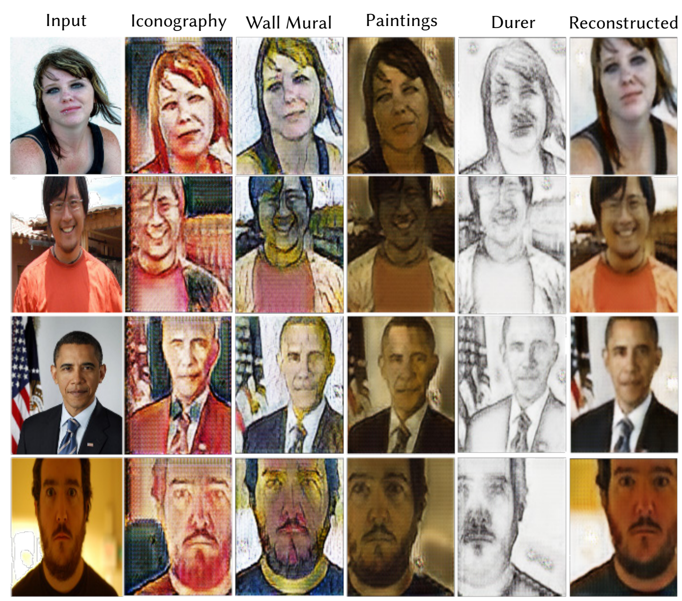

Fig. 3. Qualitative results of DD-GAN on Helen dataset.

Another important thing is the preservation of shapes and edges of human faces after style translation. We can observe that the important features of faces are preserved after style translation. The aim of DD-GAN is to make sure the preservation of face identity. As in style translation, we do not want to change the content and lose its original identity. In Fig. 4, we compared Gated-GAN with DD-GAN in reconstruction phase. We observed that black empty hole were present in most of reconstructed images of Gated-GAN. We zoomed and cropped these images and showed them in Fig. 4. The improvement in results is because of reconstruction loss formula which is comprised of Smooth L1. It helped in achieving better results by removal of distortion in generated images.

However, our results are quite better but little blurry as compared to Gated-GAN. In Fig. 5, we visually compare results of Gated-GAN with our model for style domain Iconography. Gated-GAN performed better as compared to our model in terms of texture appearance. It is obvious in this figure, that Gated-GAN learned texture and style of Iconography dataset in more efficient way and then implemented it on Helen dataset. However, it failed to preserve the content i.e. face of person. Contrary, our model preserved the identity but failed to transfer color and style texture of target dataset. Further, our resultant images contain less distortion as compared to the base model which shows superiority of our model up to some extent. In Fig. 6, we compared some style transferred images of DD-GAN and Gated-GAN. All four style domains i.e. wall mural, iconography, painting and Durer are compared in this figure. It is obvious from this comparison that our results are better as compared to the other model especially for mural, painting and Durer. However, Gated-GAN showed better results for iconography style domain as compared to DD-GAN. Our model generated style transferred images with less distortion with more clear representation of texture of target domain. However, Gated-GAN produced images with noise such as visible black dots.

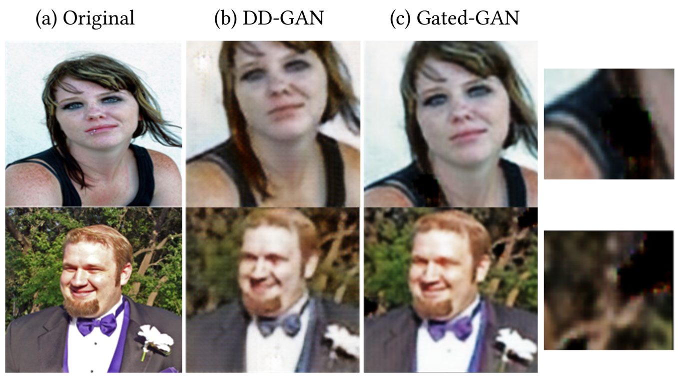

Fig. 4. Comparison between reconstructed images of Gated-GAN and DD-GAN.

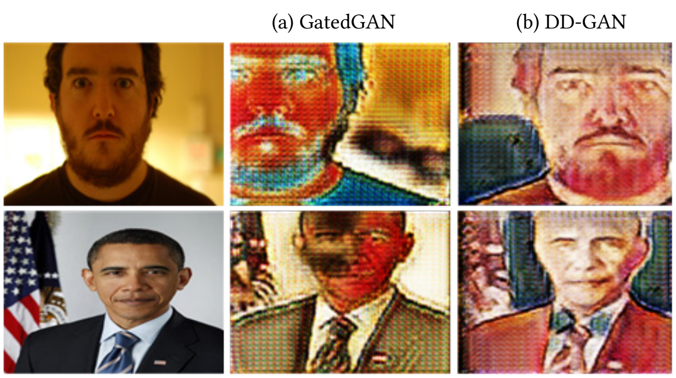

Fig. 5. Visual comparison of Iconography style transfer on Helen dataset.

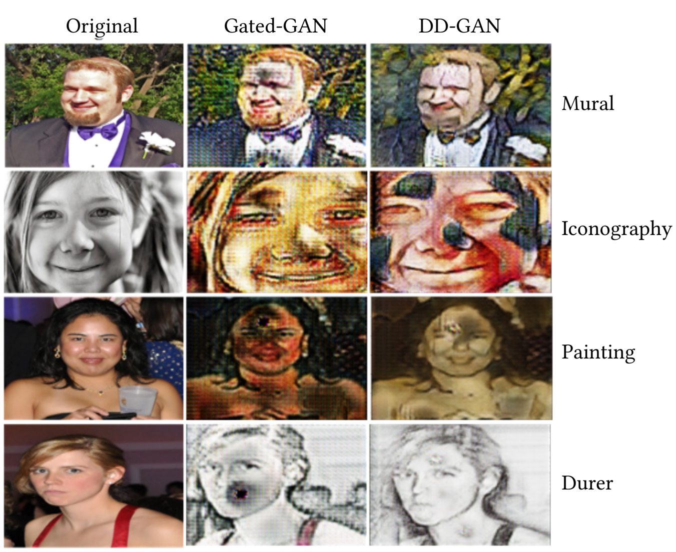

Fig. 6. Comparison of our model with the base model for all four style domains.

B. Discussion on Evaluation Metrics With Quantitative Results

In this section, we explain some popular evaluation metrics to inspect quality of generated images especially with GAN. There are some common evaluation metrics such as FID, MSE, PSNR, SSIM and MS-SSIM for the assessment of image quality [35]. Therefore, we use these five evaluation metrics to quantify our results. Mean Square Error (MSE) calculates the average of the square of difference among the target image and generated image. An MSE with small value shows higher similarity while MSE with high value shows less similarity. A smaller MSE value means that model is performing well. For example, zero MSE means that model is perfect that means the two images are identical. Peak Signal-to-Noise Ratio (PSNR) is an expression of ratio between signal and noise, where noise is the error produced by compressed image and signal depicts original image. The more the value of PSNR means better results. The more value of PSNR means that two images are more similar [35]. Structural Similarity Index (SSIM) [12] was proposed by Wang et al. to inspect the quality of an image. It is a perceptual evaluation metric and it calculates the image quality degradation. The values closer to 1 means high accuracy and values closer to zero mean less accuracy.

We use SSIM to check the similarity among original image and fake generated image after applying style transfer. Extensive version of SSIM is MS-SSIM [36] (Multi-Scale Structural Similarity Index) that calculates the similarity index among two images at different scales. It performs better than SSIM. All of above metrics are not enough to inspect efficiently the visual quality of images. Therefore, we use another state-of-the-art metric Frechet Inception Distance (FID) for our generated images. FID is a metric which is proposed to inspect quality of generated images especially by GAN. It is an improved version of Inception score. It takes a collection of original images and generated images by GAN. It basically calculates the distance among two different types of collection of images. FID for same collection of images becomes zero. The more the FID score, the more difference among two collections exits [37]. Fig. 7 shows FID score of all categories of our diverse style domains. We used two categories (original and style transferred) to calculate FID score. We can see the reconstructed images obtained the best FID score i.e. lowest score.

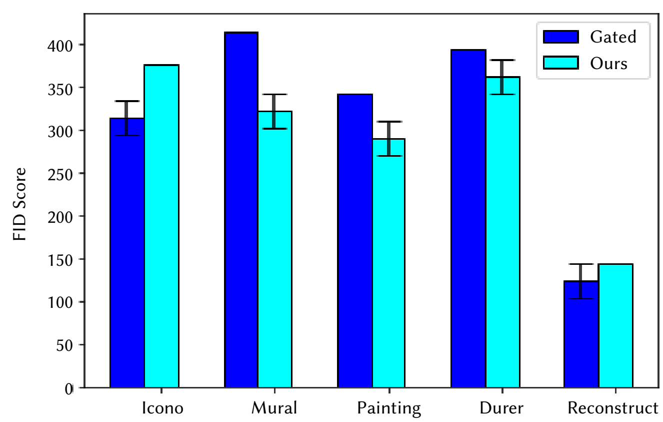

Fig. 7. Fid score for original images and style transferred images. Black lines on bars show the best fid sore.

However, Iconography obtained highest fid score which shows the average quality of style transferred images for this category. The reason of best fid score of reconstructed images is that the images are more similar to the original images. However, when we apply style to content images then texture and color of these images become change. Therefore, fid of style transferred images is slightly higher as compared to reconstructed images. If we compare all four style categories, we can observe that Painting images obtained best FID score as compared to rest of three categories. The reason of this lowest score is the less dynamic nature of this dataset. However, the Iconography paintings obtained highest fid score because the collection of these paintings possesses diverse styles. In Fig. 7, we compared FID scores of both models. Gated-GAN obtained less FID score for reconstructed images and Iconography as compared to our model. However, it produced high FID score for Durer, Wall Mural, and Painting datasets. Table III shows the comparative analysis among Gated-GAN and our model for reconstruction images. We take average of 15 images in testing phase for both Gated-GAN and DD-GAN.

TABLE III. Comparative Analysis Of Various Error Rates of Reconstructed Images

	MSE	PSNR	SSIM	MS-SSIM
Gated-GAN	699.3	19.97	0.32	0.10
Our Model	618.96	20.41	0.32	0.09

The values in Table III are comparison between original image and reconstructed image after applying style translation. Our model gives less MSE and higher PSNR value as compared to Gated-GAN which shows the superiority of our model. Because we used Smooth L1 loss function in our reconstruction phase, therefore the results are better as compared to Gated-GAN. However, our model obtained low accuracy values for MS-SSIM as compared to Gated-GAN, while SSIM values are the same for both models. In Table IV, we present MSE, PSNR, SSIM and MS-SSIM values of all four style categories. The Painting category achieved the best results as compared to remaining three style domains which shows its better visual quality. Among all datasets, Albrecht Durer obtained highest MSE and lowest PSNR which shows the complex nature of this dataset. There is always a trade-off between accuracy and computational time of any neural network. The best model focuses not only on achieving high accuracy but also on decreasing computational time. Therefore, we also compare different times for training and testing phases. Table V and VI compare time complexity of our model with the base model Gated-GAN.

TABLE IV. Comparative Analysis of Various Error Rate on All Four Style Transferred Images

	MSE	PSNR	SSIM	MS-SSIM
Wall Mural	960.62	18.43	0.15	0.04
Albrecht Durer	2139	15.29	0.21	0.02
Painting Images	854.59	19.47	0.24	0.05
Iconography Images	1383	16.55	0.10	0.003

TABLE V. Comparative Analysis of Training Time for 1 and 120 Epochs

	Gated-GAN	DD-GAN
Each Epoch	~4 to 5 minutes	~4 minutes
120 Epochs	~7 hours 54 minutes	~7 hours 30 minutes

TABLE VI. Elapsed Time for Reconstructon of Images During Testing Phase

	Gated-GAN	DD-GAN
MS-SSIM+ SSIM (ms)	20.86	19.46
MSE+PSNR(ms)	1.6	1.8

Table V shows time for first epoch and 120 epochs of Gated-GAN and DD-GAN during training phase. Our model completes training in less time as compared to the other. The reason is using a small number of residual blocks in generator and using of PReLU activation. This proves our model is a fast style transfer model for different types of images. Table VI compares time for reconstruction of images during testing period. During the testing phase, Gated-GAN achieved minimum time for the calculation of MSE and PNSR values and DD-GAN obtained minimum time for the calculation of SSIM and MS-SSIM. We also compared our model results with CycleGAN in terms of FID score. As CycleGAN is two domains generated network which can transfer to one style at a time. Therefore, we performed style transferred for two domains separately i.e. wall mural and Durer. Also, we checked the quality of reconstructed images after style translation. We noted that it took a lot of time to train CycleGAN with only one style domain. Results are comparative with our model and Gated-GAN but the drawback is domain limitation and computational time. Table VII compares FID score of our model with CycleGAN. Moreover, we conducted a short survey about quality of generated images of our model with base model. Results of this survey are given in Fig. 8. A total of 100 responses were received for this survey. We randomly choose images generated from Gated-GAN and DD-GAN from all style domains including reconstructed images. Then, we ask users to choose the best among two in each category. The purpose of this survey was to get feedback from people who do not belong to this field and only choose image according to its visual appearance. For our model, we received 64.52% positive responses while 42.2% positive response for base model. This shows better performance of our model. Category wise responses can be seen in Fig. 8.

TABLE VII. Comparison of FID Score for Cyclegan and DD-GAN

Style Domains	FID score
Wall Mural (CycleGAN)	255.60
Wall Mural (DD-GAN)	244.03
Durer (CycleGAN)	260.267
Durer (DD-GAN)	372.87
Reconstructed Images (CycleGAN)	89.86
Reconstructed Images (DD-GAN)	144.48

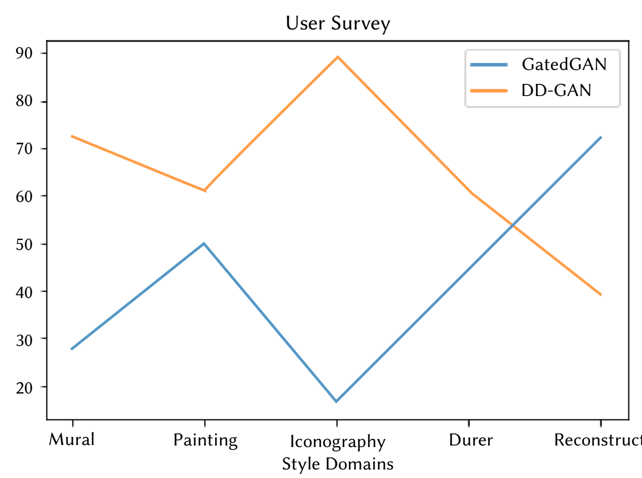

Fig. 8. User survey about style generated images between two models.

C. Ablation Study of Loss Function

In this section, we check the significance of all loss functions used in our model. The purpose is to ensure the usage of each loss function that either it is making some contribution in improvement of results or not. For this, we performed various experiments with removal of one loss function. Table VIII shows results of these experiments. Firstly, we check the significance of Total Variation (TV) loss in our model. We removed it and then accomplished our training. A clear fall in accuracy can be seen in Table VIII. The reason is that TV loss is used to remove noise by making sure the smoothness and spatial continuity in generated images. Therefore, when we removed it, increase in FID score and MSE, decrease in PSNR, SSIM and MS-SSIM can be seen. The second important loss function is reconstruction loss which plays an efficient role in performance of our model. As our model contains an encoder, decoder that makes it an auto-encoder. Basically, auto-encoder compressed an image to spatial features then reconstructs the image from these features. Hence, there is loss of some pixels and degradation of quality in generated image. For this purpose, reconstruction loss is proposed to measure the distance among original image and reconstructed image. There are many ways to implement this loss. In our model, we use Smooth L1 as a reconstruction loss function. When we remove this loss from our model, a sharp decrease of model's performance can be seen in Table VIII. This proves the importance and value of reconstruction loss in our model. We also compared training time with and without these loss functions. Table IX shows results of these experiments. The removal of TV and reconstruction losses leads to reduction the training time and accuracy. When we removed auxiliary classifier loss from our model, it resulted in no discrimination of style generated images. For example, we select Durer style to transfer on content image during testing and it gives us output image with painting style. Also, the quality of generated images is not good because loss of content structure i.e. face. Examples of some of these images are given in Fig. 9. In this figure, all three images were assigned Durer style domain at time of testing but the model failed to adopt this style and transferred mixture of other style domains. This proved the significance of auxiliary classifier loss in our model.

TABLE VIII. Ablation Study of Loss Functions in Our Model

	FID	MSE	PSNR	SSIM	MS-SSIM
DD-GAN	144.48	618.96	20.41	0.32	0.09
DD-GAN without TV loss	139.82	680.1	20.2	0.31	0.057
DD-GAN without reconstruction loss	468.30	1008	18.01	0.181	0.024

TABLE IX. Time Consumed for Training With and Without Loss Functions

	Time
Wall Mural (CycleGAN)	255.60
Wall Mural (DD-GAN)	244.03

Fig. 9. Generated images with no AC loss in Durer style domain.

D. Discussion

The major issue in style transferred methods is their evaluation. There is no exact parameter of comparing style generated images. Some researchers use feedback from different people to compare images [38]. While some use evaluation parameters such as FID, MSE etc. But there is no guarantee that small MSE means good results. During our experiments, we observed that some poorly generated images produce small MSE and high PSNR. And some best style transferred images show high MSE and low PSNR. This is the reason we used multiple evaluation parameters to compare our results. We tried our best to present the results and comparison in an efficient way. Firstly, we compared our results with base work i.e. Gated-GAN at 120 epochs. Table V shows the comparison among DD-GAN and Gated-GAN for computational time. It is clear that our model performs faster on the same dataset. We used a different approach in our model and training strategy which results in fast computational time and results are almost the same like original Gated-GAN. Increasing training time may result in better visualization results. However, our method DD-GAN is fast as compared to original Gated-GAN. Our method can be applied to those problems where fast computation and results are required. The reason of fast time processing is our simple architecture and choice of loss function that results in rapid results. We faced two main limitations of our model DD-GAN. First is the production of artifacts in generated images especially for style domains Painting and Iconography. The reason is complex and dynamic nature of these two datasets. These two datasets contain paintings from multiple artists and possess different style and color texture. Hence, some generated images after style transfer contain artifacts on images which spoil the face of a person. The second limitation is production of blurry images in the reconstruction phase.

VI. Conclusion and Future Work

In this work, we proposed a novel and fast GAN variant named DD-GAN (Diverse Domain Generative Adversarial Network) for diverse painting style transfer on human face photographs. The DD-GAN applies different styles on human faces and converts them into realistic and beautiful art pieces using one GAN model. The purpose of this research is to add a contribution in the field of neural style transfer specifically for painting style transfer to human faces. We used a new loss function in our model in order to increase the accuracy and decrease the computational cost. Moreover, we used PReLU activation function in our model in order to improve the results. We have obtained a state-of-the-art qualitative and quantitative results which shows the efficiency of our model. In the future, we want to use more dynamic and complex datasets for training. Moreover, we want to improve the visual quality of newly generated images without increasing computational time. This work can be extended by performing training with more iteration which is possible by the availability of resources. As we lack rich resources, therefore we performed and compared results with small number of epochs. In the future, we aim to improve the visual results by using efficient resources with less complex model.

Acknowledgement

This research is supported by Natural Science Foundation of China (No. 61972183).

References

[1] J. Zhu., P.Taseng, I. Philip and E. Alexie, "Unpaired image-to-image translation using cycle-consistent adversarial networks," in *Proceedings of the IEEE international conference on computer vision,* 2017, pp. 2223-2232.

[2] A. Selim, E. Mohamed and D. Linda, "Painting style transfer for head portraits using convolutional neural networks," *ACM Transactions on Graphics (ToG),* vol. 35, no. 129, pp. 1-18, 2016, doi: https://doi.org/10.1145/2897824.2925968.

[3] B. Rahul. and S. Jianlin, "Artist style transfer via quadratic potential," arXiv preprint arXiv, 2019, doi: https://doi.org/10.48550/arXiv.1902.11108.

[4] A. Khan et al., "Photographic painting style transfer using convolutional neural networks," *Multimedia Tools and Applications,* vol. 78, no. 14, pp. 19565-19586, 2019.

[5] L. Du, "How much deep learning does neural style transfer really need? an ablation study," in *Proceedings of the IEEE/CVF Winter Conference on Applications of Computer Vision*, 2020, pp. 3150-3159.

[6] C. Xinyuan, X. Chang, Y. Xiaokang, S. Li amd T. Dacheng, "Gated-gan: Adversarial gated networks for multi-collection style transfer," *IEEE Transactions on Image Processing,* vol. 28, no. 2, pp. 546-560, 2018, doi: https://doi.org/10.1109/TIP.2018.2869695.

[7] X. Li, S.Liu, K. Jan and M. Yang, "Learning linear transformations for fast image and video style transfer," in *Proceedings of the IEEE/CVF Conference on Computer Vision and Pattern Recognition,* 2019, pp. 3809-3817.

[8] I. Goodfellow et al., "Generative adversarial nets," *Advances in neural information processing systems*, vol. 27, 2014.

[9] K. Cheng, T. Rabia, L. Eric and M. Li, "An analysis of generative adversarial networks and variants for image synthesis on MNIST dataset," *Multimedia Tools and Applications*, vol. 79, no. 19, pp. 13725-13752, 2020, doi: https://doi.org/10.1007/s11042-019-08600-2.

[10] I. Phollip, J. Zhu, T. Zhou, and A. Efros, "Image-to-image translation with conditional adversarial networks," in *Proceedings of the IEEE conference on computer vision and pattern recognition*, 2017, pp. 1125-1134.

[11] S. Patsorn, J. Lu, C. Fang and F. Yu, "Scribbler: Controlling deep image synthesis with sketch and color," in *Proceedings of the IEEE Conference on Computer Vision and Pattern Recognition.* 2017, pp. 5400-5409.

[12] Z. Wang, A.C. Bovik, H.R. Sheikh, and E.P., "Simoncelli, Image quality assessment: from error visibility to structural similarity," *IEEE transactions on image processing*, vol. 13, no. 4, pp. 600-612, 2004.

[13] A. Anoosheh, A. Eirikur, T. Radu and G. Luc, "Combogan: Unrestrained scalability for image domain translation," in *Proceedings of the IEEE Conference on Computer Vision and Pattern Recognition Workshops*, 2018, pp. 783-790.

[14] Y. Choi et al. "Stargan: Unified generative adversarial networks for multi-domain image-to-image translation," in *Proceedings of the IEEE conference on computer vision and pattern recognition*, 2018, pp. 8789-8797.

[15] H. Chan, Y. Ding and Y. Li, "Image style transfer based on generative adversarial network," in *IEEE 4th Information Technology, Networking, Electronic and Automation Control Conference (ITNEC)*, vol. 1, pp. 2098-2102, 2020.

[16] L.A. Gatys, S. Alexander and B. Matthias, "A neural algorithm of artistic style," arXiv preprint arXiv:1508.06576, 2015.

[17] B. Mohammad and G. Golnaz, "Adjustable real-time style transfe, " arXiv preprint arXiv:1811.08560, 2018.

[18] G. Agrim, J. Justin, A. Alahi and F. Li, "Characterizing and improving stability in neural style transfer," in *Proceedings of the IEEE International Conference on Computer Vision.* 2017, pp. 4067-4076.

[19] J. Johnson, A. Alahi, and L. Fei-Fei. "Perceptual losses for real-time style transfer and super-resolution," in *European conference on computer vision.* 2016, pp. 694-711.

[20] K. Dmytro, S. Artsiom, P. Ma, S. Lang and B. Ommer, "A content transformation block for image style transfer," in *Proceedings of the IEEE/CVF Conference on Computer Vision and Pattern Recognition.* 2019, pp. 10032-10041.

[21] Z. Hang and K. Dana, "Multi-style generative network for real-time transfer," in *Proceedings of the European Conference on Computer Vision (ECCV) Workshops.* 2018.

[22] H. Xun and B.Serge, "Arbitrary style transfer in real-time with adaptive instance normalization," in *Proceedings of the IEEE International Conference on Computer Vision.* 2017, pp. 1501-1510.

[23] H. Fay and C.L. Chein, "Patch-based Painting Style Transfer," in *IEEE International Conference on Consumer Electronics-Taiwan (ICCE-Taiwan)*, pp. 1-2, 2020, doi: 10.1109/ICCE-Taiwan49838.2020.9258218.

[24] X. Mao et al, "Least squares generative adversarial networks," in *Proceedings of the IEEE international conference on computer vision.* 2017, pp. 2794-2802.

[25] G. Sreekumar, "How to interpret smooth l1 loss? ," *StackExchange* Sep 2018. [Online]. Available: https://stats.stackexchange.com/questions/351874/how-to-interpret-smooth-l1-loss.

[26] L.I. Rudin, S. Osher and E. Fatemi, "Nonlinear total variation based noise removal algorithms," *Physica D: nonlinear phenomena*, vol. 60, no. 1-4, pp. 259-268, 1992.

[27] A. Hussein and E. Dubois, "Image up-sampling using total-variation regularization with a new observation model," *IEEE Transactions on Image Processing*, vol. 14, no. 10, pp. 1647-1659, 2005.

[28] Z. Fang and L. Xiaofang, "DPGAN: PReLU Used in Deep Convolutional Generative Adversarial Networks," in *Proceedings of the 2019 International Conference on Robotics Systems and Vehicle Technology.* pp. 56–61, 2019, doi: https://doi.org/10.1145/3366715.3366728.

[29] K. He, X. Zhang, S. Ren and J.Sun, "Delving deep into rectifiers: Surpassing human-level performance on imagenet classification," in *Proceedings of the IEEE international conference on computer vision.* 2015, pp. 1026-1034.

[30] D. Ulyanov, A. Vedaldi, and V. Lempitsky, "Instance normalization: The missing ingredient for fast stylization," arXiv preprint arXiv:1607.08022, 2016.

[31] X. Glorot and Y. Bengio, "Understanding the difficulty of training deep feedforward neural networks," in *Proceedings of the thirteenth international conference on artificial intelligence and statistics*, 2010, pp. 249-256.

[32] T. Rabia, C. Keyang, E.K. Lubamba and M.S. Khokhar, "Multi-domain Cross-dataset and Camera Style Transfer for Person Re-Identification," *International Journal of Advanced Trends in Computer Science and Engineering*, vol. 8, pp. 2035-2041, 2019.

[33] N. Kumar, "Xavier Weight Initialization Technique in neural Networks," *The Professionals Point* 2019, [Online]. Available: http://theprofessionalspoint.blogspot.com/2019/06/xavier-weight-initialization-technique.html?

[34] V. Le, J. Brandt, Z. Lin, B. Lubomir and S.H. Thomas, "Interactive facial feature localization," in *European conference on computer vision*, 2012, pp. 679-692.

[35] U. Sara, M. Akter and M.S. Uddin, "Image quality assessment through FSIM, SSIM, MSE and PSNR—a comparative study," *Journal of Computer and Communications,* vol. 7, no. 3, pp. 8-18, 2019.

[36] Z. Wang, E.P. Simoncelli and A.C. Bovik, "Multiscale structural similarity for image quality assessment," in *The Thrity-Seventh Asilomar Conference on Signals, Systems & Computers,* vol. 2, pp. 1398-1402, 2003.

[37] H. Martin, R. Hubert, U. Thomas and B. Nessler, "Gans trained by a two time-scale update rule converge to a local nash equilibrium," in *Advances in neural information processing systems.* vol. 30, 2017.

[38] N. Hulzebosch, S. Ibrahimi, and M. Worring. "Detecting cnn-generated facial images in real-world scenarios," in *Proceedings of the IEEE/CVF Conference on Computer Vision and Pattern Recognition Workshops,* 2020, pp. 642-643.

Rabia Tahir

Rabia Tahir is currently a PhD student in Jiangsu University, Zhenjiang, China. Her interest areas are Image processing, Computer Vision, Deep Learning, Pattern Recognition and Computational Intelligence. She has published good impact factor papers in leading journals and conferences.

Keyang Cheng

Keyang Cheng is a member of CCF. He received the PHD Degree from School of Computer Science and Engineering, Nanjing University of Aeronautics & Astronautics in 2015. He has coauthored more than 30 journal and conference papers. He was at University of Warwick, UK, as a post-doctoral researcher in 2016. He is currently an associate professor and researcher in the School of Computer Science and Telecommunication Engineering of Jiangsu University. His current research interests lie in the areas of pattern recognition, computational intelligence and computer vision.

Bilal Ahmed Memon

Bilal Ahmed Memon is currently an Assistant Professor in GIKI University Swabi Pakistan. He has done his PhD in Management Sciences specialization in Finance from Jiangsu University, Zhenjiang China. He has published multiple impact factor papers in world's leading journal. His research area is complex networks in Finance. He is also reviewer of many journals.

Qing Liu

Liu Qing is currently pursuing the master's degree in computer application with Jiangsu University. His research interests include Computer Vision and Pattern Recognition.

Interactive Causal Correlation Space Reshape for Multi-Label Classification

Chao Zhang[1], Yusheng Cheng[1,2], Yibin Wang[1,2], Yuting Xu[1] *

[1] School of Computer and Information, Anqing Normal University, Anhui (China)
[2] The University Key Laboratory of Intelligent Perception and Computing of Anhui Province, Anqing (China)

Received 23 December 2021 | Accepted 2 June 2022 | Published 10 August 2022

Abstract

Most existing multi-label classification models focus on distance metrics and feature spare strategies to extract specific features of labels. Those models use the cosine similarity to construct the label correlation matrix to constraint solution space, and then mine the latent semantic information of the label space. However, the label correlation matrix is usually directly added to the model, which ignores the interactive causality of the correlation between the labels. Considering the label-specific features based on the distance method merely may have the problem of distance measurement failure in the high-dimensional space, while based on the sparse weight matrix method may cause the problem that parameter is dependent on manual selection. Eventually, this leads to poor classifier performance. In addition, it is considered that logical labels cannot describe the importance of different labels and cannot fully express semantic information. Based on these, we propose an Interactive Causal Correlation Space Reshape for Multi-Label Classification (CCSRMC) algorithm. Firstly, the algorithm constructs the label propagation matrix using characteristic that similar instances can be linearly represented by each other. Secondly, label co-occurrence matrix is constructed by combining the conditional probability test method, which is based on the label propagation reshaping the label space to rich label semantics. Then the label co-occurrence matrix combines with the label correlation matrix to construct the label interactive causal correlation matrix to perform multi-label classification learning on the obtained numerical label matrix. Finally, the algorithm in this paper is compared with multiple advanced algorithms on multiple benchmark multi-label datasets. The results show that considering the interactive causal label correlation can reduce the redundant information in the model and improve the performance of the multi-label classifier.

Keywords

Conditional Probability, Interactive Causal Inference, Label Co-Occurrence, Label Space Reshape, Multi-Label Classification.

DOI: 10.9781/ijimai.2022.08.007

I. Introduction

With the continuous development of machine learning, classification models have evolved rapidly. However, in actual scenarios, there are still problems such as unbalanced classification, multi-layer and multi-label. In multi-label classification, labels with complex dependencies are more likely to identify the same instance. Therefore, labels correlation is mostly considered when performing multi-label classification. The consideration of the unique characteristics of labels effectively reduces the difficulty of capturing important information from high-dimensional data to construct competitive classifiers. These all require in-depth exploration of potential associations or dependencies between labels [1].

In order to mine the potential information of the label space, one method is to use the feature sparsity strategy to extract the specific features of the label. Algorithms based on this strategy usually use the l_1-norm to constraint weight matrix. The l_1-norm has high sparseness, so that only some important features contribute to the model, thereby extracting label-specific features. Typical algorithms include the LLSF algorithm (Learning Label-Specific Features for Multi-Label Classification) proposed by Huang et al. [2]. This algorithm assumes that each label is only related to certain features in the original feature space. The highly correlated labels have similarities. The label correlation and l_1-norm sparsity constraints are used to extract label-specific features. Based on the same strategy, the LSF-CI (Multi-Label Learning with Label-Specific Features Using Correlation Information) algorithm proposed by Han et al. [3] assumes that labels are only related to specific features. Features contribute differently to different targets. Similar labels have similar features. The sparse feature weight matrix is constructed by considering the correlation of the targets to extract the label-specific features. The other method is based on a distance measurement strategy. The main idea of this strategy is to find a set of measurement reference points. Then calculate the distance from each label of each sample to these measurement reference points. Finally, the measurement result is used as the label-specific features of each label. The typical algorithm of the measurement strategy is the LIFT algorithm (Multi-Label Learning with Label-Specific Features) proposed by Zhang [4]. The algorithm uses k-Means clustering for

* Corresponding author.

E-mail addresses: 767991942@qq.com (C. Zhang), chengyshaq@163.com (Y. Cheng), wangyb07@mail.ustc.edu.cn (Y. Wang), 1619288826@qq.com (Y. Xu).

positive samples and negative samples respectively. The obtained cluster centers are regarded as the center of the sample. Euclidean distance is used to measure the distances of all samples to these cluster centers to achieve the extraction of label-specific features.

However, some label-specific features extraction algorithms represented by LIFT do not consider label correlation. As an important means of mining features and label latent information, label correlation is introduced into the classification model to effectively improve the accuracy of multi-label classification. Based on this concept, the LSML algorithm (Improving Multi-Label Classification with Missing Labels by Learning Label-Specific Features) proposed by Huang et al. [5] deals with the multi-label classification of the missing dataset by learning high-order label correlation matrix and label-specific features. By learning high-level label correlation, a new supplementary label matrix is augmented from the incomplete label matrix. Then, it learns a label-specific data representation for each type of label. On this basis, combine the learned high-order label correlation to construct a multi-label classifier. The FF-MLLA algorithm (Multi-Label Lazy Learning Approach based on FireFly Method) proposed by Cheng et al. [6] uses the Firefly method to fuse correlation information with sample similarity information. Finally, the classification by singular value decomposition and extreme learning machine has achieved certain results.

However, the existing classification algorithms only consider the degree of correlation between targets when contacting the correlation of targets, but ignore the causality that exists in the interactive causal correlation. Only considering the correlation of symmetric labels will often cause the problem of redundant information [7] in the model, resulting in a decrease in the performance of the classifier. In real life, this asymmetric correlation is also very common. A classic explanation is shown in Fig. 1: The crowing of a rooster symbolizes the coming of dawn. The reason for the rooster's crowing is that the hormones in the rooster's brain are sensitive to light. Therefore, the disappearance of darkness makes this physiological phenomenon occur in roosters. This phenomenon indicates that there is a correlation between dawn and rooster crowing. The dawn is the cause, and the rooster's crowing is the result. However, dawn did not appear because of the rooster's crowing. This phenomenon indicates that the interactive causal correlation between the two is asymmetric.

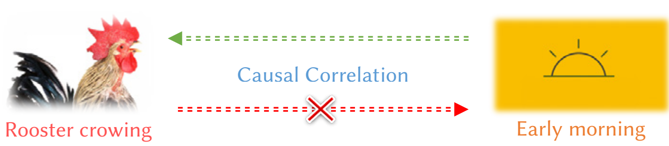

Fig. 1. Interactive Causal Correlation.

In multi-label learning, label objects with complex dependencies also have similar causality problems. Based on this fact, the ACML algorithm (Asymmetry Label Correlation for Multi-Label Learning) proposed by Bao et al. [8] uses cosine similarity to construct a label correlation matrix, and then measures the adjacency between labels to construct a label adjacency matrix. The label adjacency matrix is used to constrain the label correlation matrix to link the asymmetric label correlation. Considering the case of multi-label learning, the correlation between labels may come from the dependence of labels on the same set of features, or the dependence of one label on another label. We abstract the complex relationship between labels as a relationship--"Co-occurrence" [9]. When two label objects often appear together, we think that they have complex dependencies. The judgment of the degree of dependence between two related variables requires further consideration of directionality. The direction of greater dependence is used as the standard for inferring the interactive causal relationship between labels. Generally, we measure the co-occurrence relationship by the method of conditional probability (conditional independence test) [10]. That is, the probability P (Label2 | Label1), which represents the probability of the appearance of Label2 under the condition of the appearance of Label1. When this probability is greater than a specific threshold, we think that Label1 and Label2 have a dependency relationship. At the same time, the label-specific features take into account the unique characteristics of the label, which alleviates the high-dimensionality problem in multi-label learning to a certain extent. However, the failure of the distance measurement [11] and the problem of the l_1-norm feature sparsity parameter [12] are selected manually still exists. The constraint-based conditional independence test method considers the causal relationship between the labels while further avoiding the problem of Euclidean distance failure in the high-dimensional space. The use of naturally existing dependencies to extract label-specific features can also avoid the problem of l_1-norm relying on manual parameter selection to a certain extent. Based on this, this paper proposes the ***Interactive Causal Correlation Space Reshape for Multi-label Classification (CCSRMC)*** algorithm. By using space reshaping [13] methods to solve logical targets, there are problems such as the inability to describe the importance of different targets and the inability to fully express latent information. On this basis, the label co-occurrence matrix is constructed by combining the conditional probability test method. Then it is combined with the label correlation matrix to construct the label interactive causal correlation matrix to perform multi-label classification learning on the obtained numerical label matrix. Taking into account the sparseness of the label space, the label space reshaping method is used to transform the original discrete label into continuous label, which is used to infer the interactive causal relationship between features and labels. Then it obtains the numerical label matrix and extracts the label-specific features for multi-label classification. The algorithm in this paper carries out comparative experiments and statistical hypothesis tests with multiple advanced algorithms on multiple benchmark multi-label data sets. It also conducts ablation analysis with or without consideration of causality. The results of experiments and analysis verify the effectiveness of our algorithm.

The rest of this paper is organized as follows. In section Ⅱ, we introduce the model of the CCSRMC and the method to complete model optimization. In section Ⅲ, the algorithm pseudocode and complexity analysis of the proposed algorithm is given. In section Ⅳ, datasets, evaluation metrics, parameters setup are introduced. In section Ⅴ, we validate the proposed method with a hypothesis test and the sensitivity of the parameters was analyzed. Meanwhile experimental results on 14 benchmark datasets are given. Finally, we conclude our work in section Ⅵ.

II. The Proposed Method

A. Interactive Causal Inference Theory

Many scholars believe that there is a certain dependency in the correlation between things, which may lead to the asymmetry of the correlation. Scholars collectively call it causal inference [14]. Early causal inference algorithms can usually be divided into two categories: Constraint Based method and Function Based method. The constraint-based method is also called the method based on the independence test. The basic idea is to transform the inference problem of the direction of dependence into the problem of judging the degree of dependence between two variables. This type of algorithm first calculates the dependence of the two directions at the same time, and then takes the direction with the greater dependence as the inferred interactive causal direction. Common algorithms based on conditional independent tests include Granger Causality (GC) [15], which is a classic causality discovery tool, but it is only applicable to Gaussian cases. TE (Transfer Entropy) [16] is a non-linear promotion of GC. It uses the concept of information theory, which is equivalent to Conditional Mutual Information (CMI) [17]. In addition, you can also use the Kernel function [18] method and distance correlation [19] perform conditional independent testing. K2 search algorithm (K2 Search), PC algorithm (Peter-Clark) and IC algorithm (Inductive Causation) [20], etc. Causal inference algorithms usually have high algorithm complexity and poor adaptability to high-dimensional data in multi-label learning. In this paper, an interactive causal inference method based on conditional independence tests is used to infer the potential dependencies between multi-label learning. The label interactive causal inference method is a constraint-based algorithm, which ignores the influence of Confounder Variables. However, because only the dependency between the pair of variables is considered, the algorithm has low complexity and fast calculation speed, and can better handle high-dimensional data in multi-label learning.

Herein we introduce the label interactive causal inference method based on conditional independence test:

For a pair of variables (a, b). P(a=n) represents the probability when a=n. P(b|a=n) represents the conditional probability of variable b when a=n, let λ=P(a), μ=P(b|a). The label interactive causality inference method treats (λ, μ) as two independent random variables. The distance correlation coefficients of the two possible directions are calculated separately. The direction with the smaller coefficient is used as the inferred interactive causal direction.

Let f_λ and f_μ respectively denote the characteristic function of (λ, μ). $f_{\lambda,\mu}$ is (λ, μ) joint characteristic function, then the distance covariance $\mathcal{C}^2(\lambda, \mu)$ of (λ, μ) is:

$$\mathcal{C}^2(\lambda,\mu) = \left\|f_{\lambda,\mu} - f_\lambda f_\mu\right\|^2 \tag{1}$$

The distance correlation coefficient $\mathcal{D}(\lambda, \mu)$ is:

$$\mathcal{D}(\lambda,\mu) = \frac{\mathcal{C}(\lambda,\mu)}{\sqrt{\mathcal{C}(\lambda,\lambda)\mathcal{C}(\mu,\mu)}} \tag{2}$$

If $\mathcal{C}(\lambda,\lambda) = 0$ or $\mathcal{C}(\mu,\mu) = 0$, then $\mathcal{D}(\lambda, \mu) = 0$. Suppose the multi-label dataset contains n instances, and l labels, then for any pair of labels $(X_i, Y_j \mid i, j = 1, 2, 3,..., l)$, n groups of variables $\{(\lambda_i, \mu_j)\}_{i,j=1}^{n}$ can be constructed. For variables λ and μ, matrices $\boldsymbol{A}$ and $\boldsymbol{B}$ are constructed as follows:

$$\boldsymbol{A}_{ij} = \left\|\lambda_i - \lambda_j\right\| - \frac{1}{n}\sum_{j=1}^{n}\lambda_{ij} - \frac{1}{n}\sum_{i=1}^{n}\lambda_{ij} + \frac{1}{n^2}\sum_{i,j=1}^{n}\lambda_{ij} \tag{3}$$

$$\boldsymbol{B}_{ij} = \left\|\mu_i - \mu_j\right\| - \frac{1}{n}\sum_{j=1}^{n}\mu_{ij} - \frac{1}{n}\sum_{i=1}^{n}\mu_{ij} + \frac{1}{n^2}\sum_{i,j=1}^{n}\mu_{ij} \tag{4}$$

The distance covariance can be calculated by:

$$\mathcal{C}_n(\lambda,\mu) = \frac{1}{n}\sqrt{\sum_{i,j=1}^{n}\boldsymbol{A}_{ij}\boldsymbol{B}_{ij}} \tag{5}$$

From formula (2) and formula (5), we can know:

$$\mathcal{D}(\lambda,\mu) = n\frac{\sqrt{\sum_{i,j=1}^{n}\boldsymbol{A}_{ij}\boldsymbol{B}_{ij}}}{\sqrt{\sum_{i,j=1}^{n}\boldsymbol{A}_{ij}\boldsymbol{A}_{ij}}\sqrt{\sum_{i,j=1}^{n}\boldsymbol{B}_{ij}\boldsymbol{B}_{ij}}} \tag{6}$$

$\mathcal{D}(\lambda, \mu)$ is always greater than 0. For any pair of variables (a, b):

If $\mathcal{D}_{b\to a} > \mathcal{D}_{a\to b}$, then $a \to b$ is the inferred interactive causal direction

If $\mathcal{D}_{a\to b} > \mathcal{D}_{b\to a}$, then $b \to a$ is the inferred interactive causal direction

B. Establishment of the CCSRMC Model

In multi-label learning [21], there are input training data $\boldsymbol{X}$ and label matrix $\boldsymbol{Y}$, where $\boldsymbol{X} \in \mathbb{R}^{n\times d}$, $\boldsymbol{Y} \in \mathbb{R}^{n\times l}$, l is the number of labels, n is the number of training samples, d is the number of features. $\boldsymbol{U} = \{(x_i, y_i) \mid 1 \le i \le n\}$ is a multi-label training dataset, where $x_i = \{\boldsymbol{x}_i^1, \boldsymbol{x}_i^2, \cdots, \boldsymbol{x}_i^d\}$ is the i-th feature vector, $y_i = \{\boldsymbol{y}_i^1, \boldsymbol{y}_i^2, \cdots, \boldsymbol{y}_i^l\}$ is the i-th label vector. The task of multi-label learning is to find a mapping relationship $f: \boldsymbol{X} \to 2^Y$. The general multi-label algorithm [22] model is:

$$\boldsymbol{L}(\boldsymbol{W}) = \min_{W}\|\boldsymbol{XW} - \boldsymbol{Y}\|_F^2 + \beta\|\boldsymbol{W}\|_1 \tag{7}$$

$\boldsymbol{L}(\boldsymbol{W})$ is the loss function, β is the regularization parameter, and $\boldsymbol{W} \in \mathbb{R}^{d\times l}$ is the weight matrix.

Based on the original multi-label algorithm model, the algorithm in this paper uses the feature of linear representation between similar instances to construct the label propagation matrix $\boldsymbol{P}$. We use formula (8) to calculate an $\boldsymbol{N} \times \boldsymbol{N}$ similarity matrix $\boldsymbol{A}$ between $\boldsymbol{N}$ instances:

$$\boldsymbol{A}_{jk} = \begin{cases} \boldsymbol{exp}\left(-\frac{\left\|x_j - x_k\right\|^2}{2}\right) & \text{if } j \neq k \\ 0 & \text{if } j = k \end{cases} \tag{8}$$

Where $\boldsymbol{D} = \mathrm{diag}[\boldsymbol{d}_1, \boldsymbol{d}_2, \cdots \boldsymbol{d}_m]$, $\boldsymbol{d}_j = \sum_{k=1}^{m}\boldsymbol{W}_{jk}$.

$$\boldsymbol{P} = \boldsymbol{D}^{-\frac{1}{2}}\boldsymbol{A}\boldsymbol{D}^{-\frac{1}{2}} \tag{9}$$

The original label matrix $\boldsymbol{Y}$ is projected into a new numerical label matrix $\boldsymbol{S}$ through the label propagation matrix $\boldsymbol{P}$ to perform multi-label classification learning. After the introduction of label correlation optimization, formula (7) can be expressed as:

$$\min_{W_i}\frac{1}{2}\|\boldsymbol{XW}_i - \boldsymbol{S}\|_2^2 + \frac{1}{2}\|\boldsymbol{YP} - \boldsymbol{S}\|_F^2 + \frac{\alpha}{2}\sum_{j=1}^{l}\boldsymbol{R}_{ij}\boldsymbol{W}_i^T\boldsymbol{W}_j + \beta\|\boldsymbol{W}\|_1 \tag{10}$$

The first term of equation (10) is to minimize the error of the sum of squares. The numerical label vector $\boldsymbol{S}_i$ is used instead of the logical label vector $\boldsymbol{Y}_i$. Numerical labels bring more semantic information and are more conducive to the correlation between contact labels. The second term completes the label propagation to the original label matrix $\boldsymbol{Y}$. The third term indicates that the strong correlation between the label y_i and the label y_j leads to a great similarity between $\boldsymbol{W}_i$ and $\boldsymbol{W}_j$, where $\boldsymbol{R} \in \mathbb{R}^{l\times l}$ is the label correlation matrix, which is calculated by cosine similarity. However, some existing multi-label learning algorithms usually directly add the label correlation matrix to the model to constrain the solution space when considering the label correlation. These algorithms ignore the asymmetry of the correlation relationship between labels. The algorithm in this paper uses the label correlation matrix and the label co-occurrence matrix to construct the label interactive causal correlation matrix. The label co-occurrence matrix analyzes the potential interactive causal relationship between the labels through the conditional probability test method. Considering all binary classifiers at the same time, the optimization can be expressed as:

$$\min_{W}\frac{1}{2}\|\boldsymbol{XW} - \boldsymbol{S}\|_F^2 + \frac{1}{2}\|\boldsymbol{YP} - \boldsymbol{S}\|_F^2 + \frac{\alpha}{2}tr(\boldsymbol{WRW}^T) + \beta\|\boldsymbol{W}\|_1 \tag{11}$$

Based on the interactive causal inference theory, we get the following two definitions:

Definition 1: $\boldsymbol{V}$ is the label interactive causality correlation matrix, and $\boldsymbol{V}$ is a square matrix with a dimension of $l \times l$. If $\boldsymbol{V}_{mn} = \boldsymbol{V}_{nm} \neq 0$, there is a correlation between the corresponding labels. If $\boldsymbol{V}_{mn} = \boldsymbol{V}_{nm} = 0$, there is neither correlation nor interactive causality between the corresponding labels. If $\boldsymbol{V}_{mn} \neq \boldsymbol{V}_{nm}$ and $\boldsymbol{V}_{mn}$ or $\boldsymbol{V}_{nm} = 0$, it means that there is an interactive causal relationship between the corresponding labels.

Definition 2: $\boldsymbol{R} \in \mathbb{R}^{l \times l}$ is the label correlation matrix. $\boldsymbol{C} \in \{0,1\}^{l \times l}$ is the label co-occurrence matrix. $\boldsymbol{A} \odot \boldsymbol{B}$ is defined as a matrix operation, where $\boldsymbol{A} \in \mathbb{R}^{l \times l}$, $\boldsymbol{B} \in \{0,1\}^{l \times l}$. $\odot$ means that if $\boldsymbol{B}_{mn} = 1$, then $\boldsymbol{A}_{mn} = 0$. $\boldsymbol{C}^C$ is the complement matrix of the label co-occurrence matrix $\boldsymbol{C}$. Then the label interactive causality correlation matrix $\boldsymbol{V}$ is:

$$\boldsymbol{V} = \boldsymbol{R} \odot \boldsymbol{C}^C \tag{12}$$

y_m, y_n are a pair of labels, where $i, j = 1, 2, ..., n$. According to the description of label interactive causal inference in section II-A. Let $\lambda = \mathrm{P}(y_m)$, $\mu = \mathrm{P}(y_n | y_m)$. Assuming (λ, μ) is a pair of independent random variables, f_λ and f_μ are corresponding to its characteristic function, $f_{\lambda,\mu}$ is its joint characteristic function. According to section II-A:

If $\mathcal{D}_{y_n \to y_m} > \mathcal{D}_{y_m \to y_n}$, then $y_m \to y_n$ is the inferred interactive causal direction.

If $\mathcal{D}_{y_m \to y_n} > \mathcal{D}_{y_n \to y_m}$, then $y_n \to y_m$ is the inferred interactive causal direction.

In summary, we can get the label interactive causality correlation matrix $\boldsymbol{V} \in \{0,1\}^{l \times l}$, where $\boldsymbol{V}_{mn} = 0$ means that there is no interactive causal relationship between the m-th label and the n-th label. $\boldsymbol{V}_{mn} = 1$ means that the direction of inferring the interactive causal relationship between the m-th label and the n-th label is $m \to n$. Finally, the obtained label interactive causality correlation matrix is added to formula (11) to obtain the algorithm model proposed in this chapter:

$$\min_W \frac{1}{2}\|\boldsymbol{XW} - \boldsymbol{S}\|_F^2 + \frac{1}{2}\|\boldsymbol{YP} - \boldsymbol{S}\|_F^2 + \frac{\alpha}{2} tr(\boldsymbol{WVW}^T) + \beta\|\boldsymbol{W}\|_1 \tag{13}$$

Where $\boldsymbol{W} = (\boldsymbol{W}_1, \boldsymbol{W}_2, ..., \boldsymbol{W}_l) \in \boldsymbol{R}^{d \times l}$, $\boldsymbol{S} = (\boldsymbol{S}_1, \boldsymbol{S}_2, ..., \boldsymbol{S}_l) \in \boldsymbol{R}^{n \times l}$, $\alpha > 0$ and $\beta > 0$ are both parameters in the algorithms model. Then constraints to the reshaping process are considered to add, so that the reshaped label matrix $\boldsymbol{S}$ after the mapping has a small difference from the original label matrix $\boldsymbol{Y}$:

$$\min_W \frac{1}{2}\|\boldsymbol{XW} - \boldsymbol{S}\|_F^2 + \frac{1}{2}\|\boldsymbol{YP} - \boldsymbol{S}\|_F^2 + \frac{\alpha}{2} tr(\boldsymbol{WVW}^T) + \frac{1}{2}\|\boldsymbol{Y} - \boldsymbol{S}\|_F^2 + \beta\|\boldsymbol{W}\|_1 \tag{14}$$

Using natural interactive causality to extract label-specific features can avoid the problem that the $\boldsymbol{l}_1$-norm feature sparse strategy relies on manual parameter selection to a certain extent. Too high or too low sparsity will lead to poor classifier performance. In addition, in order to prevent the algorithm from overfitting that may be caused by the reshaping of the numerical label matrix $\boldsymbol{S}$. This paper uses F-norm to constrain matrix $\boldsymbol{S}$ and control the sparsity of matrix $\boldsymbol{W}$. In summary, the CCSRMC algorithm model proposed in this paper is as follows:

$$\min_W \frac{1}{2}\|\boldsymbol{XW} - \boldsymbol{S}\|_F^2 + \frac{\alpha}{2} tr(\boldsymbol{WVW}^T) + \frac{1}{2}\|\boldsymbol{YP} - \boldsymbol{S}\|_F^2 + \frac{1}{2}\|\boldsymbol{Y} - \boldsymbol{S}\|_F^2 + \beta\|\boldsymbol{W}\|_F^2 + \gamma\|\boldsymbol{P}\|_{2,1} + \frac{\alpha}{2}\|\boldsymbol{S}\|_F^2 \tag{15}$$

Where $\gamma > 0$ is the parameter in the algorithm model. It can be seen from the above algorithm model that when the label matrix is reshaped, it will be affected by the weight $\boldsymbol{W}$. What affects the weight $\boldsymbol{W}$ is not only the classification model after the label matrix is reshaped, but also the correlation between the labels [23]. The label correlation matrix is usually directly added to the model without considering the interactive causality of the correlation between the labels. As shown in Fig. 2, we construct a label co-occurrence matrix by combining conditional probability testing method on the basis of label propagation reshaping the rich label semantics in label space. The label co-occurrence matrix and the label correlation matrix are combined to construct the numerical label matrix obtained by the label interactive causal correlation matrix pair, so that multi-label classification learning is performed.

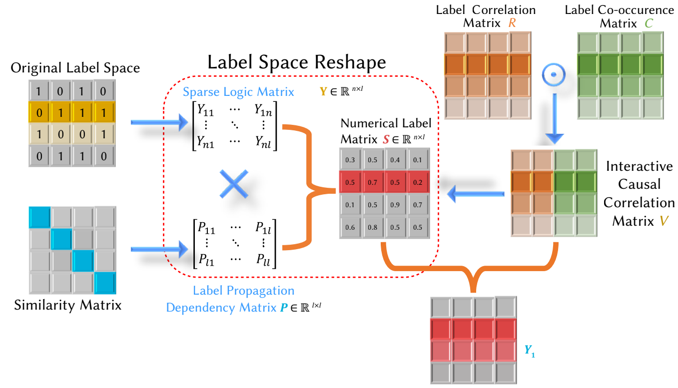

Fig. 2. Interactive Causal Correlation Space Reshape.

C. Optimization of the Model

In this paper, the three variable matrices in the label space reshaping model are calculated by using the alternate iteration method. That is the label propagation dependency matrix $\boldsymbol{P}$, the numerical labels matrix $\boldsymbol{S}$, and the weight matrix $\boldsymbol{W}$ are used to complete the optimization of the entire model and refer to the literature [24].

$$\min_P \frac{1}{2}\|\boldsymbol{YP} - \boldsymbol{S}\|_F^2 + \gamma\|\boldsymbol{P}\|_{2,1} \tag{16}$$

Where γ is parameter of the model. From the above algorithm model, it can be seen the numerical label matrix $\boldsymbol{S}$ is constantly changing. This matrix has correlation between labels, which means that when learning label-specific features, it will take the relevance between different labels into account. For the label propagation dependency matrix $\boldsymbol{P}$, we can define $\|\boldsymbol{P}\|_{2,1} = \sum_{j=1}^{l}\sqrt{\sum_{i=1}^{n}(\boldsymbol{P}_{ij})^2}$, Through the label matrix $\boldsymbol{S}$ reshaped by the $\boldsymbol{l}_{2,1}$-norm sparse label space of the matrix, the variable matrix $\boldsymbol{P}$ is obtained as:

$$\nabla\boldsymbol{P} = \boldsymbol{Y}^T\boldsymbol{YP} - \boldsymbol{Y}^T\boldsymbol{S} + 2\gamma\boldsymbol{DP} = 0 \tag{17}$$

$$\boldsymbol{P} = (\boldsymbol{Y}^T\boldsymbol{Y} + 2\gamma\boldsymbol{D})^{-1}\boldsymbol{Y}^T\boldsymbol{S} \tag{18}$$

Where $\boldsymbol{D}_{ii} = \frac{1}{2\|P_{i\bullet}\|_2}$, $\boldsymbol{D}$ is the diagonal matrix. Then calculate the numerical label matrix $\boldsymbol{S}$, the objective function is:

$$\min_S \frac{1}{2}\|\boldsymbol{XW} - \boldsymbol{S}\|_F^2 + \frac{1}{2}\|\boldsymbol{YP} - \boldsymbol{S}\|_F^2 + \frac{1}{2}\|\boldsymbol{Y} - \boldsymbol{S}\| + \frac{\alpha}{2}\|\boldsymbol{S}\|_F^2 \tag{19}$$

In training, in order to minimize the risk of label reshaping model structure and prevent the occurrence of overfitting, the model parameter α appears in the objective function as the control parameter of the model weight penalty term. The number label matrix $\boldsymbol{S}$ is obtained as:

$$\boldsymbol{S} = \frac{1}{\alpha + 3}(\boldsymbol{XW} + \boldsymbol{YP} + \boldsymbol{Y}) \tag{20}$$

Finally, the weight matrix $\boldsymbol{W}$ is calculated. The objective function is:

$$\min_W \frac{1}{2}\|\boldsymbol{XW} - \boldsymbol{S}\|_F^2 + \frac{\alpha}{2} tr(\boldsymbol{W}^T\boldsymbol{VW}) + \beta\|\boldsymbol{W}\|_1 \tag{21}$$

The composite function derivation is performed on the weight matrix $\boldsymbol{W}$. Split $\boldsymbol{W}$ into $f(\boldsymbol{W})$ and $g(\boldsymbol{W})$:

$$f(\boldsymbol{W}) = \min_W \frac{1}{2}\|\boldsymbol{XW} - \boldsymbol{S}\|_F^2 + \frac{\alpha}{2} tr(\boldsymbol{W}^T\boldsymbol{VW}) \tag{22}$$

$$g(\boldsymbol{W}) = \beta\|\boldsymbol{W}\|_1 \tag{23}$$

When learning tag information, the correlation between labels should be considered. The third item in the weight matrix $\boldsymbol{W}$ model is to use the F-norm to sparse the weight matrix $\boldsymbol{W}$. The parameter

β controls the sparsity of the weight matrix. Although formula (21) is a convex optimization problem, the objective function (21) is non-smooth due to the non-smoothness of the regular term of $\boldsymbol{l_1}$-norm. For this reason, this paper uses the near-end gradient descent method [22] to solve the optimization problem of non-smooth objective function. The objective function becomes:

$$\min_{W \in \mathcal{H}} F(\boldsymbol{W}) = f(\boldsymbol{W}) + g(\boldsymbol{W}) \tag{24}$$

$$\nabla f(\boldsymbol{W}) = \boldsymbol{X}^T\boldsymbol{X}\boldsymbol{W} - \boldsymbol{X}^T\boldsymbol{S} + \alpha\boldsymbol{W}\boldsymbol{V} \tag{25}$$

In formula (24), $\mathcal{H}$ is the Hilbert space. Both $f(\boldsymbol{W})$ and $g(\boldsymbol{W})$ are convex functions and satisfy Lipschitz condition. For any matrix $\boldsymbol{W}_1$, $\boldsymbol{W}_2$ there are:

$$\|\nabla f(\boldsymbol{W}_1) - \nabla f(\boldsymbol{W}_2)\| \le L_g\|\Delta\boldsymbol{W}\| \tag{26}$$

Where L_g is Lipschitz constant. $\Delta\boldsymbol{W} = \boldsymbol{W}_1 - \boldsymbol{W}_2$. In the process of accelerating gradient descent, $F(\boldsymbol{W})$ is no longer directly minimized. It is necessary to introduce the quadratic approximation $F(\boldsymbol{W})$ of $\boldsymbol{Q}(\boldsymbol{W}, \boldsymbol{W}^{(t)})$, so define $\boldsymbol{Q}(\boldsymbol{W}, \boldsymbol{W}^{(t)})$:

$$Q(\boldsymbol{W},\boldsymbol{W}^{(t)}) = f(\boldsymbol{W}^{(t)}) + (\nabla f(\boldsymbol{W}^{(t)}), \boldsymbol{W} - \boldsymbol{W}^{(t)}) + \frac{L_g}{2}\|\boldsymbol{W} - \boldsymbol{W}^{(t)}\|_F^2 + g(\boldsymbol{W}) \tag{27}$$

$$\boldsymbol{G}_t(\boldsymbol{W}) = \boldsymbol{W}_t - \frac{1}{L_g}\nabla f(w) \tag{28}$$

$$\begin{aligned}\boldsymbol{W} &= \arg\min_W \boldsymbol{Q}(\boldsymbol{W},\boldsymbol{W}^{(t)}) \\ &= \arg\min_W g(\boldsymbol{W}) + \frac{L_g}{2}\left\|\boldsymbol{W} - \boldsymbol{G}^{(t)}\right\|_F^2 \\ &= \arg\min_W \frac{1}{2}\left\|\boldsymbol{W} - \boldsymbol{G}^{(t)}\right\|_F^2 + \frac{\alpha}{L_g}\|\boldsymbol{W}\|_1\end{aligned} \tag{29}$$

Given in the research in [25]:

$$\boldsymbol{W}^{(t)} = \boldsymbol{W}_t + \frac{b_{t+1} - 1}{b_t}(\boldsymbol{W}_t - \boldsymbol{W}_{t-1}) \tag{30}$$

The sequence b_t satisfies $b_{t+1}^2 - b_{t+1} \le b_t^2$, which can increase the speed of convergence to $\boldsymbol{O}(t^{-2})$. So $\boldsymbol{W}_t$ can be regarded as the result of the t-th iteration of $\boldsymbol{W}$:

$$\boldsymbol{W}_{t+1} = \boldsymbol{S}_\varepsilon[\boldsymbol{G}^{(t)}] = \arg\min_W \varepsilon\|\boldsymbol{W}\|_1 + \frac{1}{2}\left\|\boldsymbol{W} - \boldsymbol{G}^{(t)}\right\|_F^2 \tag{31}$$

Where $\boldsymbol{S}_\varepsilon[\cdot]$ is a soft threshold operator. For any parameter x_{ij} and $\varepsilon = \frac{\alpha}{L_g}$, this function is defined as:

$$\boldsymbol{S}_\varepsilon(x_{ij}) = \begin{cases} x_{ij} - \varepsilon & when\ x_{ij} > \varepsilon \\ x_{ij} + \varepsilon & when\ x_{ij} < -\varepsilon \\ 0 & \end{cases} \tag{32}$$

$$\boldsymbol{W} = soft\left(\boldsymbol{G}_t(\boldsymbol{W}),\ \frac{\beta}{L_g}\right) \tag{33}$$

The Lipschitz constant is calculated as follows. For given $\boldsymbol{W}_1$ and $\boldsymbol{W}_2$, the Lipschitz condition is satisfied according to $f(\boldsymbol{W})$:

$$\begin{aligned}\|\nabla f(\boldsymbol{W}_1) - \nabla f(\boldsymbol{W}_2)\|_F^2 &= \left\|\begin{matrix}\boldsymbol{X}^T\boldsymbol{X}\boldsymbol{W}_1 - \boldsymbol{X}^T\boldsymbol{S} + \alpha\boldsymbol{W}\boldsymbol{V} \\ -(\boldsymbol{X}^T\boldsymbol{X}\boldsymbol{W}_2 - \boldsymbol{X}^T\boldsymbol{S} + \alpha\boldsymbol{W}_2\boldsymbol{R})\end{matrix}\right\|_F^2 \\ &= \|\boldsymbol{X}^T\boldsymbol{X}\Delta\boldsymbol{W} + \alpha\Delta\boldsymbol{W}\boldsymbol{V}\|_F^2 \\ &\le \|\boldsymbol{X}^T\boldsymbol{X}\Delta\boldsymbol{W}\|_F^2 + \|\alpha\Delta\boldsymbol{W}\boldsymbol{V}\|_F^2 \\ &\le 2\|\boldsymbol{X}^T\boldsymbol{X}\|_2^2\|\Delta\boldsymbol{W}\|_F^2 + 2\alpha\|\boldsymbol{V}\|_2^2\|\Delta\boldsymbol{W}\|_F^2 \\ &= (2\|\boldsymbol{X}^T\boldsymbol{X}\|_2^2 + 2\alpha\|\boldsymbol{R}\boldsymbol{V}\|_2^2)\|\Delta\boldsymbol{W}\|_F^2\end{aligned} \tag{34}$$

Therefore, the Lipschitz constant of the model is:

$$L_g = \sqrt{2\|\boldsymbol{X}^T\boldsymbol{X}\|_2^2 + 2\alpha\|\boldsymbol{V}\|_2^2} \tag{35}$$

III. Pseudocode and Complexity Analysis

A. Accelerated Gradient Descent

This section outlines the algorithm flow of CCSRMC. Solve the weight matrix $\boldsymbol{W}$ and obtain the interactive causal correlation matrix $\boldsymbol{V}$. In Algorithm 1 Step 3 and Step 4 are more complicated. Where $\boldsymbol{G}^{(t)}$ is an intermediate variable, $f(\cdot)$ represents the gradient, the algorithm complexity of calculating the weight matrix $\boldsymbol{W}$ is $\boldsymbol{O}(n^2\ d^2\ l + n^2\ dl + dl^2)$. In algorithm 2, the label interactive causality matrix: $\boldsymbol{V}$ is constructed with the conditional independence test method. Only the non-diagonal elements in the upper or lower triangular matrix need to be calculated. Therefore, the complexity of step 3 is $\boldsymbol{O}(l^2)$. Step 4 has a complexity of $\boldsymbol{O}(l^2/2)$.

The accelerated proximal gradient of CCSRMC is summarized in Algorithm 1.

Algorithm 1: The Accelerated Proximal Gradient Method

Input: Training data matrix: $\boldsymbol{X}$; Training label data set: $\boldsymbol{Y}$; Parameters: α, β, γ

Output: Weight matrix: $\boldsymbol{W}$.

1. Initialize: $b_0 = b_1 = 1$, $\boldsymbol{W}_0 = \boldsymbol{W}_1 = (\boldsymbol{X}^T\boldsymbol{X} + \gamma I)^{-1}\boldsymbol{X}^T\boldsymbol{Y}$
2. **while** not converged **do**
3. $G^{(t)} = \boldsymbol{W}^t - \frac{1}{L_g}\nabla f(\boldsymbol{W}^{(t)})$
4. $\boldsymbol{W}^{(t)} = \boldsymbol{W}_t + \frac{b_{t-1}-1}{b_t}(\boldsymbol{W}_t - \boldsymbol{W}_{t-1})$
5. $\boldsymbol{W}_{t+1} = \arg\min_W \varepsilon\|\boldsymbol{W}\|_1 + \frac{1}{2}\left\|\boldsymbol{W} - \boldsymbol{G}^{(t)}\right\|_F^2$
6. $b_{t+1} = \frac{1+\sqrt{4b_t^2+1}}{2}, t = t+1$
7. $t = t+1$
8. **end while**

B. Algorithm Pseudocode of Label Interactive Causal Inference Method

The label interactive causal inference method based on conditional independence test is summarized in Algorithm 2.

Algorithm 2: The Label Interactive Causal Inference Method based on Conditional Independence Test

Input: Label matrix: $\boldsymbol{S}$; Number of labels: l.

Output: Label interactive causality matrix: $\boldsymbol{V}$.

1. for $i = 1, 2, 3, \ldots, n$ do
2. for $j = 1, 2, 3, \ldots, n$ do
3. Construct $P(y_m)$ and $P(y_n \mid y_m)$, calculate $D_{y_n \to y_m} = D(P(y_n), P(y_m|y_n))$
   Construct $P(y_n)$ and $P(y_m \mid y_n)$, calculate $D_{y_m \to y_n} = D(P(y_m), P(y_m|y_n))$
4. end for
5. end for
6. If $\mathcal{D}_{y_n \to y_m} > \mathcal{D}_{y_m \to y_n}$, then $y_m \to y_n$ is the inferred interactive causal direction, $\boldsymbol{V}_{mn} = 1$
   If $\mathcal{D}_{y_m \to y_n} > \mathcal{D}_{y_n \to y_m}$, then $y_n \to y_m$ is the inferred interactive causal direction, $\boldsymbol{V}_{nm} = 1$
7. else, no causation, $\boldsymbol{V}_{mn} = 0$

C. Complexity Analysis

In summary, the algorithm complexity of CCSRMC is $(ndl\,(nd + n + d) + nl\,(l^2 + n^3\,l + n) + dl^2)$. In order to comprehensively reflect the performance of CCSRMC, the algorithm complexity of this paper is compared with LSML [5], LSF-CI [3], FF-MLLA [6], LLSF [2] and ACML [8]. In comparison experiments, the closest comparison algorithm to the performance of this paper are LSML and FF-MLLA [6]. The algorithm complexity of LSML is $\boldsymbol{O}\,((n + l)\,d^2 + (n + d)\,l^2 + ndl + d^3 + l^3)$. FF-MLLA does not give a specific algorithm time complexity analysis. The algorithm complexity of LSF-CI is $\boldsymbol{O}\,(nd^2 + nd + ndl + lg^2 + d^3 + d^2l)$. Although the complexity of the algorithm in this paper is slightly higher than that of the comparison algorithms, the experimental results show that the CCSRMC algorithm has a better classification effect on most multi-label datasets than the comparison algorithms. Table I summarizes the computational complexity of the proposed methods and comparisons.

TABLE I. The Computational Complexity of Different Algorithm

Methods	Computational complexity
LSF-CI	$\boldsymbol{O}\,(nd^2 + nd + ndl + lg^2 + d^3 + d^2l)$
LSML	$\boldsymbol{O}\,((n + l)\,d^2 + (n + d)\,l^2 + ndl + d^3 + l^3)$
ACML	$\boldsymbol{O}\,((n + l + nl)\,d^2 + (n + d)\,l^2 + 3/2)$
LLSF	$\boldsymbol{O}\,(d^2 + dl + l^2 + nd + nl)$
CCSRMC	$\boldsymbol{O}\,(ndl\,(nd + n + d) + nl\,(l^2 + n^3l + n) + dl^2)$

IV. Experiment

A. Dataset

To illustrate the effectiveness of the algorithm, 14 multi-label datasets from Yahoo.com and Mulan.com are selected. Table II is a detailed description. CCSRMC is a related model of multi-label classification, so in section IV-D, this paper selects multiple multi-label text classification datasets for comparison experiments. In order to reflect the universality of the algorithm in this paper, we also select other types of multi-label data sets for comparative experiments to compare and verify the effectiveness of the algorithm proposed in this paper.

TABLE II. Description of Datasets

Datasets	Train	Test	Labels	Features	Domain
Birds [2]	645	645	20	260	Image
Genbase[2]	662	662	27	1185	Biology
Enron[2]	1702	1702	53	1001	Text
Yeast[2]	2417	2417	14	103	Biology
Arts[1]	2000	3000	26	462	Text
Computers[1]	2000	3000	33	681	Text
Education[1]	2000	3000	33	550	Text
Science[1]	2000	3000	40	743	Text
Society[1]	2000	3000	27	636	Text
Entertainment[1]	2000	3000	21	640	News
Business[1]	2000	3000	30	438	News
Health[1]	2000	3000	32	612	Text
Reference[1]	2000	3000	33	793	Text
Recreation[1]	2000	3000	22	606	News

[1] Yahoo Web Pages (http://archive.ics.uci.edu/ml/)
[2] Mulan (http://mulan.sourceforge.net/datasets-mlc.html)

B. Comparison Algorithm and Parameter Settings

In this experiment, five multi-label classification algorithms are selected for comparison with CCSRMC. LSI-CI [3] is a multi-label classification algorithm that promotes label-specific features learning by learning correlation information between features and correlation information between labels. Its parameters are set to $\alpha = 2^{10}$, $\beta = 2^8$, $\gamma = 1$, $\theta = 2^{-8}$. LLSF [2] improves the performance of multi-label classification by learning the cosine similarity between labels to perform label-specific features learning. The parameters are set to $\alpha = 2^{-4}$, $\beta = 2^{-6}$, $\gamma = 1$. LSML [5] handles the multi-label classification of the default data set by learning high-order label correlation matrix and label-specific features, and the parameters are set to $\lambda_2 = 10^{-5}$, $\lambda_3 = 10^{-3}$, $\lambda_4 = 10^{-5}$. FF-MLLA [6] uses the firefly method to fuse correlation information with sample similarity information. Then it classifies through singular value decomposition and extreme learning machine. In the FF-MLLA algorithm, the number of neighbors is k=15. The regularization coefficient is set to 1. The kernel function chooses RBF. The nuclear parameter is set to 100. The training method selects linear regression fitting. The ACML [8] algorithm uses cosine similarity to construct a label correlation matrix. Then the algorithm measures the adjacency between the labels to construct the label adjacency matrix. Finally, the label adjacency matrix is used to constrain the label correlation matrix to link the interactive causal label correlation. Its parameter setting interval is $\alpha \in [2^{-10}, 2^{10}]$, $\beta \in [2^{-10}, 2^{10}]$.

C. Metric

The evaluation index of the multi-label learning system is different from the traditional single-label learning system. The output label of the multi-label learning may be partially correct, completely correct, or completely wrong. In this paper, five evaluation indicators that are widely used in multi-label tasks are compared with the above-mentioned multi-label classification algorithms, including Hamming Loss, Average Precision, One-Error rate, Ranking Loss, AUC and Coverage rate [26] [27]. The value range of these evaluation indicators varies between [0,1]. For each evaluation indicator, "↑" means the larger, the better, and "↓" means the smaller, the better. Where $\boldsymbol{D} = \{(\boldsymbol{X}_{it}, \boldsymbol{Y}_{il} \mid 1 \le t \le d, 1 \le i \le m, 1 \le l \le L)\}$ is multi-label dataset. $h(\cdot)$ is a multi-label classifier. $f(\cdot)$ is the prediction function. The definitions of 5 evaluation indicators are as follows:

Hamming Loss can be used to evaluate how many times a sample is misclassified. For example, a sample does not belong to label L_i but is incorrectly classified into label L_i. Or a sample belongs to label L_i but is not predicted as label L_i. The algorithm in this paper uses Hamming loss to calculate the numerical distance between the result sequence predicted by the classifier and the original result sequence.

$$HL_D(h) \downarrow = \frac{1}{m}\sum_{i=1}^{m}\frac{|Y_i \Delta Z_i|}{M} \tag{36}$$

Where m is the number of samples, M is the total number of labels. $\boldsymbol{Y}_i$ is the set of actual labels of i-th sample, $\boldsymbol{Z}_i$ is the set of predicted labels of i-th sample. Δ refers to the symmetric difference between the two sets. The smaller the Hamming loss, the better the prediction result.

In the ranking of all prediction results, the average precision represents the probability that the ranking is ranked before the labels of the related label set and belongs to the related label set. The indicator reflects the average precision of the classification label. This indicator was originally used in Information Retrieval (*IR*) systems to evaluate the retrieval performance of text sorting.

$$AP_D(f) \uparrow = \frac{1}{m}\sum_{i=1}^{m}\frac{1}{|Y_i|}\cdot\sum_{y \in Y_i}\frac{\left|\{y' | rank_f(x_i, y') \le rank_f(x_i, y), y' \in Y_i\}\right|}{rank_f(x_i, y)} \tag{37}$$

$rank_f$ is the ranking function. When the average precision reaches 1, the prediction effect is the best. That is, the larger the $AP_D(f)$, the higher the performance of $f(\cdot)$.

One-Error can be used to evaluate the probability that the label ranked first in the output result does not belong to the actual label set. It can reflect the times that the highest ranking object is incorrectly labeled.

$$OE_D(f)\downarrow=\frac{1}{m}\sum_{i=1}^{m} g\left[\left[arg\max_{y\in Y} f(x_i,y)\right]\notin Y_i\right],\quad g(x)=\begin{cases}0 & x\ is\ false\\ 1 & x\ is\ \ true\end{cases} \tag{38}$$

The smaller the One-Error, the better the prediction. That is, the smaller the $OE_D(f)$, the higher the performance of $f(\cdot)$.

Ranking Loss indicates how many irrelevant labels are ranked higher than related labels. The ranking loss is used to indicate the average of the probability that a label that does not belong to the relevant label set is ranked in the relevant label set in the result ranking.

$$RL_D(f)\downarrow=\frac{1}{m}\sum_{i=1}^{m}\frac{1}{|Y_i||\overline{Y_i}|}\cdot\left|\left\{\begin{matrix}(y_1,y_2)|f(x_i,y_1)\le f(x_i,y_2),\\ (y_1,y_2)\in Y_i\times\overline{Y_i}\end{matrix}\right\}\right| \tag{39}$$

The smaller the Ranking Loss, the better the prediction result. That is, the smaller the $RL_D(f)$, the higher the performance of $f(\cdot)$.

Coverage can be used to reflect the number of labels required to cover all labels in the label sequence of the evaluated object.

$$CV_D(f)\downarrow=\frac{1}{m}\sum_{i=1}^{m}\max_{y\in Y_i} rank_f(x_i,y)-1 \tag{40}$$

The smaller the coverage, the better the prediction result, and the higher the performance of $f(\cdot)$.

AUC (Area under the Curve of ROC) is an evaluation index that measures the pros and cons of a two-class model. AUC represents the probability that a positive example is ranked before a negative example. When a positive sample and a negative sample are randomly selected, the current classification algorithm ranks the positive sample ahead of the negative sample according to the calculated score value. The larger the AUC, the more likely the current classification algorithm will rank the positive samples in front of the negative samples. Therefore, the effect of classification is better.

$$AUC_D(f)\uparrow=\frac{\sum_{i\in positiveClass}^{m} rank_i-\frac{M(1+M)}{2}}{M\times N} \tag{41}$$

The area under the ROC curve is between 0.1 and 1. As a value, AUC can intuitively evaluate the quality of the classifier, the larger the value, the better the effect.

V. Analysis and Visualization

A. Analysis of the Results

In the experiment, this article uses a five-fold cross-validation method to evaluate the performance of the algorithm. Five-fold cross-validation means that all data is randomly divided into five equal subsets, each subset is tested in turn, and the remaining data is used for training. Five-fold cross-validation is iterated five times, so the average value after five runs of the experiment needs to be calculated. The five comparison algorithms selected in this article all consider different symmetric label correlations.

As illustrated in Table III, the experimental results of each algorithm under 14 datasets and the optimal experimental results have been marked in bold-type. Analyzing the above experimental results, we get the following conclusions:

1. It can be seen from Table III that in the 84 sets of experimental data, CCSRMC has the best results in 53 sets, with a dominant ratio of 63%. The evaluation index AP is significantly better than other comparison algorithms. The performance of 13 out of 14 data sets is better than other comparison algorithms. In addition, the variance of the CCSRMC algorithm is smaller, which shows that the performance of CCSRMC is more stable.
2. Compared with the ACML algorithm that also takes the interactive causal correlation between labels into account, the overall performance of CCSRMC is better than the ACML algorithm. The reason is that although the two algorithms both consider the interactive causal correlation between labels, the CCSRMC algorithm uses the label space reshaping method to transform the original discrete labels into continuous labels. The use of continuous labels to infer the interactive causal correlation between features and labels cause the results of the CCSRMC algorithm be superior to the ACML algorithm to a certain extent.
3. The algorithm LSML combines high-order label correlation matrix and specific features to process the multi-label classification of the default data set. In the five indexes of HL, OE, RL, AUC and CV, the experimental results show that the algorithm CCSRMC proposed in this paper is significantly better than the algorithm LSML, which verifies the effectiveness of the algorithm in this paper. Thus, by considering the interactive causal relationship between labels, different labels with dependencies can be better identified and the redundant information in the model is reduced, which can improve the performance of the multi-label classifier to a certain extent.

B. Ablation Analysis

In order to verify that the introduction of interactive causal label correlation in the model improves the performance of the algorithm, we conduct related experiments for ablation analysis in this section. We compared CCSRMC using an interactive causal label correlation matrix with SRMC using a label correlation matrix. Some results are shown in Fig. 3. The performance of the CCSRMC algorithm using the interactive causal label correlation matrix is better than that of the CCSRMC algorithm using the label correlation matrix. It further illustrates the effectiveness and rationality of introducing interactive causal label correlation in the multi-label algorithm.

C. Parameter Sensitivity Analysis

The algorithm CCSRMC proposed in this paper has three parameters α, β, γ. The parameter α controls the influence of the interactive causal correlation between the labels on the model coefficients and the weight constraints that minimize structural risks and prevent overfitting. The parameter β controls the sparseness of label features extracted from the label-specific features. The parameter γ controls the sparsity of the numerical label matrix S. By a method that fix two parameter values and change one parameter value to find the optimal value, we found that the parameter β has no obvious change in the six evaluation indicators. This further verifies that we did not use l_1-norm regularization to extract specific features, but use interactive causal correlation to connect specific features between labels. In this section, we use Bar-3 to visualize the parameter sensitivity comparison of parameters α and γ. The algorithm in this paper conducts parameter sensitivity experiments on the Emotions data set. According to the experimental results in Fig. 4, it can be found that the algorithm CCSRMC has different sensitivity to the regularization parameters on the six evaluation indicators. On the evaluation index of AUC, when the experimental interval of parameter α is set to $[2^7, 2^{10}]$, the parameter γ is affected, which leads to the deterioration of the performance of the algorithm. For the HL evaluation index, as the parameter α interval increases, the HL index decreases and then rises. When the parameter $\alpha > 2^6$, the correlation information between the labels obtained by the CCSRMC algorithm becomes very scarce, and the risk of the model structure increases, which may easily lead to overfitting. When the parameter $\gamma > 2^2$, the label specific features that can be extracted in the CCSRMC algorithm become very scarce, and

TABLE III-A. Test Results of Each Algorithm on 6 Evaluation Indexes (Mean ± Std)

Dataset	Metric	CCSRMC	ACML	FF-MLLA	LSML	LLSF	LSF-CI
Birds	HL↓	**0.0475**±0.0029	0.0512±0.0023	0.0476±0.0040	0.0595±0.0046	0.0506±0.0041	0.0647±0.0063
	AP↑	**0.7687**±0.0304	0.7648±0.0275	0.7517±0.0247	0.7596±0.0219	0.7582±0.0350	0.6302±0.0165
	OE↓	**0.2759**±0.0358	0.2821±0.0301	0.3007±0.0358	0.2884±0.0458	0.2915±0.0385	0.4062±0.0233
	RL↓	**0.0887**±0.0143	0.0891±0.0150	0.1067±0.0116	0.0972±0.0061	0.0962±0.0232	0.2206±0.0168
	CV↓	**0.1382**±0.0192	0.1391±0.0210	0.1512±0.0206	0.1483±0.0162	0.1471±0.0322	0.2739±0.0156
	AUC↑	**0.9112**±0.0143	0.8953±0.046	0.7714±0.0145	0.6498±0.0040	0.7690±0.0178	0.6978±0.0145
Arts	HL↓	**0.0522**±0.0007	0.0536±0.0007	0.0588±0.0015	0.0582±0.0011	0.0566±0.0009	0.0561±0.0013
	AP↑	**0.6305**±0.0072	0.6241±0.0141	0.5211±0.0101	0.5932±0.0069	0.5852±0.0147	0.5451±0.0100
	OE↓	**0.4436**±0.0087	0.4524±0.0179	0.607±0.0191	0.4762±0.0088	0.4900±0.0181	0.5090±0.0180
	RL↓	**0.1350**±0.0070	0.1405±0.0074	0.1571±0.0031	0.1770±0.0058	0.1841±0.0106	0.2621±0.0106
	CV↓	**0.2065**±0.0102	0.2141±0.0080	0.2212±0.0050	0.2567±0.0060	0.2650±0.0117	0.3448±0.0107
	AUC↑	**0.8649**±0.0070	0.7832±0.0891	0.5558±0.0059	0.6723±0.0178	0.6916±0.0114	0.7102±0.0007
Computers	HL↓	**0.0326**±0.0006	0.0339±0.0009	0.0383±0.0010	0.0391±0.0008	0.0389±0.0010	0.0415±0.0018
	AP↑	**0.7174**±0.0034	0.7093±0.0163	0.6424±0.0041	0.6915±0.0059	0.6575±0.0064	0.5839±0.0059
	OE↓	**0.3372**±0.0049	0.3466±0.0171	0.4302±0.0072	0.3608±0.0060	0.4080±0.0094	0.4614±0.0072
	RL↓	0.0903±0.0043	**0.0980**±0.0086	0.0974±0.0044	0.1230±0.0059	0.1229±0.0059	0.2299±0.0126
	CV↓	0.1330±0.0064	**0.1406**±0.0106	0.1402±0.0045	0.1725±0.0051	0.1720±0.0088	0.2888±0.0170
	AUC↑	**0.9096**±0.0043	0.7828±0.0916	0.6764±0.0041	0.7505±0.0165	0.6810±0.0136	0.7813±0.0068
Education	HL↓	0.0381±0.0003	**0.0371**±0.0008	0.0407±0.0002	0.0411±0.0003	0.0414±0.0007	0.0418±0.0012
	AP↑	**0.6670**±0.0067	0.6337±0.0153	0.5497±0.0050	0.6033±0.0082	0.5805±0.0069	0.5290±0.0166
	OE↓	0.4666±0.0083	**0.4606**±0.0203	0.5868±0.0079	0.4826±0.0178	0.5090±0.0070	0.5290±0.0166
	RL↓	**0.0990**±0.0056	0.1089±0.0057	0.1001±0.0053	0.1526±0.0068	0.1642±0.0065	0.2486±0.0081
	CV↓	**0.1444**±0.0053	0.1592±0.0086	0.1323±0.0067	0.2123±0.0077	0.2215±0.0068	0.3133±0.0115
	AUC↑	**0.9009**±0.0056	0.8709±0.0190	0.5612±0.0037	0.6435±0.0003	0.6660±0.0160	0.6784±0.0532
Enron	HL↓	0.0464±0.0005	**0.0455**±0.0006	0.0500±0.0007	0.0505±0.0014	0.0553±0.0020	0.0664±0.0066
	AP↑	**0.7061**±0.0083	0.7027±0.0099	0.6546±0.0052	0.6928±0.0088	0.6609±0.0085	0.6539±0.0060
	OE↓	0.2297±0.0179	**0.2279**±0.0216	0.2584±0.0139	0.2444±0.0156	0.2650±0.0147	0.2644±0.0114
	RL↓	**0.0841**±0.0061	0.0895±0.0039	0.1000±0.0032	0.0951±0.0043	0.1258±0.0059	0.1109±0.0023
	CV↓	**0.2430**±0.0122	0.2547±0.0072	0.2753±0.0083	0.2695±0.0100	0.3154±0.0156	0.2779±0.0045
	AUC↑	**0.9158**±0.0061	0.8367±0.0037	0.7053±0.0051	0.6329±0.0089	0.6673±0.0094	0.6307±0.0275
Genbase	HL↓	0.0023±0.0007	**0.0015**±0.0004	0.9540±0.0014	0.0010±0.0005	0.4130±0.2064	0.0040±0.0012
	AP↑	0.9946±0.0029	0.9952±0.0034	0.9926±0.0061	**0.9969**±0.0035	0.3133±0.1597	0.9966±0.0034
	OE↓	0.0015±0.0030	0.0015±0.0030	——	0.0015±0.0031	0.0061±0.2239	0.0015±0.0030
	RL↓	0.0022±0.0020	0.0029±0.0025	0.0050±0.0048	**0.0016**±0.0028	0.0645±0.0300	0.0018±0.0030
	CV↓	0.0131±0.0049	0.0123±0.0011	0.0177±0.0084	0.0125±0.0045	0.0809±0.2143	**0.0101**±0.0016
	AUC↑	**0.9977**±0.0020	0.8900±0.0039	0.6849±0.0288	0.7106±0.0044	0.7683±0.0303	0.5903±0.0013
Entertainment	HL↓	0.0532±0.0010	**0.0508**±0.0014	0.0589±0.0005	0.0570±0.0006	0.0550±0.0015	0.0550±0.0014
	AP↑	**0.6944**±0.0107	0.6925±0.0067	0.5777±0.0110	0.6731±0.0089	0.6669±0.0071	0.6351±0.0076
	OE↓	0.3948±0.0109	**0.3912**±0.0106	0.5668±0.0178	0.4072±0.0113	0.4092±0.0070	0.4166±0.0063
	RL↓	**0.1089**±0.0068	0.1163±0.0035	0.1284±0.0047	0.1422±0.0040	0.1460±0.0110	0.2215±0.0096
	CV↓	**0.1523**±0.0085	0.1605±0.0066	0.1661±0.0052	0.1897±0.0044	0.1918±0.0114	0.2717±0.0109
	AUC↑	**0.8910**±0.0068	0.8013±0.0009	0.5879±0.0035	0.6128±0.0034	0.7600±0.1127	0.5699±0.0901

TABLE III-B. Test Results of Each Algorithm on 6 Evaluation Indexes (Mean ± Std)

Dataset	Metric	CCSRMC	ACML	FF-MLLA	LSML	LLSF	LSF-CI
Business	HL↓	0.0278±0.0007	**0.0266**±0.0004	0.0261±0.0016	0.0287±0.0010	0.0295±0.0009	0.0398±0.0008
	AP↑	**0.8838**±0.0055	0.8809±0.0072	0.8805±0.0110	0.8798±0.0085	0.8484±0.0090	0.7825±0.0116
	OE↓	0.1176±0.0106	**0.1158**±0.0074	0.114±0.0101	0.1104±0.0105	0.1452±0.0112	0.2240±0.0185
	RL↓	**0.0407**±0.0018	0.0443±0.0048	0.0452±0.0049	0.0485±0.0048	0.0635±0.0041	0.1036±0.0071
	CV↓	**0.0818**±0.0045	0.0895±0.0078	0.0833±0.0068	0.0967±0.0097	0.1096±0.0064	0.1559±0.0092
	AUC↑	**0.9592**±0.0018	0.8971±0.0142	0.8520±0.0075	0.7990±0.0005	0.7168±0.0093	0.7009±0.0141
Science	HL↓	0.0322±0.0009	**0.0311**±0.0006	0.0348±0.0008	0.0333±0.0007	0.0348±0.0007	0.0348±0.0007
	AP↑	**0.6041**±0.0097	0.6077±0.0081	0.4556±0.0135	0.5890±0.0158	0.5521±0.0105	0.5166±0.0116
	OE↓	0.4846±0.0148	**0.4772**±0.0108	0.6694±0.0146	0.4884±0.0207	0.5274±0.0075	0.5512±0.0191
	RL↓	**0.1171**±0.0061	0.1289±0.0046	0.1568±0.0025	0.1530±0.0106	0.1774±0.0083	0.2473±0.0056
	CV↓	**0.1625**±0.0129	0.1778±0.0058	0.1978±0.0057	0.2048±0.0143	0.2296±0.0087	0.3027±0.0065
	AUC↑	0.8828±0.0061	0.8600±0.0003	0.5346±0.0028	0.6415±0.0340	**0.8962**±0.0031	0.7624±0.0007
Society	HL↓	0.0526±0.0020	**0.0515**±0.0010	0.0561±0.0015	0.0560±0.0010	0.0578±0.0011	0.0585±0.0013
	AP↑	**0.6397**±0.0141	0.6360±0.0076	0.5872±0.0126	0.6128±0.0118	0.5930±0.0071	0.5158±0.0108
	OE↓	0.3946±0.0183	**0.3900**±0.0106	0.4634±0.0178	0.4028±0.0183	0.4462±0.0099	0.5192±0.0192
	RL↓	**0.1407**±0.0069	0.1517±0.0061	0.1503±0.0051	0.1879±0.0054	0.1857±0.0042	0.2820±0.0071
	CV↓	**0.2245**±0.0116	0.2387±0.0115	0.2274±0.0069	0.2847±0.0064	0.2755±0.0061	0.3820±0.0090
	AUC↑	**0.8592**±0.0069	0.7723±0.0087	0.6280±0.0066	0.7098±0.0037	0.6449±0.0083	0.7222±0.0056
Yeast	HL↓	0.2055±0.0038	**0.2000**±0.0033	0.1955±0.0072	0.2608±0.0082	0.2008±0.0036	0.0585±0.0013
	AP↑	0.7504±0.0109	**0.7570**±0.0067	0.7626±0.0089	0.6102±0.0082	0.7587±0.0091	0.5158±0.0108
	OE↓	0.2407±0.0175	**0.2291**±0.0146	0.2304±0.0106	0.3583±0.0192	0.2275±0.0134	0.5192±0.0192
	RL↓	0.1727±0.0070	**0.1706**±0.0019	0.1717±0.0078	0.3463±0.0122	0.1696±0.0054	0.2820±0.0071
	CV↓	**0.4510**±0.0057	0.4534±0.0041	0.4543±0.0115	0.6233±0.0131	0.4530±0.0053	0.3820±0.0090
	AUC↑	**0.8272**±0.0070	0.7823±0.0010	0.7499±0.0089	0.6381±0.0107	0.6710±0.0036	0.6563±0.0096
Health	HL↓	**0.0301**±0.0012	0.0331±0.0008	0.0407±0.0011	0.0413±0.0006	0.0356±0.0010	0.0389±0.0009
	AP↑	**0.7840**±0.0073	0.7821±0.0062	0.7069±0.0088	0.7646±0.0098	0.7571±0.0059	0.6980±0.0094
	OE↓	0.2578±0.0138	**0.2510**±0.0068	0.3776±0.0121	0.2644±0.0109	0.2764±0.0141	0.3172±0.0162
	RL↓	**0.0609**±0.0040	0.0677±0.0041	0.0685±0.0045	0.0876±0.0044	0.0905±0.0034	0.1651±0.0060
	CV↓	**0.1183**±0.0078	0.1286±0.0072	0.1168±0.0074	0.1591±0.0060	0.1562±0.0035	0.2456±0.0067
	AUC↑	**0.9390**±0.0040	0.7906±0.0019	0.7011±0.0046	0.6954±0.0200	0.7199±0.0011	0.6435±0.0042
Reference	HL↓	**0.0004**±0.0268	0.0257±0.0008	0.0292±0.0004	0.0294±0.0010	0.0280±0.0006	0.0298±0.0014
	AP↑	0.0095±0.7090	**0.7135**±0.0033	0.6301±0.0078	0.7052±0.0072	0.6634±0.0129	0.5929±0.0173
	OE↓	**0.0122**±0.3760	0.3642±0.0090	0.4658±0.0084	0.3666±0.0088	0.4020±0.0144	0.4692±0.0178
	RL↓	**0.0045**±0.0891	0.0930±0.0047	0.0934±0.0047	0.1070±0.0060	0.1398±0.0087	0.2426±0.0149
	CV↓	**0.0069**±0.1134	0.1194±0.0079	0.1100±0.0057	0.1354±0.0072	0.1705±0.0104	0.2745±0.0171
	AUC↑	——	**0.7505**±0.056	0.6461±0.0035	0.7234±0.0093	0.6983±0.0023	0.6728±0.0003
Recreation	HL↓	0.0559±0.0014	**0.0535**±0.0011	0.9361±0.0016	0.0578±0.0008	0.0571±0.0013	0.0565±0.0003
	AP↑	**0.6436**±0.0125	0.6391±0.0043	0.4892±0.0039	0.6185±0.0097	0.5985±0.0148	0.5692±0.0097
	OE↓	0.4492±0.0199	**0.4444**±0.0092	0.6616±0.0071	0.4614±0.0102	0.4890±0.0248	0.5056±0.0113
	RL↓	**0.1416**±0.0027	0.1485±0.0037	0.1830±0.0015	0.1741±0.0107	0.1868±0.0045	0.2446±0.0075
	CV↓	**0.1898**±0.0048	0.1992±0.0059	0.2221±0.0028	0.2277±0.0123	0.2392±0.0044	0.2968±0.0088
	AUC↑	**0.8583**±0.0055	0.8022±0.0071	0.5339±0.0017	0.6991±0.0189	0.7764±0.0080	0.6101±0.0019

Note: "↑" ("↓") means that the larger (smaller) the evaluation index is, the better. The best results are displayed in bold magnification.

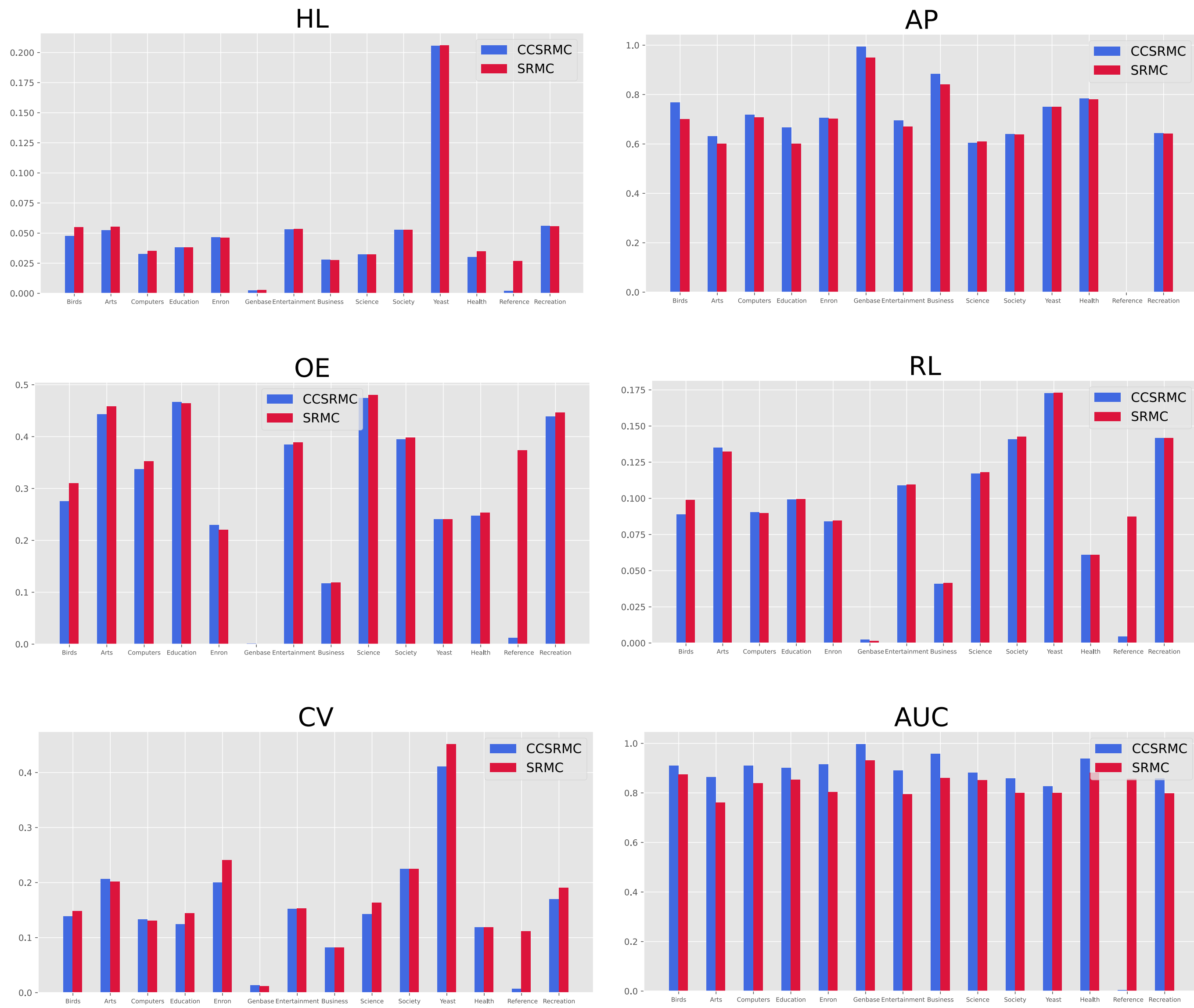

Fig. 3. Ablation Analysis of CCSRMC and SRMC on 6 Evaluation Indexes.

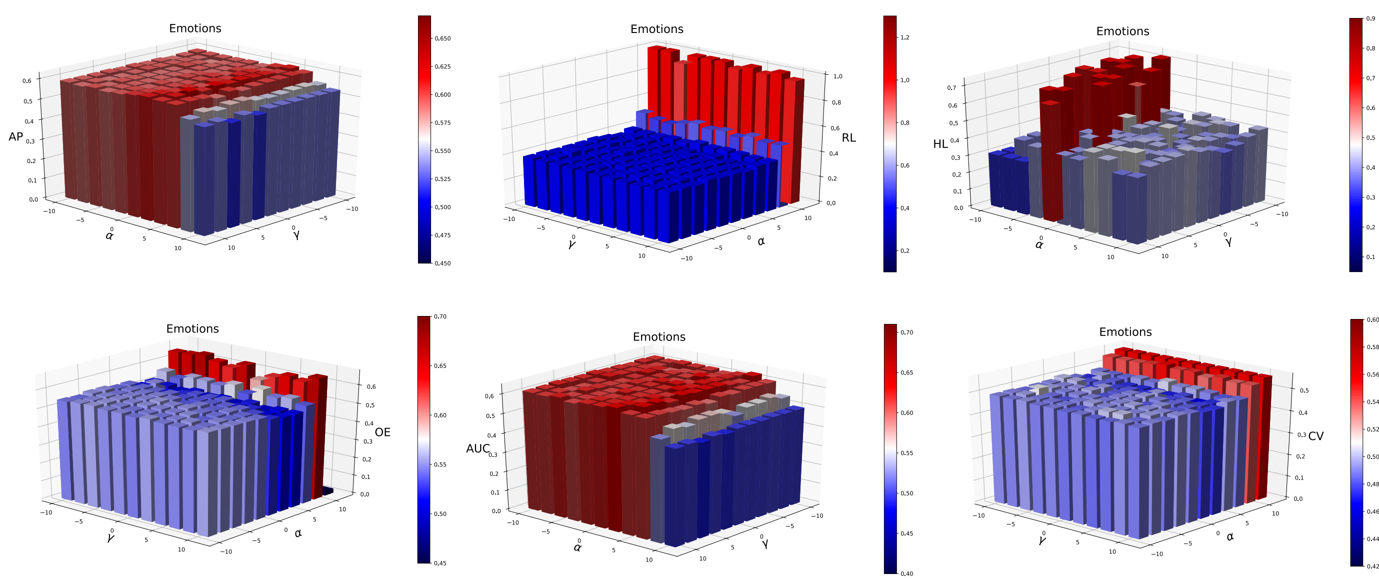

Fig. 4. Parameter Sensitivity Analysis Units.

the learning effect of label-specific features decreases. For AP and CV evaluation indexes, it can be found that the changes of the parameters α and γ have a relatively stable influence on the algorithm. In the RL evaluation index, we observe that when the parameter $\alpha > 2^8$, the performance of the algorithm drops rapidly. In the OE evaluation index, we found that as the parameter α increases, the performance of the algorithm first increases and then decreases. In the interval $[2^{-10}, 2^0]$, the performance of CCSRMC algorithm is relatively stable. Combining the sensitivity analysis of each parameter above, it is suggested that the parameter setting interval in this paper is $\alpha\epsilon[2^{-10}, 2^{-1}]$, $\beta\epsilon[2^{-10}, 2^{10}]$, $\gamma\epsilon[2^{-10}, 2^6]$.

D. Statistical Hypothesis Testing References and Footnotes

In this paper, the stability of the performance of CCSRMC and other comparative experimental algorithms on 14 datasets is compared by using the Nemenyi test [28] with a significance level of 5%. When the average ranking difference of the two comparison algorithms on all data sets is greater than the critical difference (*CD*), it is considered that there is a significant difference between the two algorithms, otherwise it is considered that there is no significant difference. The calculation formula of *CD* value is:

$$CD = q_\alpha \sqrt{\frac{k(k+1)}{6N}} \tag{42}$$

Where the significance level is $\alpha = 0.05$, $k = 6$, $N = 14$, $q_\alpha = 2.850$, so $CD = 2.2518$.

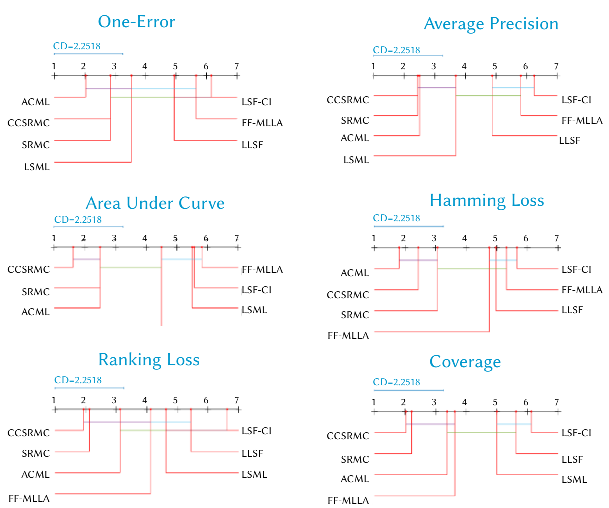

Fig.5. Parameter Sensitivity Analysis Units.

According to the results shown in Fig. 5. The higher the average ranking, the more dominant the algorithm. Compared with other comparison algorithms, the average rankings of CCSRMC are all the best on the four evaluation indexes of AP, AUC, RL, and CV. It is slightly inferior to the ACML algorithm on the OE and HL indexes. The average ranking of SRMC, which does not consider the interactive causal relationship between labels, is always inferior to CCSRMC. The validity and rationality of introducing interactive causal label correlation in the multi-label algorithm is again verified. In the OE index, the CCSRMC algorithm is significantly different from LSF-CI, FF-MLLA, and ACML. The average accuracy of CCSRMC is significantly different from LLSF, LSF-CI, and FF-MLLA. In the indexes of AUC and HL, CCSRMC is significantly different from other comparison algorithms except ACML. In the indexes of AUC and HL, CCSRMC is significantly different from other comparison algorithms except ACML. In terms of RL and CV evaluation indexes, LLSF, LSF-CI, LSML are all significantly different from CCSRMC. The results of Nemenyi test are consistent with the basic results of experimental analysis. The results of the Nemenyi test further verify the performance of the algorithm in this paper, which shows that the introduction of interactive causal inference in multi-label learning is reasonable and effective.

VI. Conclusion

This article is using the spatial reshaping method to transform the original discrete label into a continuous label. On the basic of solving the problems that the existence of logical label cannot describe the importance of different labels and cannot fully represent semantic information, the label co-occurrence matrix is constructed by combining the conditional probability test method. The label co-occurrence matrix and the label correlation matrix are combined to construct the label interactive causal correlation matrix to perform multi-label classification learning on the obtained numerical label matrix. It avoids the problem that the distance failed to measure high-dimensional space and the parameter depends on manual selection. The experimental results show that the method has a certain validity. The accuracy of multi-label classification is improved. What's more, the interactive causal situation of the correlation between the labels is considered to reduce the redundant information in the classification model. However, the method we proposed still needs improvement. For example, the problem of missing labeling and wrong labeling caused by the default of label data may affect the accuracy of interactive causal inference. The method in this paper only considers the dependency relationship between paired variables (a set of labels or labels and features), while ignoring the influence of factors such as confounding variables. The experimental results on the image data set show that only considering the dependency between paired variables is not suitable for more complex scenarios. The use of continuous labels for training should cooperate with an appropriate dynamic threshold selection mechanism. Each comparison algorithm does not fully consider the label distribution of each sample. Although the introduction of interactive causal inference in multi-label learning has achieved certain results, the method adopted is relatively simple. Thus, further study and research are necessary.

Acknowledgment

This work was supported by the National Natural Science Foundation of Anhui under Grant 2108085MF216 and Key Laboratory of Data Science and Intelligence Application, Fujian Province University (NO. D202005).Key Laboratory of Intelligent Computing & Signal Processing, Ministry of Education (Anhui University) (No.2020A003) and Anqing Normal University Graduate Innovation Fund(No.2021yjsXSCX017).

References

[1] Y. B. Wang, W. J. Zheng, Y. S. Cheng, T. C. Cao, "Multi-label classification algorithm based on PLSA learning probability distribution semantic information", *Journal of Nanjing University (Natural Science)*, vol.57, no.1, pp.75-89, 2021.

[2] J. Huang, F. Qin, X. Zheng, "Learning label-specific features for multi-label classification", *Information Sciences: An International Journal*, vol. 492, no.18, pp.124-146, 2019.

[3] H. R. Han, M. X. Huang, Y. Zhang, X. G. Yang, W. G. Feng, "Multi-label learning with label specific features using correlation information", *IEEE Access*, vol.19, no.7, pp. 11474–11484, 2019.

[4] M. L. Zhang, L. Wu, "Multi-label learning with label-specific features", *IEEE Transactions on Pattern Analysis and Machine Intelligence*, vol.37,

no.1, pp. 107–120, 2015.

[5] J. Huang, F. Qin, X. Zheng, "Improving multi-label classification with missing labels by learning label-specific features", *Information Sciences: An International Journal*, vol.492, pp.124–146, 2019.

[6] Y. S. Cheng, K. Qian, Y. B. Wang, D. W. Zhao, "Multi-label lazy learning approach based on firefly method", *Journal of Computer Applications*, vol.39, no.5, pp.1305–1311, 2019.

[7] G. M. Zhang, B. Y. Long, J. X. Zeng, J. Y. Huang, "Zero-shot attribute recognition based on de-redundancy features and semantic relationship constraint", *Pattern Recognition and Artificial Intelligence*, vol.34, no.9, pp.809-823, 2021.

[8] J. C. Bao, Y. B. Wang, Y. S. Cheng, "Asymmetry label correlation for multi-label learning", *Applied Intelligence*. Prepublish (2021), doi:10. 1007/S10489-021-02725-4.

[9] D. D. Lai, Z. H. Luo, Y. L. Ma, "Label order optimization method of classifier chains based on co-occurrence analysis", *Systems Engineering and Electronics*, vol.43, no.9, pp.2526-2534, 2021.

[10] C. X. Yan, S. G. Zhou, "Effective and scalable causal partitioning based on low-order conditional independent tests", *Neurocomputing*, vol.389, no.14, pp.146-154, 2020.

[11] X. S. Yin, T. Shu, Q. Huang, "Semi-supervised fuzzy clustering with metric learning and entropy regularization", *Knowledge-based systems*, vol.35, pp.304-311, 2012.

[12] W. B. Qian, Y. S. Xiong, J. Yang, W. H. Shu, "Feature selection for label distribution learning via feature similarity and label correlation" *Information Sciences*, vol.582, pp.38–59, 2022.

[13] Y. S. Cheng, C. Zhang, S. F. Pang, "Multi-label space reshape for semantic-rich label-specific features learning", *International Journal of Machine Learning and Cybernetics*, vol.13, pp.1005–1019, 2022, doi:10.1007/s13042-021-01432-3.

[14] A. Kale, Y. F. Wu, J. Hullman, "Causal support: modeling causal inferences with visualizations", *IEEE transactions on visualization and computer graphics*, 2021, doi:10.1109/TVCG.2021. 3114824.

[15] X. J. Song, A. Taamouti, "Measuring granger causal ity in quantiles", *Journal of Business & Economic Statistics*, vol.39, no.4, pp.1-48, 2021.

[16] De La Pava Panche Iván, Álvarez Meza Andrés, Herrera Gómez Paula Marcela, Cárdenas Peña David, Ríos Patiño Jorge Iván, Orozco Gutiérrez Álvaro, "Kernel-based phase transfer entropy with enhanced feature relevance analysis for brain computer interfaces", *Applied Sciences*, vol.11, no.15, pp.6689-6689, 2021.

[17] Z. C. Sha, Z. M. Liu, C. Ma, J. Chen, "Feature selection for multi-label classification by maximizing full-dimensional conditional mutual information", *Applied Intelligence*, vol.51, no.1, pp.326-340, 2020.

[18] X. Y. Li, H. L. Wang, B. Y. Wu, "A stable and efficient technique for linear boundary value problems by applying kernel functions", *Applied Numerical Mathematics*, vol.172, no.1, pp.206-214, 2022.

[19] G. J. Székely, M. L. Rizzo, N. K. Bakirov, "Measuring and testing dependence by correlation of distances", *The Annals of Statistics*, vol.35, pp.2769–2794, 2007

[20] R. C. Cai, Y. M. Bai, J. Qiao, Z. F. Hao, "Causal inference method based on confounder hidden compact representation model", *Journal of Computer Applications*, 2021, doi:10.11772/j.issn.1001-9081.2020 122066.

[21] Z. H. Zhou, M. L. Zhang, "Multi-label learning", *Encyclopedia of Machine Learning and Data Mining, Berlin*, 2016, pp.875–881, Springer.

[22] Y. B. Wang, W. J. Zheng, Y. S. Cheng, D. W. Zhao, "Joint label completion and label-specific features for multi-label learning algorithm", *Soft Computing*, vol.24, pp.6553–6569, 2020.

[23] A. Beck, M. Teboulle, "Fast gradient-based algorithms for constrained total variation image denoising and deblurring problems", *IEEE transactions on image processing*, vol.18, no.11, pp.2419–2434, 2009.

[24] G. C. Liu, Z. C. Lin, Y. Yu, "Robust subspace segmentation by low-rank representation", *Proceeding Twenty-Seventh International Conference on Machine Learning*, 2010, pp.663–670.

[25] Z. C. Lin, A. Ganesh, J. Wright, L. Q. Wu, M. Chen, Y. Ma, "Fast convex optimization algorithms for exact recovery of a corrupted low-rank matrix", *UIUC Technical Report* 2009, vol.09, pp.2214.

[26] Z. H. Zhou, M. L. Zhang, "A Review on multi-label learning algorithms", *IEEE Transactions on Knowledge and Data Engineering*, vol.26, no.8, pp.1819–1837, 2014.

[27] W. Weng, Y. J. Lin, Y. W. Li, "Online multi-label streaming feature selection based on neighborhood rough set", *Pattern Recognition: The Journal of the Pattern Recognition Society*, vol.84, no.1, pp.273–287, 2018.

[28] J. Demiar, D. Schuurmans, "Statistical comparisons of classifiers over multiple datasets", *Journal of Machine Learning Research*, vol.7, no.1, pp.1–30, 2006.

Chao Zhang

Graduate student of computer and Information College, Anqing Normal University. His main research includes machine learning, data mining and statistics.

Yusheng Cheng

Professor of computer and Information College, Anqing Normal University. He received his Ph.D. in the School of Computer and Information Science of Hefei University of Technology in 2007. His research interests concern the rough set theory and algorithm, semi supervised learning and data mining. He is the author of more than 50 papers in journals and conference proceedings such as Information Science, Knowledge-Based Systems, Neurocomputing, Applied Soft Computing, PAKDD and so on.

Yibin Wang

Professor of computer and Information College, Anqing Normal University. The main research directions include multi label learning, machine learning and software security.

Yuting Xu

Graduate student of computer and Information College, Anqing Normal University. Her main research includes machine learning, data mining and statistics.

unir
LA UNIVERSIDAD
EN INTERNET

Rectorado
Avenida de la Paz, 137
26006 Logroño (La Rioja)
t (+34) 941 21 02 11

www.unir.net